UNIVERSITÀ DEGLI STUDI DI BOLOGNA

FACOLTÀ DI SCIENZE MATEMATICHE FISICHE E NATURALI
DOTTORATO DI RICERCA IN FISICA, XV CICLO

PhD Thesis

The ALICE TOF (Time-Of-Flight): a powerful detector for relevant observables in nucleus-nucleus collisions at LHC

ANNALISA DE CARO

Advisor:
Prof. LUISA CIFARELLI

PhD Coordinator:
Prof. ROBERTO SOLDATI

Bologna, 2004

UNIVERSITÀ DEGLI STUDI DI BOLOGNA

FACOLTÀ DI SCIENZE MATEMATICHE FISICHE E NATURALI
DOTTORATO DI RICERCA IN FISICA, **XV** CICLO

PhD Thesis

The ALICE TOF (Time-Of-Flight): a powerful detector for relevant observables in nucleus-nucleus collisions at LHC

ANNALISA DE CARO

Advisor:
Prof. **LUISA CIFARELLI**

PhD Coordinator:
Prof. **ROBERTO SOLDATI**

Key words: ALICE, Time-Of-Flight, MRPC, QGP, ϕ meson

Bologna, 2004

Contents

List of Figures

List of Tables

Introduction

ALICE (**A** **L**arge **I**on **C**ollider **E**xperiment) is a future experiment at the CERN LHC (**L**arge **H**adron **C**ollider), optimized for the study of heavy-ion collisions at a centre-of-mass energy of $\sim 5.5\,TeV$ *per nucleon pair*.

The primary goal of the experiment is to study the behaviour of nuclear matter at high densities and temperatures, in view of detecting the transition of the hadron matter to the QGP (**Q**uark **G**luon **P**lasma) phase.

Particle identification (PID) over a large part of the phase space and for many different particles is an important design feature.

The largest detector system for the PID in ALICE is the TOF (**T**ime-**O**f-**F**light) detector, covering $\sim 170\,m^2$ of surface in the central acceptance region $|\eta| \lesssim 1$.

Here an original work on the performance of the ALICE TOF detector is presented.

In chapter 1 an introduction is given about the physical motivation for the heavy ion collision study; some *historical* results from the fixed target experiments at the CERN SPS (**S**uper **P**roton **S**ynchrotron) and some recent results from the running experiments at the Brookhaven RHIC (**R**elativistic **H**eavy **I**on **C**ollider) are also presented. Particular attention is reserved to the results on ϕ *meson* detection since the observation of this resonance may indeed probe the QGP formation.

A description of the ALICE setup and, more specifically, of its components in the central acceptance (barrel) region is illustrated in chapter 2.

Chapter 3 contains a review of the R&D activities which have led to the choice of the MRPCs (**M**ultigap **R**esistive **P**late **C**hambers) as basic elements for the ALICE TOF detector, and to the definition of their final configuration.

The ALICE TOF detector performance in terms of acceptance, occupancy and PID capability, together with the details of the offline data processing, are reported in chapter 4.

Finally, chapter 5 illustrates a Monte Carlo simulation study on ϕ *meson* detection via charged *kaon* identification. The importance of a time-of-flight detector with the features of the ALICE TOF in a very high energy heavy-ion collision experiment is discussed.

Chapter 1

Heavy Ion Collisions

1.1 Quantum ChromoDynamics

Although the existence of *quark* substructure in *hadronic* matter was experimentally verified several decades ago through evidence from deep inelastic scattering of *electrons* on *nucleons* [1], *quarks* have not been observed outside the confines of *hadronic* particles.

Strongly interacting matter is described through a non-Abelian gauge theory, called Quantum ChromoDynamics (QCD); it describes the interaction between *quarks* mediated by *gluons* that carry the colour quantum number. The effective coupling constant for strong interaction, α_s, has the following first-order expression:

$$\alpha_s(Q^2) \approx \frac{12\pi}{(33-2n_f)\ ln(\frac{Q^2}{\Lambda^2_{QCD}})} \tag{1.1}$$

where n_f is the number of *quark* flavours and $\Lambda_{QCD} \approx\ 200\ MeV$ can be interpreted as the energy scale at which the strong force becomes important. The QCD exhibits a number of remarkable features:

- at distances of the order of the size of a *hadron* ($\sim 1\ \ fm$), *quarks* do not occur isolated in nature but only confined in singlet colour (and spin) *hadronic* states as *mesons* (for instance: $\bar{u}_{antired}d_{red}$) and *baryons* (for instance: $u_{red}u_{blue}d_{green}$), effect known as *quark confinement*;
- at larger distances (or smaller momenta), *quarks* do not appear as nearly massless constituents but are endowed with a dynamically, non-perturbatively

generated mass of several hundreds of *MeV* presumably due to *chiral symmetry breaking*;

- at shorter distances (or larger momenta), *quarks* are said to be free inside a *hadron*, effect known as *asymptotic freedom*;
- at low energy, the QCD vacuum is characterized by nonvanishing expectation values of certain operators, usually called vacuum condensates, which characterize the nonperturbative physical properties of the QCD vacuum. The most important here are:
  - the *quark* condensate ($\bar{\psi}\psi \approx (235\ MeV)^3$), which describes the density of *quark*-anti*quark* pairs found in the QCD vacuum and may derive from chiral symmetry breaking, and
  - the *gluon* condensate ($\alpha_s G_{\mu\nu} G^{\mu\nu} \approx (500\ MeV)^4$), which measures the density of *gluon* pairs in the QCD vacuum and is a manifestation of the *scale invariance breaking* of QCD by quantum effects.

1.2 Quark Gluon Plasma

It is common in nature that spontaneously broken symmetries are restored at high temperature or density through phase transitions; well known examples are ferromagnetism, superconductivity, Mott transition, liquid-gas, liquid-solid, etc..

The colour confinement (see §1.1) should disappear at sufficiently high temperature and/or density values, as it can be argued from the analogy with the Debye charge screening phenomenon in atomic matter.

In a dense atomic medium, the Coulomb potential felt by an orbitating *electron* is modified by the overlapping of the atomic orbits, according to the formula:

$$V(r) \to V'(r) = V(r)\ exp\left(-\frac{r}{r_D}\right) \tag{1.2}$$

where r_D is the Debye screening radius and r is the electron distance from the nucleus. In a conductor r_D is smaller than the distance between the centre of the atom and the outermost electrons which feel a smaller electrical field so that they behave as deconfined from the atom and are free to move inside the material. In a insulator material, r_D is larger than the radius of the atom, so that the *electrons* are confined each around its own nucleus. Since r_D is inversely proportional to the matter density ρ and to the temperature T, increasing ρ or T, r_D becomes smaller and the insulator material may undergo a phase transition to conductor.

For the same reason, in a medium characterized by a very high density of colour charge or very high temperature, a screening effect should affect the potential between the *quarks*: r_D becomes smaller than the radius of the *hadron* and the binding force cannot hold the *quarks* inside the *hadron* volume anymore. This results in a phase transition from a “colour insulator” phase to a “colour conducting” phase, where the coloured *quarks* and *gluons* are deconfined and free to move over larger space-time volumes than a *hadron* volume: this is the Quark Gluon Plasma (QGP) phase.

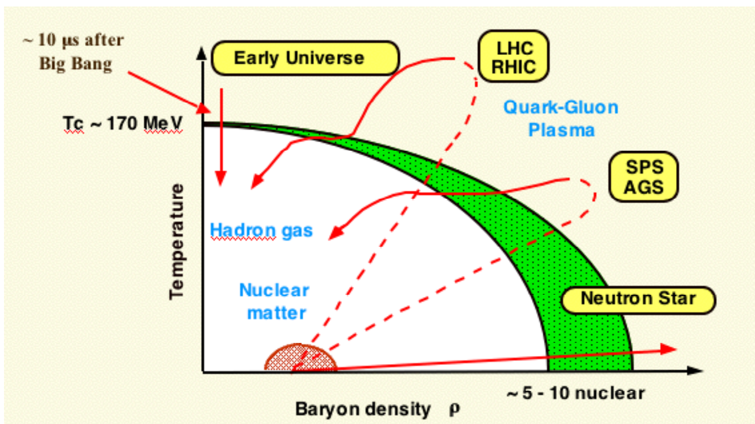

Figure 1.1: Phase diagram of temperature versus baryon density for *hadronic* matter.

The theoretical study of the conditions for the phase transition and of the properties of the QGP state cannot be performed using the perturbative QCD calculations because the perturbative approach can only be applied for small values of α_s. When studying nuclear matter under extreme density and/or temperature conditions, the perturbative approach has to be replaced by phenomenological models or by lattice QCD calculations, which simulate the QCD equation of state on a finite discretized volume of space-time.

Reliable predictions concerning the phase transition, obtained from the lattice calculations, indicate a critical temperature $T_c \sim 150 \div 200\ MeV$ at vanishing net *quark* density. Chiral symmetry, broken in standard *hadronic* matter, is also expected to be restored at high *baryon* density even at zero temperature; many model studies of this phenomenon have been performed, yielding critical densities $\rho_c \sim 5 \div 10\ \rho_0$, where $\rho_0 \sim 0.15\, nucleons/fm^3$ is the nuclear density.

Then, one expects a smooth connection between the high-T and high-ρ phase transitions, giving rise to a continuous phase boundary $T_c(\rho)$. The phase diagram of strongly interacting matter is shown in fig. 1.1, as obtained from thermodynamical models in the plane of temperature and net baryon density.

1.3 Heavy Ion Collisions and QGP conditions

Is it possible to realize a phase transition from ordinary *hadronic* matter to a QGP?

A QGP may have a place in the Universe. It is thought that at about $10^{-5}\ s$ after the Big Bang, before the Universe had expanded and cooled enough for the formation of the *hadronic* matter that exists today, the dominant state of matter was a QGP [2].

It has been proposed that at the centre of some neutron stars, the extreme gravitational pressure may result in a QGP core that affects their rotational behaviour, which can then be observed by radio astronomy [3].

To explore experimentally the possible existence of the QGP, it is necessary to create a strongly interacting system which satisfies the following requirements:

- the system should be studied using macroscopic variables: then a big system (with a size much larger than the confinement scale) consisting of **many particles** is required;

- the system should be studied using thermodynamics, then it must be in equilibrium. To reach the equilibrium condition, the system must have **a lifetime greater than the thermalization time** (which in general decreases in denser systems). To remain in equilibrium, the system must be sufficiently interacting, then the mean free path of the costituents must be smaller than the system dimensions, so that several collisions per particle can occur;

- the system must have an energy density and/or a baryon density greater than the critical values ε_c and ρ_c.

Nucleus-nucleus collisions at very high energy provide the means of creating *hadronic* states with high density and/or temperature fullfilling all these demanding requirements. For example, in a $^{208}Pb -^{208}Pb$ collision, there are

$2 \times 3 \times 208 \simeq 1000$ initial valence *quarks* available for interaction. Then, to realize a phase transition from *hadronic* matter to a QGP, the energy density and/or the baryon density must increase just to exceed the critical values.

Physicists from around the world use heavy ions accelerated to ultrarelativistic energies to try to produce the QGP in laboratory. The European Laboratory for Particle Physics (CERN) employs the Super Proton Synchrotron (SPS) and is building the Large Hadron Collider (LHC) due to come in operation in 2007. The Brookhaven National Laboratory (BNL) employs the Alternating Gradient Synchrotron (AGS) and the Relativistic Heavy Ion Collider (RHIC), now in operation. The beam species and momenta, the centre-of-mass (CM) energies, the beam longitudinal dimension Lorentz-contraction factors and the beam and target *rapidity* (see §1.4.1) are reported in table 1.1 for these facilities. The SPS and AGS are fixed target facilities, whereas both RHIC and LHC are colliders with beams travelling in opposite directions and leading to a considerably higher E_{CM}.

Accelerator/ Collider	Projectile species	p_{beam} $[AGeV/c]$	E_{CM} $[AGeV]$	γ_{beam}	γ^*_{beam} γ^*_{target}	y_{beam}	y_{target}
AGS	Au	11.6	4.84	12.4	2.58	3.1	0
SPS	S	200	19.5	213	10.4	6.1	0
	Pb	158	17.2	168	9.17	5.8	0
RHIC	Au	100	200	107	107	5.3	-5.3
LHC	Pb	2750	5500	2930	2930	8.7	-8.7

Table 1.1: Heavy ion facilities: ion beam characteristics. The γ^*_{beam} and γ^*_{target} values are calculated in the CM frame. The beam momentum (p_{beam}) and CM energy (E_{CM}) values are given per nucleon and per nucleon pair, respectively.

A summary of measurements, predictions or estimates for global event features in $Pb-Pb$ collisions is given in table 1.2 [4].

At LHC energy, the thermalization time (τ_0^{QGP}) of the dense medium is decreased. The reason is twofold: *i*) the increased interaction rate at higher parton density; *ii*) the reduced formation time of harder partons ($\propto 1/p_T$, at higher p_T). A decreased τ_0^{QGP} leads to extreme energy densities ($\varepsilon(\tau_0) \propto 1/\tau_0$) and temperatures at very early times during the collision. As the dense medium has to expand and cool to freeze-out conditions (which are similar at all energies), the QGP lifetime (τ_{QGP}), freeze-out time (τ_{fo}) and final (local) freeze-out volume (V_{loc}) likewise increase. The large QGP lifetime might be particularly relevant in order

$Pb-Pb$	SPS	RHIC	LHC
$\tau_0^{QGP}[fm/c]$	1	0.2	0.1
$\varepsilon[GeV/fm^3]$	3	35	500
$\tau_{QGP}[fm/c]$	$\lesssim 2$	$2-4$	$\gtrsim 10$
$\tau_{fo}[fm/c]$	10	$20-30$	$30-40$
$V_{loc}[fm^3]$	few 10^3	few 10^4	few 10^5

Table 1.2: Global features in $Pb-Pb$ collisions.

to enhance signals relative to the QGP phase at LHC. In summary, at LHC more partons are available, their inelastic collisions get more frequent and more effective, and the thermalized high temperature phase is established more rapidly and lasts longer. Parton dynamics is expected to dominate the fireball[1] expansion and the collective features of the hadronic final state [4, 5].

1.4 Experimental search of QGP

In the centre of mass frame, two Lorentz-contracted spheres in their flight direction (see table 1.1, fifth column), filled with *nucleons*, interpenetrate. In the initial phase of the microscopic *nucleon-nucleon* collisions, these QCD bound states get distrupted and spread out over phase space. These processes create a pre-equilibrium state of *partons* which still possess a preferential momentum orientation along the beam direction. *Partonic* rescattering will bring the reaction volume closer to a thermal distribution, with an approximate equipartition of momentum orientation, and also approaching a flavour equipartition among the three light *quark* species, *up*, *down* and *strange*. The energy density being high enough, this state may settle into the equilibrium plasma state of *quarks* and *gluons*: it is a QGP state. This phase will expand and cool until the phase transition point is reached where the *partons* recombine into *hadrons*. A decade of intense theoretical work has been devoted to the question how to define suitable observable features that might give evidence for the transient plasma and its phase transition by *hadronization*.

Moreover, experimental investigations of QGP require the identification of

[1]Region of excited *hadronic* matter.

appropriate experimental tools for observing its formation and studying its properties.

One serious problem is that the size and the lifetime of the QGP are expected to be small, i.e. at most a few fermi in diameter and $5 \div 10\ fm/c$ in duration (the time scale is the one of the strong interaction).

The QGP must undergo phase transition via hadronization into particles and resonances. According to some recent calculation results [6], a mixed *quark-hadron* phase could follow the QGP phase as a second-order phase tansition (see later on §1.4.1). In any case the spatial hadronic density would be very high and the hadrons will interact for some time among themselves (elastically and inelastically) until their spatial density decreases sufficiently and the final hadrons freeze-out. The evolution from the equilibrium plasma state to its characteristic phase transition into hadrons depends on an unknown pre-equilibrium partonic phase and is shadowed by a subsequent hadronic rescattering phase. Therefore, the QGP signals compete with backgrounds emitted from the hot *hadronic* gas phase that follows the *hadronization* of the QGP, and are modified by final state interactions in the *hadronic* gas. In spite of this, many proposals have been made on how the identification and investigation of the short-lived QGP could be accomplished.

1.4.1 QGP signatures

Connected to the possibility to observe a transition to a QGP phase by heavy ion collisions, different classes of QGP probes and signatures can be identified. Some of the most relevant ones will be briefly illustrated in the following [4, 5].

Kinematic probes

Kinematic probes aim at the determination of thermodynamical variables, namely the energy density, ε, and entropy density, s, of *hadronic* matter as a function of the temperature, T. These variables can be used to measure the number of degrees of freedom which should increase rapidly when going from a *hadron* gas to a QGP. One seeks to observe a rapid rise in the effective number of degrees of freedom over a small temperature range, i.e. a rapid rise of ε/T^4 (or s/T^4), shown in fig. 1.2. At LHC one could approach the Stefan-Boltzmann limit of an ideal gas of QCD quanta. In a heavy ion collison, measurable observables that are related to T, s and ε variables are respectively identified with the average transverse momentum, $<p_T>$, the *hadron* multiplicity, $\frac{dN}{dy}$, and the transverse energy[2], $\frac{dE_T}{dy}$, distributions in *rapidity*[3].

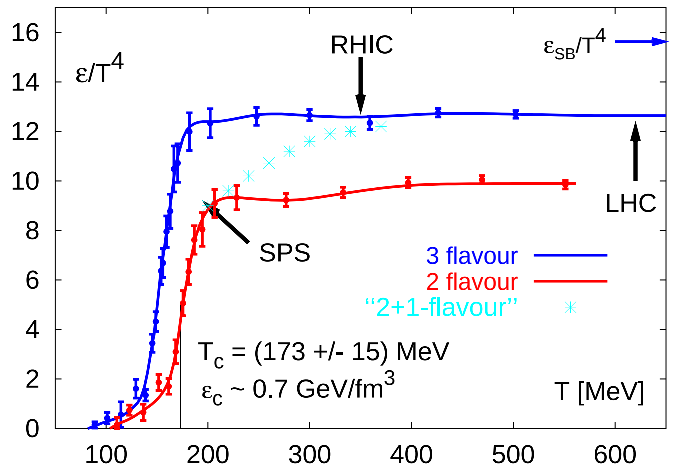

Figure 1.2: The ε/T^4 *versus* T, as resulting from calculations with three different models: 2− and 3− QCD flavours with light quarks and with 2 light and 1 heavier (*strange*) quarks.

[2]The transverse energy, E_T, is defined as:

$$E_T = E\,sin(\vartheta),$$

where ϑ is the polar angle.

[3]It is convenient to introduce the *rapidity* variable which transforms additively under Lorentz transformation:

$$y = \frac{1}{2}\,ln\left(\frac{E+p_z}{E-p_z}\right)$$

because distributions in *rapidity* have fixed shape and are simply shifted by a transformation between frames.

Since transformations are made along the beam direction, the transverse momentum of a particle, p_T, is the same in either the laboratory or CM frame. The transverse mass, m_T, is related to p_T via the following equation:

$$m_T = \sqrt{p_T^2 + m_0^2},$$

where m_0 is the rest mass of the particle considered. Therefore the transverse mass also is the same in either the laboratory or CM frame.

The energy density, ε, achieved in heavy ion collisions, can be estimated in two extreme scenarios.

In the total *baryon* stopping scenario, the colliding nuclei are expected to completly stop each other, leading to a *baryon* rich system[4]. In this regime, both nuclei occupy the same volume during the collision and the overall energy density in the CM frame is $\varepsilon = 2\gamma^2\varepsilon_0$, where γ is the Lorentz contraction factor, and ε_0 is the nuclear *baryon* density.

In the total transparence scenario, the slowed down *baryons* after the collision can still have enough momentum to proceed forward and escape from the central region, resulting in a situation with nuclear fragments well separated from the central region of particle production. In this case, a large amount of energy is deposited in a small region of space in a short duration of time[5]. The energy density is related to the total transverse energy that is produced orthogonal to the beam direction per unity of *rapidity*, $\frac{dE_T}{dy}$, at mid-rapidity, or to the particle multiplicity, $\frac{dN}{dy}$, at mid-rapidity,

$$\varepsilon = \frac{1}{\mathscr{A} c\tau_0}\left(\frac{dE_T}{dy}\right)_{y=0} = \frac{< m_T >}{\mathscr{A} c\tau_0}\left(\frac{dN}{dy}\right)_{y=0} \tag{1.3}$$

where $\mathscr{A}$ is the transverse overlapping area in the collision of the two nuclei, and τ_0 is the QGP formation time.

The actual energy density obtained in these collisions is expected (and experimentally found) to lie in between these two extreme values, approaching the $\varepsilon \propto 1/\tau_0$ regime as the energy increases up to the LHC level.

As the incoming nuclei are slowed down during the collision, the net baryon is typically distributed over $3-5$ units of rapidity. This gives a high baryon density at SPS (and AGS), while it is not sufficient to fill the central rapidity region at LHC which will have a vanishing baryochemical potential μ_b[6] (comparable to the early Universe). RHIC results seem to indicate that a small baryon excess still persists, however with $\mu_b/T \ll 1$. Therefore, depending on the energy, different regions of the phase diagram are explored (see fig 1.1).

[4]Landau scenario: full stopping.

[5]Bjorken scenario: total transparence.

[6]The baryochemical potential of a system is:

$$\mu_b = \frac{dE}{dN_B},$$

where E and N_B are the total energy and baryon number.

Another feature of LHC collisions (and to a smaller extend of RHIC collisions) is the foreseen parton saturation effect. The density of low-x partons both in the incoming and outgoing nuclei after scattering is so high that the phase space for low momentum partons nearly saturates and gluon merging becomes important. This gives access to a novel regime where strong nuclear gluon shadowing is expected and where, due to phase space saturation, classical QCD might be applicable to describe the subsequent time evolution.

The temperature at thermal freeze-out (T_{fo}) can be extracted from the transverse mass distribution for identified particles. The transverse mass distributions exhibit a typical thermal spectrum:

$$f(m_T) \sim exp\Big(-\frac{m_T}{T}\Big).$$

The inverse slope of the transverse mass (or transverse momentum) distribution is connected to the temperature of the system at the time of decoupling.

Generally, the measured temperature parameters for non *strange hadrons* are well understood by a common thermal freeze-out temperature, $T_{fo} \approx 140 MeV$. The common value of T_{fo} indicates that the fireball has thermalized. To each particle from the expanding fireball a transverse velocity boost is given and this implies a $blue-shift$ of the apparent temperature related to T_{fo} by:

$$T = T_{fo} + \frac{1}{2} m_0 \beta_T^2, \tag{1.4}$$

where β_T is the transverse velocity. Hence pion/kaon/proton identification will be an essential tool to provide information in terms of particle spectra and particle ratios about the chemical composition of the exploding fireball.

In addition to the main kinematic probes, i.e. particle multiplicities and spectra, other relevant probes should be mentioned.

A rapid increase of pressure in the QGP phase has as consequence a fast collective expansion of the system, hence the development of a large outward flow. This could be observed via modifications of particle spectra, in particular for heavier particles, namely by measuring the anisotropy of the p_T spectra relative to the reaction plane in non central collisions.

Information about the geometry of the collision and about the collective expansion may be obtained via interferometry measurements, i.e. studying Bose-Einstein correlations for identical particles. The two-(spin 0) particle correlations in three different directions with respect to the particle momenta (i.e. in the so called “out-side-long” coordinate frame, according to the Hanbury-Brown-Twiss formalism) will allow to measure the size of the fireball (i.e. the particle source) and to give insight into its expansion dynamics. Also in this respect, particle (boson/fermion) identification will be very relevant.

Hard probes

Hard probes, in particular high-p_T $jets$ and heavy *quarks*, are formed at very early times and will therefore test the surrounding dense medium.

Apart from *quarkonia* studies (see later on), open *charm* and *beauty* production at LHC will contribute in a very relevant way to the “chemical analysis” of $parton$ or *hadron* ratios, limited so far to up, *down* and *strange* quarks. This will help disentangling the different stages of the fireball, from pre-equilibrium to hadronization. $Pion/kaon/proton$ identification will of course play a basic role to detect open heavy-flavoured states.

At high energies, partons distributed inside the *hadronic* projectiles interact via hard two-to-two processes where the initial momentum is transferred to the final state partons (or $photons$). These final-state, coloured $partons$ radiate energy and hadronize into colourless *hadrons* thus producing clusters of particles with limited relative momentum ($\sim 200 MeV/c$), called $jets$ or mini$jets$ (if the CM energy of the $parton$ process is small with respect to the CM energy of the *hadronic* interaction). At LHC hard processes will sizably contribute to the total inelastic cross section and may play an important role in understanding the thermalization and thermal evolution of the system. The hight E_T or p_T $partons$ produced in the initial stage of the nucleus-nucleus collision will suffer multiple scattering and energy loss prior to fragmentation into *hadrons*. Hence, these “jet quenching” phenomena will probe the properties of the medium produced in the collision. They would be different for $quark-$ or $gluon-induced\ jets$, thus causing, not only a reduction in the yield of high-p_T particles, but also a modification of the ratios of *hadronic* species (for instance: $\bar{p}/p$).

Event-by-event probes

A unique feature of heavy ion collisions is the possibility to measure a number of observables on an event-by-event (E-by-E) basis, for instance particle (π, K, p) p_T-spectra, particle ratios and charge ratios. Non statistical fluctuations of these observables are indeed interesting since they might be associated with critical phenomena very close to the phase transition. Dynamical fluctuations carrying the real information about the properties of the system can be disentangled from trivial volume fluctuations by using observables which are indipendent from the volume of the system, for instance the π^+/π^- ratio, or almost indipendent, like the K/π ratio. The accuracy of the E-by-E fluctuations increases inversely with the number of observed particles, i.e. as $1/\sqrt{N}$ (assuming Gaussian distributions, the physics information is in the width of the Gaussians). Therefore the identification of thousands of *hadrons* in each $Pb-Pb$ final state at LHC will be extremely promising also at the E-by-E level.

Electromagnetic probes

Photons and *lepton* pairs provide probes of QGP during the earliest and hottest phase of fireball in the QGP formation, since they are not affected by final *hadronic* state interactions. Unfortunately, these probes have rather small yields and must compete with relatively large backgrounds from *hadronic* processes, especially electromagnetic *hadron* decays.

Near the critical temperature, the spectrum of *photons* from QGP (mainly from the reaction $gq \to \gamma q$) is very similar to that from *hadron* gas (produced in reaction $\pi\rho \to \gamma\rho$), both in shape and intensity.

The thermal *lepton* pair yield from QGP competes with other *dilepton* sources. At lower effective masses (i.e. dilepton invariant masses), it will be dominated by *dilepton* decays of vector *mesons*, ρ and ω. The vector *mesons* themselves, especially the ρ, can be modified in *hadronic* dense matter (see later on in this section). At higher masses, the *dilepton* yield critically depends on the QGP thermalization time and actually provides a measure of this time. This in turn determines up to which effective mass the dilepton yield would be higher than that of Drell-Yan production. Depending on the scenario, the effective mass limit reaches $5 \div 10\,GeV$. It is worth noting that in this mass region a substantial contribution to the total *lepton* pair spectra might be due to semi-*leptonic* decays of *charm* particles, and for higher masses to semi-*leptonic* decays of *beauty* particles.

It should be noted that, at LHC, in principle also Z^0 and $W^{\pm}$, i.e. weakly interacting probes, would be available to investigate the nuclear parton distributions at very high Q^2.

Quarkonium suppression

This effect would probe deconfinement. As said before in this chapter, the potential between two heavy colour charges (*charm*-anti*charm*) in a dense medium of many other lighter colour charges (*up*, *down*, *strange*) reduces its range to the screening radius, r_D, due to the screening effect. In a QGP, before the c and $\bar{c}$ *quarks* reach the distance at which they would resonate, other *quarks* from the medium already appear in between them and as consequence the *charm quarks* rather fragment into *D mesons* than form a $c\bar{c}$ bound state.

This is a completely different situation from that for *strange quarks*, where we expect an enhancement of the ϕ production (see later on in this section). The $s\bar{s}$ pairs will be also screened; however, in this case, owing to the large *strangeness* density in a QGP, the *quarks* which appear in between s and $\bar{s}$ *quarks* trying to prevent the ϕ formation would be with a fair probability also *strange*. Contrary to *charm quarks*, *strange quarks* are easy to produce (see later on, $m_s \sim T_c$). Therefore, this screening mechanisms would not alter in any significant way the ϕ production.

It was predicted that the *charmonium* state production will be suppressed with a characteristic pattern [7]. Excited states of the $c\bar{c}$ system, such as Ψ' and χ_c, are more easily dissociated and should disappear as soon as the temperature exceeds T_c: current estimations say that Ψ' suppression begins at T_c, followed by χ_c suppression, at $1.1\,T_c$, and, finally, at $1.3\,T_c$, the J/Ψ completes the *charmonium* suppression. The Ψ' and χ_c decay in J/Ψ with substantial branching ratios [8].

Therefore, we can say that, as the conditions for a QGP formation are reached, a small suppression in J/Ψ production is expected; and then, as the energy density increases, we should observe a sizable drop (of about 40%) in the J/Ψ production.

Also in a purely *hadronic* scenario (without QGP) we expect a certain *charmo – nium* suppression due to interactions with comoving *hadrons*: the cross-section is relatively small but the interactions can be very important. A further *charmonium* suppression could take place if the $c\bar{c}$ pair stays for a sufficient time in an octet colour state: such a state has a larger *hadronic* cross-section due to its larger colour charge. These effects would explain the *charmonium* suppression just in the *hadronic* scenario.

In a plasma scenario, an additional ‘anomalous’ suppression of J/Ψ production is expected, however.

Similar considerations hold true for the heavier $b\bar{b}$ quarkonium system, with shorter screening lengths than for $c\bar{c}$. The dissociation temperature for the ϒ ground state is expected at say $2.5\,T_c$ and for the ϒ' right above T_c. At LHC the classical deconfinement signal, i.e. J/Ψ suppression, could be extended to the ϒ sector.

Strangeness enhancement

Strangeness enhancement was among the first signatures proposed for the possible observation of a QGP [9, 10, 11] (here again this effect will probe deconfinement). *Strangeness* is a good quantum number because it is conserved in strong interactions; *strange quarks* decay via the weak interaction, in a typical time of $10^{-10}\,s$, not important on the time scale of the QGP *hadronization*.

There are three reasons why *strangeness* should be enhanced in a QGP. Firstly, the *strangeness* production in a QGP occurs at a lower threshold energy than in a *hadronic* gas. The production probability of a $s\bar{s}$ pair in *hadronic* matter is small due to the relatively high mass of the *strange quark* ($m_s \sim 500\,MeV$). On the contrary, in a QGP environment, *strange quarks* would be more abundantly produced due to the mass decrease of the *s quark* induced by the (partial) chiral symmetry restoration ($m_s \sim 150\,MeV$, comparable to the transition temperature, T_c).

Secondly, if the *hadronic* matter is deconfined, the deconfinement volume is already occupied by many *u* and *d quarks*; as a consequence, the production of *u* and *d quarks* is suppressed due to the Pauli blocking. Then, the production of *s quarks* will be relatively enhanced.

The last reason for the *strangeness* enhancement in QGP is due to the addition of *gluon* fragmentation channels available for *strange quark* production. *Gluons* may produce $s\bar{s}$ pairs by *gluon* fusion ($gg \to s\bar{s}$) or by *gluon* splitting ($g \to s\bar{s}$). The cross section for *gluon* processes in a QGP is about an order of magnitude greater than *quark*-anti*quark* annihilation.

Consequently, the enhancement of produced *strange* particles should manifest itself in the *kaon* to *pion* ratio, $<K>/<\pi>$, which can be compared for *hadronic* gas and QGP[7]. Under the same assumptions, *strangeness* enhancement will be more pronounced for particles with more than one *strange quark*, i.e. the ϕ *meson* and the Ξ^- or Ω^- hyperons. Theoretical studies have shown that an enhanced

[7] The mean *kaon* yield,

$$<K> = \frac{K^+ + K^- + 2K_S^0}{4}$$

is found by summing all charged and neutral *kaons*, accounting for a contribution from the unmeasured K_L^0. The mean *pion* yield,

$$<\pi> = \frac{\pi^+ + \pi^- + \pi^0}{3} = \frac{\pi^+ + \pi^-}{2}$$

accounts for all *isospin pion* states in the same way.

strangeness content cannot be destroyed nor generated by interactions during the freeze-out phase. Fragmentation processes during the *hadronization* phase of the QGP can contribute significantly to the final abundances of *strange hadrons* but presumably this will not mask the *strangeness* enhancement as a QGP signature.

ϕ meson production

The ϕ *meson* is the lightest vector *meson* with hidden *strangeness*. In *hadronic* gas, the ϕ *meson* is believed to be produced mainly via a colour singlet *gluon* configuration ($ggg \rightarrow s\bar{s}$). The ϕ production through light *quark* pair annihilation ($q\bar{q} \rightarrow s\bar{s}$, $q = u$, d) is suppressed by OZI rule[8] [12]. In a QGP, there is also the promising mechanism mentioned in the previous section, namely $gg \rightarrow s\bar{s}$. The abundance of $s\bar{s}$ pairs in a QGP will enhance the ϕ yield during the QGP *hadronization* stage [13]. An enhancement of ϕ *meson* production has been proposed [13] as a direct signature of the QGP formation; hence the ratio $\phi/(\rho+\omega)$ and its variation with *baryon* density or energy density could be a relevant observable for QGP formation.

While the $<K>/<\pi>$ ratio gives an overall indication of the *strangeness* content in the final state of *hadronization*, the ϕ/π ratio, because of the ϕ *meson quark* content ($s\bar{s}$), may provide a more sensitive measure of the *strangeness* production during the plasma phase.

Another possible mechanism for ϕ production in a QGP is based on kaon coalescence [14]. During the final stage of QGP formation, the phase-space density of K and $\bar{K}$ is much higher than in a simple *hadronic* gas. Then ϕ *meson* production may proceed via the coalescence of *hadronic*-state *kaons* forming an $s\bar{s}$ bound state, $K+\bar{K} \rightarrow \phi$. Such a mechanism seems viable because it proceeds by the exchange of soft *gluons*. If, however, one considers that *kaons* are *spin* zero particles while the ϕ has *spin* one, it now becomes evident that the *kaons* coalescence model, although favoured when considering the magnitude of the coupling constant, may be unfavoured due to the constraints imposed by the *spin* quantum number. Experimentally, the ϕ/K ratio could provide an insight to the production mechanisms for the ϕ *meson* in a QGP[9].

[8] Not connected Feynman diagrams are suppressed. The origin of the suppression is believed to lie in the non-abelian nature of QCD: since the ϕ is produced by *gluons*, *gluons* must carry higher momenta and the coupling constant is smaller.

[9] *Kaons* are produced only via pair production, very few resonances decay into *kaons* when compared to *pions*.

Medium effects on hadron properties

These effects would probe chiral symmetry restoration. Chiral symmetry, the symmetry which acts separately on left- and right-handed fields in QCD, is spontaneously broken in nature, resulting in associated Goldstone bosons in the pion field as well as the observed *hadron* mass spectra. However, it is expected that the spontaneously broken part of chiral symmetry may be restored at high temperatures and densities [15].

One expected signal of the restoration of chiral symmetry is a change of the vector *meson* properties [15]. A change in the effective mass of daughter particles can change the effective lifetime, and consequently the observed width, of the parent particle that decays in nuclear medium. Such modifications could be accompanied by a measureable change in the branching ratio of mesons decaying in the medium. The light vector mesons (ρ, ω, ϕ) offer an especially promising channel for the study of chiral symmetry effects.

The ϕ is of particular interest as the sum of the daughter mass of its di-kaon decay channel is very close to the ϕ mass. As a result, even a small change in daughter or parent masses could measureably alter the decay channel [16].

The study of vector mesons through their leptonic decay channels, either e^+e^- or $\mu^+\mu^-$, should provide the cleanest signal of the changing masses as leptons interact with the nuclear medium predominantly electromagnetically. In contrast, decays to hadrons are affected by strong final state interactions that might manifest themselves as a change (namely, a decrease) in the branching ratios of ϕ meson decays into hadrons inside the nuclear medium [17].

In fact the detection of these resonances will play a role in the late-stage rescattering. When reconstructed through their hadronic decay modes, fewer resonances (than predicted from the hadronization temperature) are expected to be found. Due to rescattering of some of their decay products via strong, quasi-elastic collisions with other hadrons (in the time interval between hadronization and freeze-out), some of the original resonances turn out to be irreconstructable and their yields lower than the original ones. What is measured is then, not the original yield at hadronization, but the reduced one just before freeze-out. When the fraction of resonance decays that occur before the hadronic rescattering has ceased is substantial, the resonance invariant-mass spectrum can appear significantly broadened by collisions. If the resonances are reconstructed via leptonic decay products that do not rescatter, one can probe their decays during the early rescattering stage. Hence it will be interesting to compare the hadronic and leptonic decays of these resonances, in particular of the ϕ *meson* since its width increase due to collision broadening would likely be substantial.

Althrough the present list of QGP signatures is far from being exhaustive, it is clear that in order to detect a QGP the identification of the largest possible number of particles escaping in empty space after the QGP phase transition will be of crucial importance.

1.5 Main experimental results (AGS, SPS, RHIC)

As reported in table 1.1, the fixed-target experiments of the AGS and SPS facilities had space constraints to insert their various detector elements. Then, each detector had optimised its components to observe a few (or only one) QGP signatures. Whereas, the experiments at RHIC and LHC colliders (will) measure many variables at the same time.

Some *historical* results from the SPS and AGS era experiments will be presented (see §1.5.1-1.5.3), together with the first significant results from RHIC (see §1.5.4).

Results on the ϕ meson from the AGS up to latest measurements from RHIC are described in a devoted section (§1.5.5).

1.5.1 Dilepton production

Dielectron production

The NA45-CERES experiment [18] was a Ring Imaging Cerenkov (RICH) detector system measuring electron-positron pair spectra to identify effects on *hadron* masses and decays due to emission from the plasma state. It used a $158\,AGeV/c$ lead beam on gold target. It detected an enhancement by a factor 2.6 in the electron-positron reconstructed mass window $250 \div 700\,MeV/c^2$, with respect to the proton-berillium data (see fig. 1.3). This enhancement was more pronounced at low p_T.

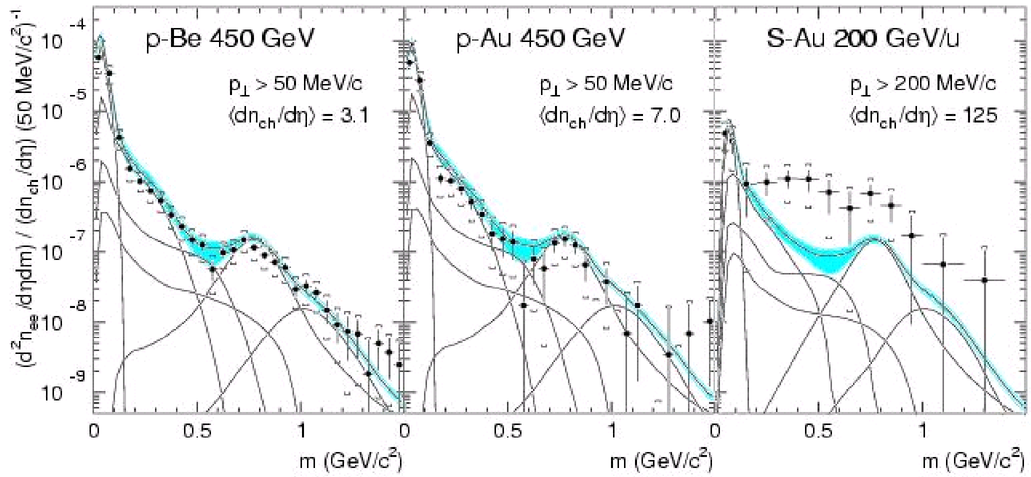

Figure 1.3: NA45/CERES experiment: invariant mass spectrum of e^+e^- pairs emitted in $158 AGeV/c$ $Pb-Au$ collisions. The solid line shows the expected yield from *hadron* decays, dashed lines indicate the individual contributions to the total yield.

Dimuon production

The NA38 [19] experiment, and the previous NA10 [20], its successor NA50 [21] and the further NA60 [22], consist in magnetic spectrometers to measure $\mu^+\mu^-$ pairs production in heavy ion collisions, investigating the predicted J/Ψ anomalous suppression and analyzing *muon* pair spectra to identify emission from the plasma state.

The NA38 experiment used the $450 GeV/c$ SPS *proton* beam and the new $200 AGeV/c$ oxygen and sulphur beams on different targets. NA50, instead, used the $200 AGeV/c$ lead beam on lead target. The NA60 experiment is equipped with a zero degree calorimeter for the new radiation level and new multiplicity.

These experiments observed an excess of *muon* pairs in the intermediate mass region, i.e. between the ϕ and the J/Ψ masses, with respect to the proton-nucleus data [23]. When they try to describe the dimuon mass spectra in this region by known sources (mixed event background, Drell-Yan and *charm* particle semi-*leptonic* decays), the data show an enhancement, which rises with the centrality of the collision, i.e. with the number of participating nucleons. The mass shape of these dimuons is compatible with that from open-*charm* particle semi-*leptonic* decays and thermal dimuons (see fig. 1.4), but much better measurements are needed.

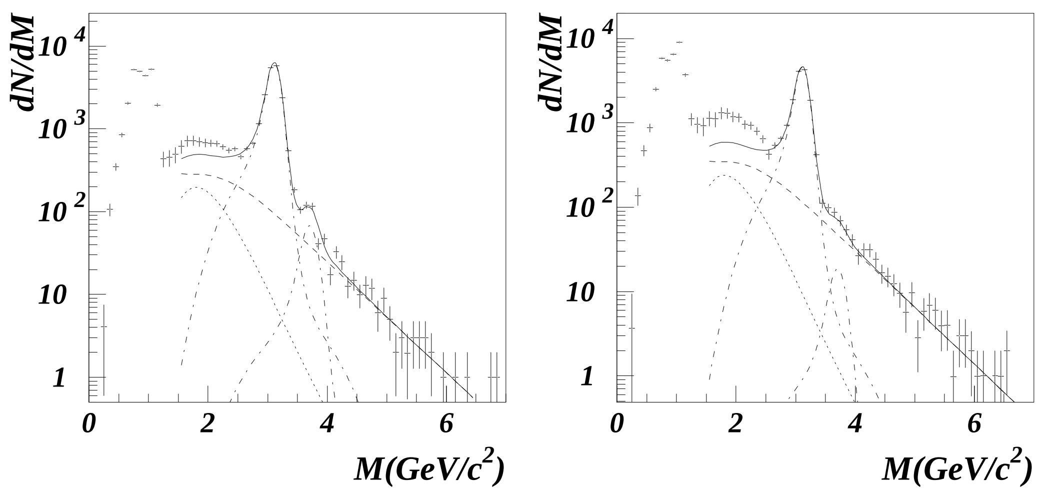

Figure 1.4: NA50 experiment: dimuon effective mass spectra for peripheral (number of participating nucleons around 110), on the left, and central (number of participating nucleons around 380), on the right, $Pb-Pb$ collisions after background subtraction. Superimposed the known sources: Drell-Yan (dashed line), open *charm* (dotted line), J/Ψ and Ψ' decays (dashed-dotted lines) and the total (full line).

1.5.2 J/Ψ suppression

NA38 results show a J/Ψ suppression compatible with the usual nuclear absorbtion; whereas NA50 results show a behaviour compatible with the *hadronic* absorption for peripheral collisions, but an absolutely anomalous suppression in high centrality production (see fig. 1.5).

The new experiment which is going to continue and to improve the NA38/NA50 studies is NA60. The detector complements the *muon* spectrometer and the zero degree calorimeter previously used in NA50 with two new silicon detectors placed in the target region (a radiation hard beam tracker and a silicon microstrip telescope). Besides studying prompt *muon* pair production with good mass resolution, the experiment intends to measure the production rate of *charmed mesons*, through their semi-*leptonic* decay, and to study the Ψ' suppression, trying to understand if this suppression follows a smooth pattern or a sudden transition. The

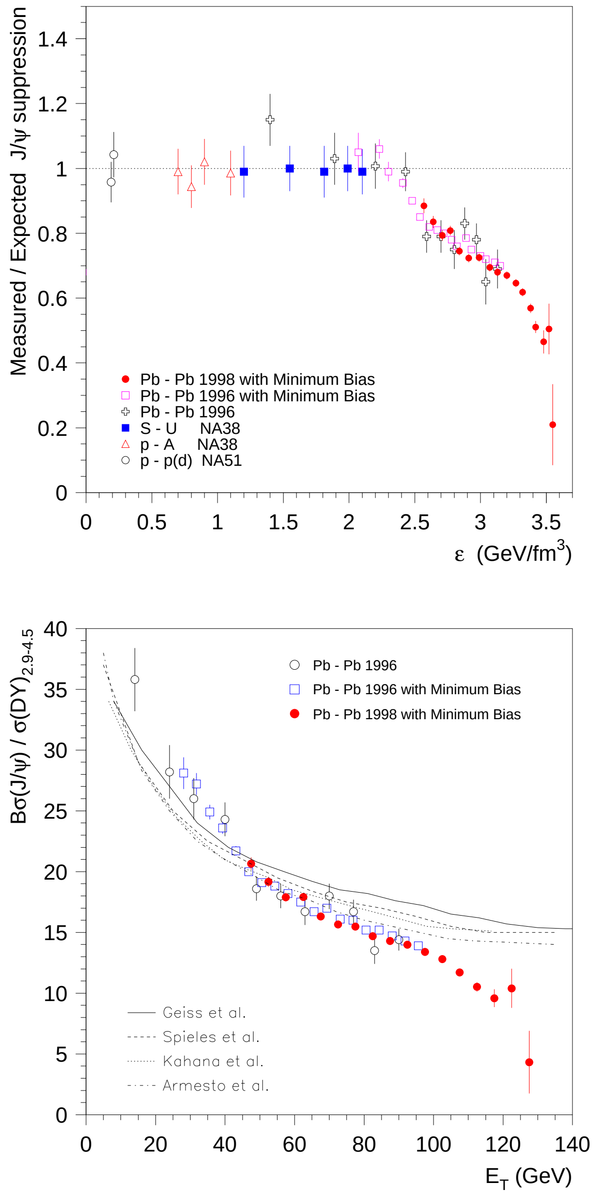

Figure 1.5: NA38/50 experiment: J/Ψ anomalous suppression: on the top, J/Ψ yield normalised to that expected taking into account the ordinary absorption in nuclear matter as function of the energy density (calculated assuming an initial thermalization time of about 1 fm/c); on the bottom, J/Ψ yield normalised to the Drell-Yan pair production as function of the transverse energy, E_T, measured in the calorimeter (as a centrality measure).

present results are not clear in what concerns the onset and pattern of the Ψ' suppression: new measurements are needed with improved mass resolution to have a cleaner separation of the Ψ' peak with respect to the the J/Ψ shoulder. The suppression pattern, in fact, could also provide a clear measurement of T_c.

1.5.3 Strangeness enhancement

As argued in §1.4.1, an enhanced multi-*strange* particle production is one of the most promising signatures of a QGP. In the sulphur beam era, two heavy ion experiments were dedicated to the study of *strangeness* production: WA85 [24] and WA94 [25]. In particular WA85 employed *proton* and sulphur beams at $200 AGeV/c$ on tungsten targets and WA94 *proton* and sulphur beams of equal momenta on sulphur targets. Both the experiments used multiwire proportional chambers: the measured particle ratios showed evidence for an enhanced production of *strange* and multi-*strange* particles in nucleus-nucleus with respect to *proton*-nucleus collisions.

Once the multiwire proportional chambers were replaced by silicon microstrips and pixels, in the lead beam era the WA97/NA57 experiment [26] found an interesting enhancement pattern (fig. 1.6): the *strangeness* enhancement increases with the *strange quark* content of the particle, and reaches a value of about 15 for $\Omega^{\pm}$.

Since the *K mesons* carry about 75 % of the global *strangeness* content of the final state, an enhancement in the *kaon* production indicates a global *strangeness* enhancement also. The *kaon* yields measured by the WA97 collaboration confirm this enhancement in $S-S$ collisions: by a factor of about two when normalized to π *meson* production [27]. The enhancement in the *kaon* production is also confirmed by the NA49 [28, 29] experiment and by the E802-E866 experiment [30, 31].

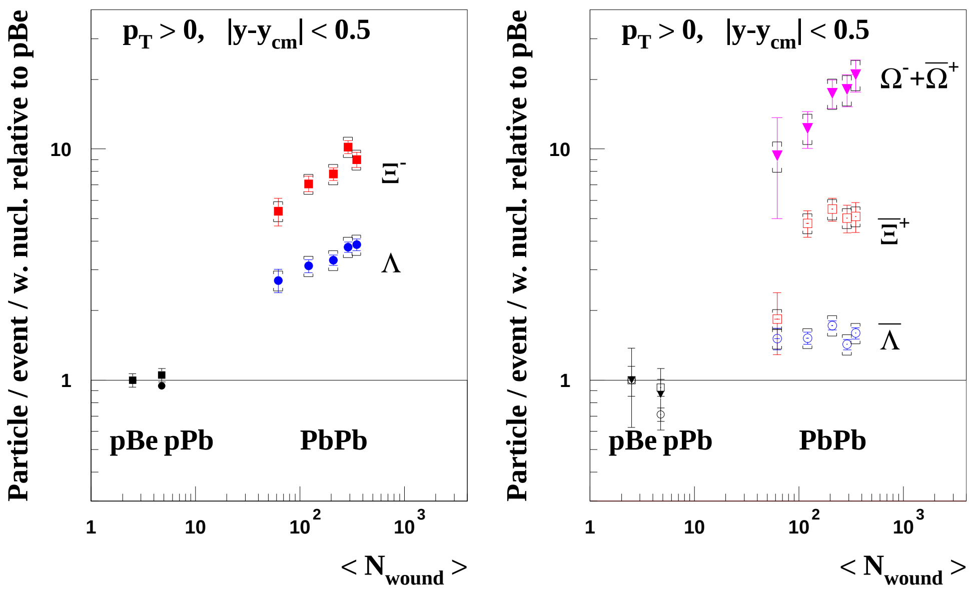

Figure 1.6: WA97 experiment: yields of different particles per wounded nucleon as functions of the number of wounded nucleons, normalised to the corresponding values in $p-Be$ collisions. The measured particles are divided in two classes: those with at least one valence *quark* in common with the nucleon and those with no valence *quark* in common with the nucleon.

1.5.4 Some RHIC results

Many results are currently being produced by the ongoing experiments at RHIC. Let me just mention a few of them relative to some basic event features.

An interesting RHIC result from PHENIX concerns the inclusive π, K, p p_T-distributions [32] shown in fig. 1.7. The data indicate that in central $Au-Au$ collisions, the π, K, p yields become equal at $p_T = (1.5-2)\,GeV/c$. At low p_T the inverse slopes increase with the particle masses and the distributions are differently shaped, being "convex" for K, p and "concave" for π. In peripheral $Au-Au$ collisions, the distributions at low p_T are almost parallel to each other and almost superimposed for K and p. These results could find a possible explanation in the framework of a hydrodynamic collective flow model (see §1.4.1).

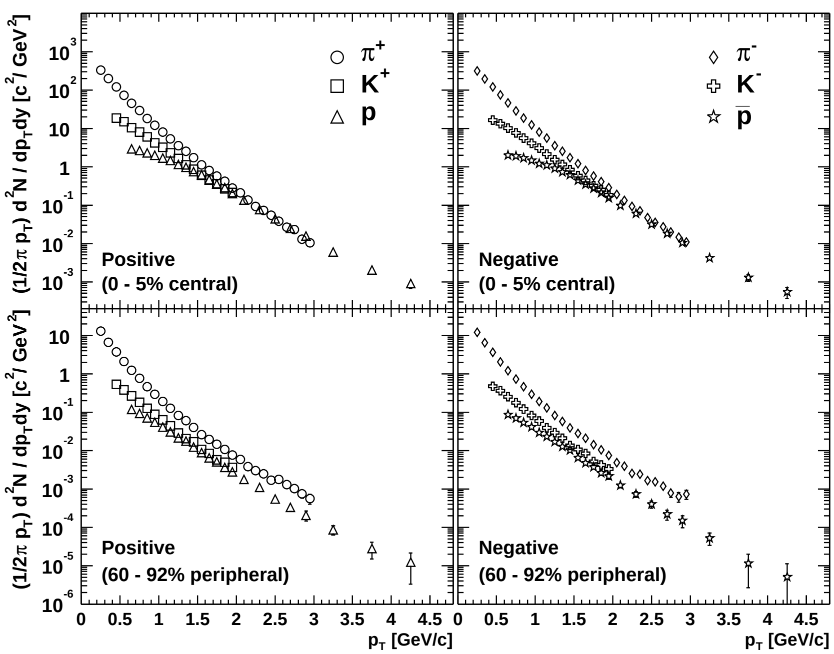

Figure 1.7: Transverse momentum distribution for *pions* (circles), *kaons* (squares) and $p\ \bar{p}$ (triangles) in the $0-5\%$ most central events (upper panels) and $60-92\%$ most peripheral events (lower panels) at $\sqrt{s_{NN}} = 200\,GeV$ in $Au-Au$ collisions.

Furthermore, fig. 1.8 shows the charged particle yield per unit rapidity at mid-rapidity as function of the number of participants, as measured in the four RHIC experiments (BRAHMS [33], PHENIX [34], PHOBOS [35] and STAR [36]) in $Au-Au$ collisions at different CM energies per nucleon pair ($\sqrt{s_{NN}}$). In fig. 1.9 the same quantity, measured by PHOBOS and normalized to the average number of participants, is shown as a function of $\sqrt{s_{NN}}$ and compared with $e^{+}-e^{-}$ and $p-p$ or $p-\bar{p}$ data [37]. Apart from the overall good consistency of the results from different experiments, the data in fig. 1.9 show that $Au-Au$ and $e^{+}-e^{-}$ data have the same behaviour *vs.* $\sqrt{s}$ while $p-p$ and $p-\bar{p}$ data need a rescaling of $\sqrt{s}$ by a factor ~ 2. This is a consequence of the well-known "leading" effect present in $p-p$ or $p-\bar{p}$ but absent in $e^{+}-e^{-}$ interactions [37]. This effect is related to the quantum number flow (baryon number for $p-p$ or $p-\bar{p}$) from the initial to the final state. Once an "effective energy" is considered by subtracting from $\sqrt{s}$ the amount of energy carried away by the outgoing leading protons or antiprotons (the outgoing baryons are uncorrelated and each of them carries away on the average about one half of the incident energy per CM hemisphere), the $e^{+}-e^{-}$ and $p-p$ or $p-\bar{p}$ results indeed coincide. Hence the RHIC data indicate that no leading baryon effects are present in high energy, central $Au-Au$ collisions.

Another interesting result, obtained by STAR and PHENIX, is the gradual disappearing of the back-to-back azimuthal correlations of high-p_T particles with increasing collision centrality [38]. In fig. 1.10 the azimuthal correlations of charged particles with respect to a high-p_T trigger particle are shown for peripheral and central collisions and compared with reference data from $p-p$ collisions: in the central collisions the opposite-side correlation is strongly suppressed with respect to $p-p$ and peripheral $Au-Au$ cases. This effect suggests the absorption of one of the two *jets*, produced in a hard parton scattering, in the hot matter formed in central collisions.

It is also worth noting that the effects showing up in figs. 1.9 and 1.10 are not observed in $d-Au$ (deuteron-gold) collisions at $\sqrt{s_{NN}} = 200\,GeV$ [38] where the formation of a dense medium is not expected.

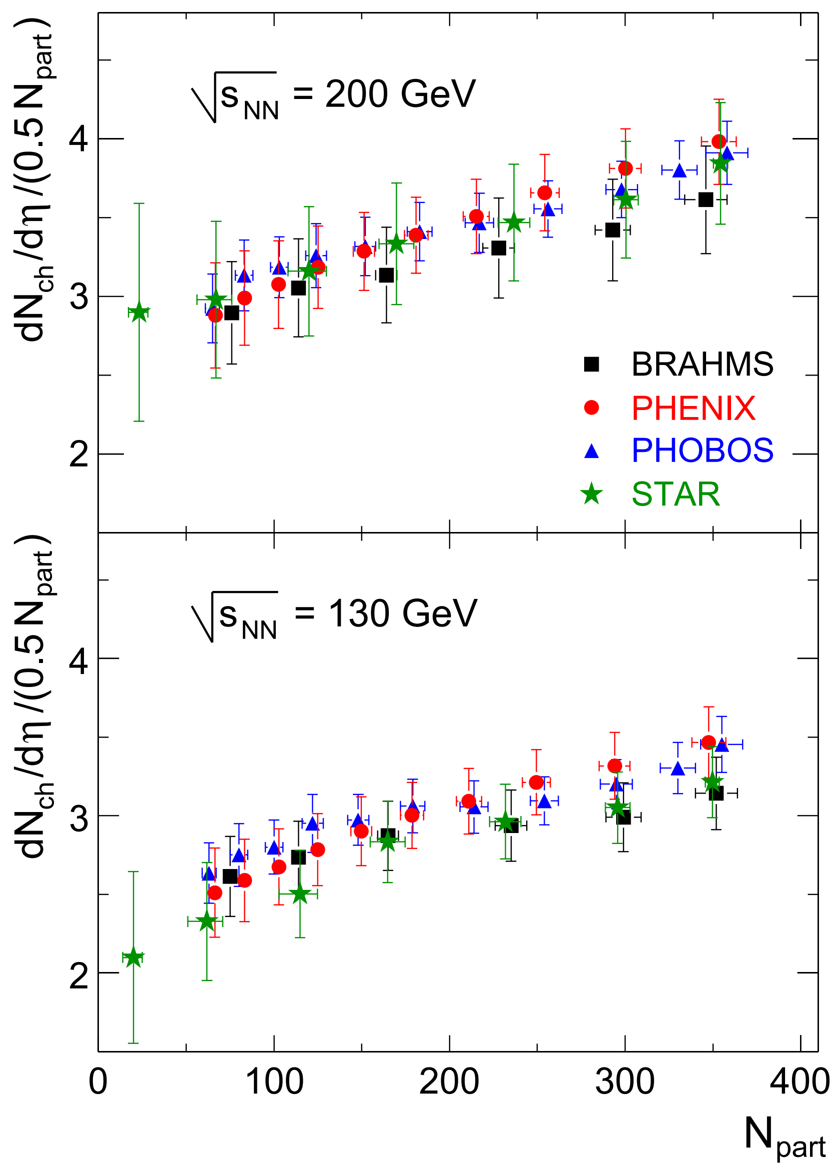

Figure 1.8: Charged particles per participant pair as a function of the number of participants for $\sqrt{s_{NN}} = 130\,GeV$ and $\sqrt{s_{NN}} = 200\,GeV$ for all the four RHIC experiments.

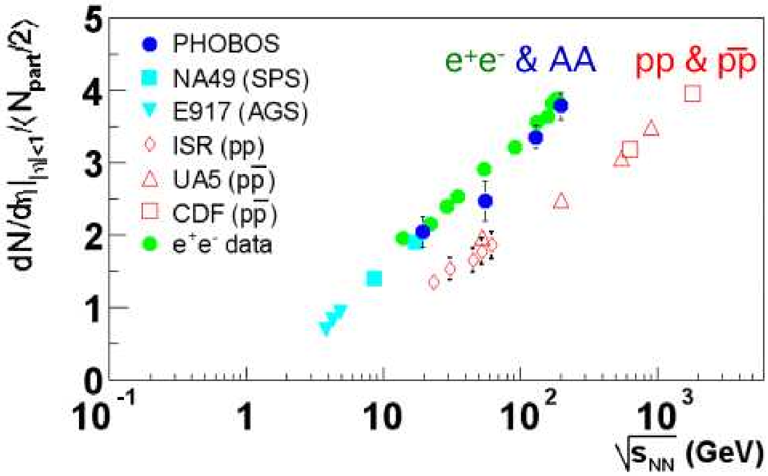

Figure 1.9: The charged multiplicity at mid-rapidity ($dN/d\eta_{|\eta|<1}$) for $p-p$, $p-\bar{p}$, $e^+ - e^-$ and central $Au-Au$ events as a function of $\sqrt{s_{NN}}$. The $Au-Au$ are normalized by $N_{part}/2$, where N_{part} is the number of participants.

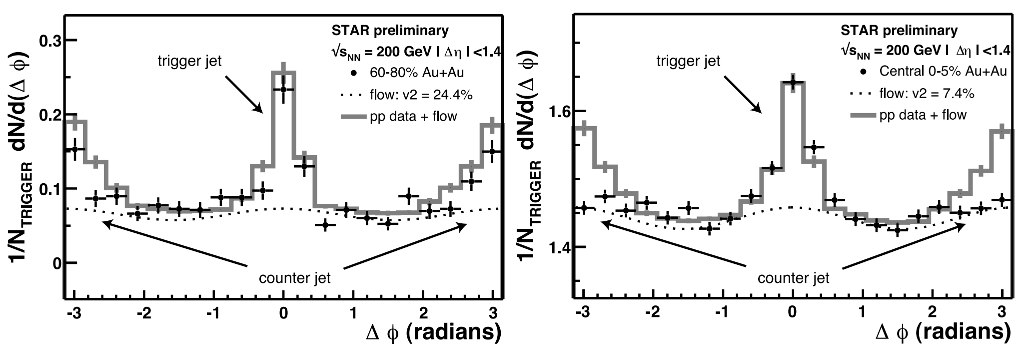

Figure 1.10: Azimuthal correlations of charged particles relative to a high-p_T trigger particle for peripheral (left) and central (right) $Au-Au$ collisions at $\sqrt{s_{NN}} = 200\,GeV$ [38].

1.5.5 ϕ meson results

The ϕ *meson* production at SPS energy (see table 1.1) has been measured by two experiments: NA49 [28] and NA50 [21]. The first reconstructs ϕ *mesons* via the K^+K^- decay channel and the second via the $\mu^+\mu^-$ decay channel. Both the experiments observe an enhancement of the ϕ production with the event centrality. NA49 measures an enhancement in the $\phi/\pi^{\pm}$ ratio by a factor 2.8 for global yields, between central $Pb-Pb$ collisions and $p-p$ interactions [39]. NA50 detects an increase of the $\phi/(\omega+\rho)$ ratio with the event centrality in $Pb-Pb$ collisions [40].

The E917 experiment at AGS [41] studied ϕ production in $Au-Au$ collisions at $11.6 AGeV/c$ via K^+K^- identification. The results confirmed the NA49 findings, namely that the ϕ yield increases with the event centrality [42].

STAR [36] and PHENIX [34] experiments are also studying the ϕ *meson* production in $Au-Au$ collisions at 130 and $200 GeV$ per nucleon pair. The first reconstructs the ϕ via K^+K^- identification with the TPC. It detects an enhancement of the ϕ production per rapidity unit as a function of the centrality of the event. The second reconstructs the ϕ both via K^+K^- identification (with a time-of-flight system and an electromagnetic calorimeter), and e^+e^- identification (with a ring-imaging-Cherenkov detector and an electromagnetic calorimeter). Within the large statistical and systematic errors of the preliminary analysis, the average number of ϕ *mesons* at midrapidity ($|y| < 0.5$) for $\phi \rightarrow K^+K^-$ [45, 46, 47, 48] and $\phi \rightarrow e^+e^-$ [48] are consistent. Both experiments confirm the ϕ production increase with the event centrality.

Figure 1.11 shows the ϕ to $\pi^{\pm}$ ratio as function of energy in the CM system, i.e. $\sqrt{s_{NN}}$, from AGS, through SPS, to RHIC energies: a constant increase of this ratio is evident [49].

1.5.6 The ϕ meson inverse slope parameter

Significantly different values for the ϕ slope parameter have been obtained from exponential fits to the measured m_T spectra in central $Pb-Pb$ collisions when using the K^+K^- and the $\mu^+\mu^-$ decay channels of the ϕ *meson* [39, 40]. This difference, however, is not present in peripheral collisions [39]. A possible scenario to explain the results is the following: rescattering of the *kaon* daughters in the nuclear medium could mimic or obscure effects of chiral symmetry restoration by causing the reconstructed invariant mass to fall outside the *vector meson* peak, effectively decreasing the measured yields [43, 44] (see §1.4.1).

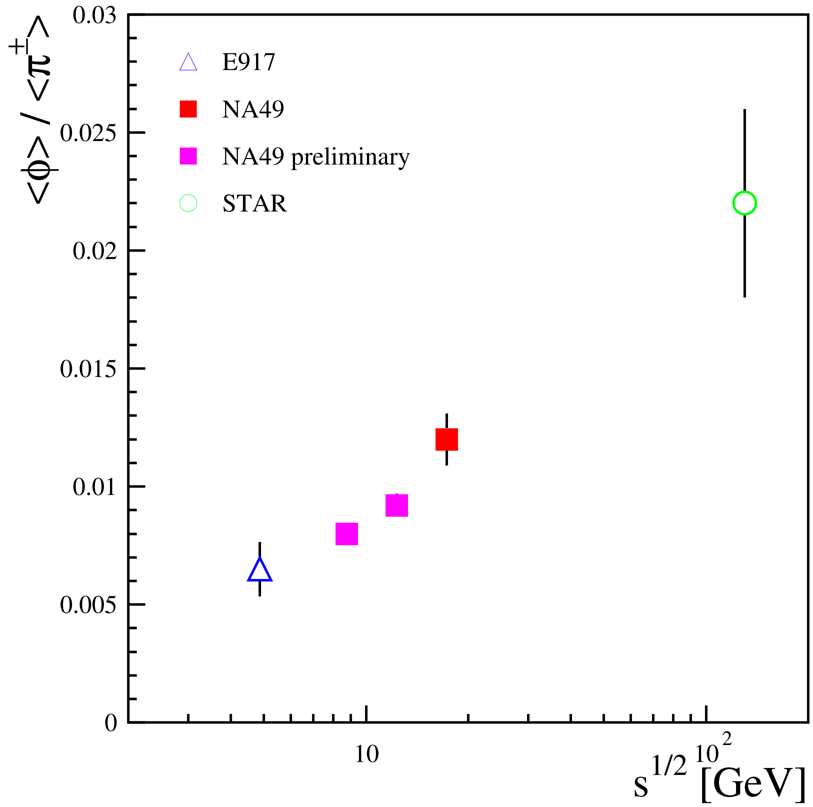

Figure 1.11: $\phi/\pi^{\pm}$ ratio in heavy ion collisions as a function of $\sqrt{s_{NN}}$ from AGS to RHIC energies. The point corresponding to the highest (RHIC) energy is evaluated at mid-rapidity.

The ϕ inverse slope parameter resulting from the analysis of the data taken by the STAR detector at $\sqrt{s_{NN}} = 200\,GeV$, is $T = 357 \pm 14(stat) \pm 10\%(syst)\,MeV$ at mid-rapidity ($|y| < 0.5$) and for the centrality range $0-10\%$ [45, 46, 47]. The temperature values of the ϕ meson clearly increase when going from the AGS [50], through the SPS [39, 40], to the RHIC energies [45], as shown in fig. 1.12.

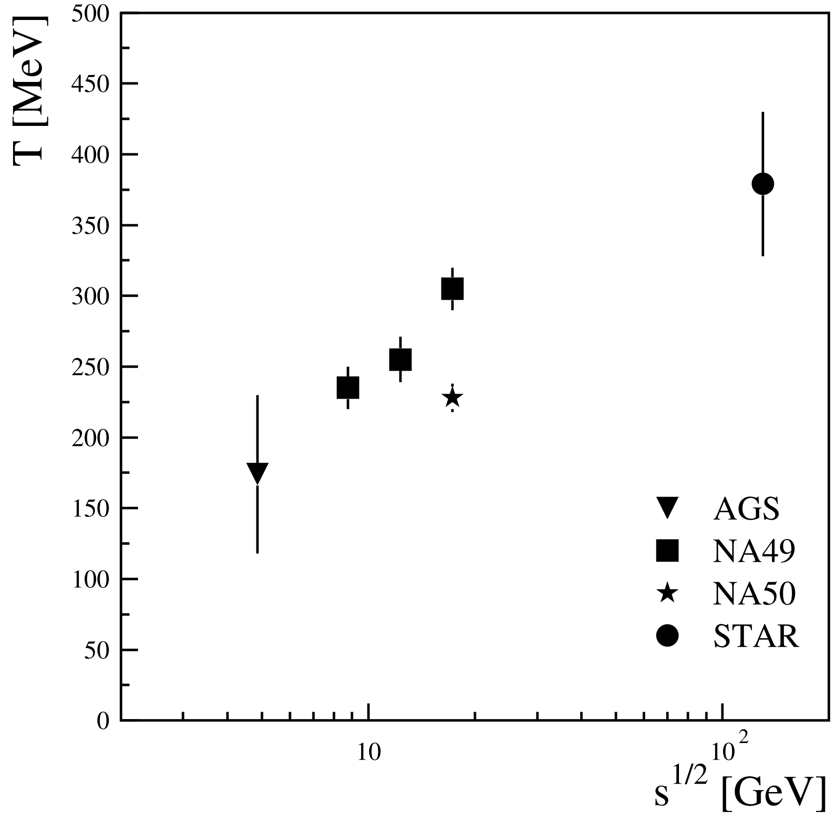

Figure 1.12: $\sqrt{s_{NN}}$ dependence of ϕ inverse slope parameter, T_ϕ, for central heavy ion collisions, from AGS to RHIC energies.

Chapter 2

A Large Ion Collider Experiment (ALICE)

The aim of the ALICE experiment is the study of heavy ion collisions at LHC energies ($\sqrt{s_{NN}} \sim 5.5\, TeV/nucleon\ pair$), and of the properties, the dynamical evolution and the phenomena associated with the possible phase transition from the ordinary *hadronic* matter to a $quark - gluon$ plasma [51].

To achieve this goal, ALICE, as the only dedicated heavy ion experiment at LHC, is designed to measure a large set of observables over as much of phase space as achievable: *hadronic* and $leptonic$ observables as well as $photons$.

The average charged particle multiplicity per unit rapidity is the most fundamental 'day one' observable. As reminded in the previous chapter (§1.4.1), it is related to the energy density and enters the calculation of most of the other observables.

Another important 'day one' observable is the total transverse energy per rapidity unit at mid-rapidity, dE_T/dy: it determines how much of the total initial longitudinal energy, $A\sqrt{s} \approx 200^1 \times 5500\, GeV$, is converted into transverse debris of QCD matter.

On the experimental side, the particle multiplicity fixes the main unknown in the detector performance: whether the charged particle multiplicity per unit rapidity is 3000 or 8000 will largely determine the accuracy with which many observables can be measured.

Despite their fundamental theoretical and experimental importance, there is no

[1]The value ≈ 200 represents a realistic number of participant pairs one may expect in central $Pb - Pb$ collisions.

first principle calculation of these observables starting from the QCD Lagrangian. Hence we will assume herein the highest charged particle multiplicity value.

The ALICE detector has been designed according to the following criteria:

- since a single dedicated heavy ion detector is foreseen at the initial stage of LHC, it has to cover, as completely as possible, the full range of sensitive signatures; its design must be conservative and robust;

- the detector will concentrate on physics at mid-rapidity, i.e. in the region where the number of baryons is minimum and the energy density is maximum, which are the unique features of LHC compared to the lower energy machines SPS and RHIC;

- an open geometry will facilitate future modifications and upgrades if first physics results suggest focusing on specific signals, selective triggers or larger acceptance.

The main emphasis will be on data taking at the highest possible energy density, i.e. with *Pb* beams. In addition, running with one or two intermediate mass nuclei will provide the necessary means to vary the energy density. Running with protons will be required initially to start the detector operation (tests, calibrations, etc.) and to provide the nuclear programme with reference data. Special schemes are under investigation that would allow $p-p$ running at a luminosity adapted to the rate capability of the detector without any effect on the other high luminosity interaction regions of the collider. Asymmetric beam collisions, in particular $p-A$ reactions, are permitted as well; these will be important for disentangling initial state effects (like nuclear shadowing) from final state interactions in hard probe signals, such as jet quenching and quarkonium production.

The rapidity acceptance has to be large enough to allow some variables to be studied on an event-by-event basis (particle ratios, p_T spectra), which means typically several thousands of reconstructed particles per event.

Good efficiency to detect the decay of particles at $p_T < m$ requires about 2 units in rapidity (for masses above $1-2\,GeV/c^2$) and a corresponding coverage in azimuth. In addition, efficient rejection of low-mass Dalitz decays, which is necessary for lepton pair measurements, can only be approached with full azimuthal coverage. The rapidity coverage of the ALICE central detector ($|y| \lesssim 1$) has been chosen as a compromise between acceptance and cost.

In order to have some sensitivity to the global event structure, some multiplicity detectors in a large rapidity window ($|y| < 4$) outside the central acceptance should be employed.

Track finding in the environment of heavy ion collisions at LHC presents one of the greatest challenges for the detector. Therefore, the design of the ALICE tracking system has been driven primarily by the requirement of a reliable and powerful pattern recognition. It employs mostly three-dimentional hit information, with many points and a magnetic field.

The momentum cut-off should be as low as possible in order to study collective effects associated with large length scales. A low p_T cut-off is essential as well to suppress soft γ conversions and Dalitz background in the lepton pair spectrum. The most stringent limit on momentum resolution in the low p_T region is imposed by identical particle interferometry. For intermediate momenta, the mass resolution should be of the order of the natural width of the ω and ϕ in order to maximize the signal-to-background ratio and, more important, to study the mass and width of these *mesons* in the dense medium. At high momenta, the resolution has to be sufficient to measure the spectrum of jets via leading particles. Detection of secondary particles from *strange* and, in particular, *charm* and *beauty hadrons* requires a vertex detector with high resolution at a small distance from the interaction point. The ALICE tracking system together with a solenoidal magnetic field has been designed to fulfill all the above requirements.

Particle identification (PID) over a large part of the phase space, and for many different particles, is an important design feature. The event-by-event (E-by-E) hadron identification will give the opportunity to measure, with high statistics, on a single event basis the shape of the p_T distributions for π, K and p, their average transverse momenta (i.e. individual temperatures) and the $\pi/K/p$ ratios. Consequently, it will provide information in terms of QCD thermodynamics, separately for different particle species, on possible thermodynamical instabilities during phase transitions resulting in temperature fluctuations, on the degree of thermal equilibrium and on expansion dynamics. In addition, *kaon* identification will provide information on flavour composition to probe the level of *strange quark* density which is expected to be large as a consequence of partial chiral symmetry restoration in a QGP. Identified *kaons* are also particularly important for the identification of $\phi \to K^+K^-$ decays (particle mass and decay width), while the measurement of the ϕ yield sets more stringent constraints on the origin of the observed flavour composition, as compared to the K/π ratio. Finally, identified *kaons* are essential, coupled with secondary vertex detection, to identifiy open *charm* decays such as $D^0 \to K^- \pi^+$ and $D^+ \to K^- \pi^+ \pi^+$. The detection of open *charm* might in turn to the detection of open *beauty*. Owing to their large mass, the *charm* and *beauty quarks* can only be produced in the early stage of the heavy ion collision and they probably end up in the final state, mostly in the form of open *charm* and *beauty hadrons*, due to their very low annihilation probability. The degree of open *charm* and *beauty* enhancement is expected to be sensitive to the parton kinematics at the primordial stage. Additionally, the detection of open *charm* and *beauty* will be essential for cross section normalization, necessary in the detection of the J/Ψ suppression (measured at SPS) or Υ suppression that will likely probe the QGP formation. In order to measure inclusive particle ratios and p_T spectra in the mini-*jets* some limited PID coverage extending towards higher momenta is also needed. The e/π rejection power must be sufficient to reduce the combinatorial background caused by misidentification to below the level of the remaining unrejected Dalitz pairs.

Probing the production of heavy-flavoured quarkonia, one of the most crucial goals in a heavy ion experiment, can be achieved with a powerful *muon* detector. This will have the task to measure the *dimuon* decay of heavy quark resonances (J/Ψ, Ψ', Υ, Υ', etc.) with sufficient mass resolution in order to separate as many as possible states of system spectroscopy.

Besides measuring π^0 and η spectra, with a momentum accuracy better than for charged particles, the measurement of the direct photon spectrum will also be very challenging. The accuracy of the latter will be determined in the range of interest ($p_T < 10\,GeV/c$) by systematic errors in photon reconstruction efficiency and knowledge of decay background. A sensitivity for direct photons at the level of 5 % of decay photons requires a knowledge of the reconstruction efficiency and of the π^0 cross-section up to $\leq 3\,\%$, and of the η cross-section up to $\leq 10\,\%$. An acceptable systematic error can be obtained only at low occupancy and therefore a calorimeter with small Molière radius at a large distance ($\geq 5\,m$) from the vertex is needed. The minimum size is determined by the acceptance for the $2\,\gamma$ decays of π^0 and η at low p_T. The signal-to-background ratio in the two-photon invariant mass spectra improves proportionally to the energy resolution of the calorimeter.

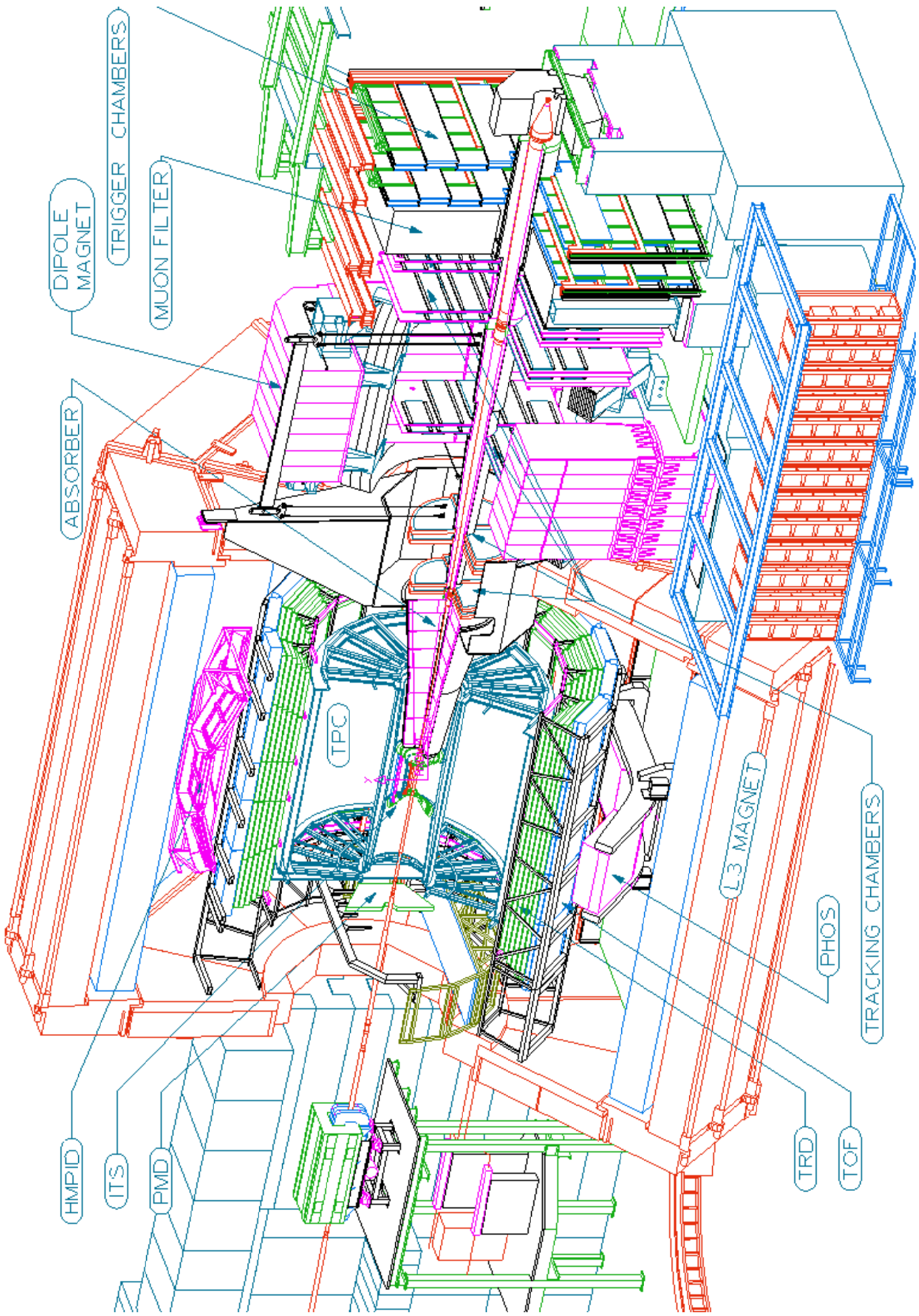

Figure 2.1: ALICE experiment: setup.

2.1 Detectors

The overall detector layout of the ALICE experiment is shown in fig. 2.1. The experiment will have a central barrel, housed in a solenoidal magnet[2], covering the range $|\eta| \leq 0.9$ in pseudorapidity[3], with complete azimuthal coverage. This central barrel comprises (from the inside out) an Inner Tracking System (ITS) of silicon detectors, a large Time Projection Chamber (TPC), a Transition Radiation Detector (TRD), and a Time-Of-Flight (TOF) detector. In addition, there will be two single arm detectors close to mid-rapidity: an array of Ring-Imaging-Cherenkov counters to identify hadrons up to high momenta (HMPID) and an array of crystals for photon detection (PHOS).

This central barrel is complemented by other forward and backward detectors that will measure the multiplicity of charged particles and the reference time of the beam-beam interaction, for trigger purposes as well. At pseudorapidities of $2.5 \leq \eta \leq 4.0$ there will be a forward muon spectrometer (FWM) with its own dipole magnet. In the pseudorapidity region $-2.6 \leq \eta \leq -1.8$ there will be a photon multiplicity detector (PMD). The setup is completed by a set of zero-degree calorimeters (ZDC) located far downstream in the machine tunnel.

The detectors dedicated to charged particle identification are in the central barrel, where we expect higher charged particle multiplicity values.

In the following paragraphs only the detectors involved in the present study will be briefly described.

2.1.1 ITS

The main purpose of ITS [52] is the detection of the secondary vertices (of *hyperons* and heavy flavoured *hadrons*) and the stand-alone track finding of low p_T charged particles, down to $\sim 20 MeV/c$ for electrons. It has a number of additional roles: improvement of the momentum resolution at large momenta, momentum reconstruction of the low energy particles and their identification via dE/dx in the $1/\beta^2$

[2]This actually is the solenoid already installed and used in the L3 experiment at LEP.

[3]The *pseudorapidity* variable is defined as:

$$\eta = -ln(tg(\frac{\vartheta}{2})).$$

For relativistic particles, i.e. $\beta \rightarrow 1$, $\eta \simeq y$.

region, and definition of the angles of the tracks for the two-identical particle interferometry analysis.

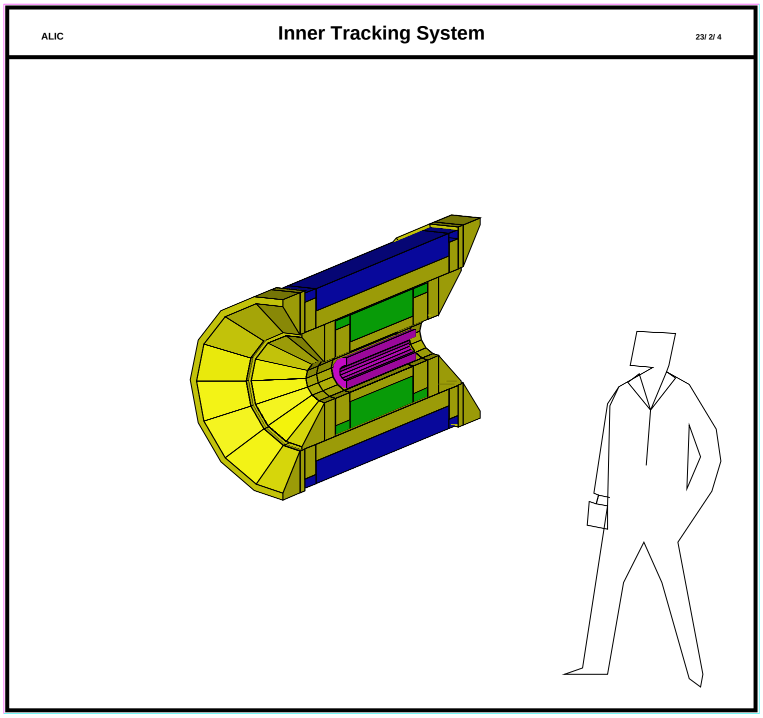

Figure 2.2: ITS detector layout.

These basic functions are achieved with six barrels of high resolution detectors (fig. 2.2). The number of layers and their position have been optimized for efficient pattern recognition and impact parameter resolution: in particular, the outer radius is determined by the track matching with the TPC, and the inner one is the minimum compatible with the radius of the beam pipe ($3\,cm$). Because of the high particle density (up to $\sim 90\,cm^{-2}$), the four innermost layers ($r \leq 24\,cm$) must be truly two-dimensional devices, i.e. silicon pixels and silicon drift detectors. The outer two layers at $r \approx 45\,cm$, where the the track densities are below $1\,cm^{-2}$, will be equipped with double-side silicon microstrip detectors. With the exception of the two innermost pixel planes, all layers will have analogic readout for indipendent particle identification via dE/dx in the non relativistic region, which will give the inner tracking system a stand-alone capability as a low p_T particle spectrometer.

The main parameters for each of the three detector types, spatial precision and two-track resolution, are reported in table 2.1 (extracted from table 1.3 in [52]).

Parameter	Silicon Pixel	Silicon Drift	Silicon Strip
Spatial precision $r\varphi$ [μm]	12	38	20
Spatial precision z [μm]	70	28	830
Two-track resolution $r\varphi$ [μm]	100	200	300
Two-track resolution z [μm]	600	600	2400

Table 2.1: Spatial precision and two-track resolution for each of three ITS modules and in the two cylindrical directions z and $r\varphi$.

2.1.2 TPC

The task of the TPC [53] is track finding, momentum measurement and particle identification via dE/dx. The most important design goal for all the components of the TPC is to achieve a good two-track resolution in order to cope with the expected high multiplicity at LHC ($dN_{ch}/dy = 3000-8000$). The inner radius of the TPC ($r \approx 80\,cm$) is given by the maximum acceptable hit density ($0.1\,cm^{-2}$). The outer radius ($r \approx 250\,cm$) is determined by the length required for a dE/dx resolution of $\leq 7\%$. The design of the readout and of the end plates, based on recent developments for other heavy ion TPCs, as well as the choice of the operating gas, have been optimized for good double-track resolution (fig. 2.3).

For hadron identification, a dE/dx resolution of 8% is desirable. The two-track resolution has to be such that Bose-Einstein correlation measurements for two identical particles can be performed with a resolution in relative momentum of a few (< 5) MeV/c. This may require running at magnetic fields higher than 0.2 T. The L3 magnet can be operated to reach 0.5 T.

For electron identification with momenta $\geq 1\,GeV/c$, the TPC should have a tracking efficiency larger than 90%, a momentum resolution (for electrons with momenta of about $4\,GeV/c$) better than 2.5% (achievable only in conjunction with the ITS and when running at magnetic fields around 0.4 T), and a dE/dx resolution of better than 10% in the high multiplicity environment of a $Pb-Pb$ collison.

The current TPC design should secure:

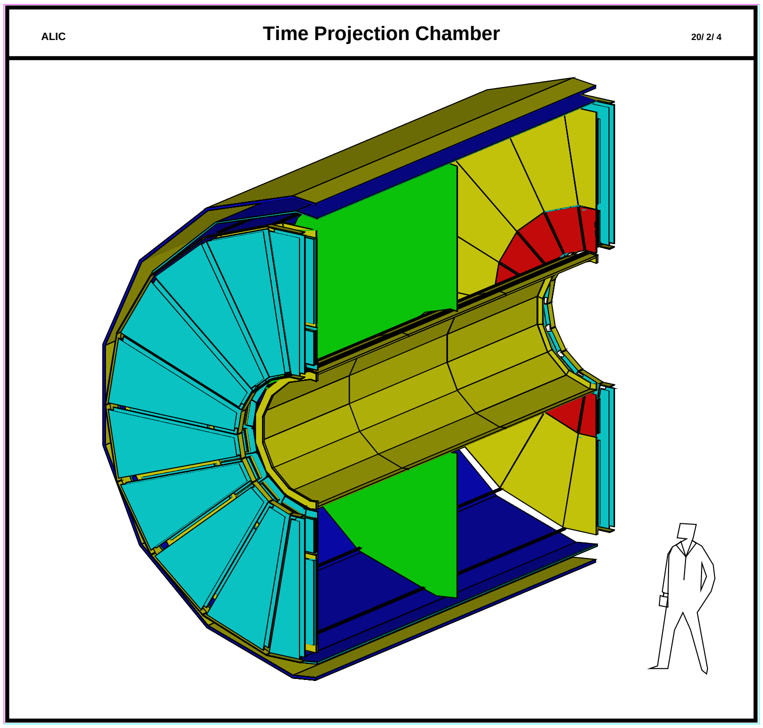

Figure 2.3: TPC detector layout.

- $\delta p/p \sim 1.2 - 1.5\,\%$ for MIP[4] and about $5\,\%$ for $5\,GeV/c$ electrons (standalone);
- $dE/dx < 10\,\%$ in high track density region;
- signal-to-noise ratio for MIP better than $\sim 20:1$ in the case of small readout pads in inner sectors and $30:1$ for larger pads in outer sectors;
- track finding efficiency $\geq 90\,\%$;
- two cluster resolution $\sim 1\,cm$ in both $r\varphi$ and z directions.

[4]Minimum ionizing particle.

2.1.3 TRD

The chief goal of the TRD [54] is to provide electron identification in the central barrel at momenta $> 1\,GeV/c$ where the pion rejection via energy loss measurement in the TPC is no longer sufficient. The goal is a factor 100 in pion rejection for electron transverse momenta above $3\,GeV/c$. While the requirement for the Υ is less stringent, the light vector mesons ρ, ω and ϕ as well as the di-electron continuum between the J/Ψ and the Υ masses are only accessible with this kind of performance.

The TRD consists of six individual layers along the radial direction (fig. 2.4). Following the segmentation in azimuthal angle (φ) of the TPC there are 18 sectors; along the beam direction (z), there is a 5-fold segmentation. Each module consists of a radiator of $4.8\,cm$ thickness, a multiwire proportional readout chamber and the front-end electronics for this chamber. The signal induced on the cathode pads is readout.

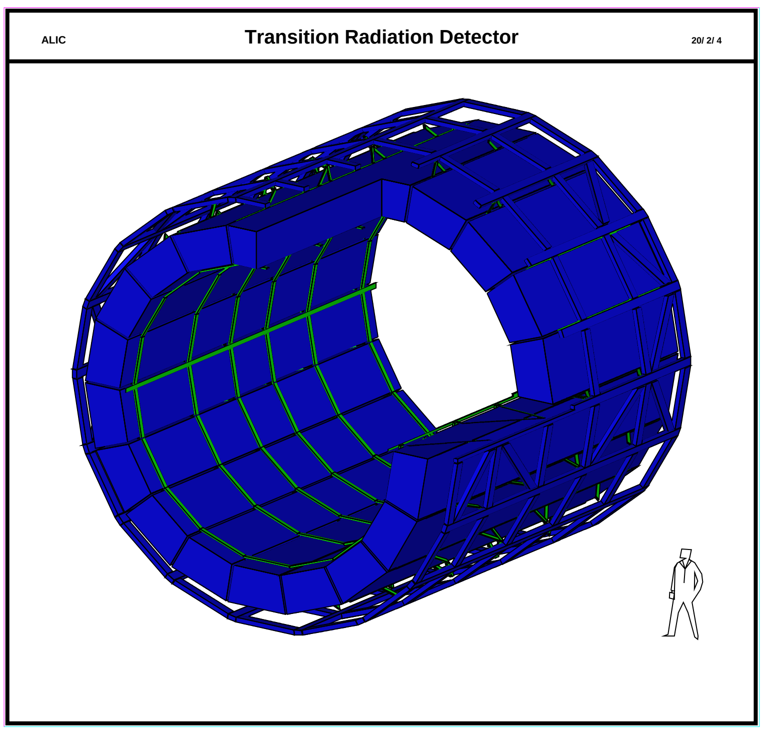

Figure 2.4: TRD detector layout in the ALICE space frame.

At $dN_{ch}/dy = 8000$, the pad occupancy[5] will be 34%. The space point resolution is $600\,\mu m$ with some unfolding. The momentum resolution of the TRD in stand-alone mode is:

$$\frac{\delta p}{p} = 2.5\% + \frac{0.8}{GeV/c}\%. \tag{2.1}$$

This last value leads to a pointing accuracy of 30% of the padwidth allowing matching with the exception of very close hits.

2.1.4 TOF

All the basic physics goals, described at the beginning of this chapter and in chapter 1, demand a TOF [55, 56, 57, 58] detector with outstanding intrinsic characteristics. The TOF rapidity acceptance has to be large enough to cover the full central acceptance of ALICE, in order to allow a significant study of the observables of interest. This implies that a large number of hadrons should be measured. More precisely, the TOF detector should cover a momentum range from about $0.5\,GeV/c$ (upper limit for dE/dx in the TPC for a K/π separation) up to a few GeV/c. The target is a system resolution (i.e. including all other sources of timing errors in addition to the detector resolution itself) of $100\,ps$. This resolution would guarantee a 3σ K/π separation up to $p_{3\sigma} = 2.1\,GeV/c$ (with a TOF detector at $r = 3.7\,m$). A resolution of $150\,ps$ would still be acceptable ($p_{3\sigma} = 1.7\,GeV/c$), whereas $200\,ps$ or worse ($p_{3\sigma} \leq 1.4\,GeV/c$) would leave a substantial fraction of the momentum spectrum unmeasured. The performance of a TOF system for particle identification depends on the intrinsic timing resolution of the detectors it is made of, as well as on the system resolution. To evaluate the influence of different parameters of the TOF system on the PID quality, let us consider the following expression:

$$m = \sqrt{E^2 - p^2} = p\sqrt{\frac{t^2}{l^2} - 1} \tag{2.2}$$

where m is the mass of the particle, p its momentum, E its energy, t the time-of-flight and l the track length. It is simple to show that the $\partial m/m$ resolution has the following main contributions:

$$\frac{\partial_p m}{m} = \frac{\delta p}{p} \tag{2.3}$$

[5]Number of particles per detector cell.

$$\frac{\partial_t m}{m} = \left(\frac{E}{m}\right)^2 \frac{\delta t}{t} \tag{2.4}$$

$$\frac{\partial_l m}{m} = \left(\frac{E}{m}\right)^2 \frac{\delta l}{l} \tag{2.5}$$

and that, at relatively high momenta, it is driven much more by the errors on the particle flight-time and flight-length measurements than by the error on the momentum determination.

The technique adopted (see chapter 3) for the ALICE TOF detector should reach an intrinsic resolution better than 70 ps. Including the other sources of timing errors (see §4.2.1), a resolution of about 120 ps is expected.

Besides, a large coverage, powerful TOF detector, operating efficiently in extreme multiplicity conditions ($\frac{dN_{ch}}{dy} = 3000-8000$), beyond the excellent intrinsic response required, should have an overall occupancy not exceeding the $10-15\,\%$ level. This implies a design with more than 10^5 indipendent TOF channels for a detector coverage range of $|\eta| < 0.9$.

The foreseen ALICE TOF detector covers a cylindrical (lateral) surface of $3.7\,m$ in radius and $7.4\,m$ in length around the interaction vertex (fig. 2.5).

The system has a modular structure corresponding to 18 sectors in φ angle and 5 modules along the beam direction, and each module contains $15-19$ elements. Every element is a Multigap Resistive Plate Chamber (MRPC)-strip made of a double-stack arrangement of two chambers with common anode. The strip active area is $\sim 7 \times 120\,cm^2$, corresponding to a matrix of 2×48 readout pads (each of $2.5 \times 3.5\,cm^2$) (see §3.3). The resulting total number of readout channels is $\sim$ 157000. The strips are tilted inside the modules in order to minimize the traversal paths for particles coming from the interaction vertex.

As it will be explained in detail later on (chapter 3), after an intensive R&D program, we have been able to produce MRPC-strips optimised for the stringent requirements of our time-of-flight detector: i.e. with $\sim 99\,\%$ detection efficiency and $\leq 70\,ps$ time resolution.

The TOF detector is therefore a high-granularity hodoscope capable to perform very accurate time-of-flight measurements. Its main paramenters are:

- radius: $r_{TOF} = 3.7\,m$; length: $l_{TOF} = 7.4\,m$;

- overall thickness: $30\,cm$, i.e. 20% of X_0;

- polar-angle coverage: $45° \leq \vartheta \leq 135°$; full φ coverage;

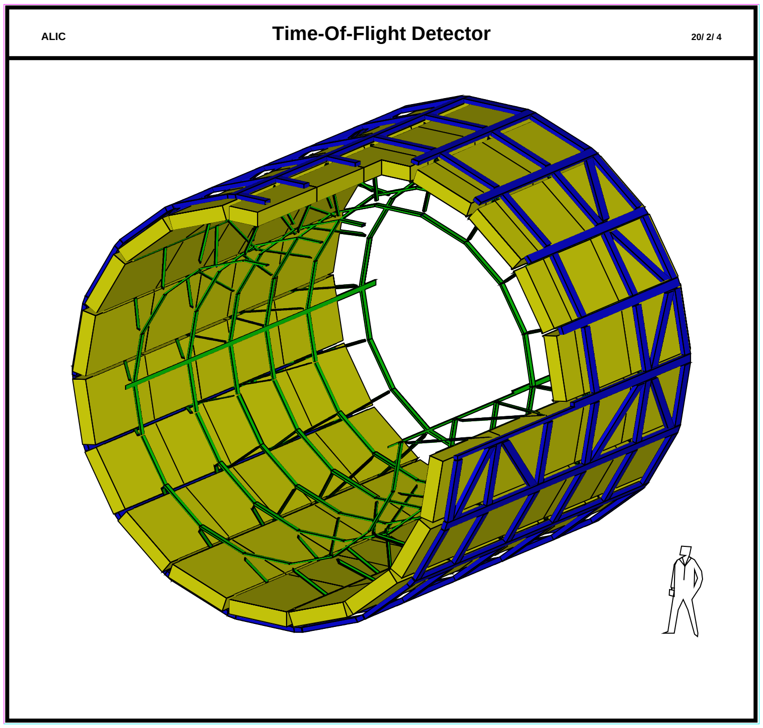

Figure 2.5: TOF detector layout in the ALICE space frame.

- total number of modules: 90, i.e. 18 (along φ) $\times$ 5 (along ϑ);
- total number of MRPC strips: 1638, with $15 - 19$ strips/module;
- total number of readout pads: 157248, with 2 $\times$ 48 readout pads/strip;
- total surface: $\sim$ 170 m^2; total sensitive surface: $\sim$ 150 m^2; sensitive area/strip: 7.4 $\times$ 122 cm^2; individual readout pad size: 2.5 $\times$ 3.5 cm^2;
- dead space: $\sim$ 10% of total surface;
- intrinsic time resolution: $\leqslant$ 70 ps; overall time resolution: 120 ps (including all other additional sources of time jitter).

Chapter 3

R&D for the MRPC as time-of-flight detector

The double-stack Multigap Resistive Plate Chamber (MRPC)-strip is the result of six years of R&D devoted to the optimization of the RPC as the basic time-of-flight detector element for the ALICE experiment.

3.1 Historical view: from RPC to MRPC

The resistive plate chamber (RPC [59]) is a parallel plate gaseous device with resistive electrodes. These resistive electrodes quench the streamers so that they do not initiate a spark breakdown. Thus RPCs can operate at much higher gains in avalanche mode; streamer mode operation is also possible. Resistive plate chambers are well known for their use as muon detectors[1], for large area coverage.

The LAA project at CERN has studied resistive plate chambers with the goal of improving their operation characteristics so that they could be used in future hadron colliders.

One of the earlier attempts to improve the $2\,mm$ gap resistive plate chamber was to increase the size of the gas gap. This device (known as the "wide gap RPC", [60]) had a gas gap of $6-8\,mm$. It had many advantageous features when compared to the conventional $2\,mm$ gap chamber:

[1]Typically the rate capability required for this kind of detector is not so high and fits the standard RPC rate capability.

- the gap tolerance was less critical for a wide gap, which resulted in a corresponding easing of problems with the construction;

- it allowed the use of a "light" gas (high fraction of Argon). This light gas mixture had a much lower electronegativity compared to the Freon-rich mixtures used in $2\,mm$ gap chambers. The problem with electronegative gases is that there is a much-increased ionic current (i.e. there is a much higher charge produced in the gas gap); this compromises the rate capability. Indeed, the wide gap chamber had a rate capability a factor 10 higher than the $2\,mm$ gap RPC [60].

The only disadvantage of the wide gap RPC was a significant worsening of the time resolution.

It is clear that, ideally, one would like to keep the advantages of the wide gap (looser mechanical tolerance, improved rate capability) and, at the same time, improve the time resolution with smaller gas gaps.

The multigap RPC is a solution that offers both small gas gaps and a large total gas gap. It consists of a series of gas gaps, with one set of read-out strips reading out the signal sum of all gas gaps. The intermediate plates are electrically floating and achieve the correct voltage by electrostatic effect. They are kept at the correct voltage by the flow of electrons and positive ions, created by avalanches in the gas gaps. In fact, there is a strong feedback mechanism that forces the gas gain to be equal in all subgaps.

With a multigap made of a series of 3 gaps, each of $3\,mm$, a time resolution similar to a single $2\,mm$ gap [61] was obtained. However, providing the multigap with an Argon-based gas mixture (which is not electronegative), a rate capability 10 times higher than for a single $2\,mm$ gap RPC, filled with a Freon gas mixture (strongly electronegative), was achieved.

There is a further advantage in subdividing the gas gap into many small gaps. A through-going particle produces individual and separate clusters of primary ionization; each of these clusters will start an avalanche and the final signal will be the sum of all the avalanches.

In a single wide gap RPC the inherent fluctuations within the avalanche mechanism dominate[2] and the resultant signal is as if there was only one large "merged"

[2]The clusters of primary ionization (whose number depends on the gas mixture used) are produced and start avalanches in the same gas volume. This means that the avalanche associated to the cluster closer to the read-out electrode will accumulate less charge than the one relative to a farther cluster.

avalanche (the charge spectrum has an exponential shape). In a multigap RPC, the sheets of resistive material electrically floating and transparent to the fast signals generated by the avalanches, allow the simultaneous readout of many (sub) gaps, and then the signal is truly the sum of independent avalanches[3] (the charge spectrum has a Γ shape, similar to a Landau distribution). An exponentially-shaped charge spectrum is difficult to handle, since one is forced to keep the threshold as low as possible, to avoid a large reduction in efficiency. The charge spectrum from the multigap has a peak well separated from zero, and thus the setting of the threshold is far less critical. This improvement in the shape of the charge spectrum further increases the high rate capability of this device [62].

The goal of the development of the multigap resistive plate chamber was to profit from the good time resolution of the small gaps, while keeping the advantages of having a large total gas gap. A further improvement of time resolution was achieved by reducing the gas gaps to $700\,\mu m$ or less. Multigap RPCs with 4 gaps ($0.7\,mm$ of thickness) have been built and operated with a heavy Freon gas mixture at atmospheric pressure. The result is a time resolution of less than $1\,ns$ (without any corrections for pulse height) [63].

3.2 Towards the MRPC as a Time-0f-Flight Detector

At the begining of 1999, following the positive results obtained with a single-cell MRPC (see later on), an R&D activity was started towards a final prototype of microgap (§3.3), double-stack (§3.4) MRPC optimised for the ALICE Time-Of-Fight detector.

3.2.1 Test area set-up

The test beam area reserved to ALICE is the T10 beam line of the East Hall Proton-Synchrotron (PS) at CERN. All tests have been performed using a $7\,GeV/c$ beam of negative particles (π, μ). The experimental set-up consists of (see fig. 3.1):

- two pairs of crossed scintillators, the coincidence of which defines a $1\,cm^2$

[3]The avalanches occur in independent subgaps. Then each avalanche - at least one per subgap, depending on the gas mixture - accumulates the same charge.

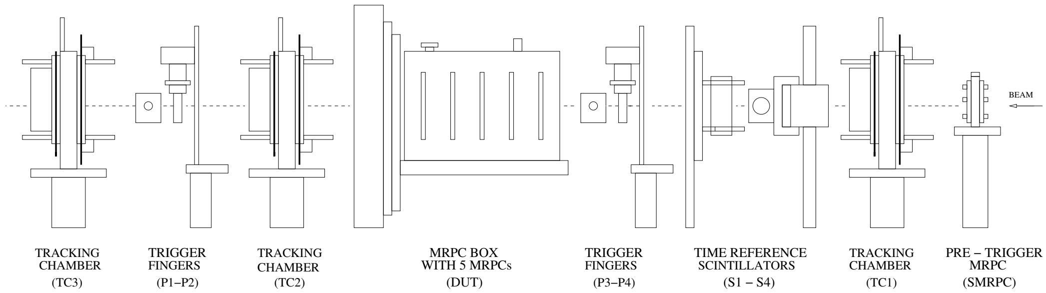

Figure 3.1: T10 experimental area.

area[4] and provides the trigger.

- a small fast scintillator which acts as a pre-trigger providing the start to the TDCs and the gate to the ADCs;

- three tracking chambers, each consisting of 2 planes of strips with $4\,mm$ pitch, to provide information on the beam position;

- two fast scintillator bars ($2 \times 2 \times 10\,cm^3$) equipped with two photomultipliers each, to provide accurate time reference;

- the detector under study (MRPC strip).

The electronics used for the readout of the above detectors consisted of CAMAC TDCs (LRS 2228A with a bin width set to $50\,ps$) and CAMAC ADCs (LRS 2249W). For the readout of the tracking chambers, VME ADCs were used (CRAMS with pedestal subtraction and zero suppression).

A pre-trigger was generated by the small fast scintillator; this pre-trigger was used to generate the gates and start signals for the CAMAC ADCs and TDCs (working in ‘common start’ mode). A trigger was provided by the two pairs of crossed scintillators at a later time. If no trigger was produced, the ADCs and TDCs were cleared.

[4]The upstream pair defines a $2 \times 2\,cm^2$ area; the downstream pair, instead, a $1 \times 1\,cm^2$ area.

3.2.2 First results: single-cell MRPC and 2×8-cell MRPC

The initial (autumn 1998) tests [64] concerned the choice of glass instead of melamine sheets as resistive plates for MRPCs[5]: the best result in terms of time resolution (100 ps) was obtained with a double[6] two-gap device, named 'single cell' because of its sensitive area ($4 \times 4\,cm^2$), with glass sheets as resistive plates and flushed with a gas mixture of 90 % $C_2F_4H_2$, 5 % SF_6 and 5 % Isobutane [63]. This is a non-flammable gas that has caused no problems. Indeed, it is the best mixture and has been adopted for the final design of the ALICE TOF MRPC.

During 1999, using a smaller ($3 \times 3\,cm^2$) single-cell MRPC with glass sheets (of 500 μm thickness for the inner ones[7] and 2 mm for the outer ones), mechanically strengthened with two sheets of 12 mm honeycomb, and 5 gas gaps of 220 μm thickness, a time spectrum with very small tails (see fig. 2.28 in [55]) was obtained. The efficiency was 99 % at 12 kV, and the time resolution 70 ps after T(A) (time vs. pulse amplitude) corrections (see fig. 2.30 in [55]). These good results suggested a possible ALICE TOF detector design as made up of an array of single cells. Such an array is obtained by segmenting the anode and cathode of the detector into appropriately shaped "readout pads", still keeping a unique gas volume and unsegmented glass sheets. To each pair of anode and cathode pads corresponds an individual cell.

A detector consisting of a long strip of cells turned out to better match the ALICE geometry requirements[8]. Besides, if the strip is made 2 cells wide (fig 3.2), it is easier to connect the electronics to readout both the anode and cathode pads in order to reduce the possible 'boundary effects' between two neighbouring cells (see later on); we can thus obtain a differential signal from the detector. This is shown schematically in fig. 3.3. In addition, we experienced at first hand the ease of connecting fast and sensitive amplifiers to a device that produces a differential signal.

A 2×8-cell MRPC, as shown in fig. 3.2, was tested in November 1999. The MRPC has 5 gas gaps of 350 μm thickness; the internal glass plates have 550 μm thickness and the external layers 3.2 mm.

For one of these cells, the efficiency, time resolution and time-walk (i.e. the change in absolute time due to charge, i.e. applied voltage, variation) after T(A)

[5]The melamine is less rigid than the glass: this causes non-uniformity in the gas gap thickness.

[6]This was a prototype of "double-stack" device, see later on §3.4.

[7]See §2.4.1.1 in [55] for more details about the kind of glasses and resisitivity.

[8]The ALICE detector space-frame has a modular structure: 18 sectors in the azimuthal angle (φ) and 5 slices in the longitudinal coordinate (z) along the beam direction (see figs. 2.5 and 4.2).

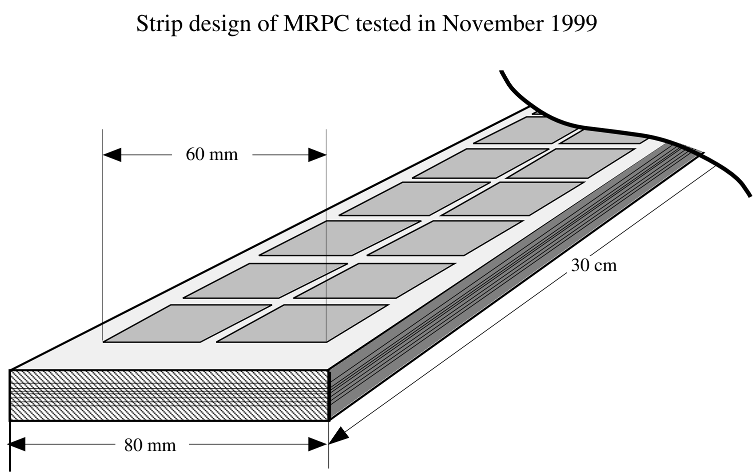

Figure 3.2: Schematic view of a strip detector used in the November 1999 test beam.

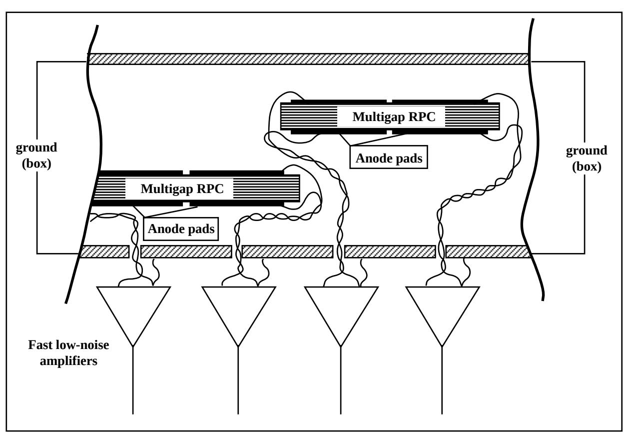

Figure 3.3: Schematic layout of the readout of a MRPC strip. The MRPC generates a differential signal; the signal return is not through the box.

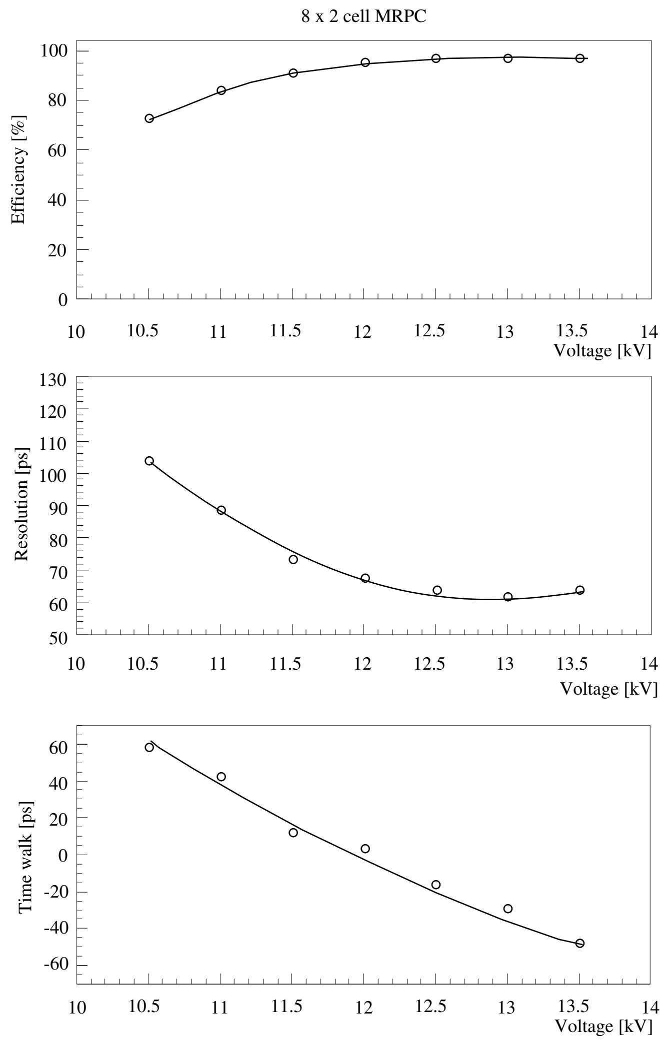

Figure 3.4: Efficiency, time resolution and time-walk as a function of applied voltage for one of the cells of the MRPC strip.

corrections, as a function of high voltage, are similar to those obtained with the single cell previously discussed. Hence there is no degradation in performance by increasing the active area of the detector, as can be seen in fig. 3.4.

First studies on boundary effects

Boundary effects between two cells have been carefully investigated.

For all the tests described above, the trigger was based on two pairs of crossed scintillators (see §3.2.1); the upstream cross defined a $2 \times 2\,cm^2$ area while the downstream cross defined a $1 \times 1\,cm^2$ area. Thus, even though we were using a defocused beam, the trigger selected a small area of the chamber under test.

In order to examine the edges between two cells, we removed the downstream $1 \times 1\,cm^2$ scintillators from the trigger. This caused some $5\,\%$ to $10\,\%$ of the through-going tracks to be misreconstructed. The resulting efficiency of the cells was obviously lower than previously measured. Figure 3.5 illustrates the layout of the cells and the region scanned when examining the boundary between two cells (numbered 20 and 28) and their outer edges. The front-end electronics was connected to the outer edge of the cell readout pads as shown in fig. 3.5.

In fig. 3.6 we show the cell efficiency versus beam position. There is a region, at the boundary between the two cells, where both pads record valid hits; this is the effect of charge sharing; this region will get smaller once the device will be optimised (see later on § 3.4.1). For both cells the efficiency remains high up to the edge of the pad active area. Outside the pads the efficiency should be zero; actually, in fig. 3.6 it has a value between $5\,\%$ and $10\,\%$ due to the above mentioned problem of track misreconstruction.

In fig. 3.7, the time resolution is shown as a function of position. At the boundary, there is a visible degradation (up to $130\,ps$) of the resolution. This is so because the time spectrum contains a mixture of events; some of which are 'true' events which occur and some which are 'cross-talk' events when the avalanche is really on the neighbouring pad.

Using the weighted average of the times measured by the two pads, where the weight is proportional to the measured pulse height for each pad, an improvement of the time resolution at the boundary between the pads can be obtained, as shown in fig. 3.8. One assumes that part of this improvement is due to having two independent electronic channels. Whether such technique can be used in the experiment to avoid the degradation of the time resolution at the boundaries between pads will depend on the overall occupancy (see §4.2.1) of the detector in $Pb-Pb$ collisions at LHC.

A possible improvement of the MRPC response at the boundary between two

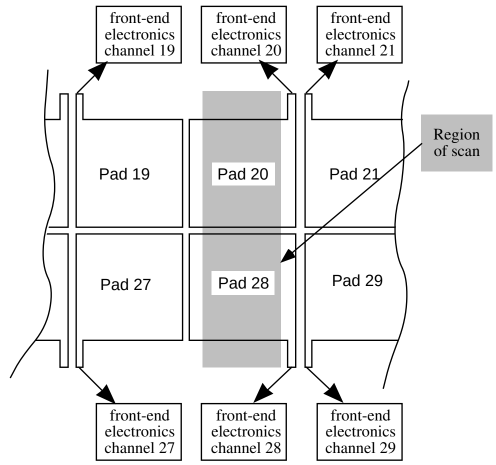

Figure 3.5: Layout of the cells (corresponding to pad 20 and pad 28) and of the region of scan (grey area).

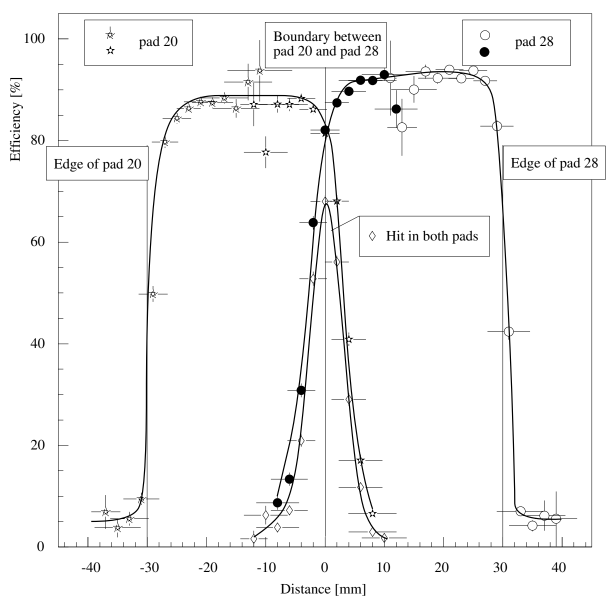

Figure 3.6: Efficiency as a function of position. The solid lines are to guide the eye.

pads has been further investigated using a differential amplifier for the readout which has been included in the design of the front-end electronics.

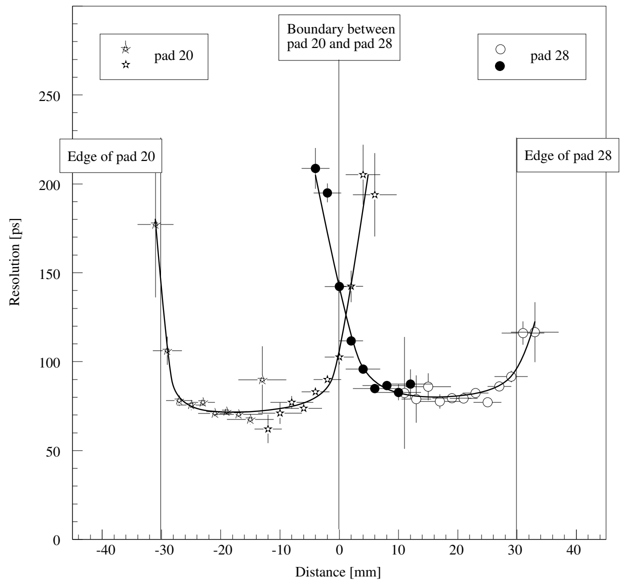

Figure 3.7: Time resolution as a function of position. The solid lines are to guide the eye.

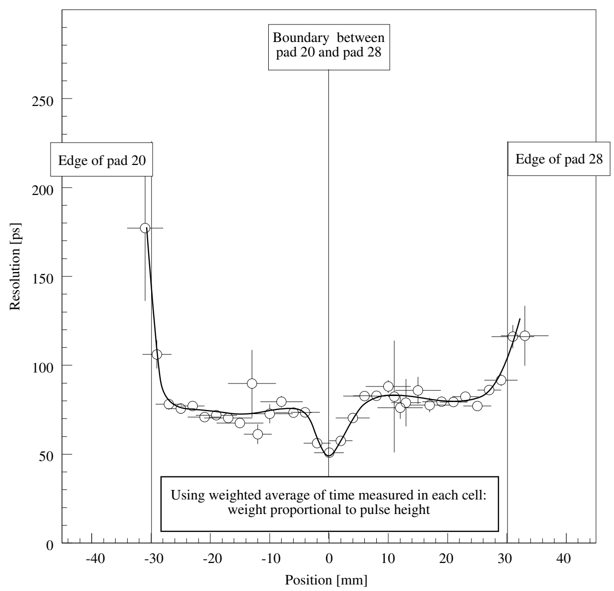

Figure 3.8: Time resolution as a function of position using the weighted average of the times measured by two pads. The weight is proportional to the measured pulse height from each pad. The solid lines are to guide the eye.

3.3 From 2×8-cell MRPC to 2×48-cell MRPC-strip

The main goal of the R&D effort during the year 2000 was to investigate the problems associated with scaling up from a small test MRPC-strip [55] (with 2×8 readout pads of $3 \times 3\,cm^2$) to a long MRPC-strip (with an active area of $7 \times 120\,cm^2$ read by a matrix of 2×48 pads, each of $3.5 \times 2.5\,cm^2$ area[9]).

The goal was to understand which parameters were critical to build full-sized TOF MRPC-strips namely:

- gas gap number;
- gas gap thickness;
- resistive (glass) sheet thickness[10].

In the test beam experimental set-up, the pre-trigger system was changed and a small MRPC of $10\,cm^2$ active area was included. This 'start' MRPC was a small chamber consisting of a single-stack of glass plates defining 5 gaps of $230\,\mu m$ thickness; it has been used in our test beam set-up for two years and has given no problems. Even though this cannot be regarded as an aging test, it does give us confidence about the stability of this technology.

The first full-sized strips that we constructed had good efficiency (98%) but 'bad' time resolution ($\sim 150\,ps$). We eventually understood this was due to non-uniformity of the thickness of the gas gaps. Increasing the width of the active area from $6\,cm$, as in the 2×8-cell MRPC-strip [55], to $7\,cm$, as in the full-sized MRPC-strip, allowed the glass sheets to further distort, and maybe even to touch in some places. We decided to space the glass sheets by running a plastic fiber across the width of the active area every $2.5\,cm$ (i.e. between consecutive readout pads). A nylon fishing line was used wrapped around plastic screws (so the fiber was continuous). This is shown in fig. 3.9 to be compared with fig. 3.10, illustrating our previous technique based on spacer buttons. This nylon fishing line comes in a variety of thicknesses (by $20\,\mu m$ steps in the range around $200\,\mu m$) and is very uniform; we have adopted this as the spacer material for all the following strips and for the final design of the TOF MRPC-strips. These fibers are aligned with each other and will not create a significant dead region since they are small

[9]Even though it is conceivable to build the $160\,m^2$ ALICE TOF detector from ~ 160000 individual readout cells, it is much easier to build larger detector units and segment the readout.

[10]The gas gap number controls the device efficiency; the gas gap thickness controls the time resolution. A correlation exists between these parameters.

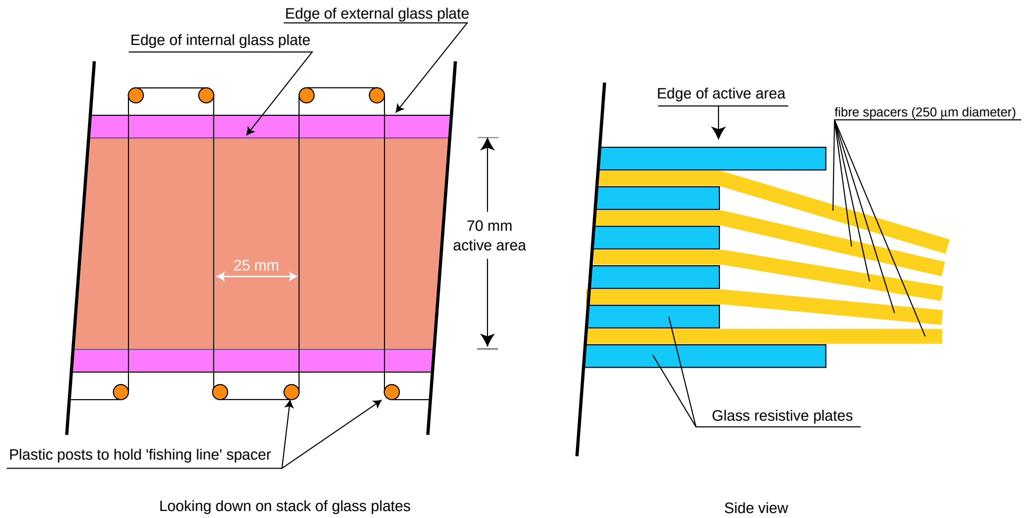

Figure 3.9: Possible scheme for spacing the resistive plates of a long MRPC-strip. A fiber is run across the width of the active area and around a plastic screw (to hold it in position). The edge of the active area is defined by the cut edge of the internal glass sheets.

($200-280\,\mu m$ diameter) and if the traversing particles are not normal to the glass plates[11], it is likely that they would only pass through one fiber at most and be able to initiate gas avalanches in the other gas gaps. Hence the scheme shown in fig. 3.9 could be adopted for the final TOF MRPC design.

Two MRPC-strips with 6 gas gaps and 2×48 readout pads showed $70\,ps$ time resolution and $>96\,\%$ efficiency (see details in §2.2.2 of [57]). Of these two prototypes, one strip had internal glass plates of $600\,\mu m$ thickness and worked better than the other one, where the thickness was $1.1\,mm$ [57]. A glass thickness of $550\,\mu m$ was then adopted.

The effects of the variation of the gap width were studied by constructing three MRPC-strips, each with 6 gas gaps, with identical characteristics (plate material and thickness), apart from the gap width. These strips, numbered 6, 7 and 8 (for

[11] According to the Monte Carlo simulations, in ALICE the average incident track angle on a pad, in the final tilted-strip version of the TOF detector (see §4.2.2 in [55] and §5.2.2 in [57]), measured with respect to the normal to the pad at the incident point, will be much greater than 0°. This angular deviation, mainly caused by the magnetic field, will be $\sim 17°$ at $B = 0.2$ T and $\sim 27°$ at $B = 0.4$ T (see fig. 5.7 in [57]).

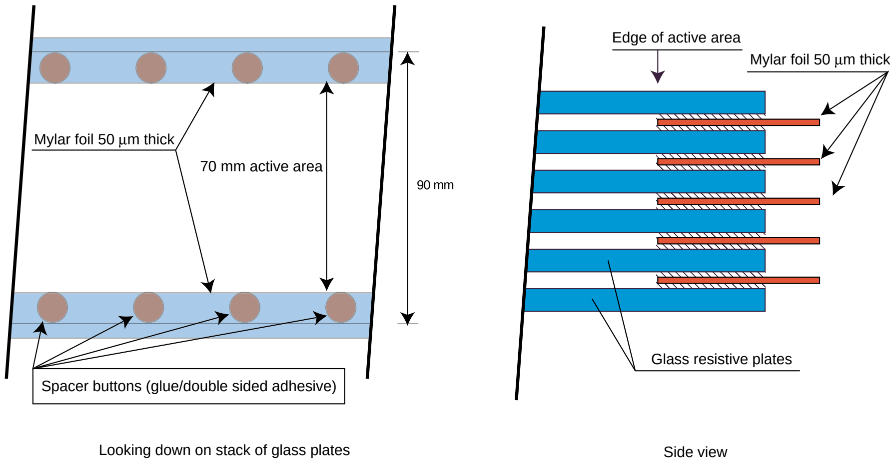

Figure 3.10: Original scheme for spacing resistive plates. The outer $1\,cm$ of the glass plate was used to place the spacer button; this outer region was made dead by means of mylar foil, with the edge of this mylar foil defining the edge of the active area.

chronological reasons) had the following characteristics:

- $550\,\mu m$ internal plates from Glaverbel glass;
- $2.5\,mm$ external plates from Schott black welding glass;
- 6 gas gaps of width: $250\,\mu m$ each (strip 6), $220\,\mu m$ each (strip 7), $280\,\mu m$ each (strip 8).

Special care was taken to use exactly the same electronics for comparative measurements. In fig. 3.11 we show plots of efficiency, resolution and time-walk as functions of applied high voltage, for all the three strips. As one can see, the 'knee' of the efficiency plateau is roughly at $16\,kV$ for all the three strips. At $\sim 16\,kV$ the best time resolution is achieved in all the strips. The right hand plot in fig. 3.11 shows the time-walk versus applied voltage. For each MRPC-strip the same T(A) corrections[12] have been used for all voltages. The MRPC-strip with the smallest gas gap ($220\,\mu m$) has the lowest time-walk ($< 50\,ps/kV$ change).

From fig. 3.11 one can conclude that the width of the gas gap is not so critical; it can be varied from 220 to $280\,\mu m$ without changing the operating voltage.

[12]The function used for T(A) corrections was derived by fitting the data taken at the highest voltage, $18\,kV$.

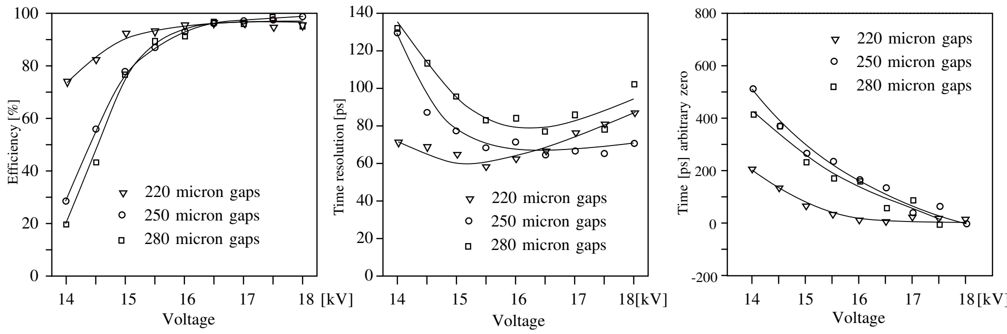

Figure 3.11: Efficiency, time resolution and time-walk for strips 6, 7 and 8 as a function of the applied voltage.

Smaller gaps give better time resolution and lower time-walk, while relatively larger gaps increase the 'streamer-free' region of the plateau and enhance the efficiency. We finally selected a gap size of $250\,\mu m$. This invariance with gap size is a key ingredient in building large strips. It would be impossible to build units of this size if all the gas gaps had to be uniform to better than, for example, $5\,\mu m$ as it is usual for parallel plate chambers with metallic plates. The results indeed indicated that devices of active area $7 \times 120\,cm^2$ are a realistic choice.

3.4 From single- to double-stack MRPC-strip

In the year 2001, the design of the TOF MRPC-strips was changed. Instead of a single-stack MRPC, described so far, a double-stack version was introduced. The two different types of MRPCs are shown schematically in fig. 3.12. The double stack structure consists of 2 MRPCs, built on each side of the anode pickup pads. The signal measured in this case is the sum of the signals of the two MRPCs.

The reasons for this change in design were the following :

- the signal from the double-stack MRPC is larger by a factor of 2 compared to that from a single-stack MRPC with the same characteristics (same number of gaps and same gap width);

- the anode and cathode can be moved closer, as compared to the single-stack device, thus making the charge projection area of the avalanche (on the

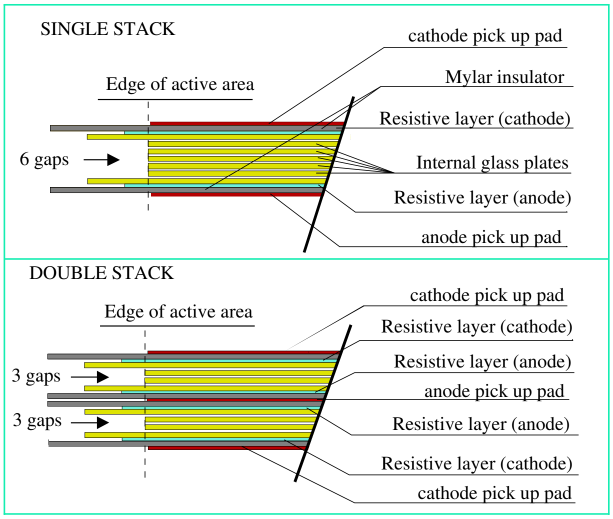

Figure 3.12: Cross sections of a single-stack and a double-stack MRPC with a total of 6 gas gaps.

pickup pads) smaller; this could sharpen the boundaries between pads (see later on §3.4.1);

- a single-stack device needs a factor 2 higher applied voltage than a double-stack one (in case each stack in the double-stack has half the number of gaps of the single-stack);
- as a consequence of the above points, devices with increased numbers of gaps (to increase the efficiency) can be built, since the practical limitations (high voltage power supplies) become less critical.

A number of such double-stack MRPC-strips were built and tested during the spring and summer of 2001. Following the numbering of the full-size MRPC prototypes built in 2000, these were strips $9-12$ and had the following characteristics:

- strip 9 : 2 stacks of 3 gaps of 220 μm;
- strip 10 : 2 stacks of 5 gaps of 220 μm;
- strip 12 : 2 stacks of 5 gaps of 220 μm.

Internal plates of $550\,\mu m$ thick Glaverbel[13] glass and external plates of $620\,\mu m$ thick Glaverbel glass were used to build these strips. For strips 9 and 10, the HV electrodes were made out by sticking a double-sided adhesive carbon tape of $200\,k\Omega/\Box$ on one surface of each external glass; for strip 12, a resistive layer of $5\,M\Omega/\Box$ was used[14].

The results, plotted in fig. 3.13 as a function of the electric field inside the gas gap (calculated by dividing the applied voltage by the total gas gap width), show that:

- the efficiency of the 10-gap MRPC is close to $100\,\%$ and reaches the plateau at lower electric field, thereby extending the plateau of operating voltage (from $5.7\,kV$ to $6.6\,kV$)[15];
- a time resolution, for the electric field corresponding to the knee of the high voltage plateau, between $40\,ps$ and $50\,ps$ is observed.

[13] Glaverbel VERTEC Sales, Brussels, Belgium.

[14] The technique for applying it on each external glass was different in this case: one surface of the glass was painted with a specially developed (DETEC, Turin, Italy) acrylic paint loaded with metal oxides.

[15] Note that the boundary for streamer production is at $120\,kV/cm$, as could be deduced from the tests of single-stack strips with 6 gas gaps (see §3.3). Streamers produce a second peak in the pulse height distribution and a worsening in time resolution.

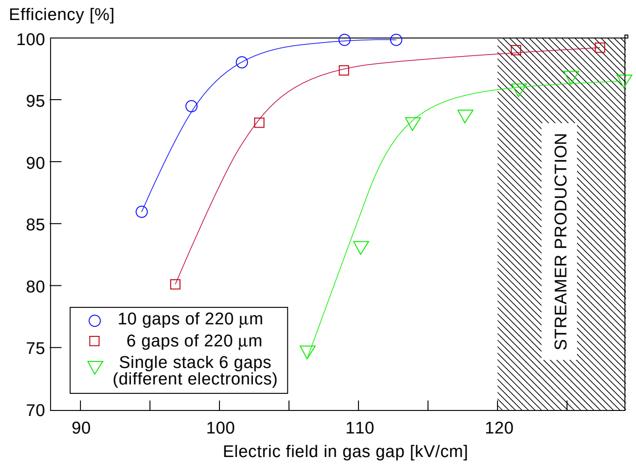

Figure 3.13: Efficiency versus electric field in the gas gap for double-stack strips 9 and 10, and for single-stack strip 7. All the strips had a total of 6 gaps, each of 220 μm.

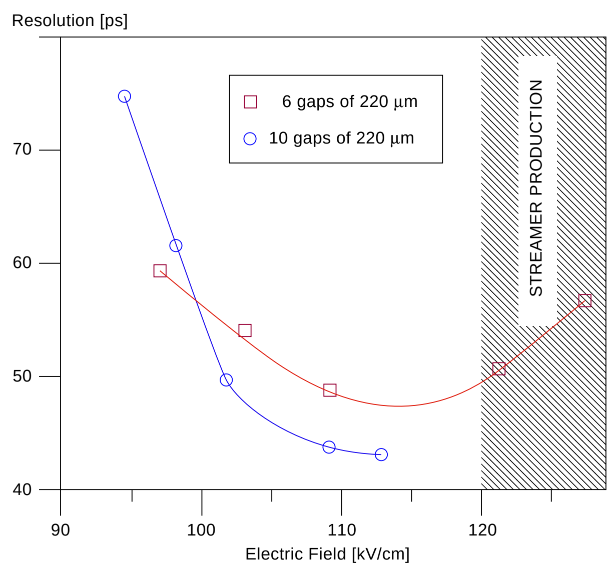

Figure 3.14: Time resolution as a function of the electric field for double-stack strips 9 and 10.

3.4.1 New studies on boundary effects

The fact that the TOF system consists of long strips read out by individual pads, with some *mm* spacing between them, means that, at the boundaries between pads, there will be a possible charge sharing between the pads, as already pointed out in §3.2.2. This would lead to a loss in efficiency, on one hand, and to a degradation of the time resolution, on the other. In addition the double hit probability (in neighbouring pads) would increase. In the final system, the boundaries have to be optimised so that these effects are minimised.

To study the boundary effects we scanned many MRPC-strips (see fig. 3.15) along the length of the strip (pad A-pad B-pad C, longitudinal scan) and across the width of the strip (pad B-pad D, transverse scan), moving the chambers by 5 *mm* steps on the beam line.

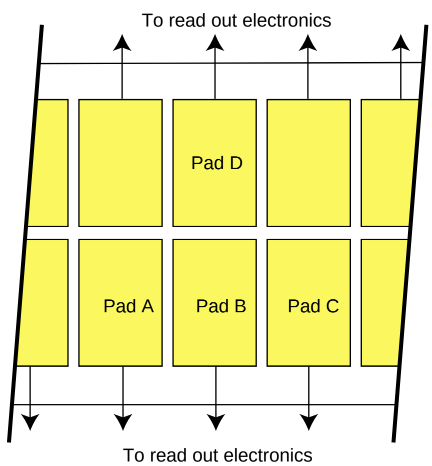

Figure 3.15: The boundaries were evaluated by scanning along the length and across the width of the strip; the labelling of the pads used in other figures is shown here to clarify which boundaries were under test.

The factors that play a role in the change of performance at the boundaries of the pads are:

- the exact threshold and the dynamic range of the charge spectrum;
- the size of the charge projection area of the avalanche on the pickup pads.

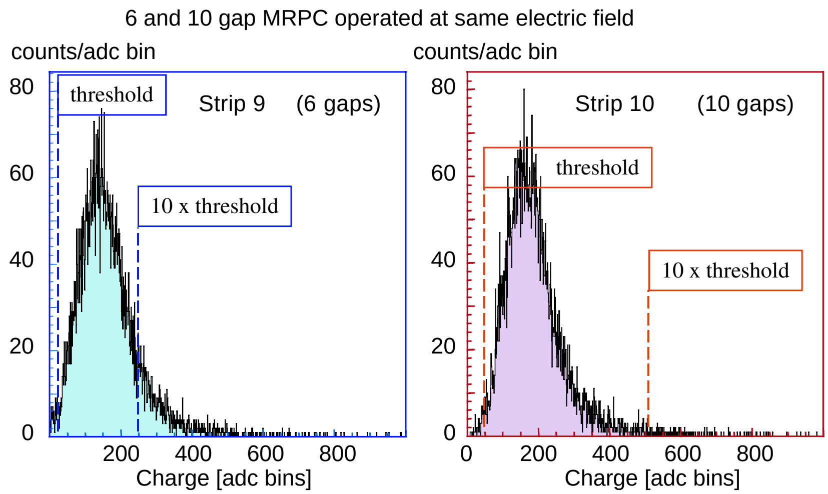

Figure 3.16: Charge distribution in the pad centre for double-stack strips 9 and 10.

As regards the first point, let us consider an event close to the boundary between two neighbouring pads A and B, producing 90 % of the charge on pad A and 10 % of the charge on pad B: in the ideal case we want pad A to see a hit and pad B to see nothing. To achieve this, the threshold has to be set so that in most cases the 10 % level of charge seen on pad B does not fire the discriminator; however, the discriminator has to be set at a level low enough so that the efficiency on pad A is not compromised. Figure 3.16 shows the charge spectrum for strips 9 and 10, at the same electric field. From the different shape of the two distributions near zero one can see that a very low threshold is needed for the 6-gap MRPC for the efficiency to be high and this would result in the boundaries not being ‘sharp’ enough. The 10-gap MRPC can be operated at a higher threshold with no significant loss in efficiency; thus this produces sharper boundaries.

Concerning the second point, the size of the charge projection area of the avalanche depends on the total distance between anode and cathode and on the resistivity of the layer between the HV electrodes and the external surface of the last glass sheets. The higher resistivity coating makes the boundaries sharper (fig. 3.17, right), thus the lower resistivity carbon layer does spread the charge projection (fig. 3.17, left).

The efficiency as a function of the beam position along the strip, for strips 10 and 12, is shown in fig. 3.18. Here the sharpness of the boundaries is similar, due

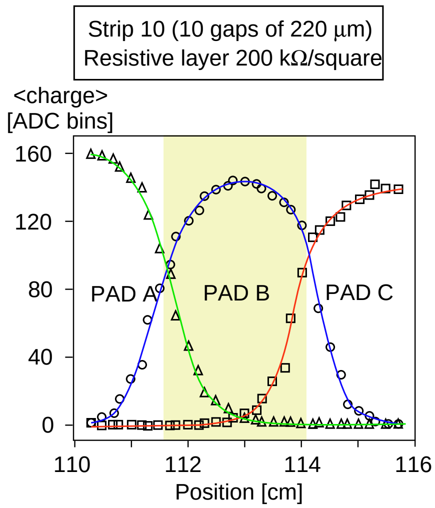

Figure 3.17: Average charge as a function of the beam position along the strip, for strips 10 and 12.

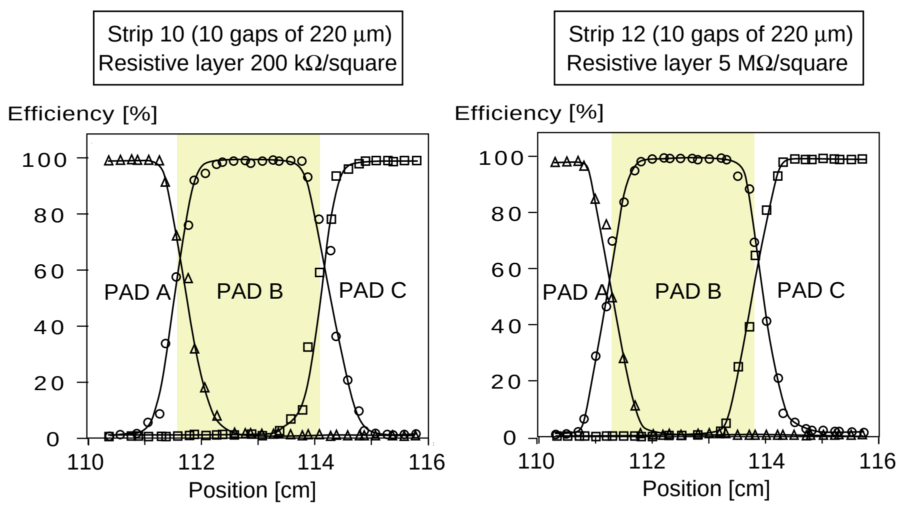

Figure 3.18: Efficiency as a function of the beam position along the strip, for strips 10 and 12.

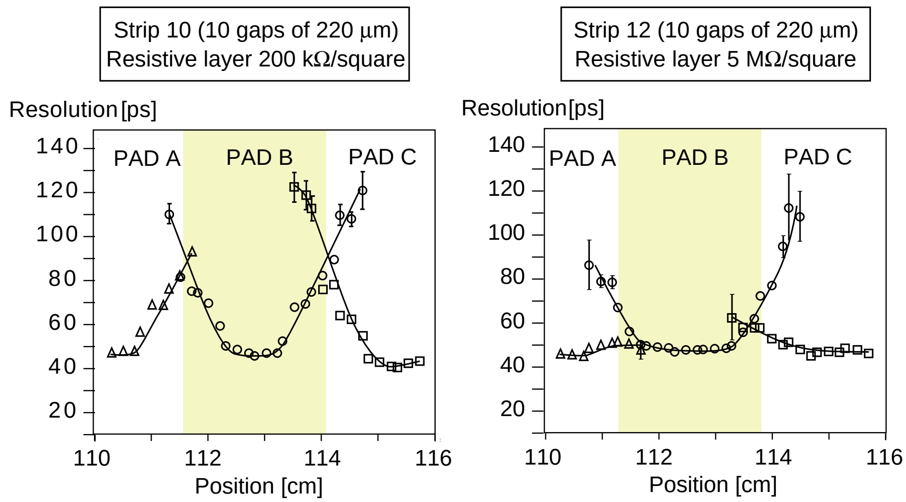

Figure 3.19: Time resolution as a function of the beam position along the strip, for strips 10 and 12.

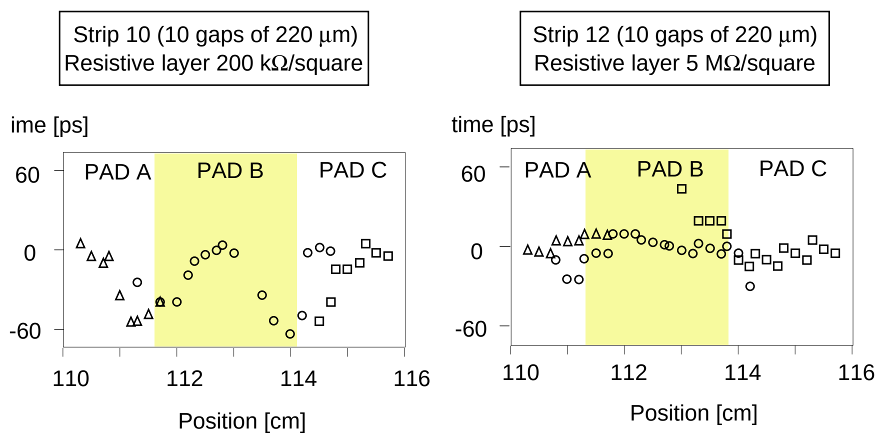

Figure 3.20: Time-walk as a function of the beam position along the strip, for strips 10 and 12.

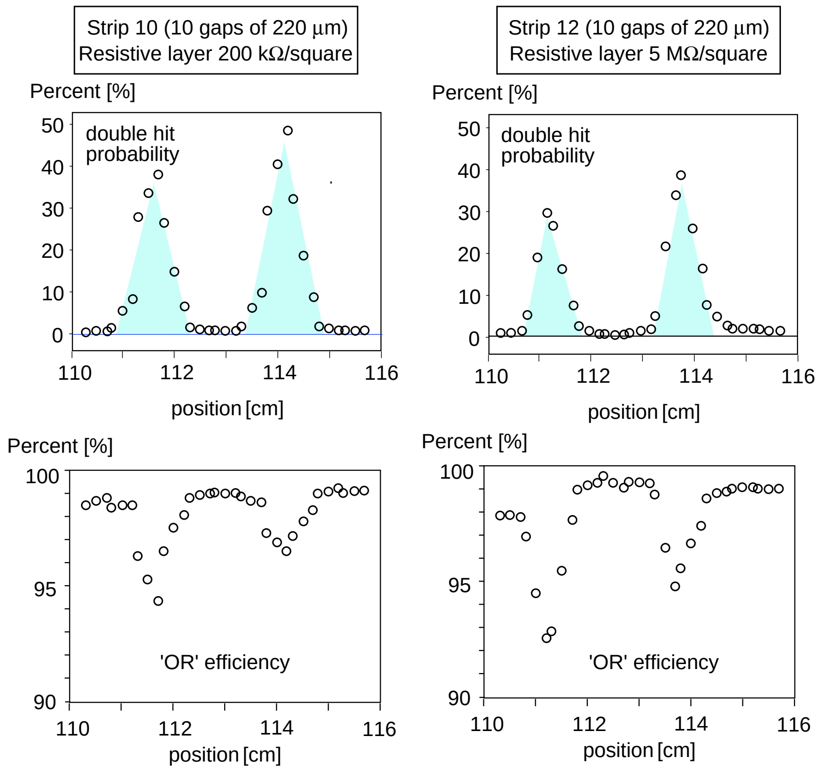

Figure 3.21: Double-hit probability and global efficiency (OR of neighbouring pads) as functions of the beam position along the strip, for strips 10 and 12.

to the finite dynamic range of the charge spectrum of the 10-gap MRPC.

The charge uniformity observed for strip 12 affects the time resolution (fig. 3.19): strip 12, which has the $5M\Omega/\Box$ coating, has much more uniform resolution, which is expected to be due to the uniformity of the charge.

Figure 3.20 shows the time-walk as a function of the beam position along the strip, for strips 10 and 12. Again the variation of charge at the boundaries shows up as deviation in absolute time: the high resistivity coating of strip 12 implies much smaller deviations.

Figure 3.21 shows the double-hit probability and the global efficiency (OR of neighbouring pads) as functions of the beam position along the strip, for strips 10 and 12. For strip 10 (left) one can observe a 1.5 % drop in global efficiency at the boundary and 12.5 % double-hit probability; for strip 12 (right), a 2 % drop in

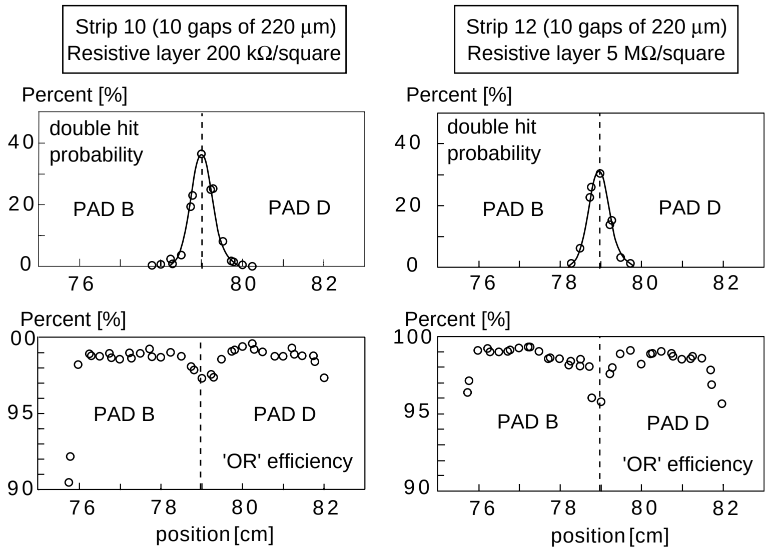

Figure 3.22: Double-hit probability and global efficiency (OR of neighbouring pads) as functions of the beam position across the strip, for strips 10 and 12.

global efficiency at the boundary and 8.5 % double-hit probability.

Concerning the transverse scan (across the central boundary) of the strips, the results for strips 10 and 12 are shown in fig. 3.22, again in terms of global efficiency and double-hit probability as functions of the beam position across the strip. For strip 10 (left), the double-hit probability at this boundary is 3.8 %, whereas for strip 12 (right) it is 3.2 %.

In conclusion, a comparison can be made of figs. 3.18, 3.19, 3.21 and 3.22, relative to the two double-stack strips 10 and 12, with fig. 3.6 and fig. 3.7, relative to the 2×8-cell single-stack MRPC. The performance of the double-stack MRPC (strips 10 and 12) clearly improves with respect to that of the single-stack (2×8-cell) device:

- the efficiency and time resolution values in the middle of the pad improve (from $\sim 90\%$ to $> 99\%$, and from $\sim 70\,ps$ to $40-50\,ps$);
- the border region between two neighbouring pads is reduced by a factor of 2 (from $\pm 1\,cm$ to $\pm 5\,mm$);
- the total double-hit probability decreases from $\geq 20\%$ to $\sim 12-16\%$.

The higher resistivity of the paint between the HV electrodes and the external resistive plates (strip 12 compared with strip 10) produces a smaller charge projection area on the signal pickup pads, and, as a consequence, the time-walk and the time resolution are more uniform all over the pad.

Weighting double (or multiple) hits

A detailed study has been performed on how to introduce a weight for the signal(s) induced in the neigbouring pad(s) surrounding the pad hit by a particle.

The pulse height or a power of it is a good candidate (see §3.2.2). From our test-beam data on border effects between the pad actually hit by a particle, 1, and any of its neighbouring pads, 2, we observed:

- a linear decrease, from positive values down to *zero*, of the logarithmic charge-ratio of signal pairs from adjacent pads, $ln(q_1/q_2)$, when moving from the centre towards the border of the hit pad;
- a linear decrease of the relative delay of signal pairs from adjacent pads, $|t_1 - t_2|$, as the logarithmic charge-ratio decreases from positive values to *zero*, i.e. when moving from the centre to the border of the hit pad; notice that the smaller the pulse height, the larger is the signal delay.

The results are illustrated in figs. 3.23 and 3.24 for the longitudinal scan of the pads (see fig. 3.15). Very similar results are obtained for transverse scan.

3.4.2 Rate tests of double-stack MRPC-strips at the GIF

In the summer of 2001, the double-stack MRPC-strips 10 and 12, described in the previous section, were tested at the Gamma Irradiation Facility (GIF) at CERN. The purpose of these tests, presented in detail in [65], was to verify whether the performance of the MRPC will remain unchanged during many years of operation at the continuous rate of charged particles expected at LHC.

The main result was that this device can indeed operate far in excess of the $50\,Hz/cm^2$, which is the maximum rate expected for the ALICE TOF, over a period equivalent to 1000 days of $Pb-Pb$ collision runs. The reason for this excellent behaviour is due to (a) the choice of the bulk resistivity of the glass sheets and (b) the small amount of charge produced for each through-going charged particle.

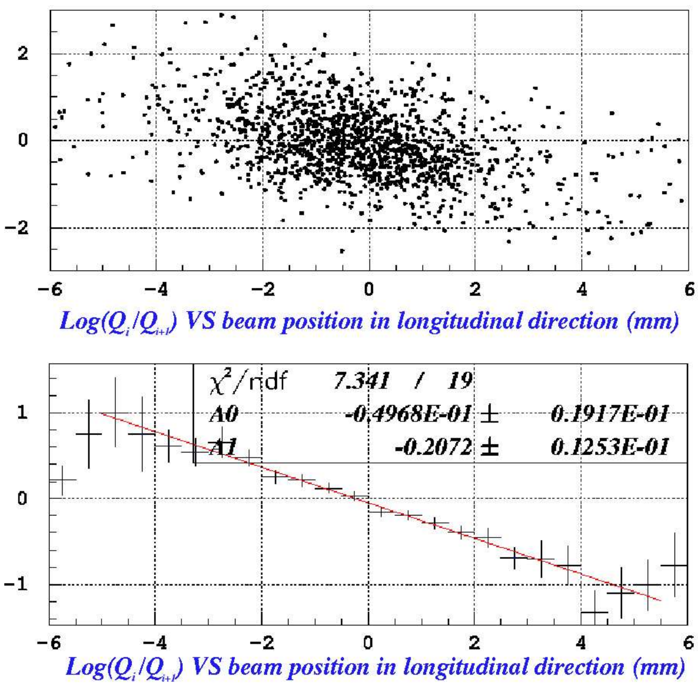

Figure 3.23: Logarithm of the ratio q_1/q_2 - see text for details - *vs.* hit position along the pad: it decreases linearly when moving from the centre of pad 1 (at $-25\,mm$) towards the centre of pad 2 (at $+25\,mm$) across the boundary between the pads (at $0\,mm$).

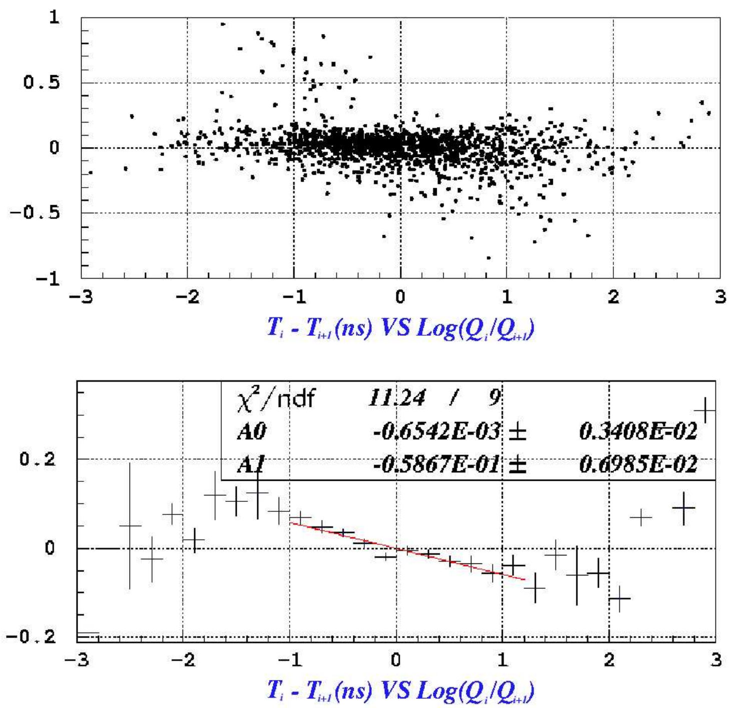

Figure 3.24: Difference between t_1 and t_2 - see text for details - *vs.* logarithm of the ratio q_1/q_2.

3.5 ALICE TOF Detector: central module test

In the autumn of 2001, two prototypes of the central module of the TOF detector (see later on §4.1.1) were constructed, equipped with double-stack MRPC-strips and measured in the T10 beam line (see §2.5 in [57] for details). Each module is an aluminium box with dimensions $125 \times 114 \times 16\,cm^3$, designed to contain 15 MRPC-strips. These are placed in two layers and overlapped so as to minimize the dead areas (see later on fig. 4.3). For this purpose, a first test of mass pre-production of MRPC-strips was performed: 18 strips were built in two laboratories, Bologna and CERN. The strips had the same[16] characteristics as strip 12 (described in §3.4.1), which had given the best performance. They had a double-stack configuration and for each stack:

- 5 gas gaps of $250\,\mu m$;
- an internal glass thickness of $400\,\mu m$;
- an external glass thickness of $550\,\mu m$;
- fishing line spacers across the strip width every $2.5\,cm$.

The modules were mounted on moving frames (see fig. 3.25), so that it was possible to illuminate with the beam any strip inside them. The high voltage *plateau* was systematically studied for all the 18 strips.

Figure 3.26 shows the efficiency and the time resolution as functions of the applied differential high voltage for 15 strips of the two modules (three strips were excluded from this comparison because of well understood construction problems). Although all strips appear to be at full efficiency at $\pm 6.25\,kV$, there are visible differences at voltages below the ‘knee’ voltage. These slight variations can be attributed to differences in the exact gap width, since different methods of applying pressure on the stack of glass plates were used during the production of the strips. At the nominal working voltage of $\pm 6.25\,kV$, most strips have a time resolution between 45 and 65 ps, and only one strip has a substantially worse time resolution of 80 ps.

The tests of the two prototype modules were successful; the performance of the strips was as expected from previous tests; however, the uniformity of the strips responses could be further improved.

[16] The thickness of internal plates for three of the strips was $400\,\mu m$, instead of $550\,\mu m$. The resistive coating for the high voltage electrodes had a value of $1\,M\Omega/\square$ for most strips; however one strip had $5\,M\Omega/\square$ and another had $18-20\,M\Omega/\square$.

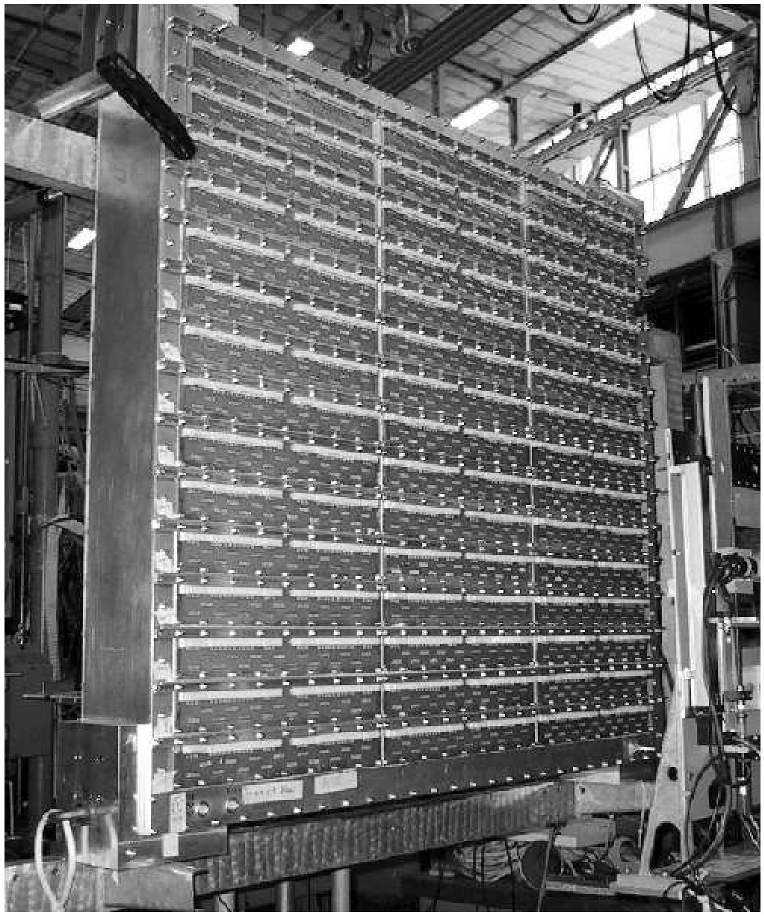

Figure 3.25: View of the prototype of the ALICE TOF central module inside the T10 beam area, showing the module board equipped interface cards; the front-end electronics cards are plugged into the connectors on this board.

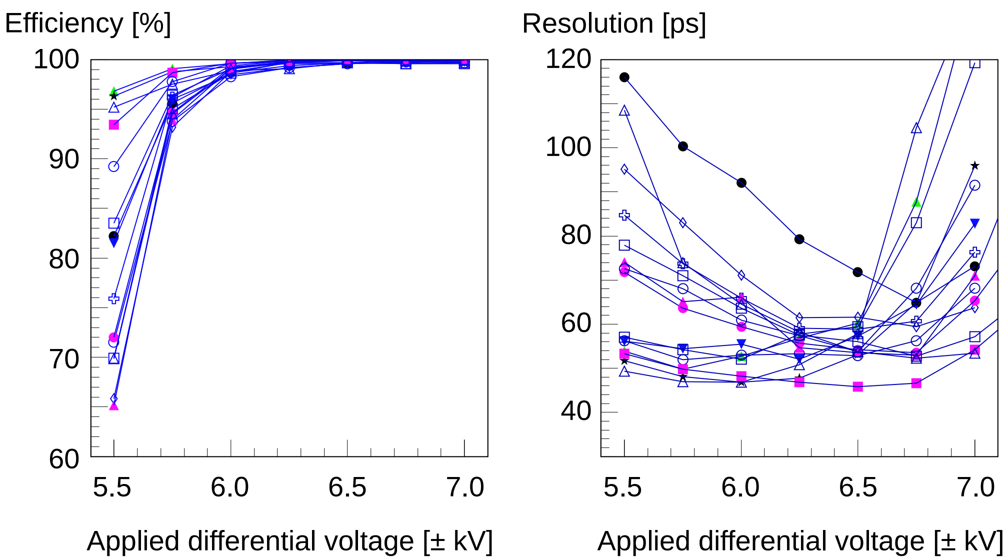

Figure 3.26: Efficiency and time resolution as functions of the applied differential voltage for 15 MRPC-strips.

As a consequence, another test (autumn 2002) of a further mass pre-production of 17 MRPC-strips was performed. Positive results were obtained. All strips were built according to the design shown in details in fig. 3.27, which will presumably be adopted for each detector element of the ALICE TOF system. Each element will be a double-stack MRPC-strip of $7 \times 120\,cm^2$ active area; each stack will have:

- 5 gaps with a gap size of $250\,\mu m$;
- outer glass sheets of $550\,\mu m$ thickness; inner glass sheets of $400\,\mu m$ thickness;
- resistive coating to apply high voltages, with acrylic paint of $5\,M\Omega/\square$ surface resistivity;
- PCB boards with pickup pads of $0.8\,mm$ thickness: the centres of the pads will be on a $2.5\,cm \times 3.5\,cm$ grid with $3\,mm$ spacing at all pad boundaries;
- fishing line spacers.

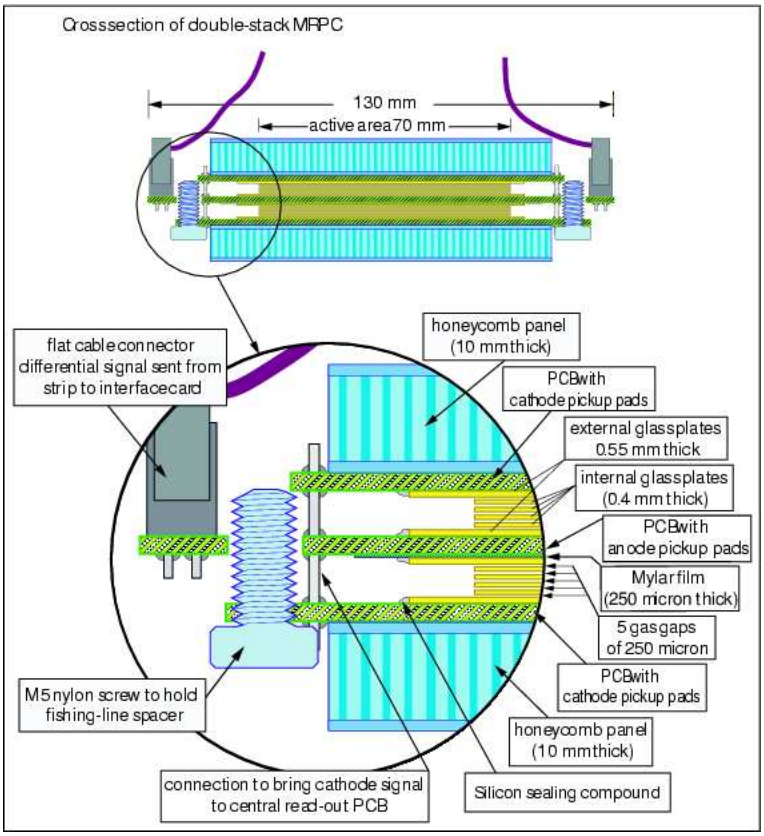

Figure 3.27: Schematic cross section of the double-stack MRPC-strip.

The 17 strips built with the characteristics recalled above behaved as our reference strip 12 (see §3.4.1). The uniformity of the strip responses was checked with several measurements along each strip and from one strip to another, with a total of over 130 pad measurements, and turned out to be satisfactory:

- in the distribution of efficiency values (see fig. 3.28) the mean value is 99.6 %, with $\varepsilon > 99\%$ for almost all the data (the $\varepsilon = 95-99\%$ tail, which corresponds to less than 10% of the measurements, was however well understood);
- in the distribution of time-resolution values (see fig. 3.29) the mean value of the gaussian fit is (63 ± 9) *ps*.

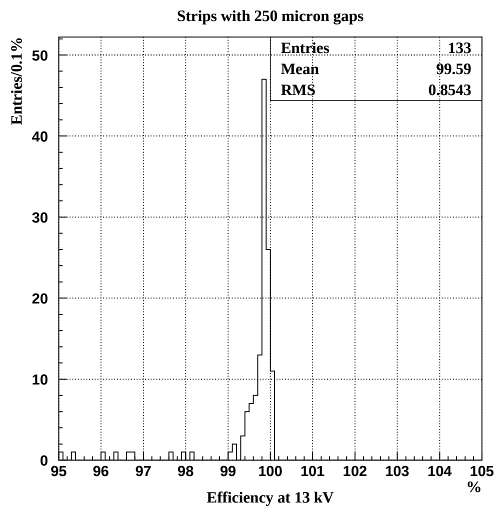

Figure 3.28: Distribution of efficiency values for all the 17 strips tested at $HV = \pm 6.5\,kV$.

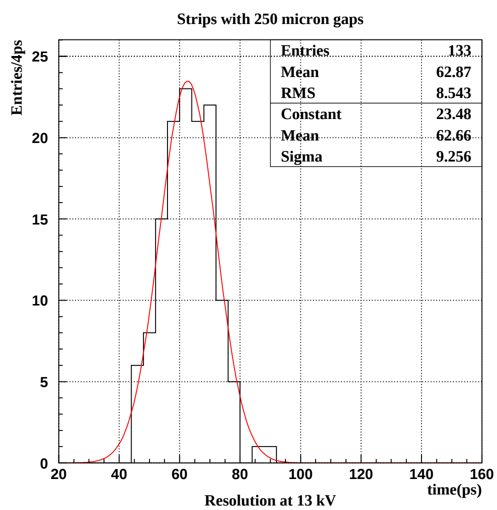

Figure 3.29: Distribution of time-resolution values for all the 17 strips tested at $HV = \pm 6.5\,kV$.

Chapter 4

TOF Detector Performance

As already pointed out (see chapter 2), the particle identification (PID) power of a very large TOF system covering the central rapidity region ($|y| \lesssim 1$) is of crucial importance in the ALICE experiment.

The goal of this chapter is to show that the ALICE TOF detector (described in §2.1.4 and §3.5) has the features appropriate to identify *pions*, *kaons* and *protons* in the intermediate momentum range (from a few hundred MeV/c to a few GeV/c).

By means of detailed Monte Carlo simulations, the ALICE TOF system PID capability has been tested in a "real" heavy ion collision environment, in terms of inclusive acceptances, matching efficiencies with the tracking detectors (ITS, TPC and also TRD), and PID efficiencies and contaminations for different particle species.

4.1 AliROOT framework

The present Monte Carlo simulation studies have been performed using AliROOT v3-09-Release [66], the release of the ALICE off-line code implemented in the ROOT [67] framework for event simulation, reconstruction and analysis.

4.1.1 Detector layout

The TOF detector geometry, the characteristics of which are reported in the following, has been implemented in the GEANT3 [68] tracking package of AliROOT.

The detector covers a cylindrical surface of polar acceptance $|\vartheta - 90°| < 45°$: the internal radius is $370\,cm$, the external one $399\,cm$. The overall TOF barrel length is $740\,cm$. In terms of material, the whole device thickness ($\sim 30\,cm$) corresponds to $\sim 20\%$ of a radiation length.

It has the modular structure shown in fig. 4.1, corresponding to 18 sectors in φ (the azimuthal angle) and to 5 segments in z (the longitudinal coordinate along the beam axis). Along z, we have a central module, two intermediate modules placed on both sides of the central one and two outer modules.

Each module has an internal structure organised in planar strips of double-stack MRPCs (15 in the central, 19 in the intermediate and 20 in the external modules), as shown in fig. 4.2. In order to minimise the trasversal path through the strips for particles coming from the interaction vertex, the strips are tilted by an angle progressively increasing with the distance from the interaction vertex (fig. 4.3).

Each strip is equipped with a mosaique of 2×48 sensitive pads, with a sensitive area of $2.5 \times 3.5\,cm^2$ per pad. The total surface is $\sim 170\,m^2$, the total sensitive surface $\sim 150\,m^2$, hence only $\sim 10\,\%$ of the total surface is dead.

4.1.2 Monte Carlo event generators

Different event generators are available to simulate $ion - ion$ collisions at $\sqrt{s_{NN}} = 5.5\,TeV/nucleon\ pair$. For the TOF preformance studies, we have essentially used two of them, SHAKER [69] and HIJING [70]. These are briefly described in the following.

Heavy Ion Jet INteraction Generator

The HIJING Monte Carlo model was developed to simulate particle production in $h-h$, $h-A$ and $A-A$ reactions at collider energies with special emphasis on the role of minijets in the heavy ion collisions [70]. It combines the Dual Parton model, which provides a unique picture for particle production in $h-h$, $h-A$ and $A-A$ interactions at high energies, with the Lund FRITIOF and the successful implementation of perturbative QCD processes in PYTHIA. Detailed systematic comparison of HIJING results with a very wide range of data demonstrates that a quantitative understanding of the interplay between soft string dynamics and hard QCD interaction has been achieved. In particular, HIJING reproduces many inclusive spectra, two-particle correlations, and can explain the observed flavour

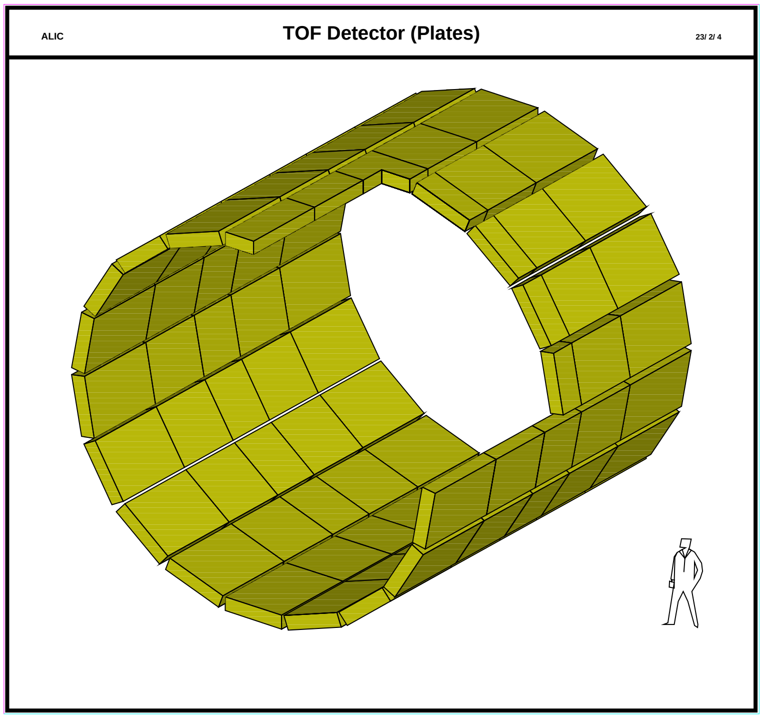

Figure 4.1: Time-Of-Flight (TOF) detector layout in AliROOT: modular structure.

and multiplicity dependence of the average transverse momentum.

SHAKER

The SHAKER event generator has been developed to describe the central rapidity region of heavy ion events at LHC [69]. It is derived from the Lund model, within the framework of JETSET 7.3 [71]. The main ingredient of this simple phase space generator is the density of particles at central rapidity, according to which the various particles (π^0, η, π^+, p, K^+, K^0) and antiparticles are produced. A rapidity plateau can be obtained between fixed limits. The p_T spectra of the generated particles reproduce those measured at the Tevatron [72]. For the η particle, the p_T distribution is derived from the experimental π^0 distribution using m_T-scaling [73]. Particle ratios are derived from Tevatron measurements [72] and isospin invariance. In SHAKER particle ratios, multiplicities and p_T distributions are easily adjustable.

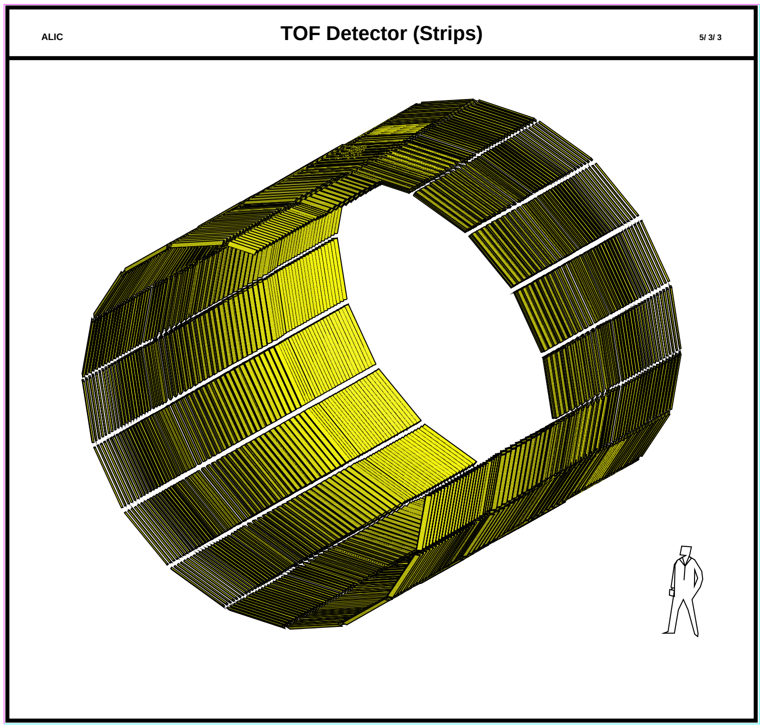

Figure 4.2: Time-Of-Flight (TOF) detector layout in AliROOT: strip visualization.

4.1.3 Event simulation

In average, in one $Pb-Pb$ central[1] collision at LHC energy, the total particle multiplicity was 78000, using the HIJING model. The time to track all these particles through $\sim 350\,m^3$ of ALICE detector, including all physics processes (decays, multiple scattering, interactions, etc.), is $\sim 12\,h$[2] and the disk space $1.5\,Gbytes$.

To reduce the CPU time and the disk space needed for the event simulation, only the particles generated in the $|\vartheta - 90°| < 45°$ angular region, corresponding to the ALICE TOF acceptance, were tracked through the ALICE detector. The simulation time was reduced in this way by a factor ~ 9.5 and the disk space by a factor ~ 7.5. The following event samples were considered for our studies:

[1]The impact parameter range is [0;3] fm.

[2]Pentium 4, dual-processor PCs have been used (each with 1.80 GHz clock and 256 KB RAM): all the ‘ALICE objects' defined in the AliROOT framework are ‘switched on'.

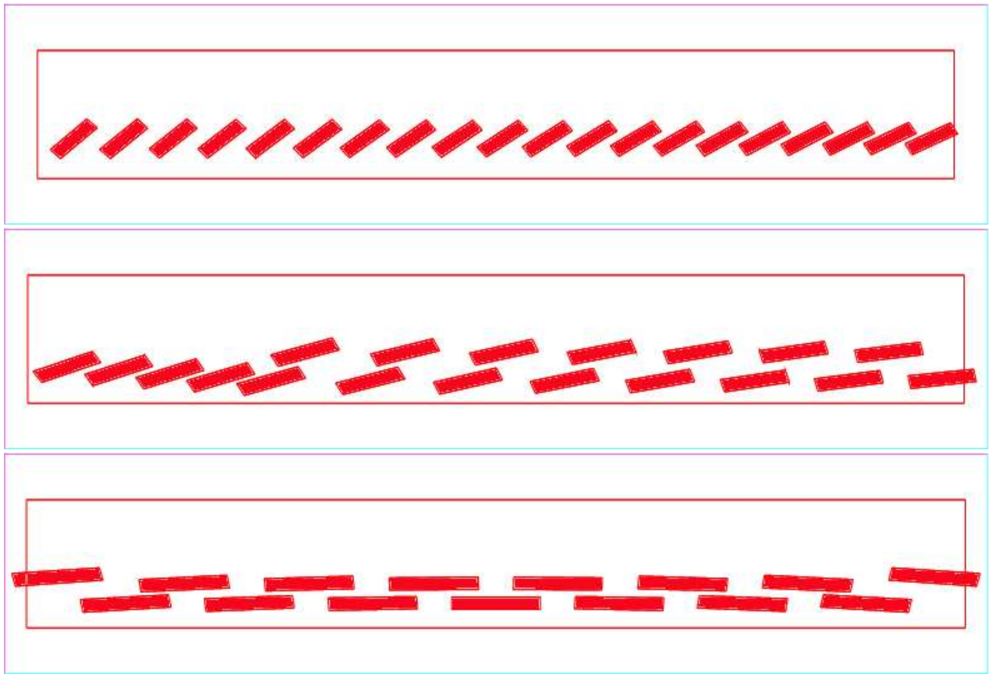

Figure 4.3: Time-Of-Flight (TOF) detector layout in AliROOT: side view (along the z axis) of the three module types: the external one (top), the intermediate one (middle) and the central one (bottom).

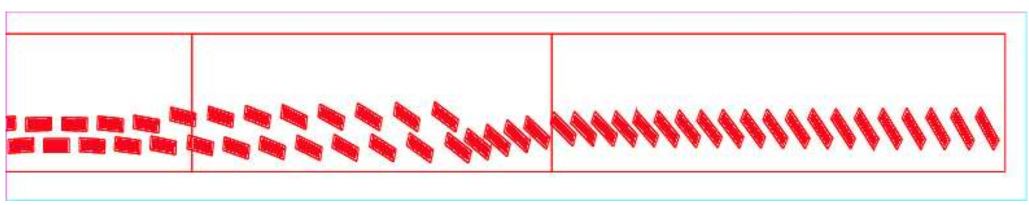

Figure 4.4: Time-Of-Flight (TOF) detector layout in AliROOT: side view (along the z axis) of a semi-sector (2.5 modules). The interaction vertex is at the left end of the drawing.

- central HIJING events in the TOF acceptance (i.e $|\vartheta - 90°| < 45°$), with an average charged particle density $dN_{ch}/dy = 7200$ for $|y| \leq 1$. The total multiplicity of primaries per event is ~ 78000 while the total charged

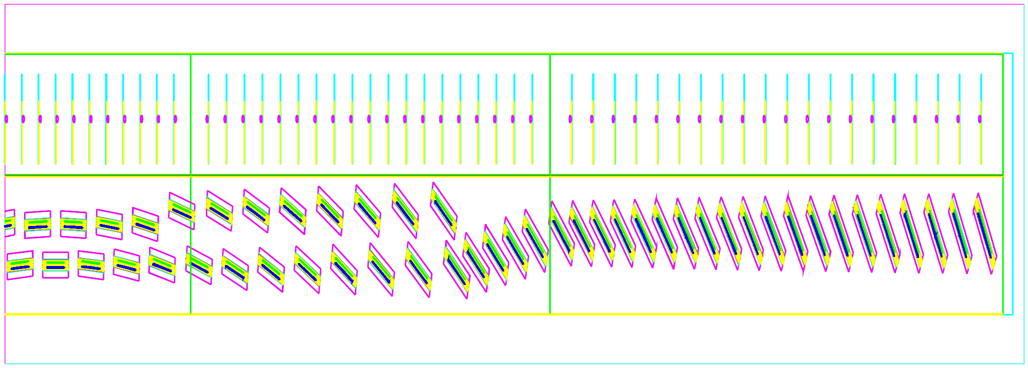

Figure 4.5: Same as in fig. 4.4 with additional details, namely the electronics cards and the cooling tubes in the upper part of the drawing.

multiplicity is ~ 44000;

- SHAKER events in the TOF acceptance, with $dN_{ch}/dy = 8000$. Notice that the very high value of the charged particle density chosen for SHAKER events will be useful to test the TOF detector performace in a critical environment.

It is also worth recalling what the particle ratios are in these event generators, namely: $K/\pi = 0.13$ (0.20) and $p/\pi = 0.08$ (0.07) in HIJING (SHAKER).

4.2 Detector acceptance studies

As already reported in §2.1.4, the ALICE experiment will operate in the presence of a solenoidal magnetic field directed along the beam axis, with a field value in the range [0.2, 0.5] T. The reference value is 0.2 T which is a good compromise among the several needs of the different detectors. The greater the magnetic field, the better would be the identification of high-momentum particles, but on the other hand, both the track finding process carried on by the TPC [53] and the ITS [52], and all the matching procedures are affected and their power lowered. A good solution can be to operate at different magnetic fields, 0.2 T and 0.4 T, so as to satisfy the different components. Hence, the need for a detailed simulation of the TOF performance at 0.4 T was straightforward. The Monte Carlo event samples have therefore been tracked twice: at $B = 0.2$ T and at $B = 0.4$ T.

Figures 4.6 and 4.7 show the distributions of various kinematical and geometrical variables for all charged primary particles generated with HIJING in the $|\vartheta - 90°| < 45°$ region and tracked with a magnetic field value respectively equal to 0.2 and 0.4 T. The corresponding distributions for charged primaries reaching the TOF barrel are superimposed in figs. 4.6 and 4.7.

The occupation of the (p, y) plane by charged primary hadrons reaching the TOF is shown in figs. 4.8 and 4.9 for HIJING events and for both magnetic field values. Different empty regions for *pions*, *kaons* and *protons*, are due to magnetic field and polar angle acceptance. Particle decays are also taken into account. Hence the K/π and p/π ratios at the TOF detector level turn out to be lower than the original ones at the generator level.

The overall TOF acceptances for charged primaries produced in the $|\vartheta - 90°| < 45°$ region and, in particular, for different hadron species, are given in table 4.1 (where both HIJING and SHAKER event generators and both the magnetic field values are considered). The TOF acceptances for π, K and p decrease by the factors 0.78, 0.92 and 0.91, respectively, when the magnetic field is strengthened. This loss mostly concerns low-momentum *pions*.

Table 4.1: TOF acceptance (%) for charged primary particles produced in the $|\vartheta - 90°| < 45°$ region, for 250 HIJING events and, in brackets, for 100 SHAKER events.

B (T)	$\pi^{\pm}$	$K^{\pm}$	$p(\bar{p})$	All
0.2	46 (48)	24 (27)	44 (48)	44.5 (45)
0.4	36	22	40	35

Figure 4.10 shows the time-of-flight distributions of all charged primaries reaching the TOF, at $B = 0.2$ T and $B = 0.4$ T: the magnetic field strengthening corresponds to 200 ps shift of the mean value and 200 ps widening of the spectrum.

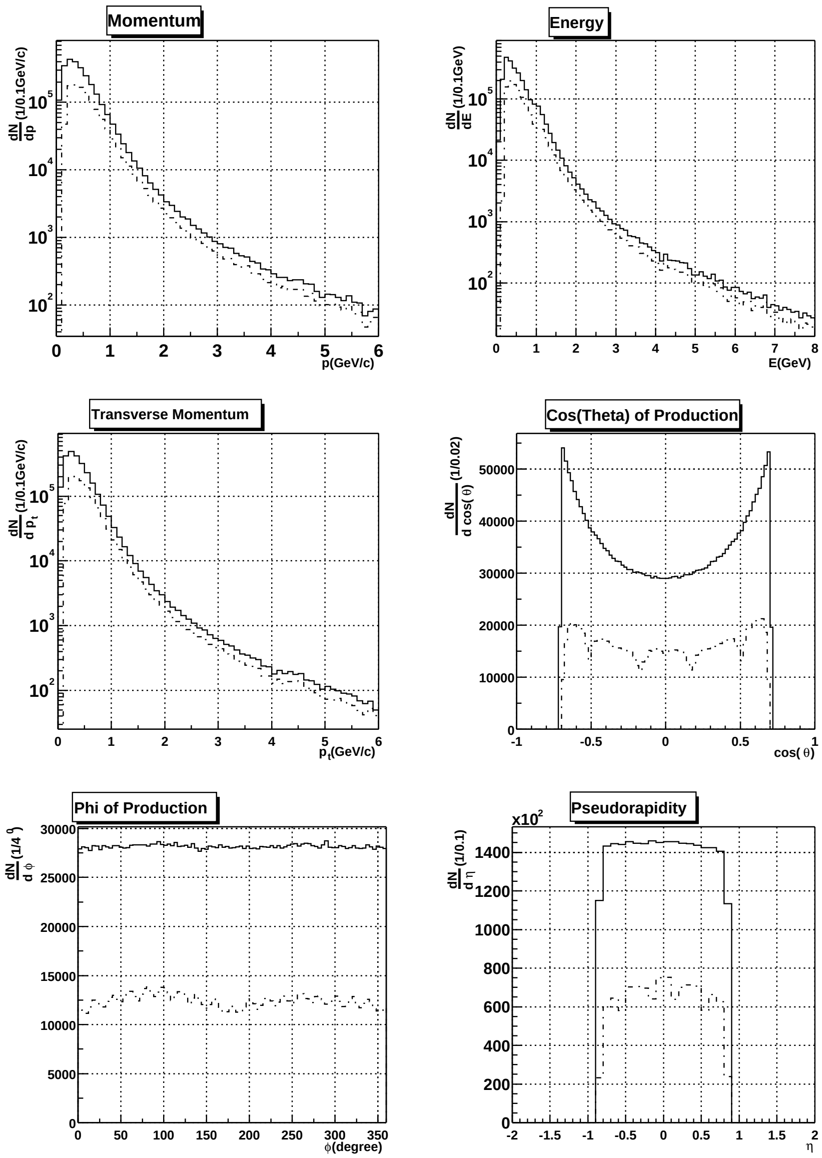

Figure 4.6: Kinematical and geometrical variables of all charged primary particles generated with HIJING (250 events) in the $|\vartheta - 90^{\circ}| < 45^{\circ}$ central region (solid-line histograms). Superimposed the same distributions for all charged primary particles reaching the TOF (dashed-line histograms). The magnetic field value is 0.2 T.

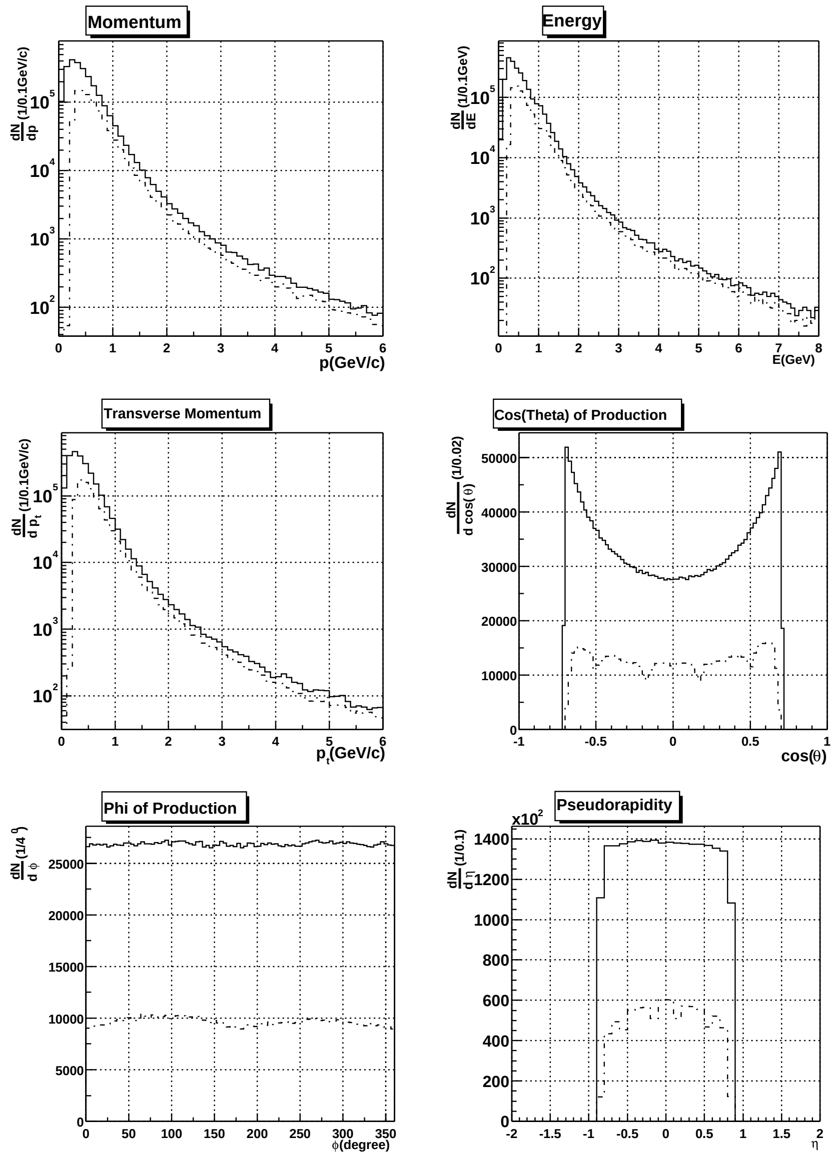

Figure 4.7: Same as fig. 4.6, for $B = 0.4$ T (250 HIJING events).

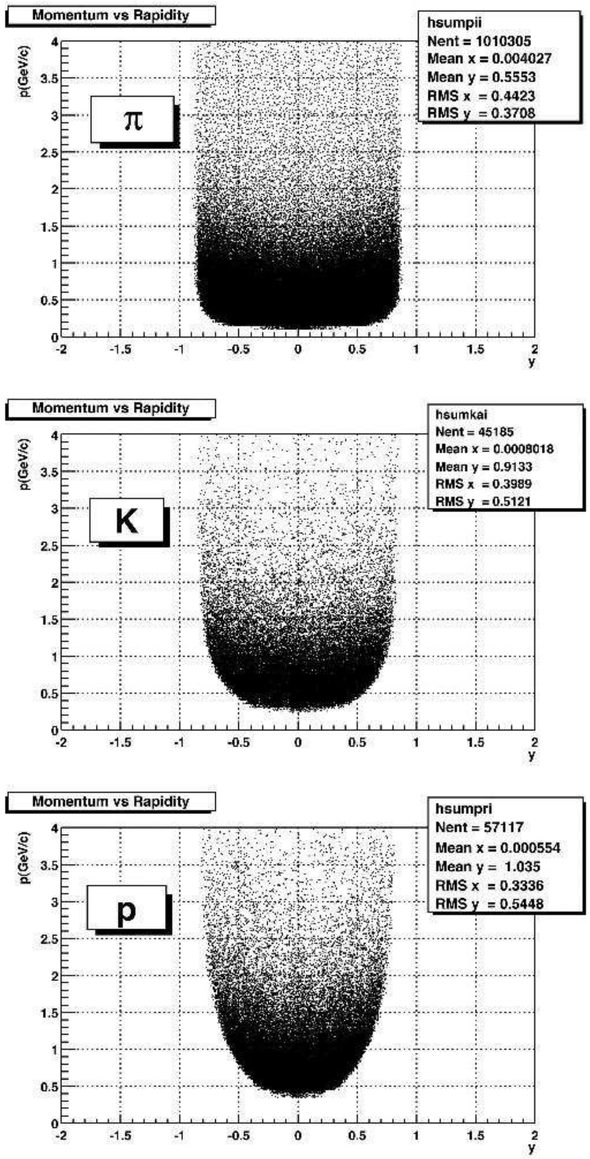

Figure 4.8: TOF acceptance regions for charged primary hadrons produced with $|\vartheta - 90°| < 45°$ tracked with a magnetic field value $B = 0.2$ T: from top to bottom, for *pions*, *kaons* and *protons* (250 HIJING events).

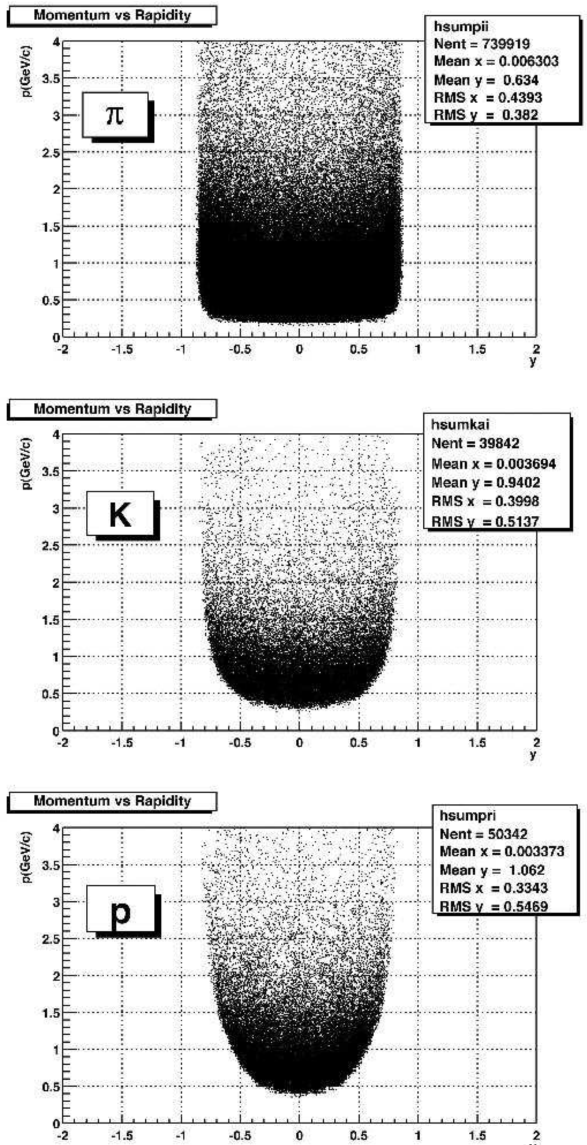

Figure 4.9: Same as fig. 4.8, for $B = 0.4$ T (250 HIJING events).

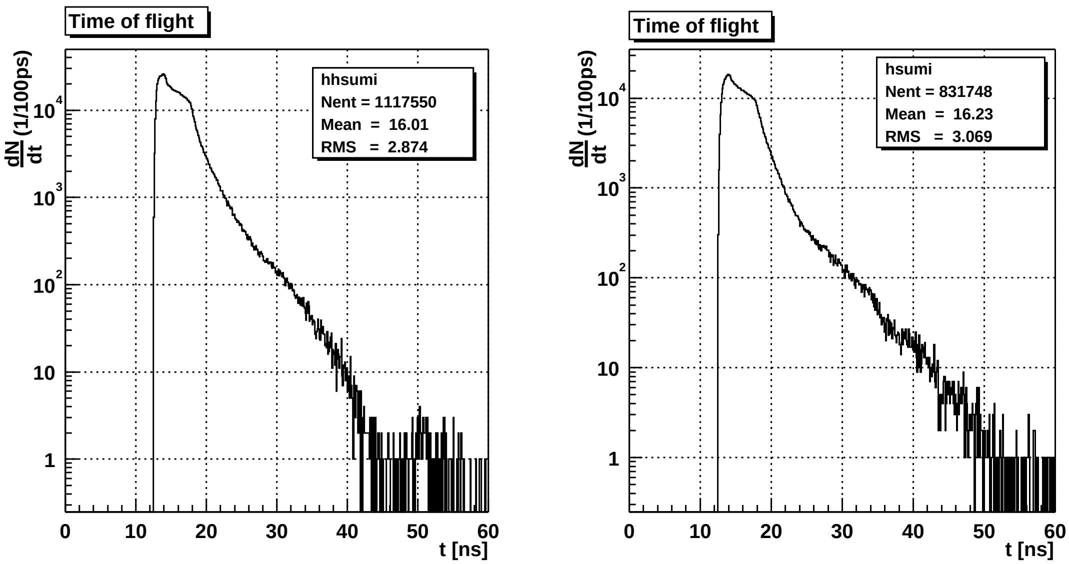

Figure 4.10: Time-of-flight distributions for primary particles from the $|\theta - 90°| < 45°$ region reaching the TOF with $B = 0.2$ T (left) and $B = 0.4$ T (right) magnetic field, as obtained with 250 HIJING events.

4.2.1 Occupancy

In a single complete central HIJING event there are on the average $\sim$ 19000 fired[3] pads: then, we have a TOF occupancy of $19000/158000 \simeq 12\,\%$ (including 'border effects', as described later on). At the highest charged particle density (SHAKER, $dN_{ch}/dy = 8000$) and with a magnetic field value equal to 0.2 T, the occupancy grows up to $\sim 16\,\%$.

Only 25% of the fired pads are hit by reconstructed tracks in the TPC (as explained in the next paragraph), in their first crossing of the TOF-sensitive surface. A further 40% are hit by tracks not reconstructed in the TPC (in one or more crossings) as well as by reconstructed tracks in the TPC in their second, third, etc. crossings. We define the latter percentage of hits as noise from the $|\vartheta - 90°| < 45°$ central region (71% are $e^{\pm}$, see §5.4.3 in [57]). The rest of the fired pads, 35%, are hit by particles originating from the $|\vartheta - 90°| \geq 45°$ outer region. The number of TOF hits due to this outer region has been estimated as follows. A sample of

[3]Taking into account the TOF MRPC efficiency.

primary particles has been generated in each of the forward and backward regions, using the HIJING generator and tracked with $B = 0.2$ T. Additional TOF pads hit by the charged products (from decays, interactions, backscattering, etc.) of these primaries have been found, summing up to a total of $\sim$ 9000 per event at $B = 0.2$ T, and also taken into account.

For each event, the background hits are spread on the TOF surface according to parametrised distributions [55, 56], namely a uniform φ-distribution, in the transverse plane, and a polynomial z-distribution (reproducing the small forward/backward asymmetry), along the beam direction. The corresponding time spectrum has an exponential behaviour [55, 56], with a characteristic time of $20\,ns$. Small differences in the background simulation, when going from 0.2 to 0.4 T, have been duly taken into account.

Additional hits from electronics noise have not been included. However this contribution is expected to bery small.

Border effects

Due to the readout structure of the MRPC strip[4], when a particle goes through the strip close to a pad border, ionizing the gas inside the gaps and inducing a certain amount of charge on the pad, a smaller amount of charge may sometimes be induced on the neighbouring pad(s). These signals, of course, will contribute to noise and occupancy.

Border effects between adjacent pads have been simulated [56] starting from the test beam results of the TOF detector prototypes (see §3.4.1) as far as the pad efficiency (ε) and intrinsic time resolution (σ_{intr}) are concerned.

The border between two pads is defined as a $\pm 5\,mm$ wide region (centred on the border between two pads) where the efficiency of one pad decreases (from 99 % to *zero*) according to the fit curve of test beam results (see fig. 3.4.1), while the efficiency of the nearby pad correspondingly increases (from *zero* up to 99 %). This effect concerns three sides of each pad. Along the fourth side (which has no neighbouring pad) there is only a $5\,mm$ wide region where the efficiency slightly decreases (dropping to $\sim$ 60 % at the pad edge).

By appropriately combining the experimental efficiency curves obtained in our beam tests of MRPC prototypes, relative to transverse (across the strip, see for instance fig. 3.18) and longitudinal (along the strip) scans of the MRPC pads,

[4] As already pointed out in §3.4.1, with the double-stack MRPC the border effects between neighbouring pads have been reduced by a factor of 2.

with particular care about the pad corners (for which up to four neighbouring pads may pick-up charge, althrough with a very small probability, see later on eqs. 4.1-4.3), we can obtain two-dimensional parametrized efficiency functions as shown in fig. 4.12.

To understand the plots in fig. 4.12 (and those in fig. 4.13), we can refer to fig. 4.11, where the pad structure is shown for a single strip. *Pad* 1 in fig. 4.11 is the one actually crossed by a track. The other pads (labelled as *Pad* 2, *Pad* 3, *Pad* 4, *Pad* 5 and *Pad* 6) are adjacent to *Pad* 1 and may be affected by border effects. The efficiency as a function of the track crossing point coordinates in *Pad* 1 reference frame is shown in the plot labelled as *Pad* 1. By calling:

- $\varepsilon(1)$, the two-dimensional (X *vs.* Z) efficiency of *Pad* 1;
- $\varepsilon_X(1)$, the efficiency curve of *Pad* 1 (longitudinal scan along X) when this pad is actually hit;
- $\varepsilon_Z(1)$, the efficiency curve of *Pad* 1 (transverse scan along Z) when this pad is actually hit;

we defined:

$$\varepsilon(1) = \max(\varepsilon_X(1), \varepsilon_Z(1)).$$

The plot with the label *Pad* 2 in fig. 4.12 shows the efficiency as a function of the crossing point coordinates in *Pad* 1 reference frame; the same holds true for all the other pads. By calling:

- $\varepsilon(2)$, the two-dimensional efficiency of *Pad* 2;
- $\varepsilon_Z(2)$, the efficiency curve of *Pad* 2 when *Pad* 1 is hit (transverse scan along Z);
- $\varepsilon(3)$, the two-dimensional efficiency of *Pad* 3;
- $\varepsilon_X(3)$, the efficiency curve of *Pad* 3 when *Pad* 1 is hit (longitudinal scan along X);
- $\varepsilon(5)$, the two-dimensional efficiency of *Pad* 5;
- $\varepsilon_X(5)$, the efficiency curve of *Pad* 5 when *Pad* 1 is hit (longitudinal scan along X);

we defined:

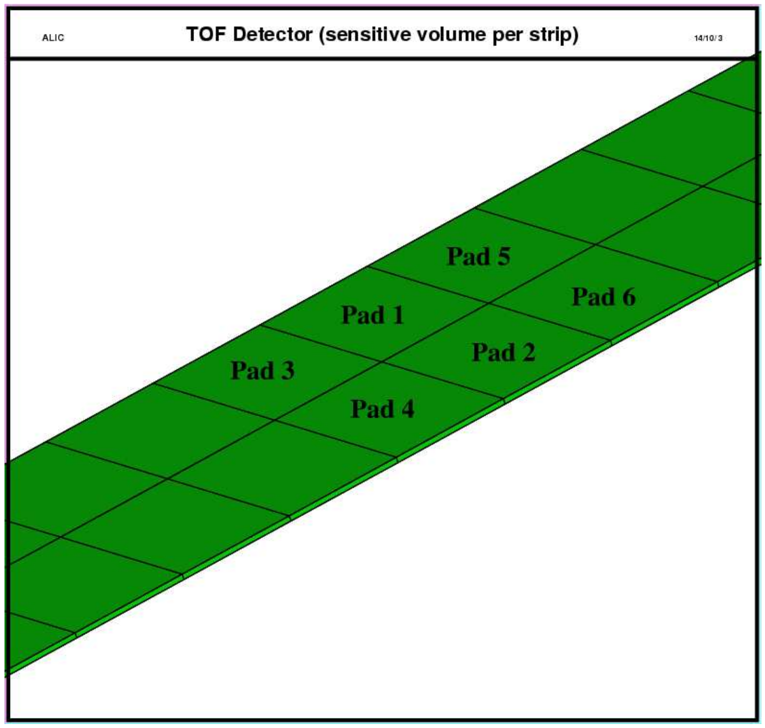

Figure 4.11: The pad structure in a single strip.

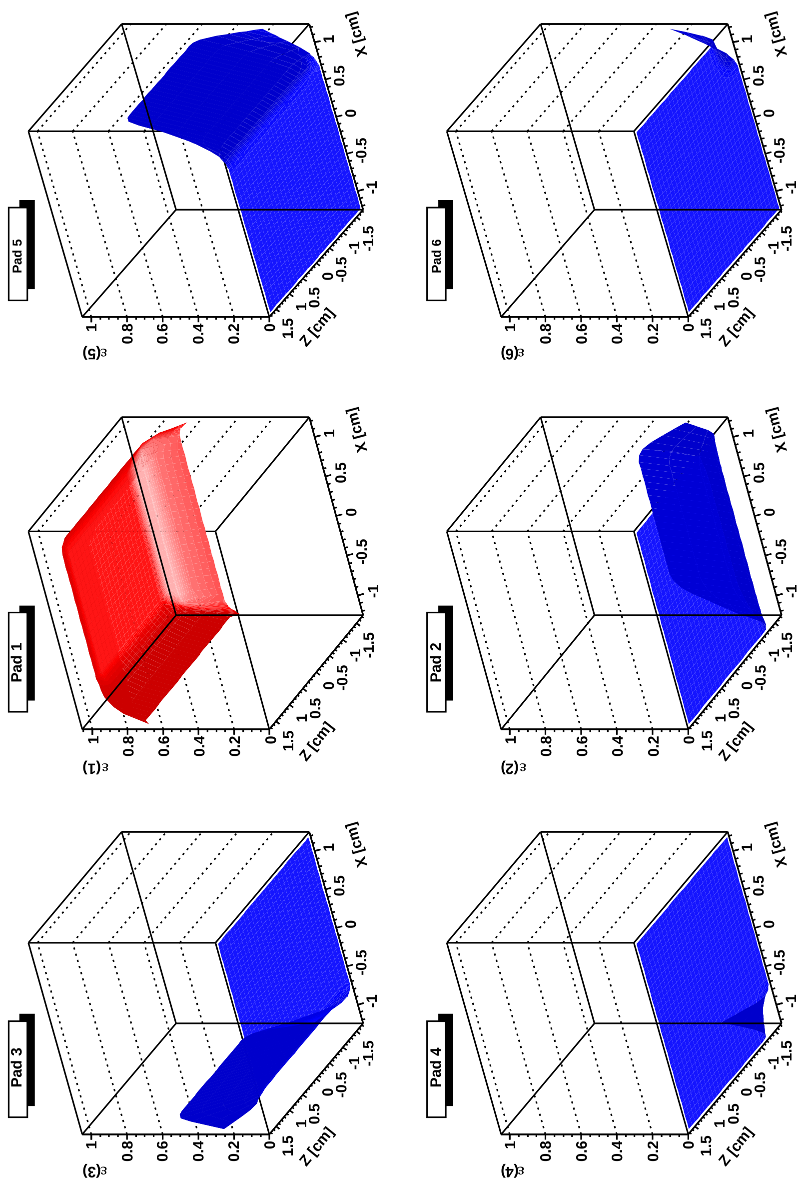

Figure 4.12: Efficiency values for six neighbouring pads of a MRPC strip. The pad labelled as *Pad* 1 is the one actually fired by a through going particle; the other adjacent the pads may be activated by border effects. The *X* and *Z* coordinates always refer to *Pad* 1.

$$\varepsilon(2) = \varepsilon_Z(2) \times \Big((1-\varepsilon_X(3))_{X<0} + (1-\varepsilon_X(5))_{X>0}\Big),$$
$$\varepsilon(3) = \varepsilon_X(3) \times (1-\varepsilon_Z(2)),$$
$$\varepsilon(5) = \varepsilon_X(5) \times (1-\varepsilon_Z(2)),$$
$$\varepsilon(4) = \varepsilon(2) \times \varepsilon(3),$$
$$\varepsilon(6) = \varepsilon(2) \times \varepsilon(5).$$

According to our test beam results, the intrinsic double-stack MRPC time resolution (σ_{intr}) increases when going from the centre to the border of a pad from a minimum value of $\sim 50\,ps$ up to a maximum of $\sim 70\,ps$ for a fired pad and up to $\sim 110\,ps$ for the neighbouring ones (see for instance fig. 3.19). With a procedure analogous to the one described above for the pad efficiency, we derived the two-dimensional (*X vs. Z*) parametrized time resolution functions for the pads possibly affected by border effects as shown in fig. 4.13. We defined in this case:

$$\sigma(1) = min(\sigma_X(1), \sigma_Z(1)),$$
$$\sigma(2) = \sigma_Z(2),$$
$$\sigma(3) = \sigma_X(3),$$
$$\sigma(5) = \sigma_X(5),$$
$$\sigma(4) = min(\sigma_X(3), \sigma_Z(2)),$$
$$\sigma(6) = min(\sigma_X(5), \sigma_Z(2)),$$

where σ stands for σ_{intr} .

Finally, again from our test beam data on border effects (see figs. 3.23 and 3.24), the correlation between the charge ratio of signal pairs from adjacent pads (q_i/q_1, $i=2,3,4,5,6$) and their relative delay (t_i-t_1, $i=2,3,4,5,6$) has been parametrized. The behaviour of $ln(q_i/q_1)$ as a function of the hit coordinates in *Pad* 1 reference frame is shown in fig. 4.14. Here again the index 1 refers to the pad actually hit by a particle, the index i to each of its five neighbouring pads (*Pad* 2, 3, 4, 5, 6). A linear decrease of (t_i-t_1) *versus* $ln(q_i/q_1)$ has been found in the above defined border region, with a maximum delay of only $\sim 120\,ps$. This effect has also been included in our simulations.

Therefore, each charged particle impinging on the TOF sensitive surface across a given pad (*Pad* 1) can be associated to a pad cluster of up to four pads. Namely the cluster dimension can be: $n_{cl}=1$ (*Pad* 1), $n_{cl}=2$ (*Pads* $1+2$, $1+3$, $1+4$, $1+5$, $2+3$, $2+4$, $2+5$, $2+6$, $3+4$, $5+6$), $n_{cl}=3$ (*Pads* $1+2+3$, $1+2+4$, $1+2+5$, $1+2+6$, $1+3+4$, $1+5+6$, $2+3+4$, $2+5+6$), and $n_{cl}=4$ (*Pads* $1+2+3+4$, $1+2+5+6$).

We can estimate a global pad efficiency function corresponding to the 'OR' between the six pads shown in fig. 4.12, and the double, triple and quadruple

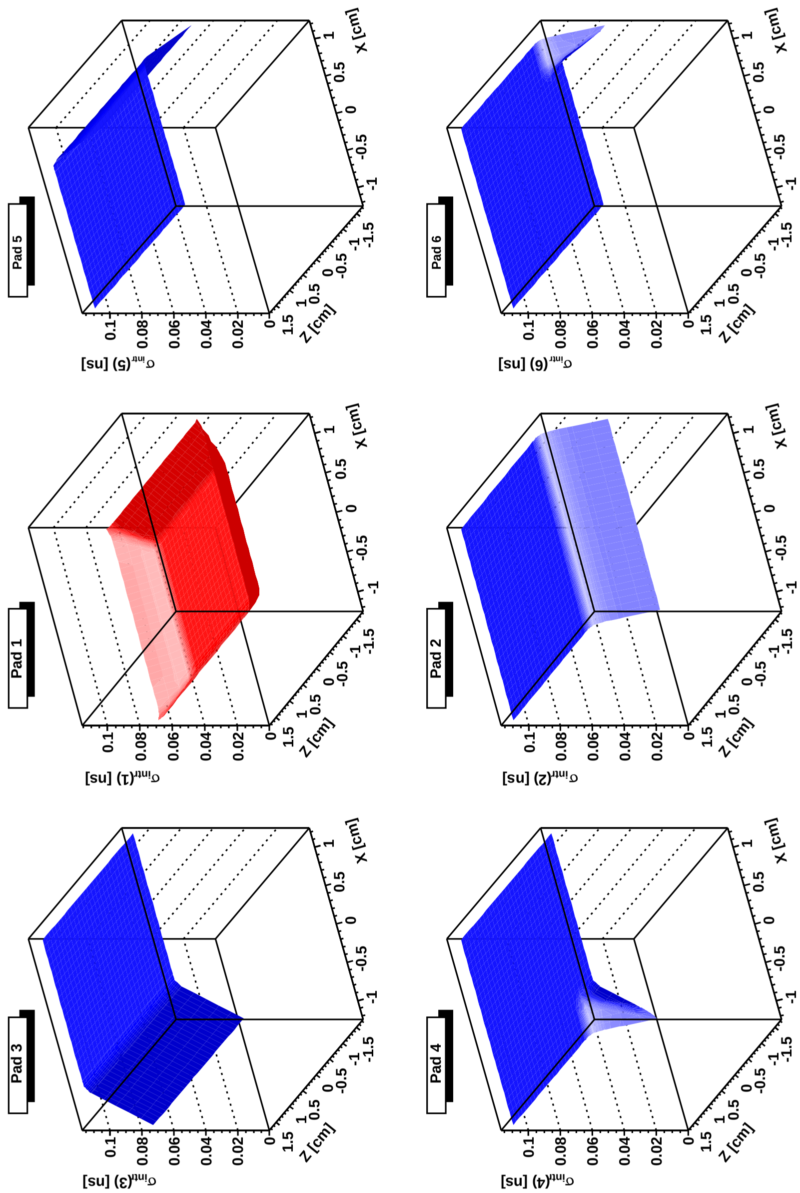

Figure 4.13: Intrinsic time resolution (*ns*) values for six neighbouring pads of a MRPC strip. The pad labelled as *Pad* 1 is the one actually fired by a particle; the other adjacent pads may be activated by border effects. The *X* and *Z* coordinates always refer to *Pad* 1.

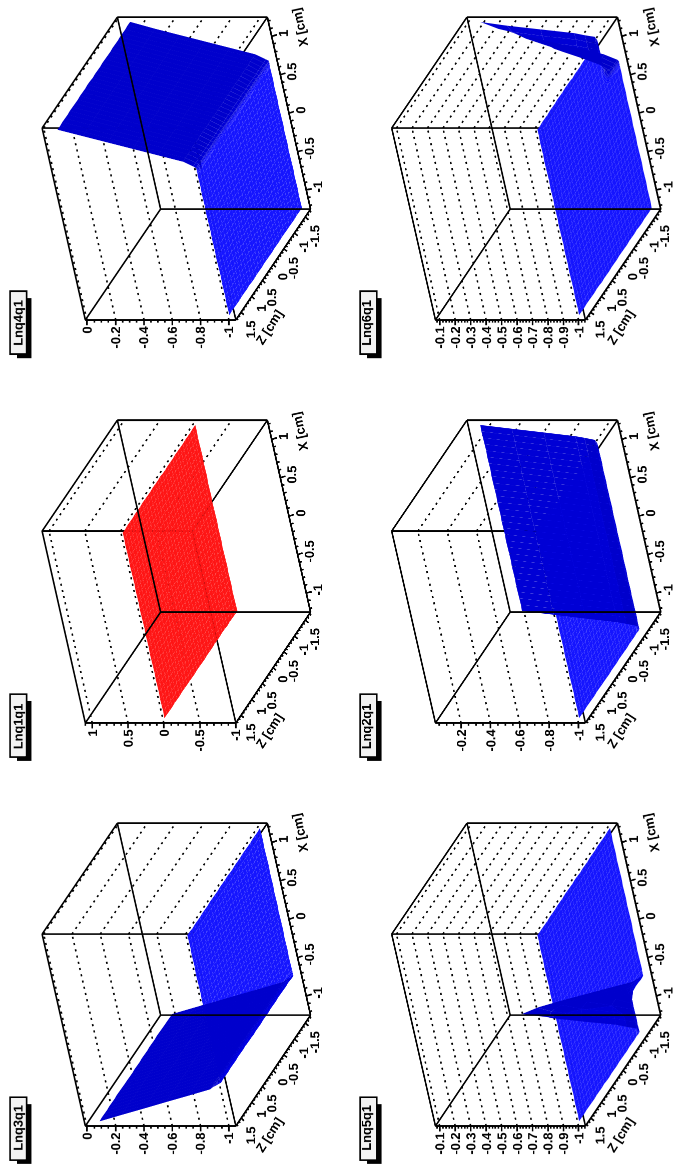

Figure 4.14: Logarithm of the charge ratio between the signals from *Pad* 1 (q_1) and each of the five (*Pad* 2, 3, 4, 5, 6) neighbouring ones (q_i) in case of border effect, as a function of the track hit point coordinates in *Pad* 1 reference frame.

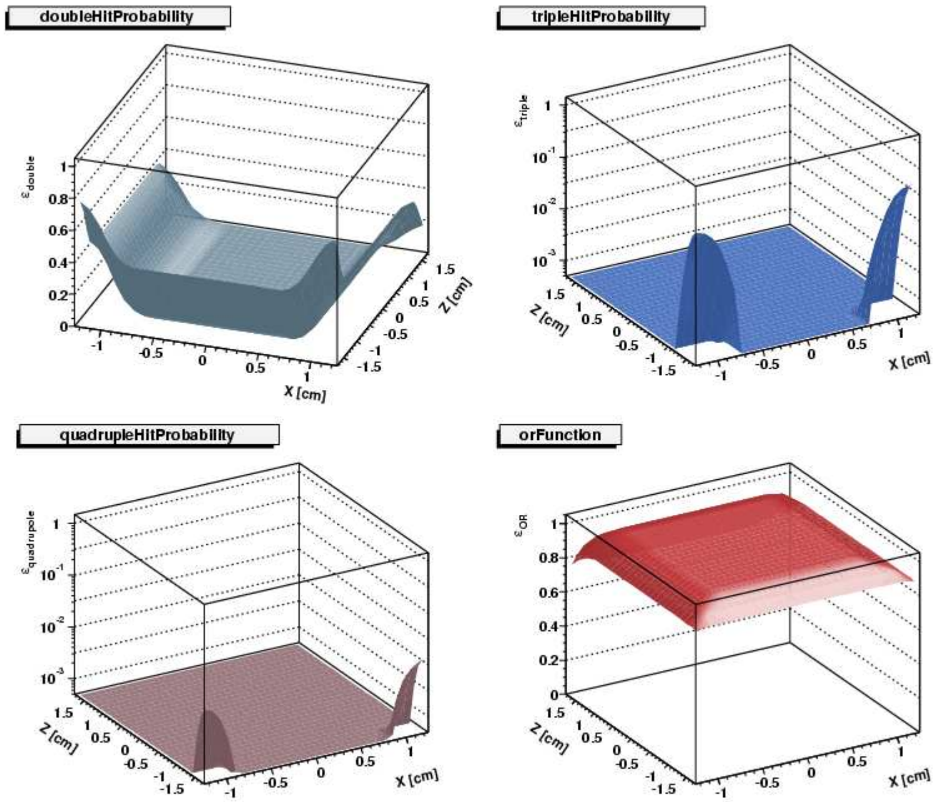

Figure 4.15: Multihit probabilities and 'OR' efficiency (see text) for a MRPC pad. From top to bottom: double hit probability (left) and triple hit probability (right); quadruple hit probability (left) and 'OR' efficiency (right). The triple and quadruple hit probabilities are shown in logarithmic scale.

hit probabilities, as reported in fig. 4.15. The double, triple and quadruple hit probabilities are calculated as:

$$\int_{pad\ area} \frac{\varepsilon_{double}}{\varepsilon_{OR}}\, dX\, dZ \sim 12\%, \tag{4.1}$$

$$\int_{pad\ area} \frac{\varepsilon_{triple}}{\varepsilon_{OR}}\, dX\, dZ \sim 4 \times 10^{-3}, \tag{4.2}$$

$$\int_{pad\ area} \frac{\varepsilon_{quadruple}}{\varepsilon_{OR}}\, dX\, dZ \sim 3 \times 10^{-4}, \tag{4.3}$$

where:

$$\varepsilon_{double} = \sum_{i=1,2,3} \varepsilon(i) \times \sum_{\substack{j=2,3,4 \\ j>i}} \varepsilon(j) + \sum_{i=1,2,5} \varepsilon(i) \times \sum_{\substack{j=2,5,6 \\ j>i}} \varepsilon(j) - \varepsilon(1) \times \varepsilon(2), \tag{4.4}$$

$$\varepsilon_{triple} = \sum_{i=1,2} \varepsilon(i) \times \Big[\sum_{\substack{j=2,3 \\ j>i}} \varepsilon(j) \times \sum_{\substack{k=3,4 \\ k>j}} \varepsilon(k) + \sum_{\substack{j=2,5 \\ j>i}} \varepsilon(j) \times \sum_{\substack{k=5,6 \\ k>j}} \varepsilon(k) \Big], \tag{4.5}$$

$$\varepsilon_{quadruple} = \varepsilon(1) \times \varepsilon(2) \times \Big[\varepsilon(3) \times \varepsilon(4) + \varepsilon(5) \times \varepsilon(6) \Big], \tag{4.6}$$

$$\varepsilon_{OR} = \varepsilon(1) \times \Big(1 + \sum_{i \neq 1} \varepsilon(i) \Big), \tag{4.7}$$

and the efficiency functions $\varepsilon(i)$, for $i = 1,2,3,4,5,6$, are given in fig. 4.12.

The double hit calculation is indeed in agreement with the experimental data, see §3.4.1. The border effect contribution to the overall TOF occupancy ($12-16\%$) is only $\sim 2\%$, i.e. drastically lower than in the past [56] thanks to the new double-stack MRPC strip performance (see §3.4).

Each pad of the cluster produces, with a given efficiency ($\varepsilon(i)$, as given in fig. 4.12), a time signal corresponding to the track time-of-flight. This time is smeared according to the overall TOF time resolution, $\sigma_{TOF}(i)$, and corrected for the time delay due to border effects, if any. Besides the intrinsic double-stack MRPC time resolution, $\sigma_{intr}(i)$, the time measurement is affected by other contributions, σ_{add}, to be quadratically added in order to obtain the overall TOF time resolution. Assuming $\sigma_{add} \sim 100\,ps$ (see table 4.2 in [57]), the overall TOF time resolution is $\sigma_{TOF}(i) = \sqrt{\sigma_{add}^2 + \sigma_{intr}^2(i)}$, where $\sigma_{intr}(i)$ is variable according to the functions shown in fig. 4.13. This overall time resolution is shown in fig. 4.16 for each pad possibly associated to a track. For a pad actually hit by the track (*Pad* 1), $\sigma_{TOF}(1)$ is $\lesssim 120\,ps$ nearly over the whole pad area.

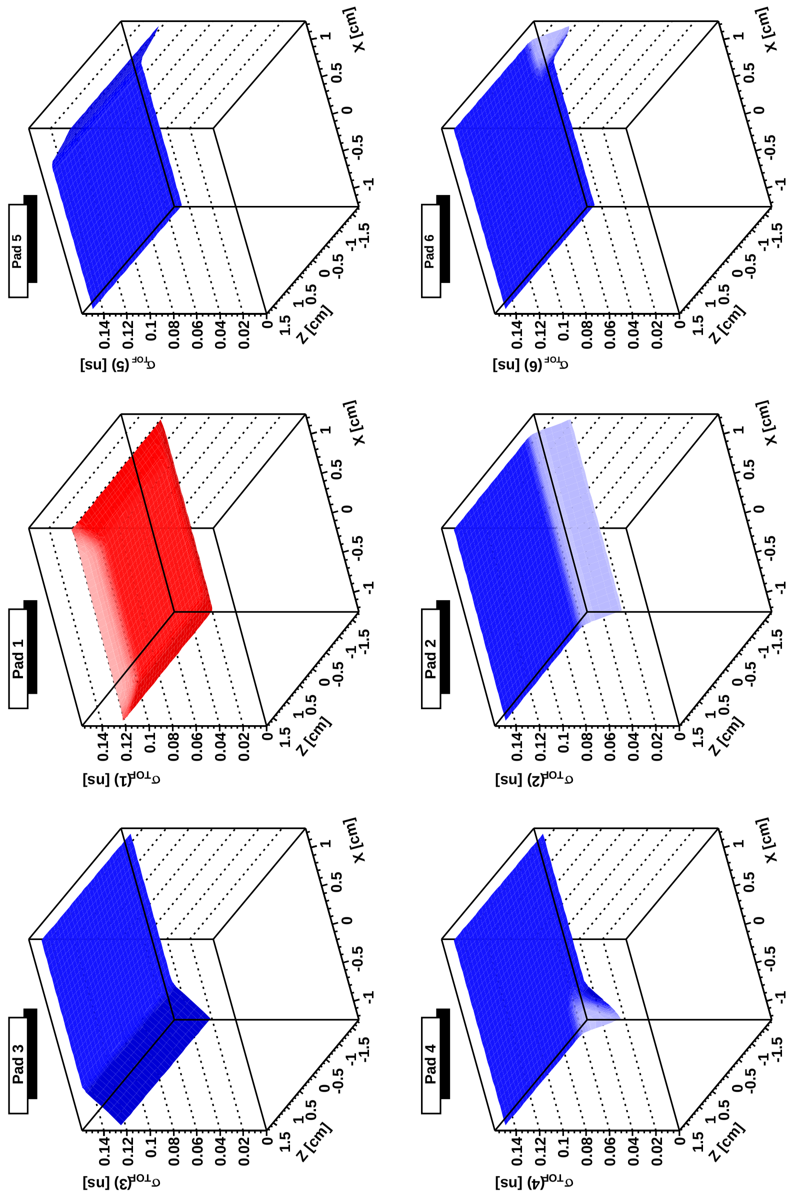

Figure 4.16: Same as in fig. 4.13 for the overall TOF time resolution.

4.3 Matching between the reconstructed tracks and the TOF information

A brief description of the algorithm used to match the tracks reconstructed in the tracking detectors (in particular, the TPC and the TRD) and the appropriate pads of the TOF detector, providing the time-of-flight measurements, is reported in this paragraph.

4.3.1 Track reconstruction

The track finding in the ALICE experiment is based on the Kalman-filtering approach [74]. For details on the Kalman-filtering procedure developed in the ALICE reconstruction algorithm, see chapter 4 in [75]. Here only the main steps used to reconstruct the tracks in the ALICE experiment will be illustrated.

The ALICE TPC is the main tracking detector. The track reconstruction begins in this detector, from the outermost layer, where the occupancy is lower, towards the innermost layer.

Each of the other tracking detectors, i.e. the ITS and the TRD, is then used to extend the track finding procedure starting from the TPC reconstructed tracks. Figures 4.17 and 4.18 show the reconstruction efficiency, i.e. the ratio between the number of tracks reconstructed and the original number of primary particles generated in the $|\vartheta - 90°| < 45°$ region, for the TPC and the TRD, respectively, as a function of the momentum and pseudorapidity. In all these figures, the acceptance for TPC-reconstructed tracks reaching the TOF is also shown superimposed. According to fig. 4.18, this acceptance is defined as the ratio between the number of TPC-reconstructed tracks corresponding to primary particles actually reaching the TOF surface and the number of the primary particles originally generated in the $|\vartheta - 90°| < 45°$ region. It is clear that the TOF acceptance is bigger than the TRD track reconstruction capability. Then, the matching algorithm between the reconstructed tracks and the TOF pads will take into account two samples of reconstructed tracks:

- tracks reconstructed in both the TPC and the TRD,
- tracks reconstructed in the TPC but not in the TRD.

If not explicitely specified, in the following we will refer to the latter also as ‘reconstructed tracks’.

The effect produced on the TOF acceptance and on the TRD reconstruction efficiency by the metallic bars of the ALICE space frame (see figs. 2.4 and 2.5) is evident in figs. 4.17 and 4.18 where the pseudorapidity distributions (right) show periodical ondulations. Since the TRD coverage is not complete in the $\vartheta \simeq 90°$ region, a hole is also visible in fig. 4.18 (right) (see [66] for details).

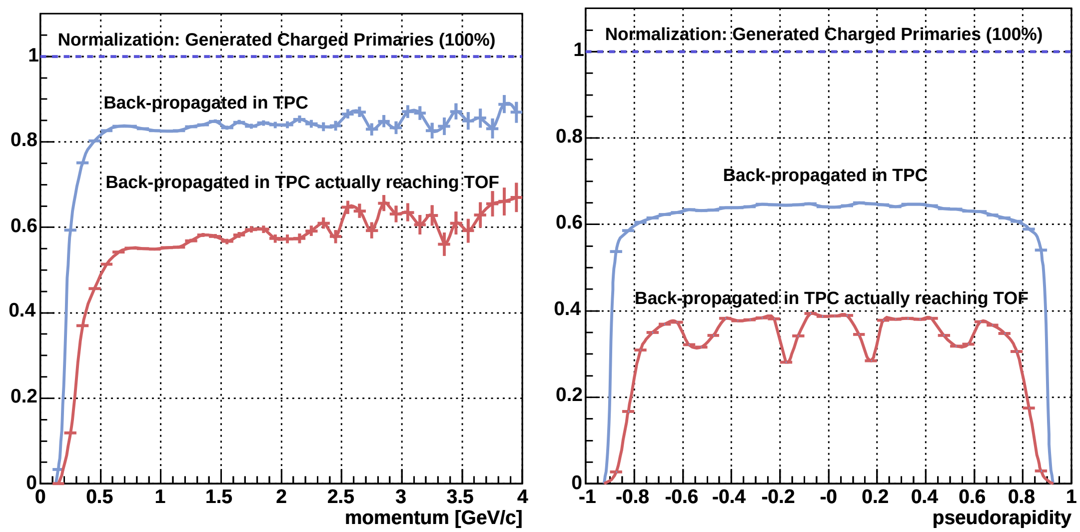

Figure 4.17: The TPC reconstruction efficiency for primaries generated in the $|\vartheta - 90°| < 45°$ region and tracked with $B = 0.4$ T, as a function of momentum (left) and pseudorapidity (right). Superimposed the acceptance for TPC-reconstructed tracks reaching the TOF.

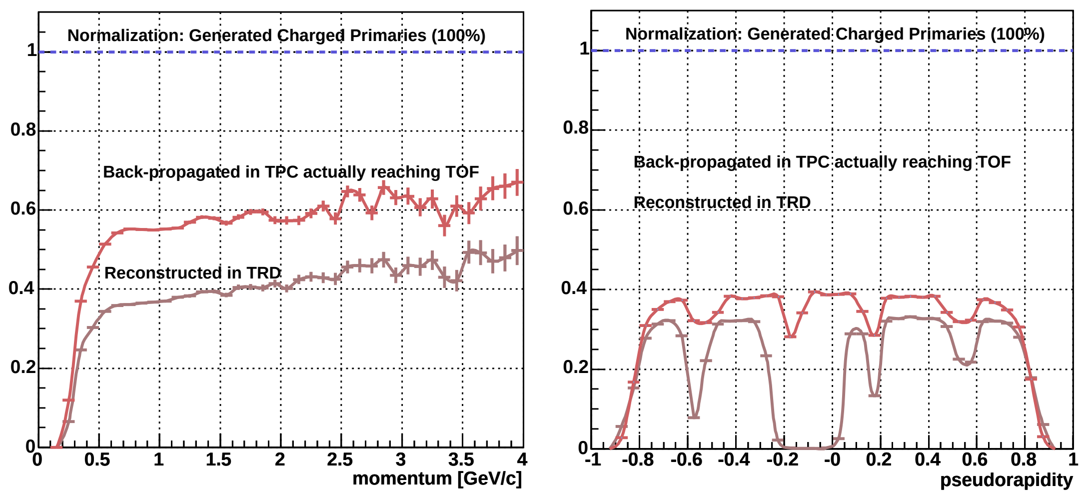

Figure 4.18: The TRD reconstruction efficiency for primaries generated in the $|\vartheta - 90°| < 45°$ region and tracked with $B = 0.4$ T, as a function of momentum (left) and pseudorapidity (right). Superimposed the acceptance for TPC-reconstructed tracks reaching the TOF.

4.3.2 Matching efficiency and contamination

Let us specify the definitions used in the matching analysis [58, 57, 56, 55]. Given N reconstructed tracks matched with the TOF surface, these are subdivided into two sets: 'mismatched' tracks, N_{mis}, and 'well' matched ones, N_{match}, with $N = N_{mis} + N_{match}$.

A 'mismatched' track is a track to which we cannot unambiguously attribute a time-of-flight: when the pad has not fired or when it is associated to more than one track or when a TOF dead region is associated to the track. For the 'well' matched tracks, to which a time-of-flight can be unambiguously attributed, one can distinguish between those matched with 'true' time (i.e. matched with the pad which was actually fired by the tracked particle, hence the pad providing the correct time-of-flight information), N_t, and those matched with 'wrong' time (i.e. matched with the pad fired by another particle), N_w, with $N_{macth} = N_t + N_w$. Notice that the N_w contribution is mostly due to background from the outer regions (see §4.2.1).

The matching procedure can be evaluated in terms of efficiency and contamination, defined as follows:

$$\textit{matching efficiency} = \frac{N_t}{N}, \qquad \textit{matching contamination} = \frac{N_w}{N_{match}}.$$

Matching the information acquired by the TOF with the reconstructed tracks was done using a combined Kalman-filtering [74] and 'probe-track' [58, 57, 55, 56] algorithm. For details on the matching procedure adopted for the ALICE-TOF detector, see §4 in [75]. Here only the main steps will be illustrated.

Each TPC- or TPC-TRD-reconstructed track ('mother' track) is back-propagated to the TOF inner-surface (at $3.70\,m$ radius, in cylindrical coodinates) taking into account all the intermediate materials (in terms of radiation length, volume density, etc.): more than one step could be necessary due to the non-homogeneity of the materials crossed by the track. At each propagation step, the track helix parameters in the magnetic field and the corresponding errors (covariance matrix) are re-evaluated using the information about the energy loss and multiple scattering.

Once the extrapolated hit point of the reconstructed track on the TOF inner-surface is found, a careful search is started for a fired TOF pad (if any) to match with this track.

Around the extrapolated track point on the TOF inner-surface, we define a window in the local TOF plane using the uncertainties in the track parameters[5]. Inside this window, a statistically significant sample of 'daugther tracks', called 'probe tracks', (N_{probe}) is considered[6]; each probe track is prolonged through the TOF volume to find a pad[7].

Every probe track can cross a TOF pad (or a TOF dead region) and be assigned a weighting contribution: $weight_1 = \varepsilon(1)$[8] if the sensitive pad hit has fired, $weight_1 = 1 - \varepsilon(1)$ if the sensitive pad hit has not fired.

[5]A first attempt is performed using a window of area $3\sigma_{y'} \times 3\sigma_{z'}$, where y' and z' are the coordinates in the local reference frame. If no time-of-flight measurement is found, a second check is performed using a window of wider area $9\sigma_{y'} \times 9\sigma_{z'}$.

[6]The number of 'probe tracks' per reconstructed track (N_{probe}) must be adeguate (the larger area window around the extrapolated point on the TOF inner surface, the larger this number should be). We have chosen here $N_{probe} = 20$, for the first attempt, and $N_{probe} = 60$, in the second one, as a good compromise between statistical requirements and CPU time.

[7]It is also worth recalling that the sensitive TOF pads inside the TOF tilted strip, are not parallel to the TOF inner-surface (see figs. 4.2-4.5).

[8]See §4.2.1 for the definition of $\varepsilon(1)$.

As already described in §4.2.1, a particle crossing a TOF pad can sometimes induce a signal on the neighbouring pad(s) and this signal can be slightly delayed (the lower the charge induced, the longer the delay). Therefore, to each fired pad we assign an additional weighting factor, $weight_2 = q^2_{induced}$, where $q_{induced}$ is the (normalized) charge induced on the pad, so that its resulting weight is: $weight = weight_1 \times weight_2$.

For a given reconstructed track, we have then a set of TOF pads and TOF dead regions crossed by the probe tracks. A reconstruced track may be matched with a dead region when none of the pads crossed by the probe tracks has fired and when the number of probe tracks crossing the dead region is larger than the number relative to the non firing pads. Otherwise, the track is matched with a pad. For each TOF pad a total weight is defined as the sum of the weighting contributions from all the probe tracks that cross it. The pad with the largest weight is chosen to be the TOF match for the reconstructed track. Notice that since tracks are curled in the magnetic field and may sometimes spiral this match is chosen as a first-crossing match on the TOF surface, for each track.

The momentum and pseudorapidity dependences of the matching efficiency and contamination are shown in figs. 4.19 and 4.20, for $\pi^{\pm}$, $K^{\pm}$, $p(\bar{p})$ and for all charged primaries. In figs. 4.21 and 4.22 the same distributions are also displayed in two-dimensional plots in terms of pseudorapidity *versus* momentum. In table 4.2 the integrated (in momentum and pseudorapidity) values for the matching acceptances or efficiencies of $\pi^{\pm}$, $K^{\pm}$ and $p(\bar{p})$ are reported. All figures and tables are obtained with 250 HIJING events at $B = 0.4$ T.

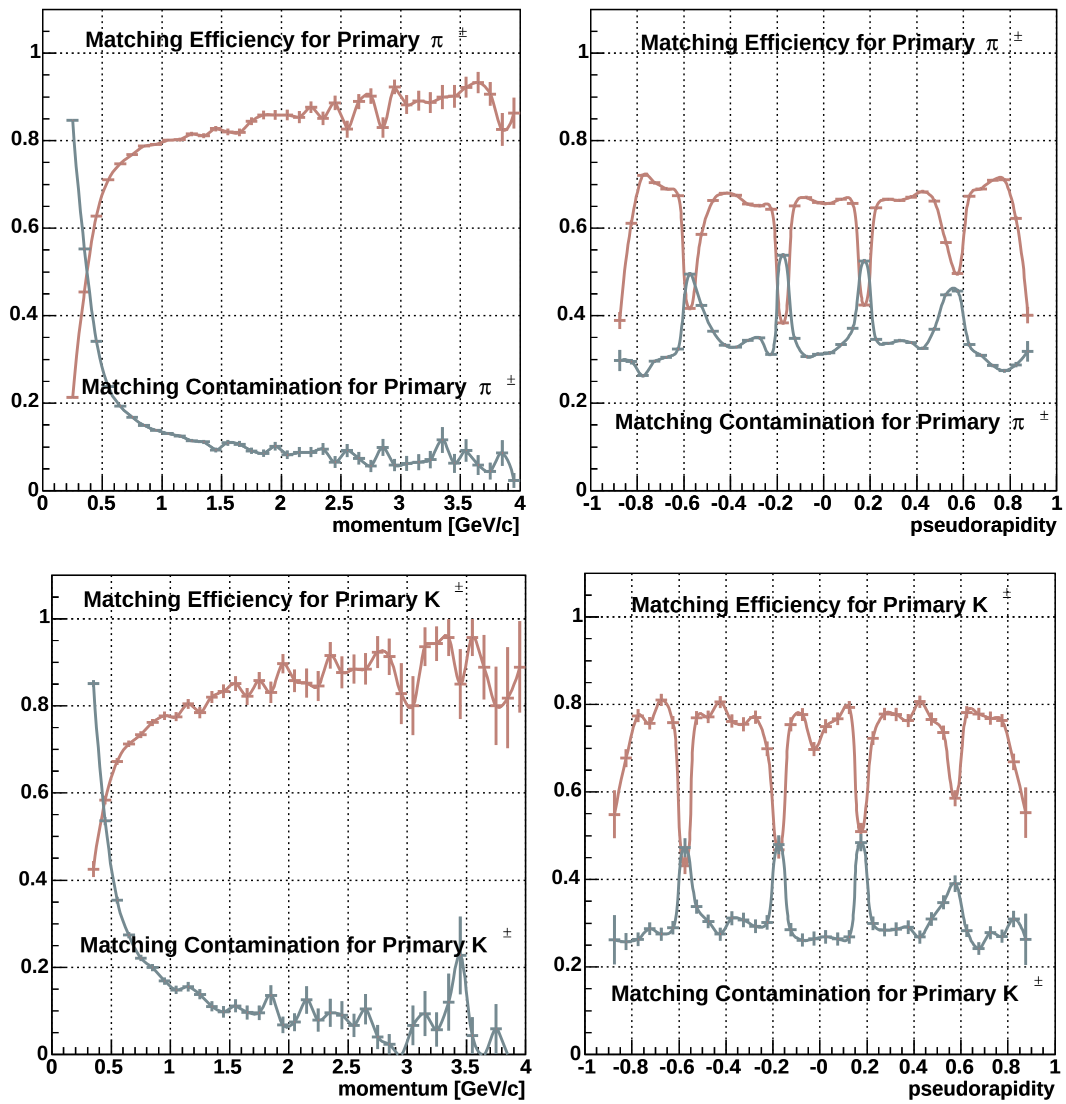

Figure 4.19: The matching efficiencies and contaminations for primary $\pi^{\pm}$ (top) and $K^{\pm}$ (bottom) generated in the $|\vartheta - 90°| < 45°$ region and tracked with $B = 0.4$ T, as functions of momentum (left) and pseudorapidity (right).

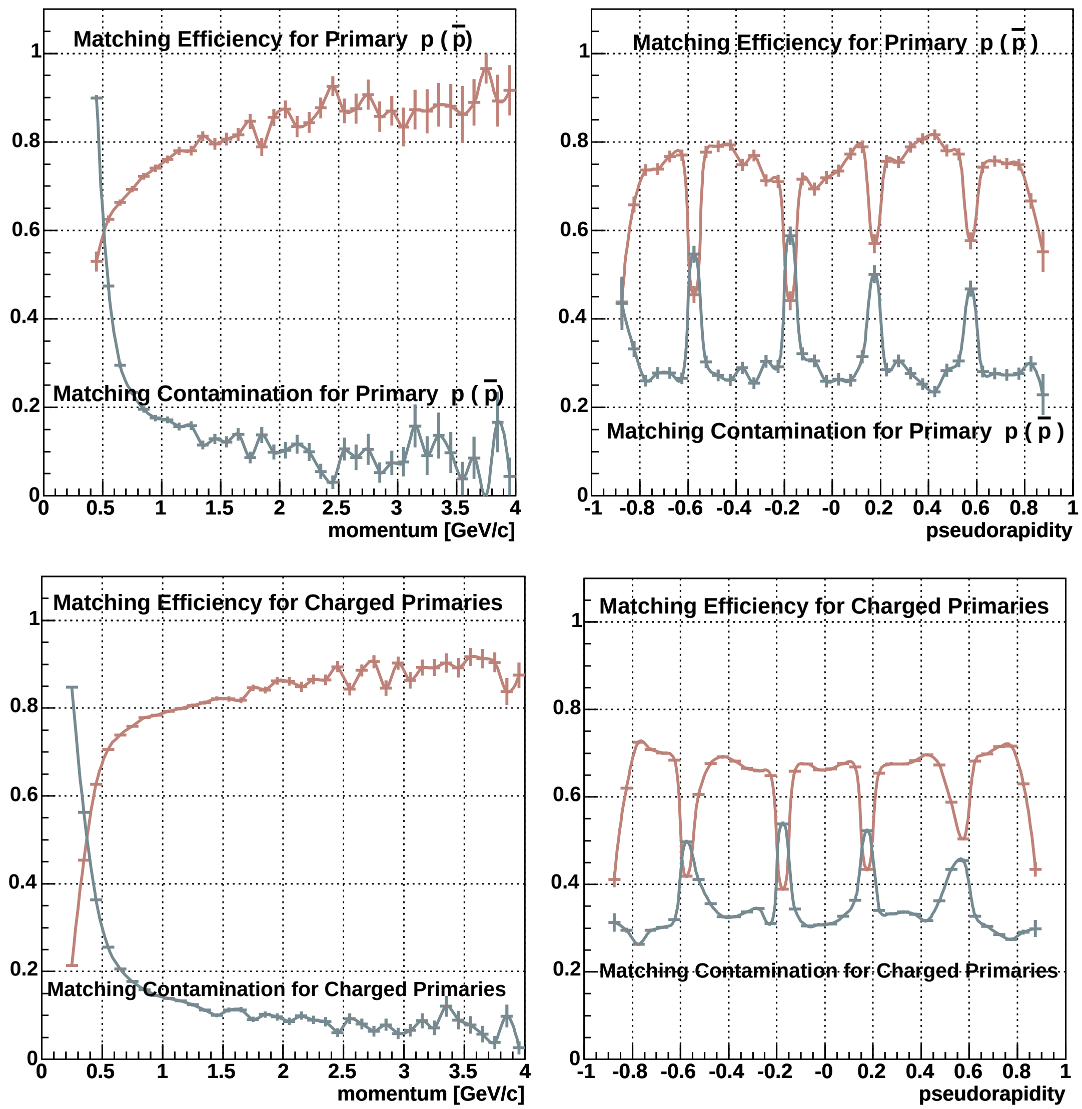

Figure 4.20: Same as fig. 4.19 for primary $p(\bar{p})$ (top) and for all charged primaries (bottom).

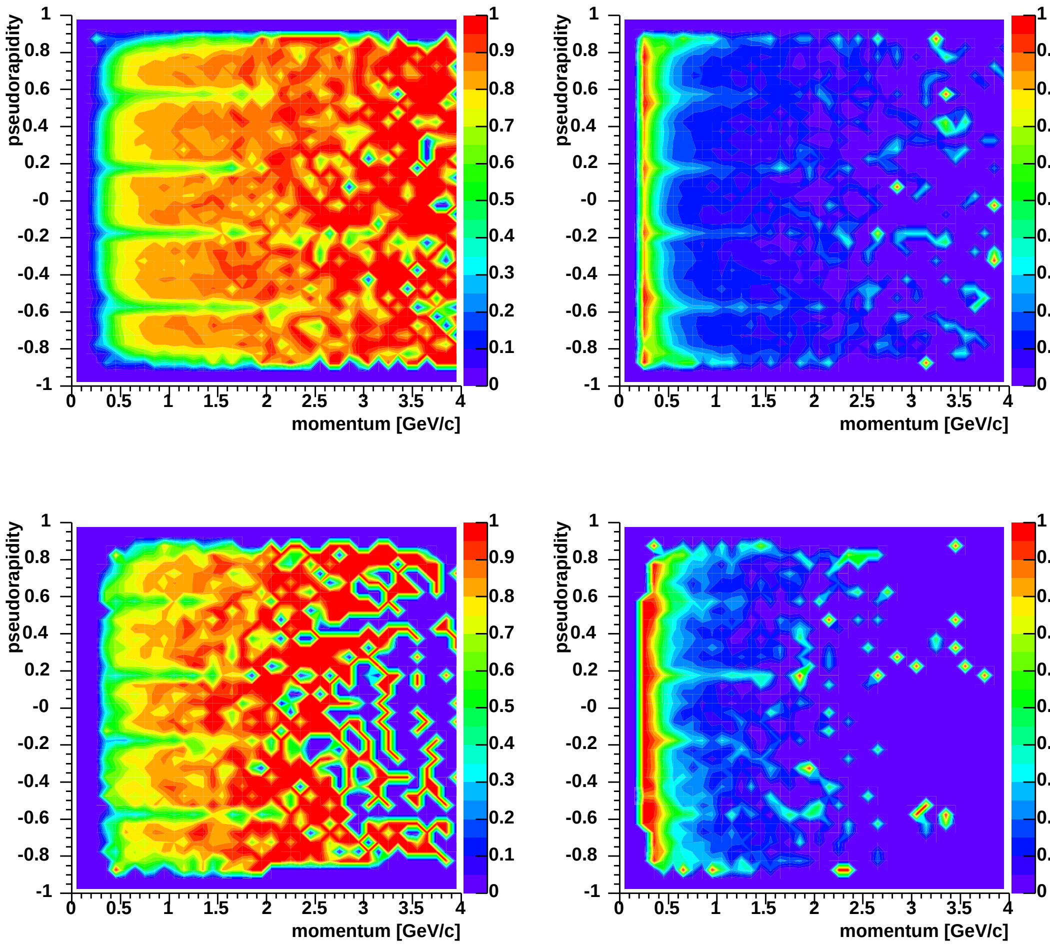

Figure 4.21: The matching efficiencies (left) and contaminations (right) for primary $\pi^{\pm}$ (top) and $K^{\pm}$ (bottom) generated in the $|\vartheta - 90°| < 45°$ region and tracked with $B = 0.4$ T, as functions of momentum and pseudorapidity.

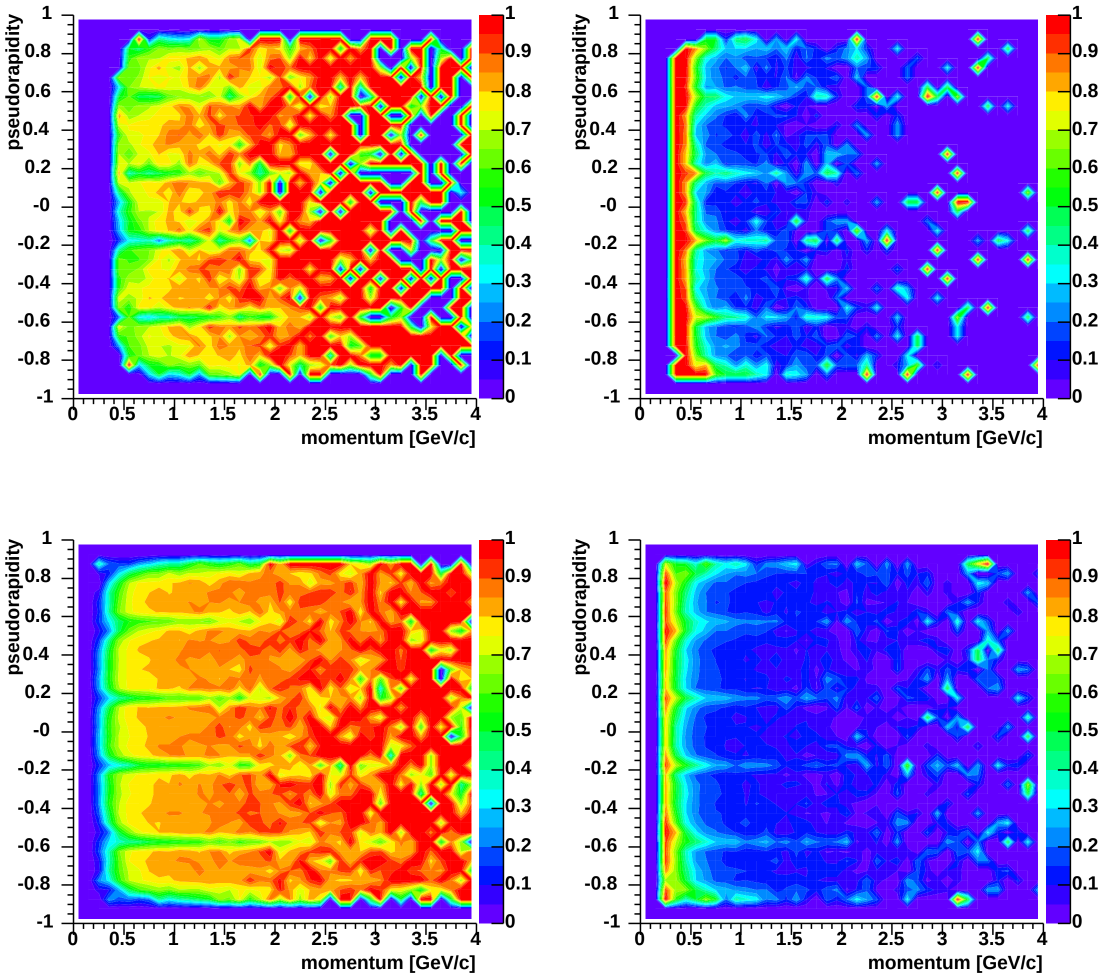

Figure 4.22: Same as fig. 4.21 for primary $p(\bar{p})$ (top) and for all charged primaries (bottom).

Table 4.2: Percentages of primaries matched with true and wrong time for $\pi^{\pm}$, $K^{\pm}$, $p(\bar{p})$ and for all charged hadrons produced in $|\vartheta - 90°| < 45°$ region (250 HIJING central events tracked at $B = 0.4$ T). The percentual acceptances or efficiencies relative to various steps of the TOF matching procedure are also reported.

	$\pi^{\pm}$	$K^{\pm}$	$p(\bar{p})$	All
Primaries (%)	100	100	100	100
Reconstructed in the TPC (%)	64.56±0.04	44.73±0.14	76.28±0.14	63.00±0.04
Reconstructed in the TPC and TRD (%)	22.36±0.03	16.09±0.10	31.07±0.17	22.08±0.03
Reconstructed in the TPC and reaching the TOF sensitive surface (%)	34.02±0.04	22.17±0.12	39.56±0.16	33.02±0.04
Matched with true time (%)	22.17±0.03	15.51±0.10	27.71±0.12	21.68±0.03
Matched with wrong time (%)	11.85±0.03	6.66±0.07	11.85±0.11	11.34±0.02

4.4 Particle identification

Using the tracking and timing information, particle identification (PID) may be performed. Different methods can be adopted for this PID task [58]. A simple ‘contour’ method (where the contour is formed by a number of straight lines in the mass-momentum plane to define the PID selection region) was adopted in this thesis.

4.4.1 Contour cut method

All reconstructed and TOF matched primary particles are entered in a momentum versus mass plot as shown in fig. 4.23 for 250 HIJING events. Negative mass values in this figure correspond to negative square-root arguments in the mass determination equation

$$m = p\sqrt{\frac{t^2}{l^2} - 1},$$

where p and l are the reconstructed particle momentum and track length, and and t is the measured time-of-flight (by the TOF pad associated to the track).

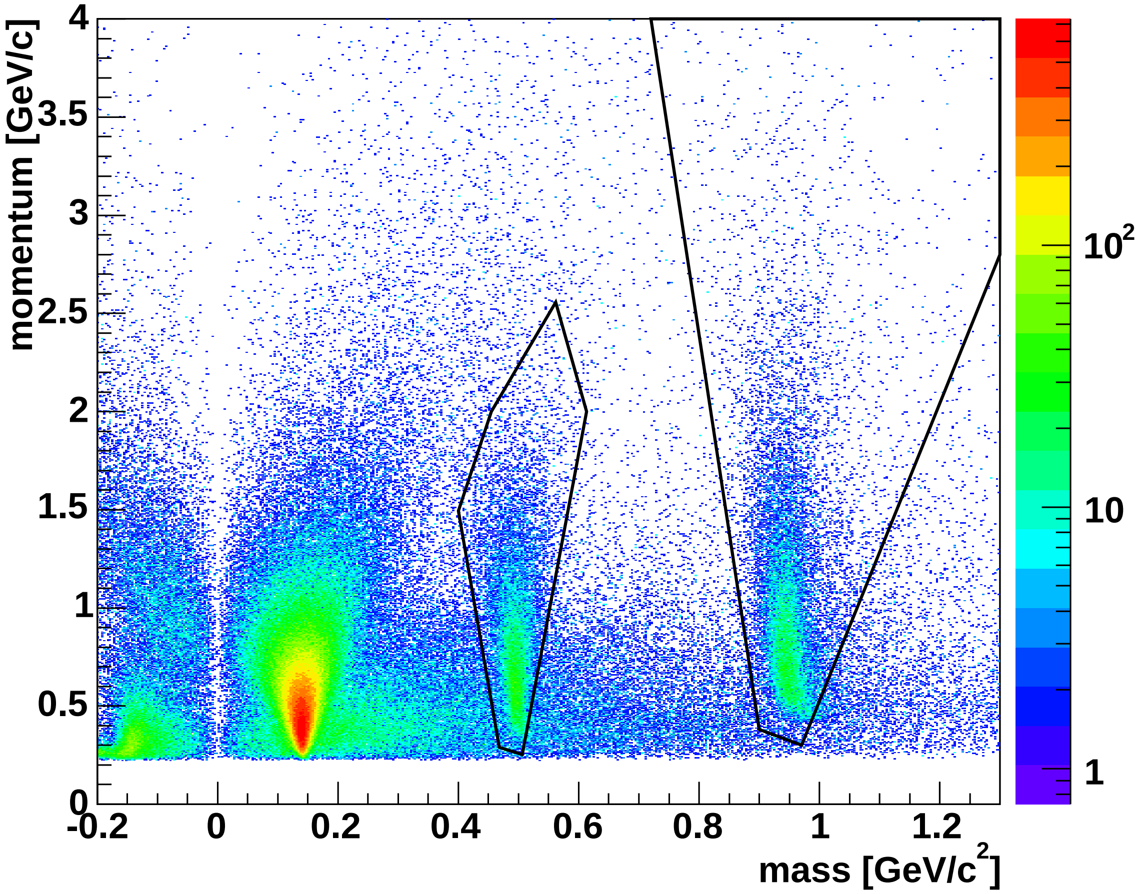

Figure 4.23: Mass separation with the TOF detector as a function of reconstructed momentum for 250 HIJING events with $B = 0.4$ T.

Notice that in this plot we have all the particles for which a time-of-flight measurement is available. One can observe distinct clusters of points corresponding to *pions*, *kaons* and *protons* as well as a horizontal broad band which corresponds to mismatched tracks, with pads giving wrong times (see previous section). This leads to contamination, even in the low momentum region where the mass resolution ($\partial m/m$) is good. At larger momenta, the particle clusters become obviously wider because the mass resolution increases with the particle momentum (see eqs. 2.3-2.5 in §2.1.4) even for practically constant time resolution.

For the identification procedure some specific contour cuts, shown in fig. 4.23, for *kaons* and *protons*, are considered. The shape of the contours is dictated by the concern to extend the range of pure identification to the largest momenta, even at the expense of efficiency.

Besides these graphical cuts, in the PID procedure described herein, different contour cuts were applied to different particle species. The most stringent contour cuts were applied to *kaons* (because of the large *pion* contamination).

For *pions*, *kaons* and *protons* only reconstructed tracks having a time-of-flight measurement were selected. For $Pb-Pb$ collisions we do not consider any contour cut for attempting *electron* identification (below say $0.5\,GeV/c$) since the *pion* contamination is prohibitive in this case.

4.4.2 PID efficiency and contamination

Let us call $N_{id}(i)$, with $i = \pi, K, p$, the number of identified hadrons of different species according to the criteria specified in the previous section. This number is obviously $N_{id}(i) = N^t_{id}(i) + N^w_{id}(i)$, where $N^t_{id}(i)$ is the number of well identified particles of type i and $N^w_{id}(i)$ the number of non-type i particles misidentified as particles of type i. The efficiency and contamination of the PID procedure, for each type of particle, are then:

$$PID\ efficiency = \frac{N^t_{id}(i)}{N(i)}, \qquad PID\ contamination = \frac{N^w_{id}(i)}{N_{id}(i)}$$

where $N(i)$ is the total number of particles of type i present in the (m,p) scatter-plot. The momentum dependence of the results relative to the last step of our PID procedure (i.e. once the TPC-TRD-TOF track matching is achieved) is presented in figs. 4.24, 4.25 and 4.26 respectively for π, K and p. These figures characterize the performance of the method itself. Figures 4.27, 4.28 and 4.29 show the final PID power of the TOF detector for *pions*, *kaons* and *protons*, expressed in terms of "overall PID efficiencies" which include all the acceptance and efficiency factors involved in the analysis. In this case we have:

$$\textit{overall PID efficiency} = \frac{N^t_{id}(i)}{N_{TOT}(i)},$$

where $N_{TOT}(i)$ is the total number of primary hadrons of type i originally generated in the angular region $|\vartheta - 90°| < 45°$. When folding in the inclusive particle momentum spectra, the results, integrated over the whole PID momentum interval, are given in table 4.3. In figs. 4.30, 4.31 and 4.32 the overall PID efficiencies and contaminations are also displayed in two-dimensional plots in terms of pseudorapidity *versus* momentum, for $\pi^{\pm}$, $K^{\pm}$ and $p(\bar{p})$. All figures and tables are obtained with 250 HIJING events at $B = 0.4$ T.

Table 4.3: Overall PID efficiencies (%) and PID contaminations (%) in different momentum (GeV/c) ranges for primary hadrons generated in the $|\vartheta - 90°| < 45°$ region (250 HIJING events, tracked with $B = 0.4$ T).
$^{(*)}$*Identifi ed pions, kaons and protons have respectively:* $p \geq 0.2$, 0.3 *and* $0.4\,GeV/c$.

Primary hadron	Momentum range $[GeV/c]$	Efficiency [%]	Contamination [%]
$\pi^{\pm}$	$^{(*)}p < 2.5$	33.74 ± 0.04	6.26 ± 0.04
$K^{\pm}$	$^{(*)}p < 2.5$	16.93 ± 0.12	14.8 ± 0.3
$p(\bar{p})$	$^{(*)}p < 4.5$	31.3 ± 0.2	5.18 ± 0.12
$\pi^{\pm}$	$0.5 < p < 2$	48.24 ± 0.07	6.26 ± 0.05
$K^{\pm}$	$0.5 < p < 2$	22.78 ± 0.16	12.8 ± 0.2
$p(\bar{p})$	$0.5 < p < 2$	35.54 ± 0.2	5.15 ± 0.12

The results presented herein obviously depend on the event generator parameters (dN_{ch}/dy density, p_T spectra, K/π and p/π particle ratios, etc.) and the simulated experimental conditions (in the presence of different materials, magnetic field values, etc.). Notwithstanding the uncertainties at the present stage, one can confidently see that in each $Pb-Pb$ final state the ALICE TOF detector will be able to identify thousands of *pions*, and hundreds of *kaons* and *protons*, with $\lesssim 15\,\%$ or less contamination in the momentum range exceeding $\sim 2\,GeV/c$ for *kaons*, and extending up to $\sim 4\,GeV/c$ for *protons*.

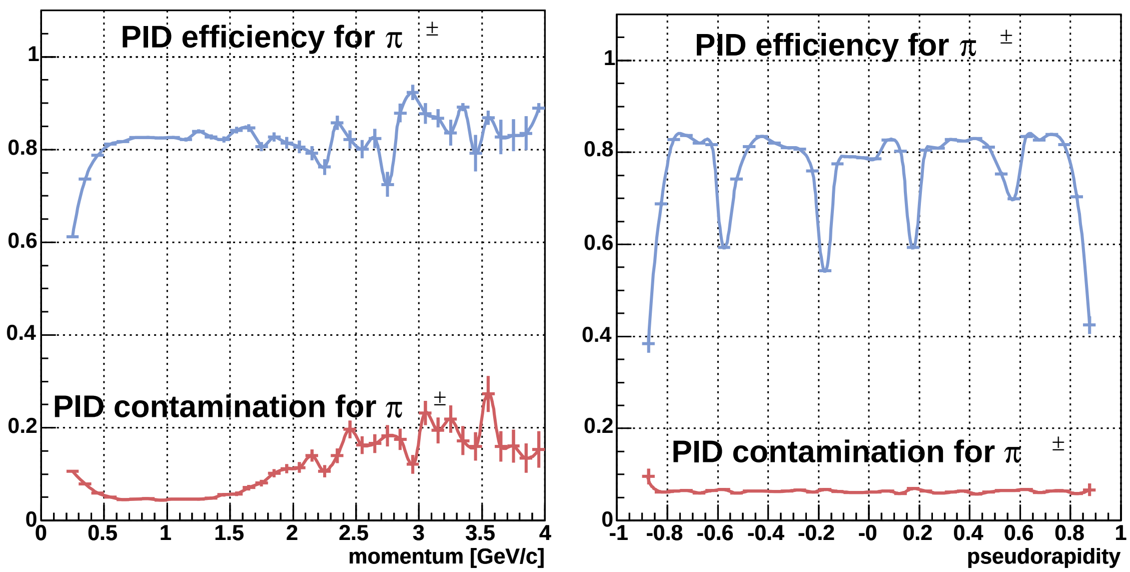

Figure 4.24: The momentum (left) and pseudorapidity (right) dependences of the efficiency and contamination of the PID procedure for primary $\pi^{\pm}$ matched with the TOF (250 HIJING events with $B = 0.4$ T).

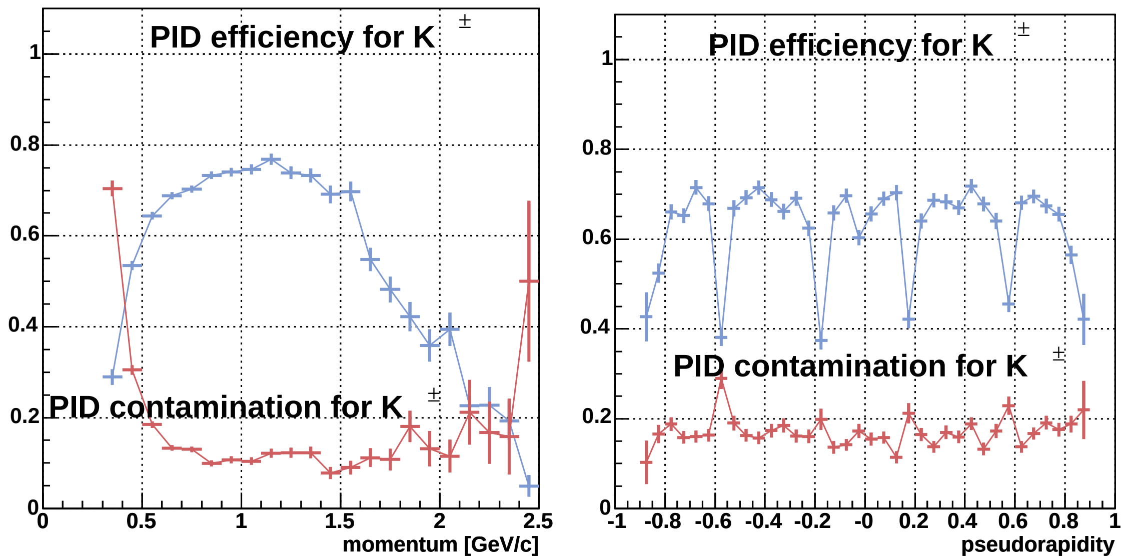

Figure 4.25: Same as fig. 4.24 for primary $K^{\pm}$.

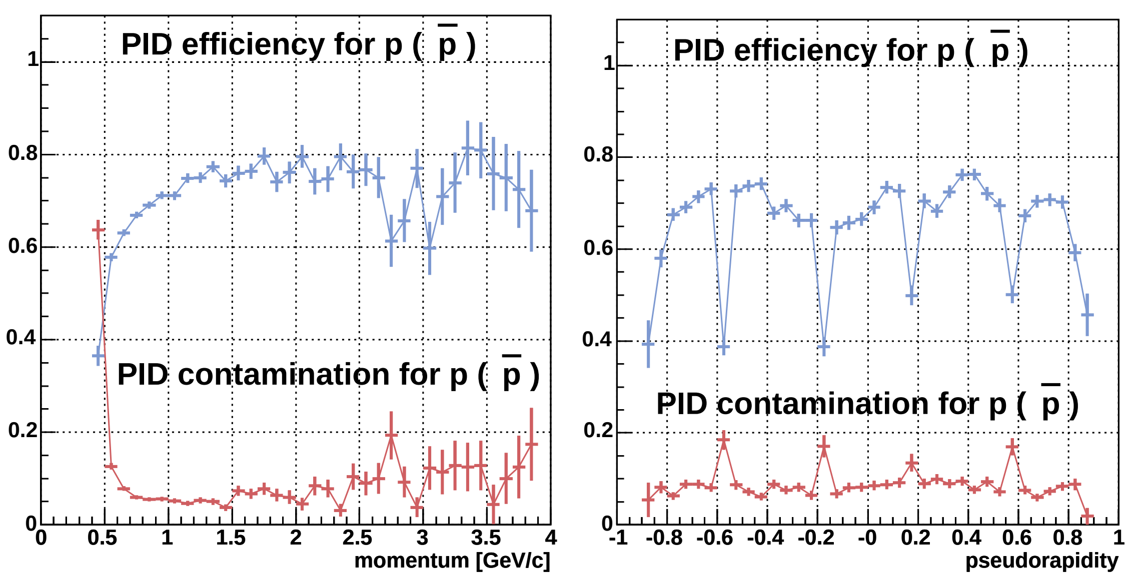

Figure 4.26: Same as fig. 4.24 for primary $p(\bar{p})$.

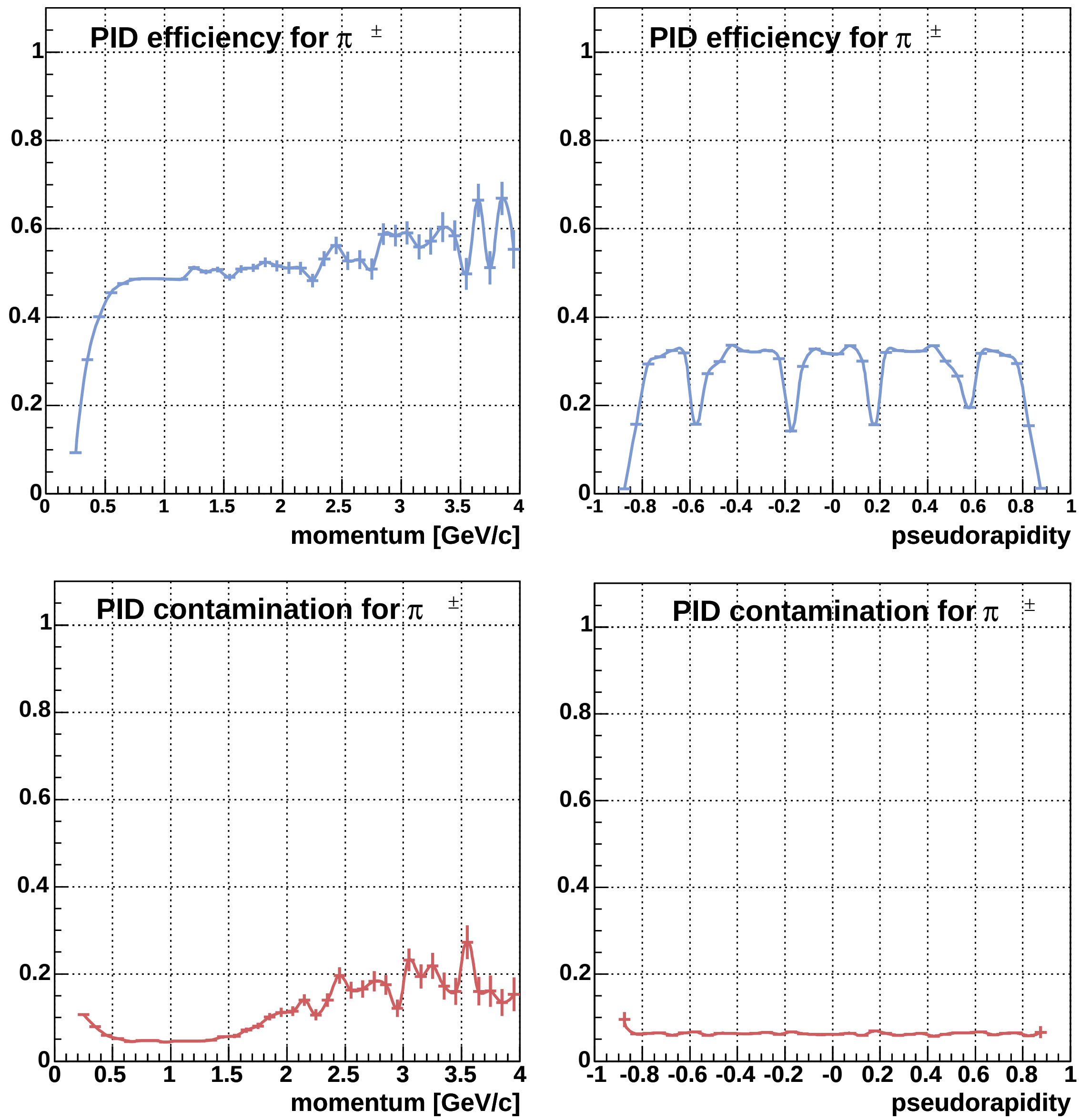

Figure 4.27: The momentum (top left) and pseudorapidity (top right) dependences of the overall efficiency of the PID procedure for primary $\pi^{\pm}$ matched with the TOF (250 HIJING events with $B = 0.4$ T). The PID contamination plots of fig. 4.24 are shown again (bottom).

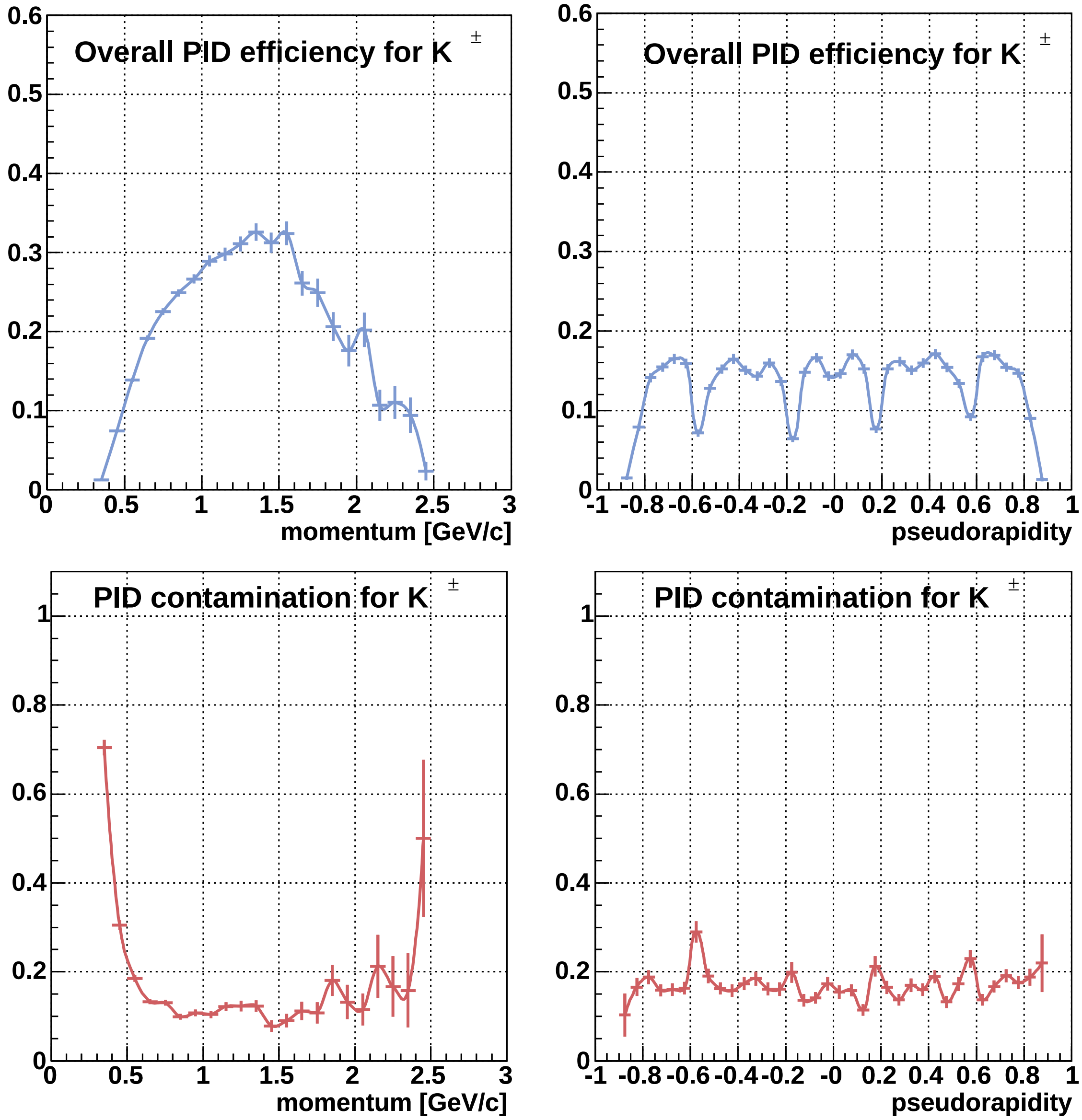

Figure 4.28: The momentum (top left) and pseudorapidity (top right) dependences of the overall efficiency of the PID procedure for primary $K^{\pm}$ matched with the TOF (250 HIJING events with $B = 0.4$ T). The PID contamination plots of fig. 4.25 are shown again (bottom).

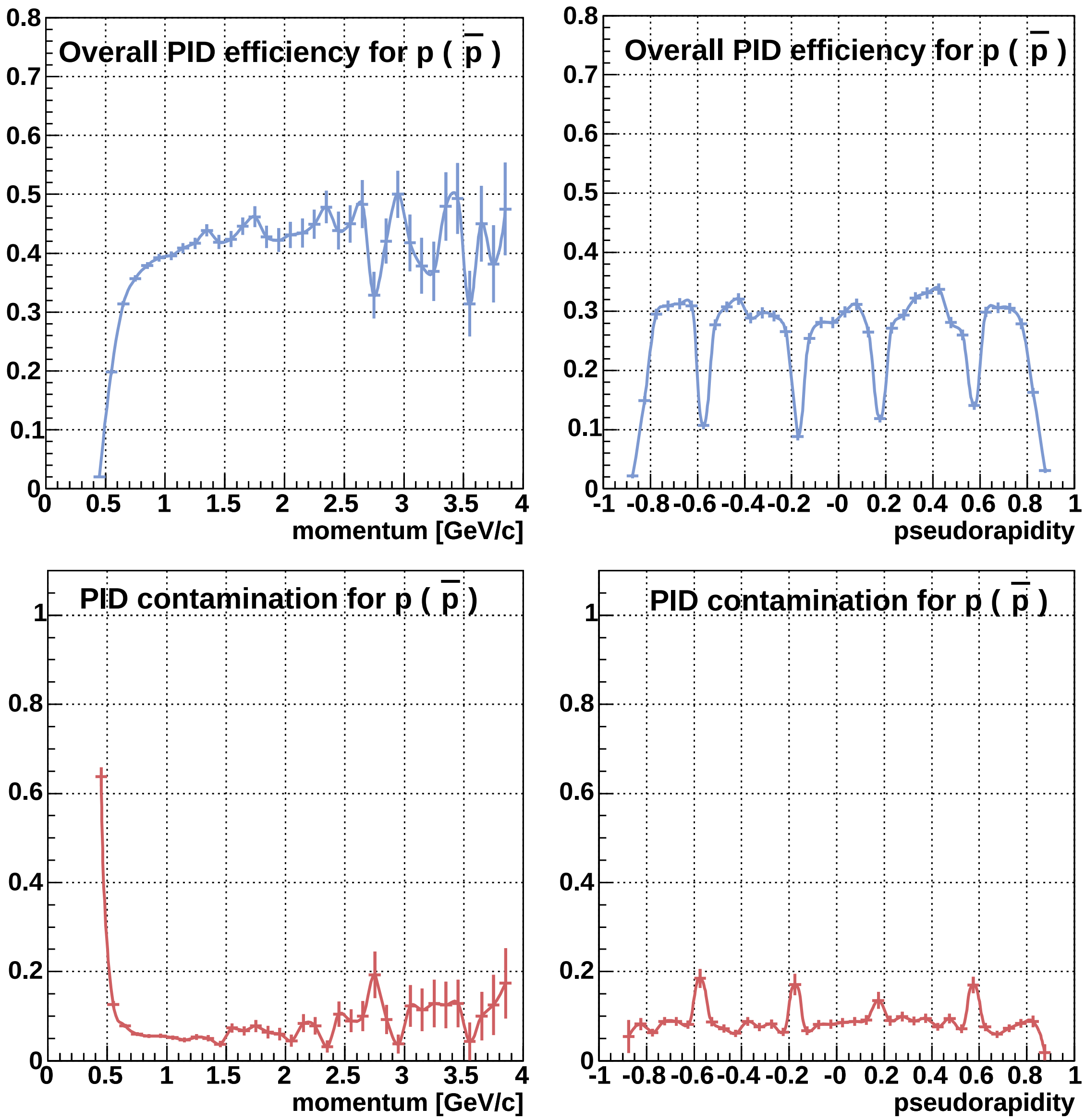

Figure 4.29: The momentum (top left) and pseudorapidity (top right) dependences of the overall efficiency of the PID procedure for primary $p(\bar{p})$ matched with the TOF (250 HIJING events with $B = 0.4$ T). The PID contamination plots of fig. 4.26 are shown again (bottom).

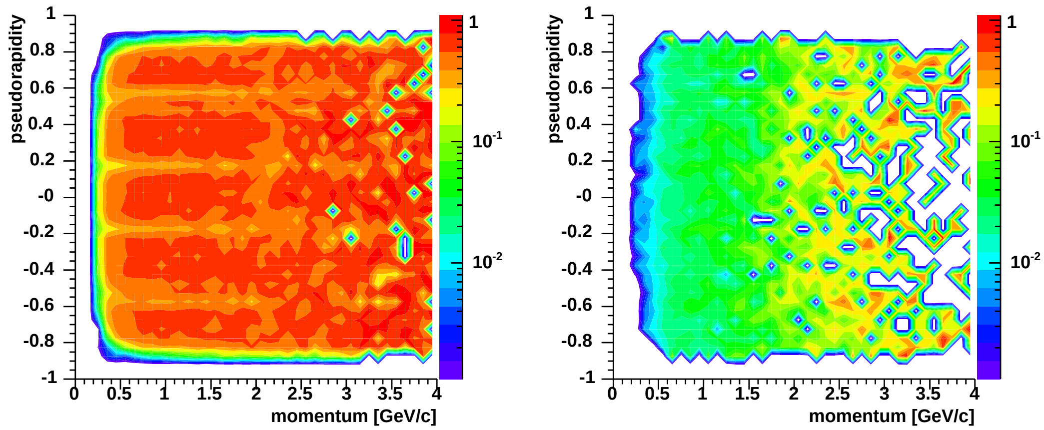

Figure 4.30: The momentum and pseudorapidity dependence of the overall efficiency and contamination of the PID procedure for primary $\pi^{\pm}$ matched with the TOF (250 HIJING events with $B = 0.4$ T).

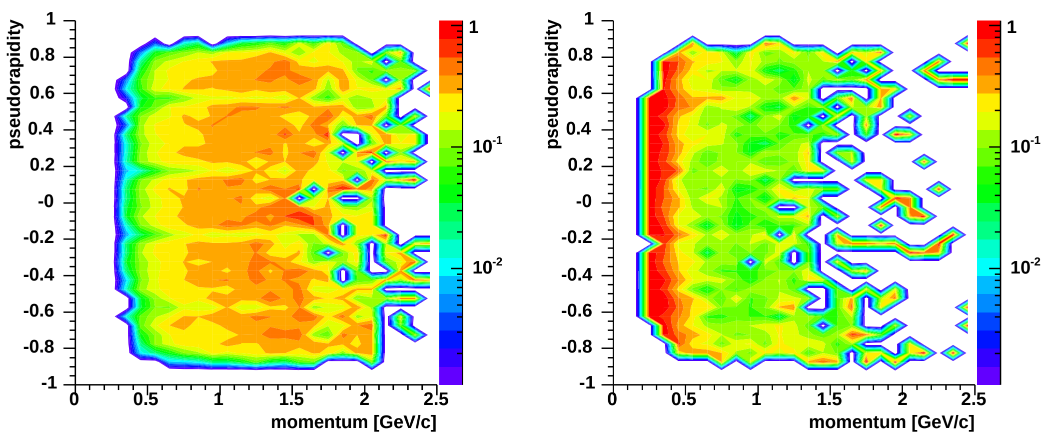

Figure 4.31: Same as fig. 4.27 for primary $K^{\pm}$.

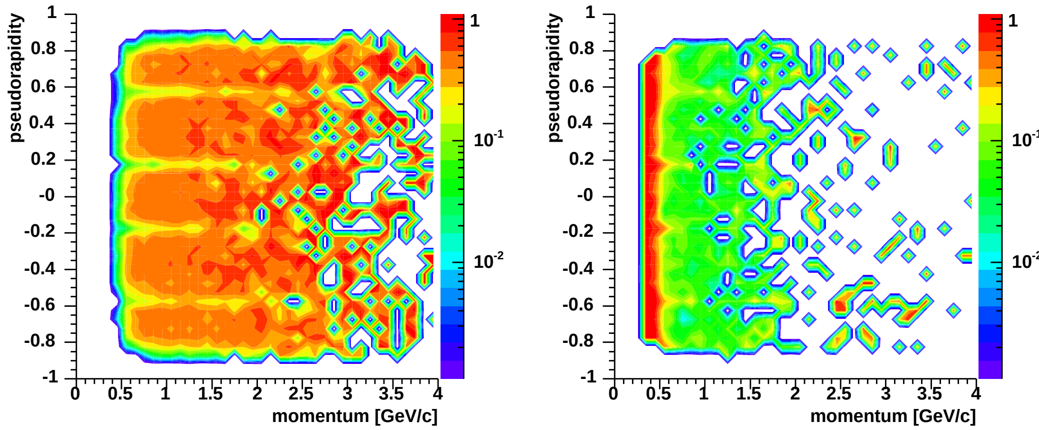

Figure 4.32: Same as fig. 4.30 for primary $p(\bar{p})$.

Chapter 5

Analysis of $\phi \to K^+K^-$ in the ALICE TOF acceptance

As pointed out in §1.4.1, the study of the ϕ meson represents an interesting instrument to investigate a possible phase transition to a QGP: in fact an enhancement in the ϕ production or a change in the shape of the resonance (mean value and width), or a modification of the ϕ transverse momentum spectrum, in particular of the inverse slope parameter of this spectrum which is directly related to the global temperature at the thermal freeze-out (T_{fo}, see §1.4.1 [4, 5, **?**]), are considered amongst the signatures of a transition to a Quark Gluon Plasma phase.

In this chapter, we will describe the strategy adopted to produce Monte Carlo data for the ϕ meson analysis in a "real" heavy ion collision environment (see §5.1 and in [78, 79]). We will present Monte Carlo simulation results about ϕ detection by means of *kaon* identification separately with the ALICE TPC detector, with the ALICE TOF detector and with both the ALICE TPC and TOF detectors together (§5.2). The comparison between these Monte Carlo studies shows how important is the contribution that a Time-Of-Flight detector, with the characteristics of the ALICE TOF, can give to the study of the transition to the QGP phase: the transverse momentum (or transverse mass) coverage due to the *kaon* identification in the TOF turns out to be sensibly increased, hence the estimate of the inverse slope parameter of the ϕ meson correspondingly improved (§5.3).

Preliminary Monte Carlo studies about the possibility of ϕ *meson* detection via *kaon* identification in ALICE experiment were reported in [78]. Here the HIJING model [70] is used to simulate the heavy ion collision environment. A further study on the ϕ detection in ALICE considering an heavy ion environment with charged primary multiplicity higher than the HIJING one was reported in [79].

5.1 Strategy

The main problem in the study of the hadronic decays of particles -in general- and of the charged-*kaon* decay of the ϕ meson -in particular- in heavy ion collisions at LHC, is represented by an extremely high combinatorial background. In fact, taking into account the HIJING model, one finds that, in a $Pb-Pb$ central event at $\sqrt{s_{NN}} = 5.5\,TeV$ per nucleon pair, the average number of ϕ mesons is ~ 370, while the average number of charged *kaons* is ~ 4600. Furthermore, referring to the region of interest, corresponding to the TOF geometrical coverage $|\vartheta - 90°| < 45°$, a signal to background ratio $(S/B) \sim 10^{-4}$ is found in the dikaon invariant mass interval $|m_{K^+K^-} - m_\phi| \leq \Gamma_\phi/2$, where m_ϕ and Γ_ϕ are, respectively, the mean value and the full width at half maximum (FWHM) of the ϕ meson resonance, as reported in the Particle Data Book [8], i.e. $m_\phi = 1019.456 \pm 0.020\,MeV/c^2$ and $\Gamma_\phi = 4.26 \pm 0.05\,MeV/c^2$. Our objective is an accurate study of the invariant mass spectrum of the ϕ meson resonance (i.e. mean value, width, area and shape), but also of its transverse momentum (p_T) and invariant transverse mass (m_T) spectra (to measure, in particular, its inverse slope parameters). To this purpose a careful analysis of ϕ meson production both integrating and slicing the transverse momentum and transverse mass distributions is to be done. Therefore, the data sample required in order to obtain a sufficient statistical significance in each p_T (or m_T) bin under study should be of the order of one million of events.

As mentioned in §4.1.3, the long CPU time and the enormous disk space needed to process and store all these events[1] forced us to adopt some strategies to overcome severe technical problems.

As a first step, since the bulk of final state particles of an ion-ion collision are strongly uncorrelated, parametrized rapidity (y) and p_T distributions for both 'background' particles ($\pi^\pm$ and $K^\pm$ mesons)[2] and 'signal' particles (ϕ mesons), can be used to generate our data sample, instead of a full-event generator (like HIJING [70]). The CPU time is reduced because the particle production mechanism merely consists of a random generation of numbers according to parametrized distributions, without any reference to the underlying physical processes.

[1] $\sim$ 12000 PC (Pentium 4, 1.8 GHz) running for one week can produce a sample of 10^6 events of $Pb-Pb$ collision at $\sqrt{s_{NN}} = 5.5\,TeV$ per nucleon pair, with the HIJING Monte Carlo event generator.

[2] In the present excercise, the only 'background' particles considered are the following *mesons*: $\pi^\pm$, $K^\pm$, while *protons* and *antiprotons* are neglected.

As a second step, corrections of these distributions can be performed according to the parametrized detector response in terms of: *i)* track reconstruction momentum and angular resolutions; *ii)* particle identification efficiency and contamination. Hence the CPU time is further drastically reduced because the track reconstruction (mainly) and particle identification processes are bypassed by a smearing procedure, followed by a weighting procedure, of the generated distributions, as described below.

5.1.1 Building the data sample

As anticipated in §4.1.2, the AliROOT framework provides a complete set of instruments to fully simulate the LHC collisions. It is interfaced to the external generators (HIJING, SHAKER, DPMJET [76]), and, furthermore, it is equipped with a set of tools which allow to perform fast simulations of the heavy ion collision environment using the above strategy. In fact, we have:

- the AliROOT libraries for y and p_T distributions, called *AliGenLib*,
- a tool to construct a particle generator using parametrized y and p_T distributions, called *AliGenParam*,
- and, finally, a tool to assemble 'background' particles (charged *pions* and *kaons*, in the present work) and 'signal' particles (ϕ mesons), called *AliGen−Cocktail*.

The 'mother' class of all distribution libraries (*AliGenLib*) works as a function factory: in each 'daughter' class, a list of particles can be found and, for each particle type, a parametrization of its y and p_T distributions. The library considered herein, *AliGenSTRANGElib*, contains parametrizations for both 'background' particles ($\pi^{\pm}$ and $K^{\pm}$) and ϕ 'signal' particles.

The p_T distributions implemented in *AliGenSTRANGElib* are derived from the p_T distribution of *pions*[3] using the transverse mass scaling (m_T-scaling) [73]. The y distribution is a gaussian function centred at *zero* value and with $\sigma = 4$ for all the mesons we considered. Figures 5.1, 5.2 and 5.3 show the p_T, y and invariant m_T distributions respectively for 'background' $\pi^{\pm}$, $K^{\pm}$ and for 'signal' ϕ mesons, as parametrized in *AliGenSTRANGElib*. Figure 5.4 shows the same distributions for *kaons* from ϕ-meson decays.

[3] The *pion* p_T distribution is a parametrization of that measured at CDF [77]: it is a power law for $p_T > 500\,MeV/c$ and uses a m_T scaling law, with $T = 160\,MeV$, for $p_T \leq 500\,MeV/c$.

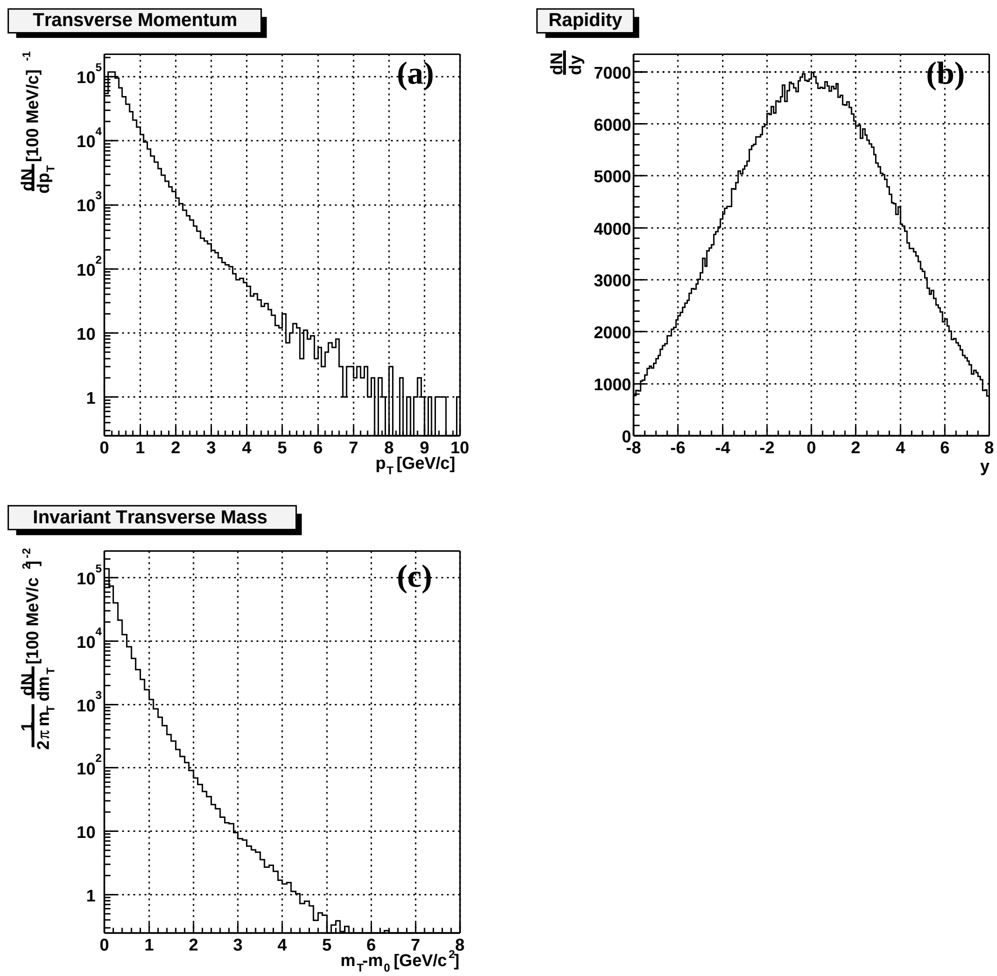

Figure 5.1: The transverse momentum **(a)**, rapidity **(b)** and invariant transverse mass **(c)** distributions for 'background' $\pi^{\pm}$ mesons.

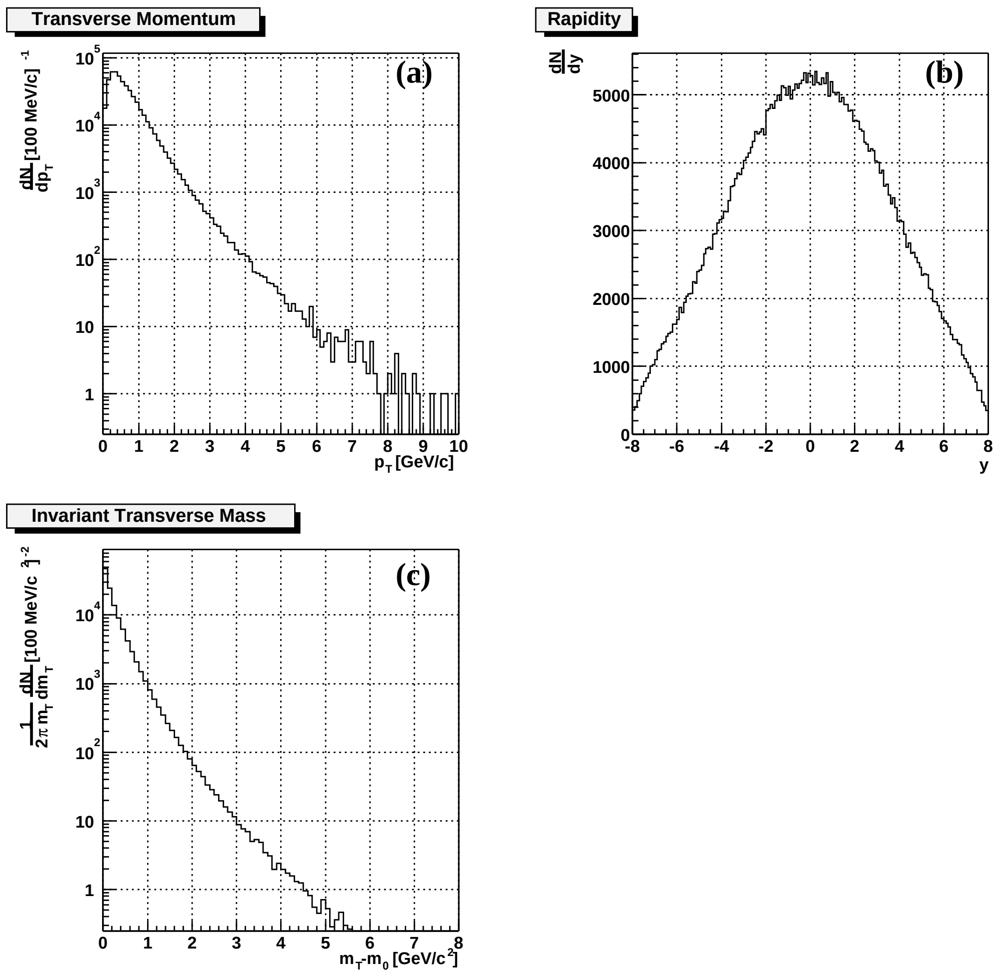

Figure 5.2: The transverse momentum **(a)**, rapidity **(b)** and invariant transverse mass **(c)** distributions for 'background' $K^{\pm}$ mesons.

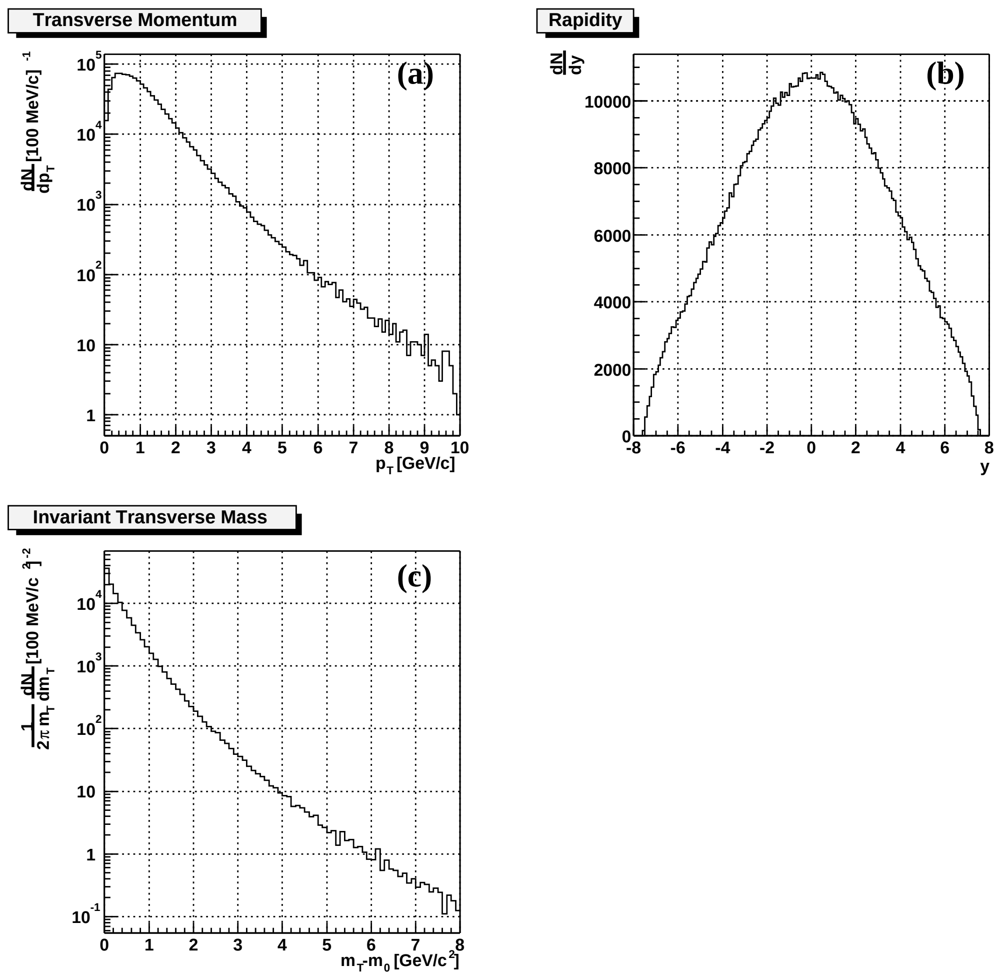

Figure 5.3: The transverse momentum **(a)**, rapidity **(b)** and invariant transverse mass **(c)** distributions for ϕ mesons.

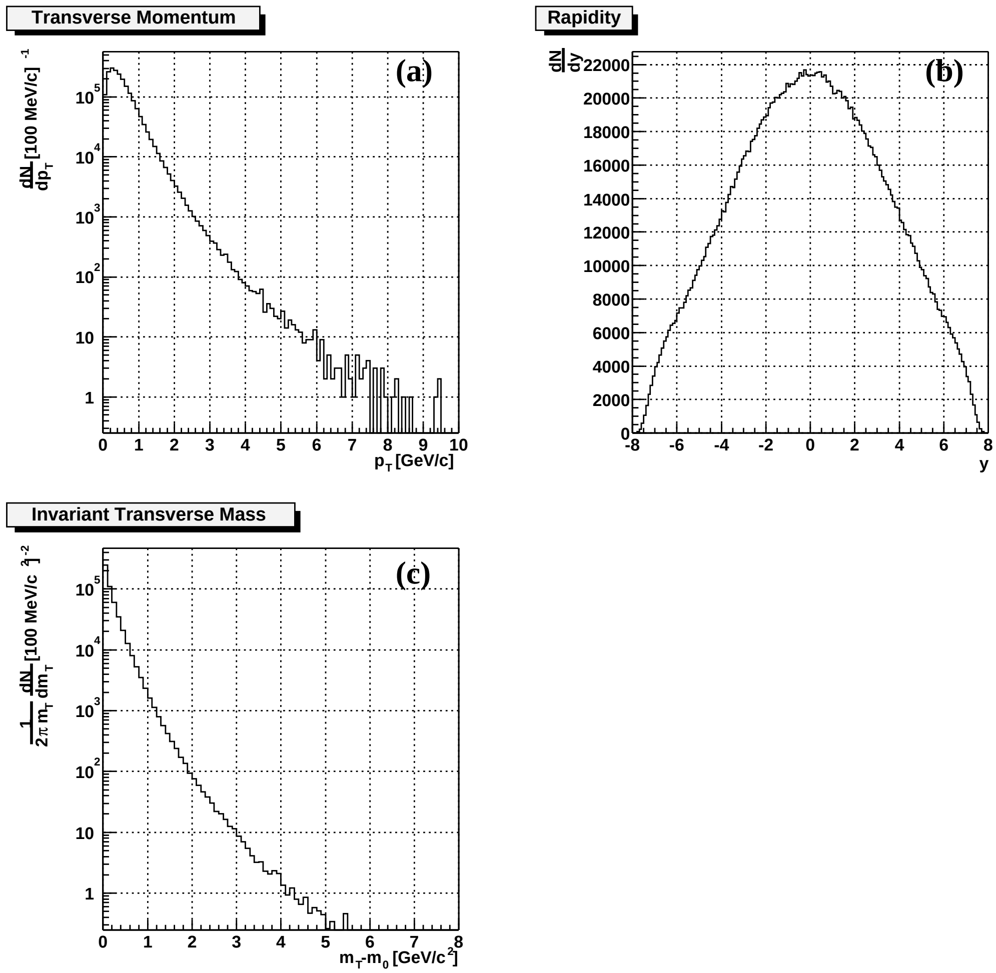

Figure 5.4: The transverse momentum **(a)**, rapidity **(b)** and invariant transverse mass **(c)** distributions for charged *kaons* from ϕ-meson decays.

At the generation level, it is possible to introduce some geometrical or kinematical cuts, and to modify the branching ratios (BR) of particle decay channels. In order to further reduce the CPU time, the following constraints were introduced: the generation of 'background' particles was confined to the TOF acceptance region, i.e. $|\vartheta - 90°| < 45°$; the ϕ mesons were forced to decay into charged *kaons* (K^+K^-) and the same geometrical cut relative to the TOF acceptance region (see above) was imposed on each of these *kaons*. Figures 5.5, 5.6, 5.7 and 5.8 show the p_T, y and invariant m_T distributions respectively for 'background' $\pi^\pm$ and $K^\pm$, for ϕ mesons and for $K^\pm$ from ϕ decays once the above constraints have been applied.

From a comparison of figs. 5.1 and 5.5, and defining R_π the fraction of charged *pions* generated in the $|\vartheta - 90°| < 45°$ region, we find $R_\pi = 0.23$; analogously, a comparison of figs. 5.2 and 5.6, gives for the fraction of *kaons* in the $|\vartheta - 90°| < 45°$ region a value $R_K = 0.18$; finally, from a comparison of figs. 5.3 and 5.7, the fraction of ϕ *mesons* the decay *kaons* of which are in the $|\vartheta - 90°| < 45°$ region is $R_\phi = 0.185$.

With these ingredients, we can now proceed to simulate the data sample for our analysis. We want to create a data sample equivalent to 10^6 events of $Pb-Pb$ collisions at $\sqrt{s_{NN}} = 5.5\,TeV$ per nucleon pair, tracked and reconstructed in the ALICE detector in the presence of a magnetic field with $B = 0.4$ T. Let us start from the HIJING predictions, in terms of particle numbers and ratios, as reported in the following:

- the average number of charged *pions* per event is $< \pi^\pm > \sim 41400$,
- the charged *kaon* to *pion* ratio is $\frac{<K^\pm>}{<\pi^\pm>} \sim 0.105$, hence the average number of charged *kaons* per event is $< K^\pm > \sim 4600$,
- the ϕ meson to negatively charged *pion* ratio is $\frac{<\phi>}{<\pi^->} \sim 0.009$, hence the average number of ϕ mesons per event is $< \phi > \sim 370$.

Taking into account the distributions shown in figs. 5.5, 5.6 and 5.7 and the $BR(\phi \to K^+K^-)$ forced to be 100%, 10^6 events were generated in the $|\vartheta - 90°| < 45°$ region, each containing:

- a number of charged *pions*, called $N_{\pi^\pm}$, equal to

$$N_{\pi^\pm} = R_\pi \times \mathcal{N}_{\pi^\pm}{}^4,$$

[4] A statistical fluctuation in the number of charged particles per event was considered with-

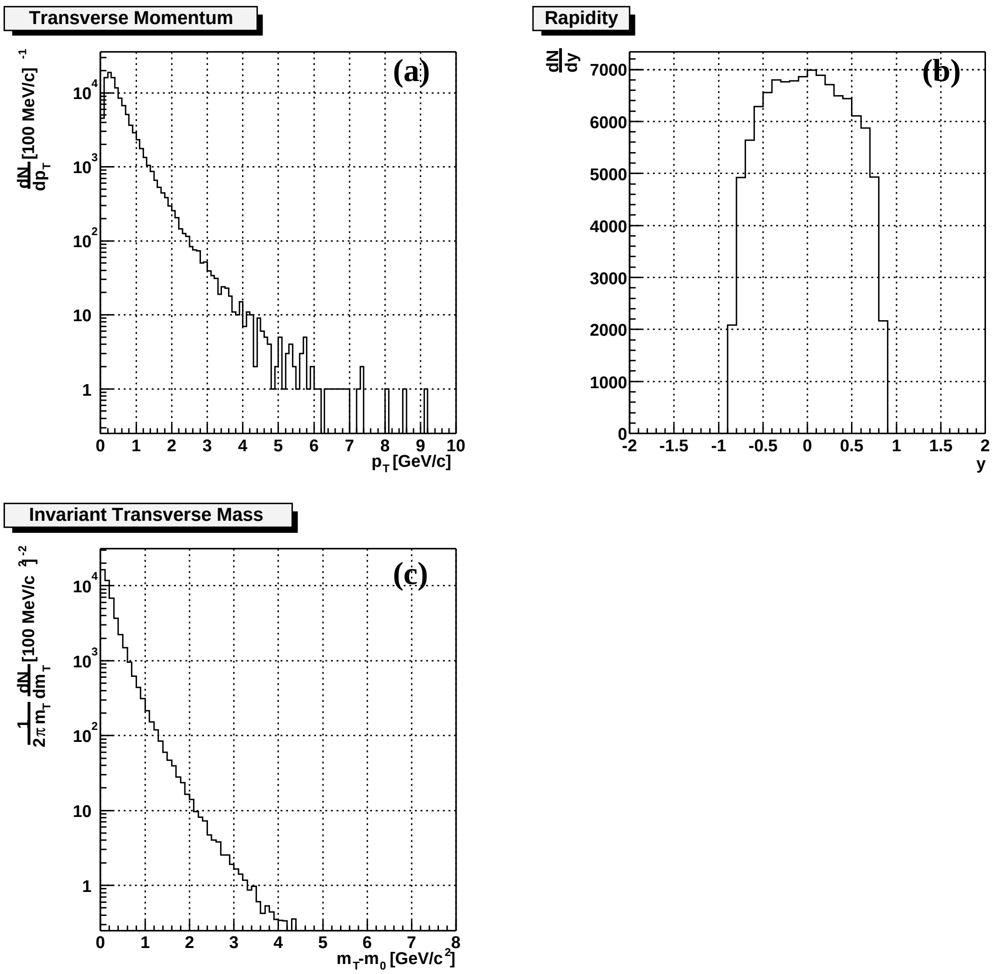

Figure 5.5: The transverse momentum **(a)**, rapidity **(b)** and invariant transverse mass **(c)** distributions for 'background' $\pi^{\pm}$ mesons with $|\vartheta - 90°| < 45°$.

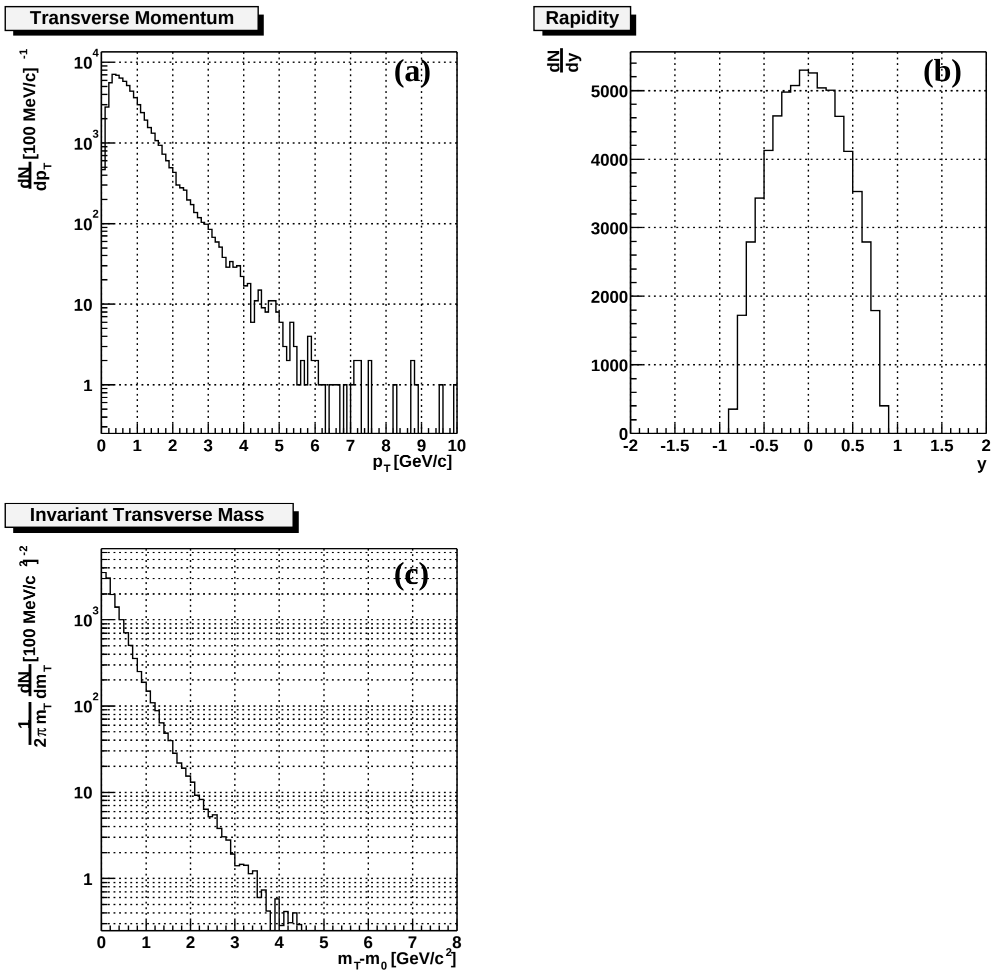

Figure 5.6: The transverse momentum **(a)**, rapidity **(b)** and invariant transverse mass **(c)** distributions for 'background' $K^{\pm}$ mesons with $|\vartheta - 90°| < 45°$.

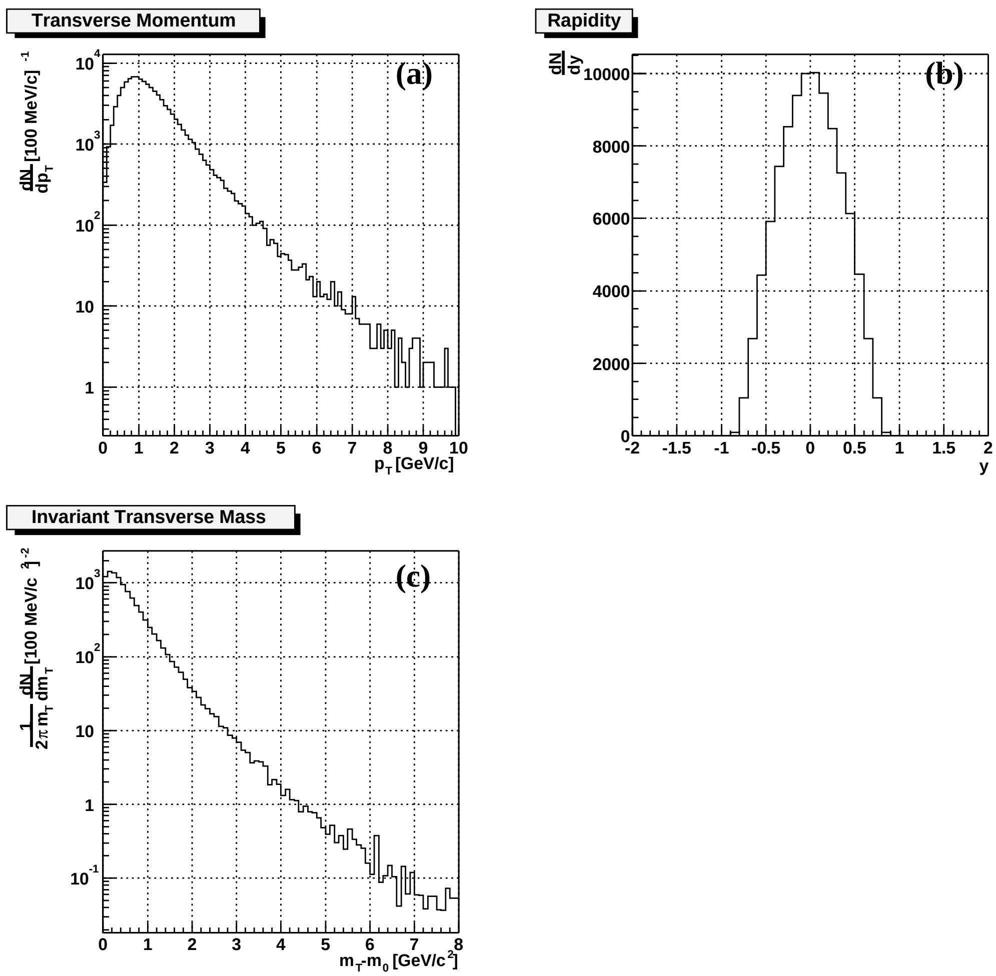

Figure 5.7: The transverse momentum **(a)**, rapidity **(b)** and invariant transverse mass **(c)** distributions for ϕ mesons, the daughters of which are charged *kaons* with $|\vartheta - 90°| < 45°$.

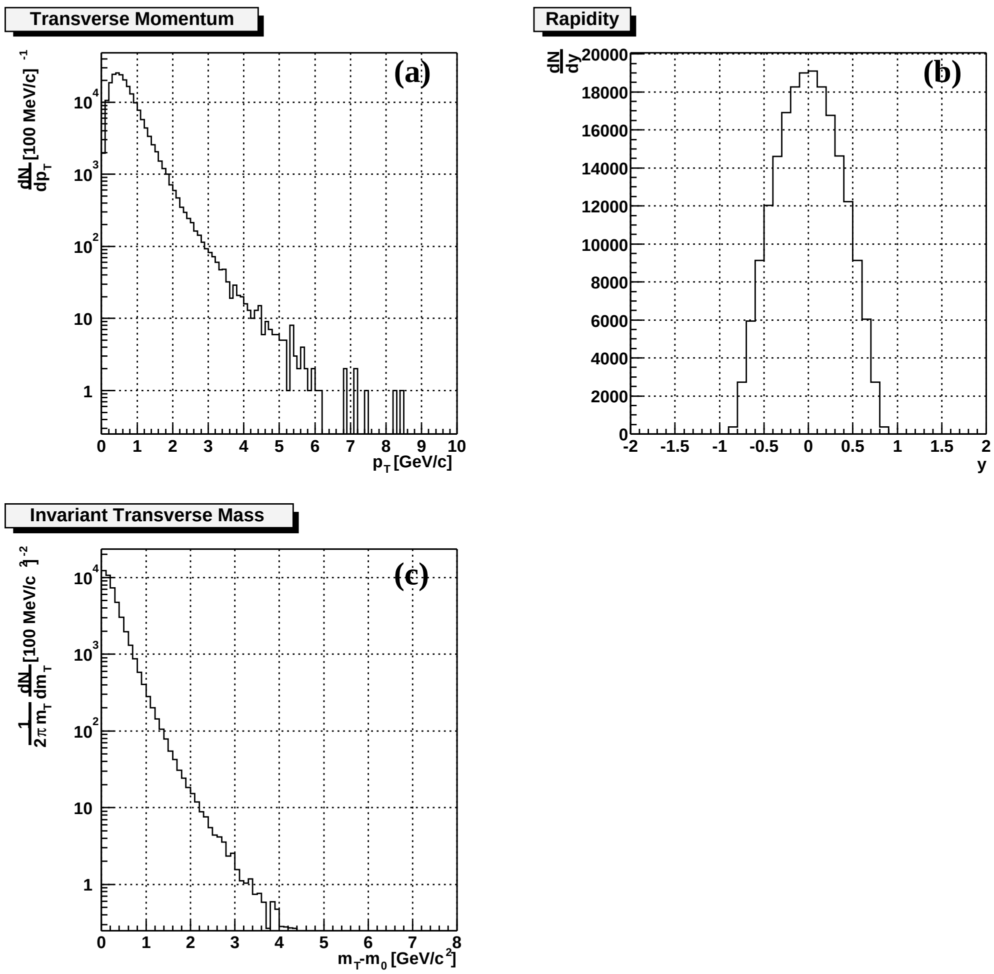

Figure 5.8: The transverse momentum **(a)**, rapidity **(b)** and invariant transverse mass **(c)** distributions for $K^{\pm}$ mesons, from ϕ meson decays, both with $|\vartheta - 90°| < 45°$.

where $\mathcal{N}_{\pi^\pm}$ is the total number of charged *pions* in the corresponding full phase-space event,

- a number of charged *kaons*, $N_{K^\pm}$, equal to

$$N_{K^\pm} = R_K \times \frac{< K^\pm >}{< \pi^\pm >} \times \mathcal{N}_{\pi^\pm},$$

- and a number of ϕ *mesons*, N_ϕ, equal to

$$N_\phi = BR(\phi \to K^+K^-) \times R_\phi \times \frac{< \phi >}{< \pi^- >} \times \frac{\mathcal{N}_{\pi^\pm}}{2}.$$

As just said at the beginning of this chapter, the reconstruction process is replaced by a 'corruption' process of the generated distributions. In fact, the momentum and angles of the charged particles were smeared according to the ALICE detector resolution; figures 5.9 and 5.10 show the errors introduced by the ALICE tracking detectors (only the TPC, for the time being) in the transverse momentum, ϑ angle and φ angle measurements of a track, as functions of p_T. These curves were obtained by the full-event simulation of 250 central HIJING events tracked in the ALICE detector with a magnetic field value $B = 0.4$ T.

Finally, for the particle identification process, a weighting procedure of the generated distributions was performed on the basis of the particle identification power of the ALICE TPC and TOF detectors.

Figure 5.11 shows the efficiency for charged *kaon* identification achieved with the ALICE TPC detector, as a function of p_T and in four pseudorapidity (η) bins. Here again 250 central HIJING events, tracked at $B = 0.4$ T, were processed to obtain these efficiency distributions.

Referring to the careful study of the ALICE TOF detector performance made in the previous chapter (see chapter 4), figure 5.12 shows the charged *kaon* identification efficiency and the charged *pion* misidentification probability, i.e. the probability for a charged *pion* to be identified as a charged *kaon*, as functions of generated momentum (p) and pseudorapidity (η). Referring to the same notation used in §4.4, let us recall the definition of the overall TOF PID efficiency:

$$\textit{overall PID efficiency} = \frac{N^t_{id}(i)}{N_{TOT}(i)},$$

out changing the particle ratios: for each event the actual number of *pions*, $\mathcal{N}_{\pi^\pm}$, was randomly extracted according to a Poisson distribution with mean value equal to $< \pi^\pm >$.

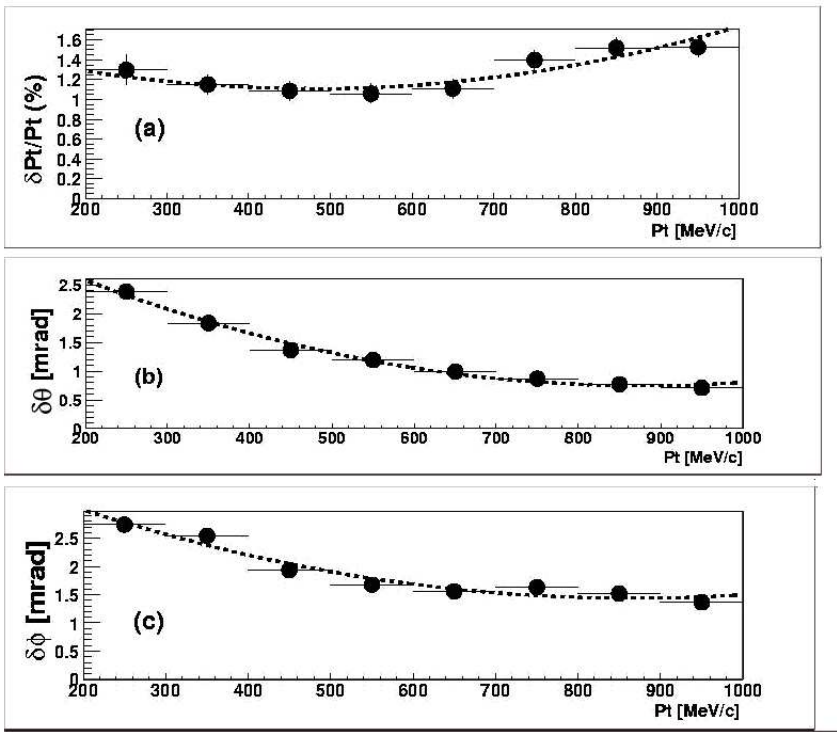

Figure 5.9: The transverse momentum (p_T) dependence of track reconstruction resolution in the ALICE TPC for $p_T < 1\,GeV/c$: from top to bottom, the relative p_T resolution (%) **(a)**, the ϑ angle resolution (*mrad*) **(b)** and the φ angle resolution (*mrad*) **(c)**. The curves are the results of second order polynomial fits [79].

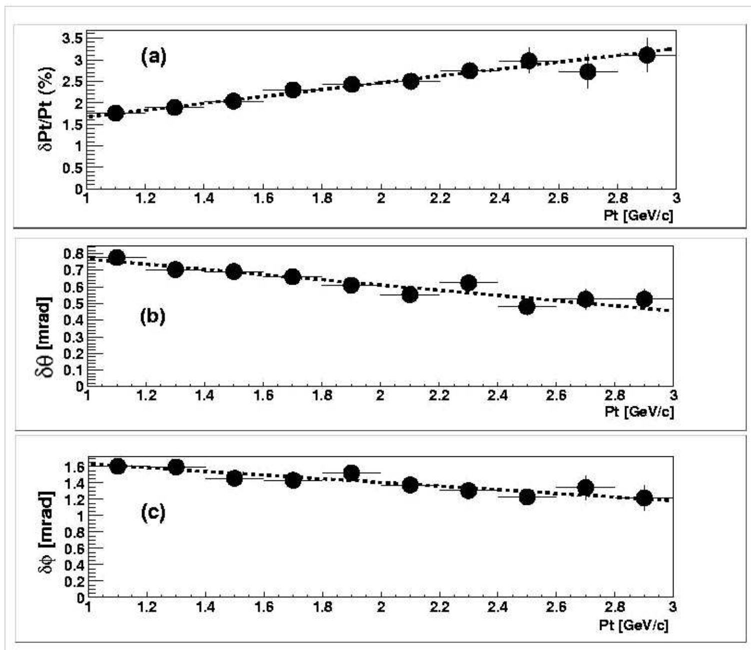

Figure 5.10: Same as fig. 5.9, for $p_T > 1\, GeV/c$.

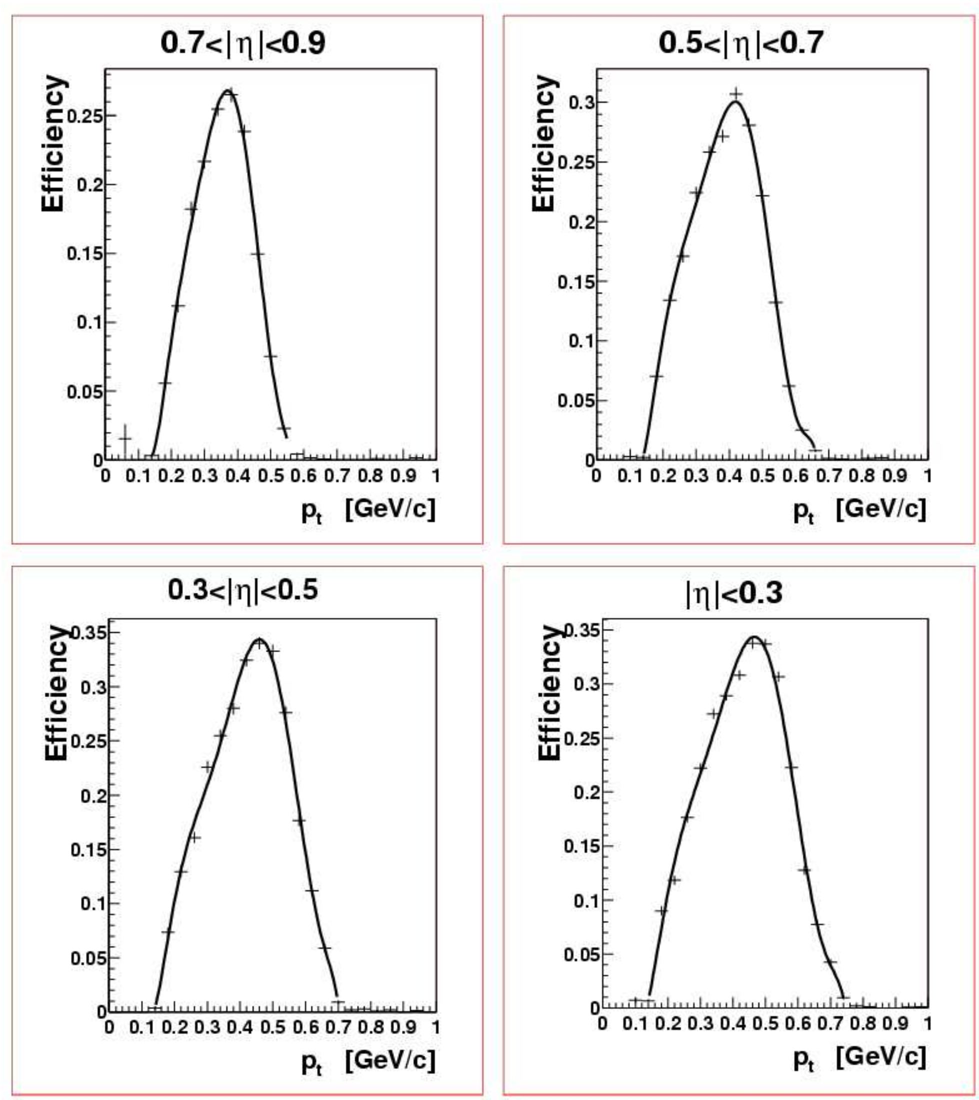

Figure 5.11: The overall *kaon* identification efficiency of the ALICE TPC detector as a function of p_T in four pseudorapidity (η) bins, as indicated. The curves are the results of polynomial fits [79].

and define the TOF misidentification probability as follows:

$$misidentification\,probability = \frac{N_i^w(j)}{N_{TOT}(j)},$$

where $N_{TOT}(i)$ is the total number of primary hadrons of type i originally generated in the angular region $|\vartheta - 90°| < 45°$, $N_{id}^t(i)$ is the number of well identified particles of type i and $N_i^w(j)$ the number of type j particles misidentified as particles of type i, where i and j stands for $\pi^{\pm}$, $K^{\pm}$, $p(\bar{p})$. Therefore, the probability for a *pion* to be misidentifed as a *kaon* by the ALICE TOF is the following:

$$pion\,misidentification\,probability = \frac{N_{K^{\pm}}^w(\pi^{\pm})}{N_{TOT}(\pi^{\pm})}.$$

In fig. 5.13 the overall TOF identification efficiency for charged *kaons* and the TOF probability to misidentify charged *pions* as *kaons* are also displayed in two-dimensional plots in terms of pseudorapidity (η) *versus* momentum (p).

It has been assumed that the contamination for *kaons* only comes from *pion* misidentification, mostly at lower momenta, while the contribution due to *protons* -mainly at higher momenta (see §4.4)- was not considered. Notice that, due to the overwhelming number of *pions*, this is a resonable approximation.

Then, the following three event samples were defined:

- **Sample I:** where the events are generated according to the distributions in figs. 5.6 and 5.8, and weighted according to the *kaon* TPC identification efficiency (fig. 5.11).

- **Sample II:** where the events are generated according to the distributions in figs. 5.5, 5.6 and 5.8, and weighted according to the *kaon* TOF identification efficiency and the *pion* TOF misidentification probability (fig. 5.12).

- **Sample III:** where the events are generated according to the distributions in figs. 5.5, 5.6 and 5.8, and weighted for the *kaon* TOF or TPC identification efficiency (figs. 5.11 and 5.13 **(a)**) and the *pion* TOF misidentification probability (fig. 5.13 **(b)**).

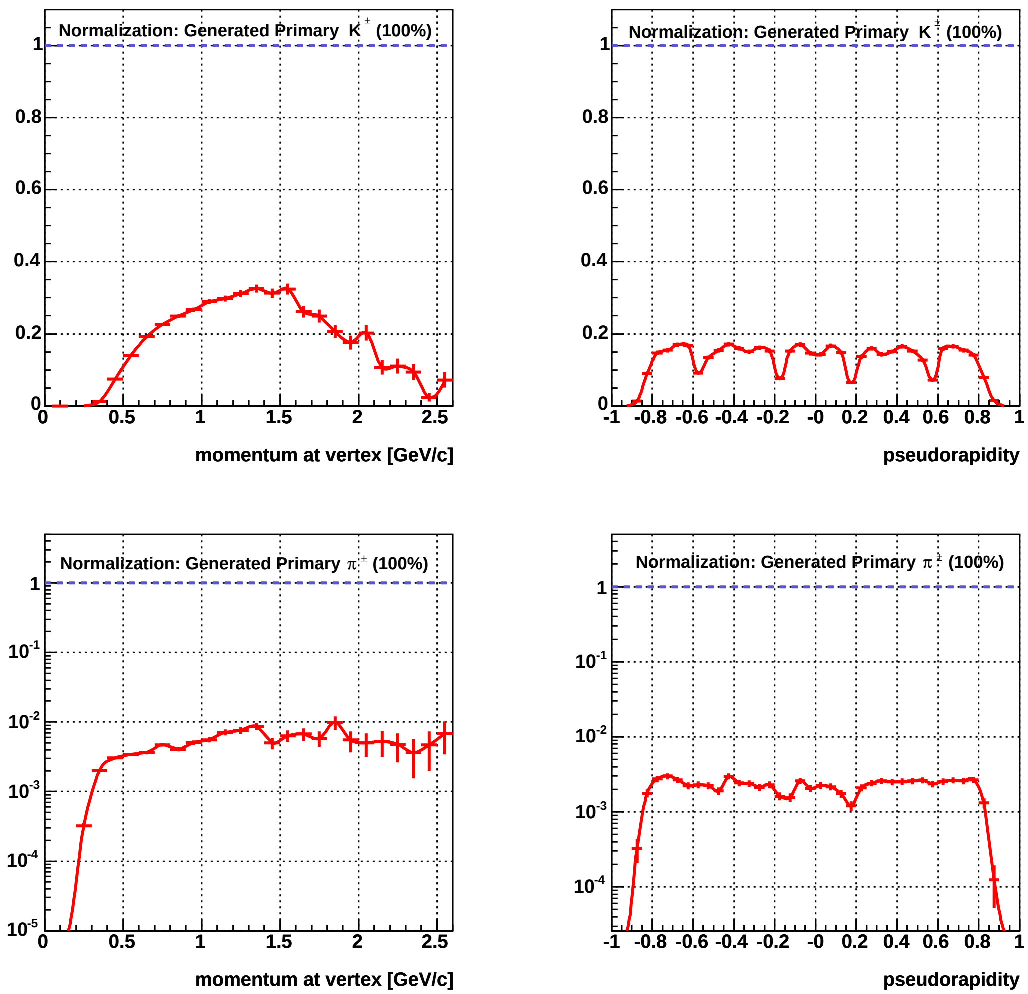

Figure 5.12: Overall TOF PID identification efficiency for *kaons* (top) and TOF probability to misidentify a *pion* (bottom) as a *kaon*, as a function of p (left) and η (right). The misidentification probability is shown on logarithmic scale.

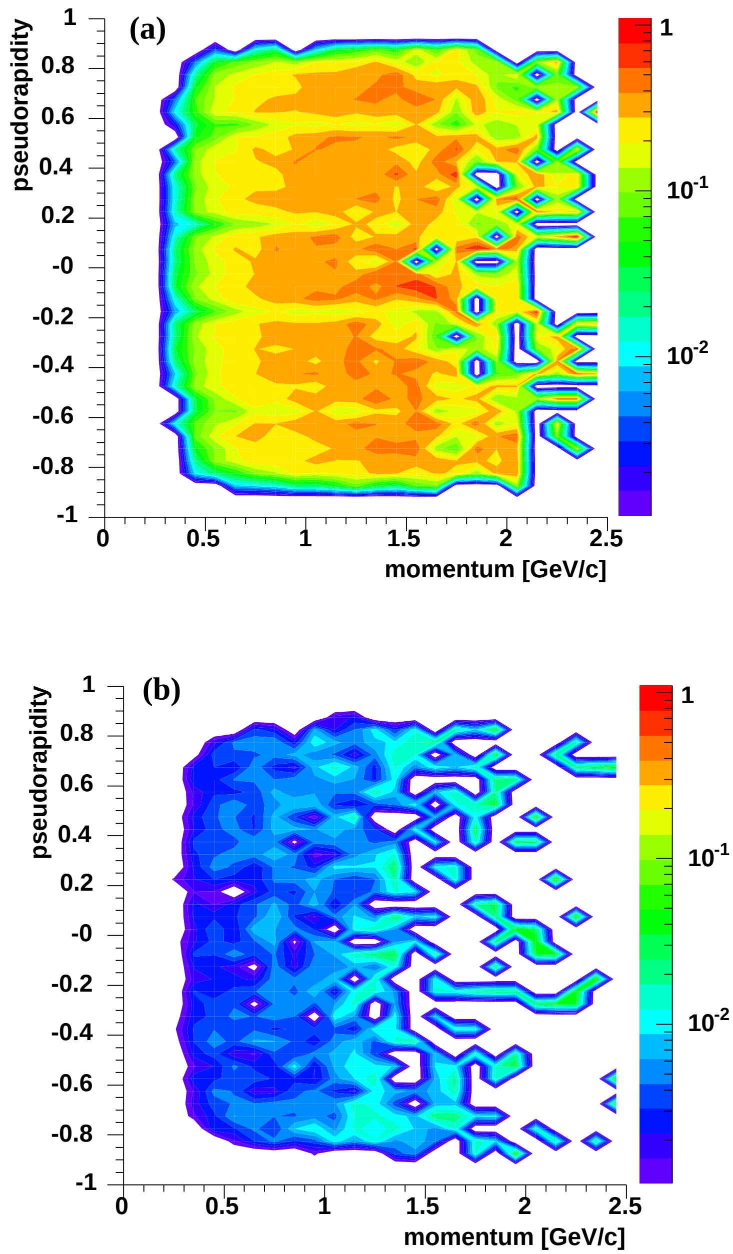

Figure 5.13: (a) Overall TOF identification efficiency for *kaons*, as a function of p and η. **(b)** TOF probability to misidentify a *pion* as a *kaon*, as a function of p and η.

5.2 Construction of K^+K^- invariant mass spectrum

All charged particles that passed the geometrical and *kaon* identification cuts are combined in unlike-sign pairs (N_{+-}) for all possible combinations to construct the K^+K^- invariant mass distribution.

The K^+K^- invariant mass distributions are shown for the event samples I, II and III respectively in figs. 5.14, 5.17 and 5.24. Figures 5.15 and 5.16 show the K^+K^- invariant mass distributions for the event sample I, as obtained by slicing the K^+K^- pair transverse momentum in seven bins (in the range $0.2 < p_T < 1.2\,GeV/c$); analogously, in figs. 5.18-5.23, the K^+K^- invariant mass distributions are shown in 24 p_T bins (with $0.4 < p_T < 5.2\,GeV/c$) for the event sample II and in figs. 5.25-5.31 in 26 p_T bins (with $0.2 < p_T < 5.2\,GeV/c$) for the event sample III.

For the background estimate, all identified *kaons* in each event are combined in like-sign pairs (N_{++}, N_{--}) and their invariant mass spectrum analogously derived.

As far as normalization is concerned, we assumed that below and above the ϕ resonance, i.e. in the interval of dikaon invariant mass $[0, m_1[\cup]m_2, \infty[$, where $m_1 = m_\phi - 3\Gamma_\phi$ and $m_2 = m_\phi + 3\Gamma_\phi$ (m_ϕ and Γ_ϕ the ϕ mass and width values as in §5.1 [8]), the invariant mass distribution of the like-sign pairs should be equal to that of the unlike-sign pairs. Therefore, the numbers of like-sign and unlike-sign pairs in $[0, m_1[\cup]m_2, \infty[$ should be equal. The following normalization factor:

$$\frac{\int_0^{+\infty} \frac{dN_{+-}}{dm} dm - \int_{m_1}^{m_2} \frac{dN_{+-}}{dm} dm}{\int_0^{+\infty} \frac{d(N_{++}+N_{--})}{dm} dm - \int_{m_1}^{m_2} \frac{d(N_{++}+N_{--})}{dm} dm}$$

turned out to be approximately 1 (with fluctuations of the order of 10^{-4}) in all cases, i.e. for all types of event samples and in any p_T bin.

In figs. 5.14, 5.17 and 5.24, respectively for the event samples I, II and III, as well as in figs. 5.15-5.16, 5.18-5.23, and 5.25-5.31 corresponding to various p_T slices, the normalised ($K^+K^+ + K^-K^-$) background distributions, are superimposed to the K^+K^- distributions. The ϕ signal peak is visible on top of a large combinatorial background. It should be noticed that, after normalization, the invariant mass distributions of like-sign pairs approximate very well the invariant mass distributions of unlike-sign pairs in the mass region external to the ϕ meson resonance. In other words, the shapes of these mass spectra are indeed the same.

Another contribution to the K^+K^- invariant mass spectrum could come from misidentified decay products of other resonances such as K^0_S or $K^{\star 0}$ [5] [45, 46, 47]. As already said, in this analysis the *kaon* contamination was assumed to come only from *pion* misidentification in the ALICE-TOF detector. However since such a contamination is lower than 15% (see table 4.3 in the previous chapter), the possibility for the above particles to sizeably contribute to the K^+K^- invariant mass distribution was neglected.

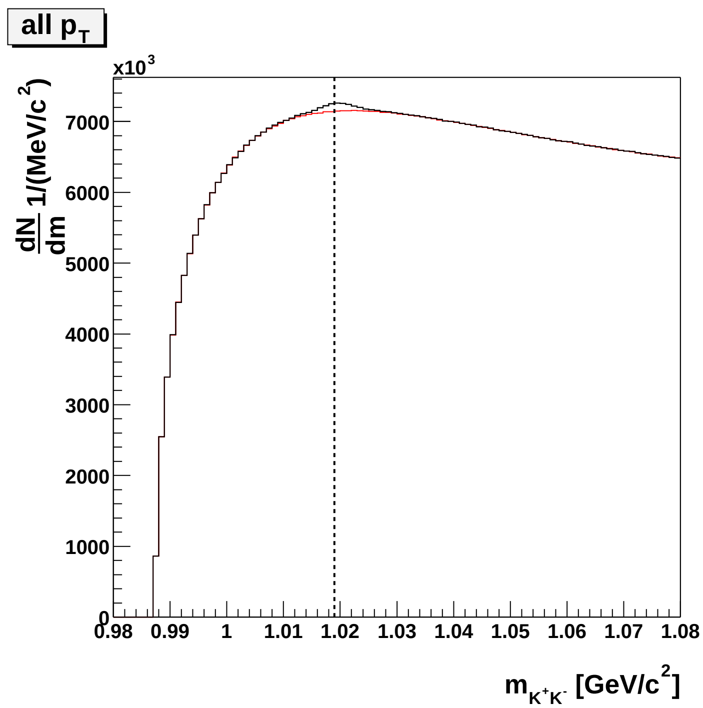

Figure 5.14: K^+K^- invariant mass distribution for the event sample I. The like-sign distribution is also shown.

[5] K^0_S decays in $\pi^+\pi^-$ with $BR = (68.95 \pm 0.14)\%$; and $K^{\star 0}$ decays in $K^\pm\pi^\mp$ with $BR = (99.770 \pm 0.020)\%$ [8].

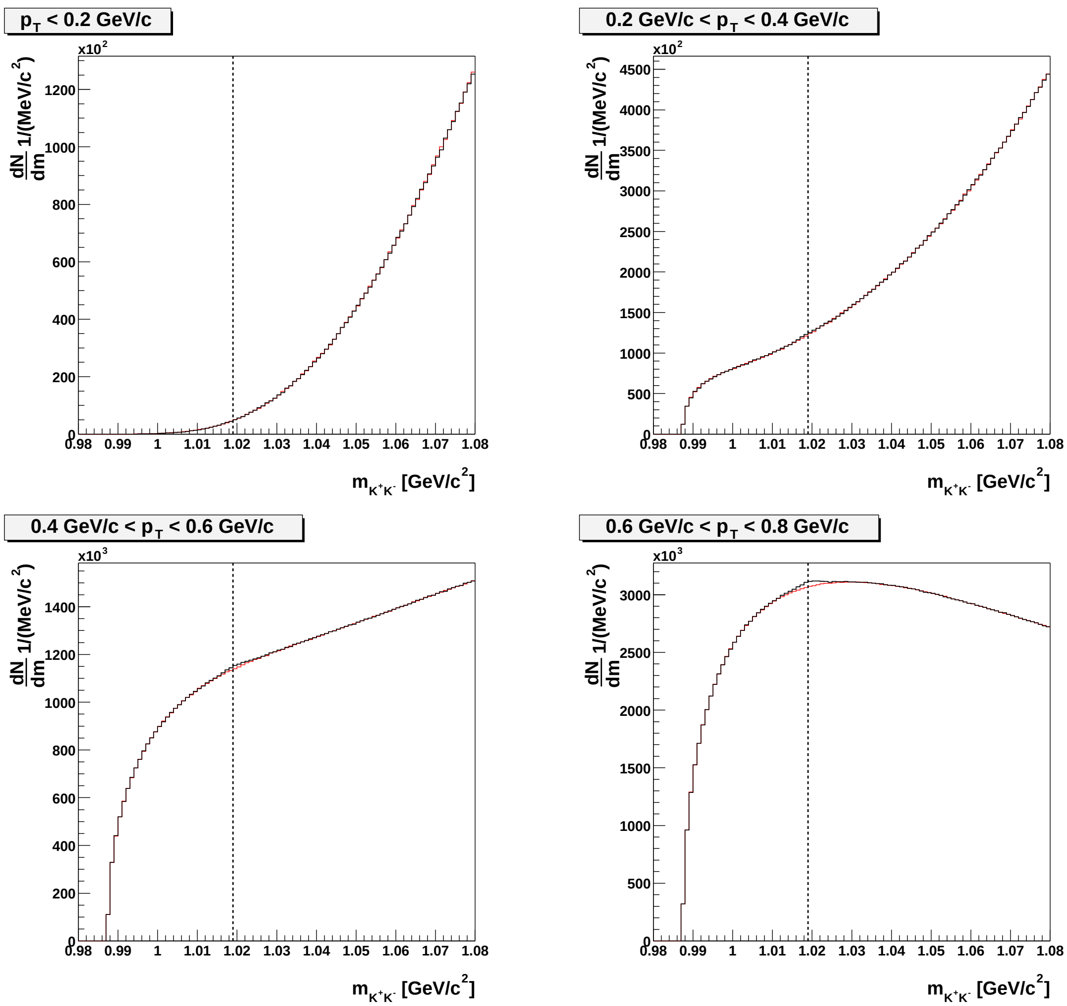

Figure 5.15: K^+K^- invariant mass distributions for the event sample I and for four p_T bins in the range $[0;0.8]GeV/c$. The like-sign distributions are also shown.

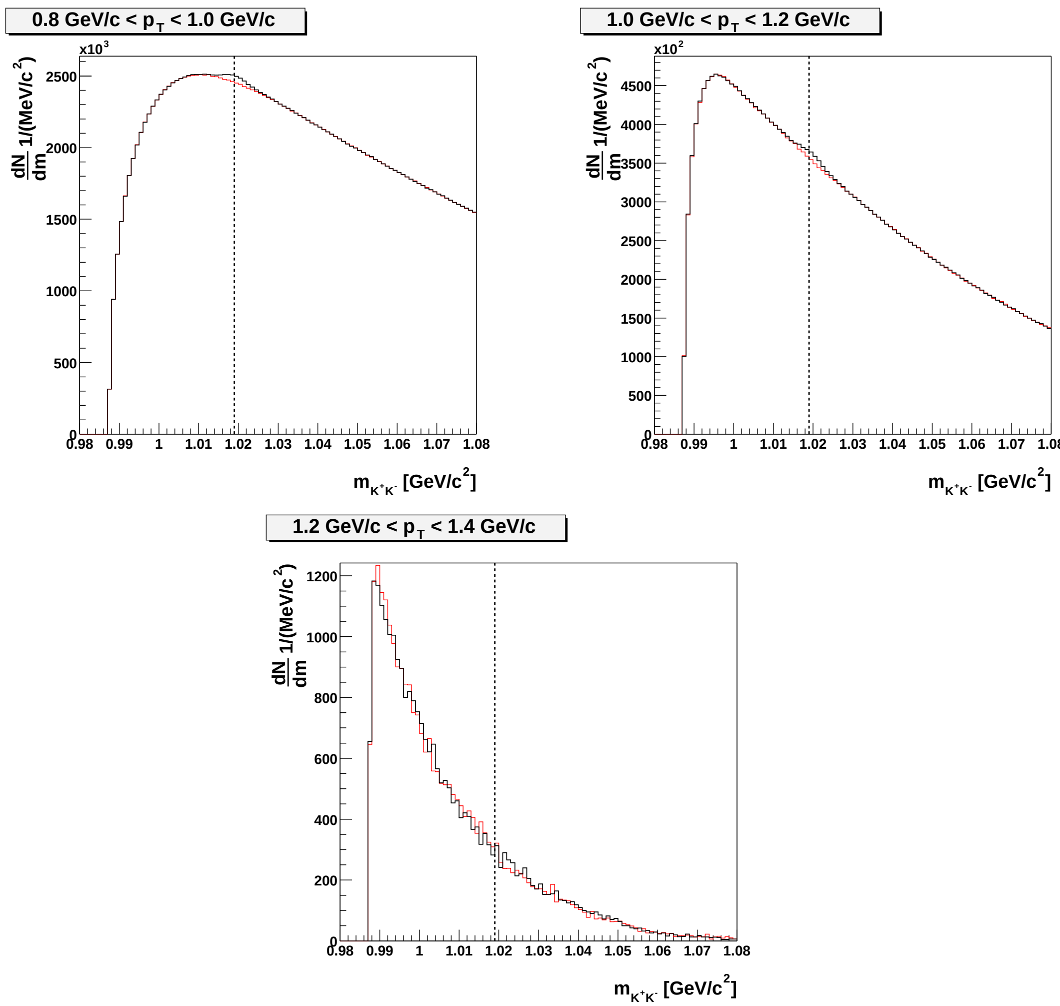

Figure 5.16: K^+K^- invariant mass distributions for the event sample I and for three p_T bins in the range $[0.8; 1.4] GeV/c$. The like-sign distributions are also shown.

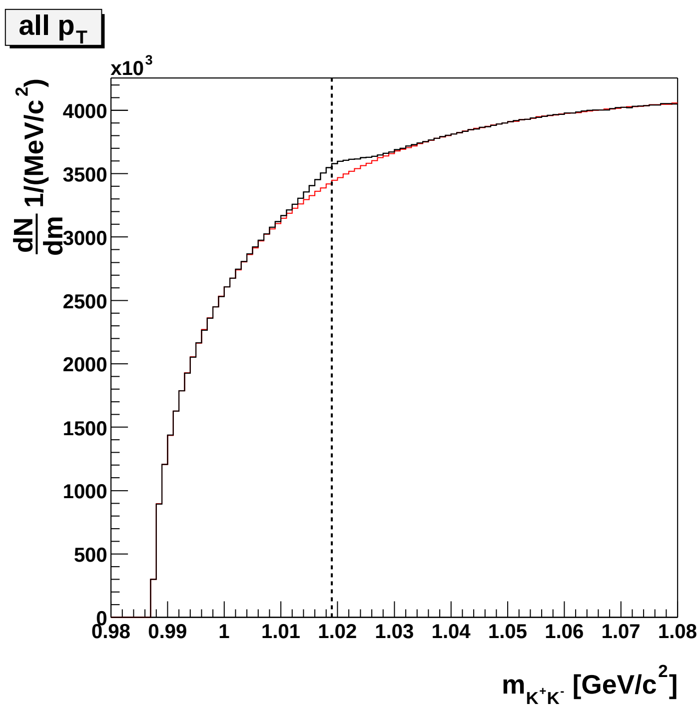

Figure 5.17: K^+K^- invariant mass distribution for the event sample II. The like-sign distribution is also shown.

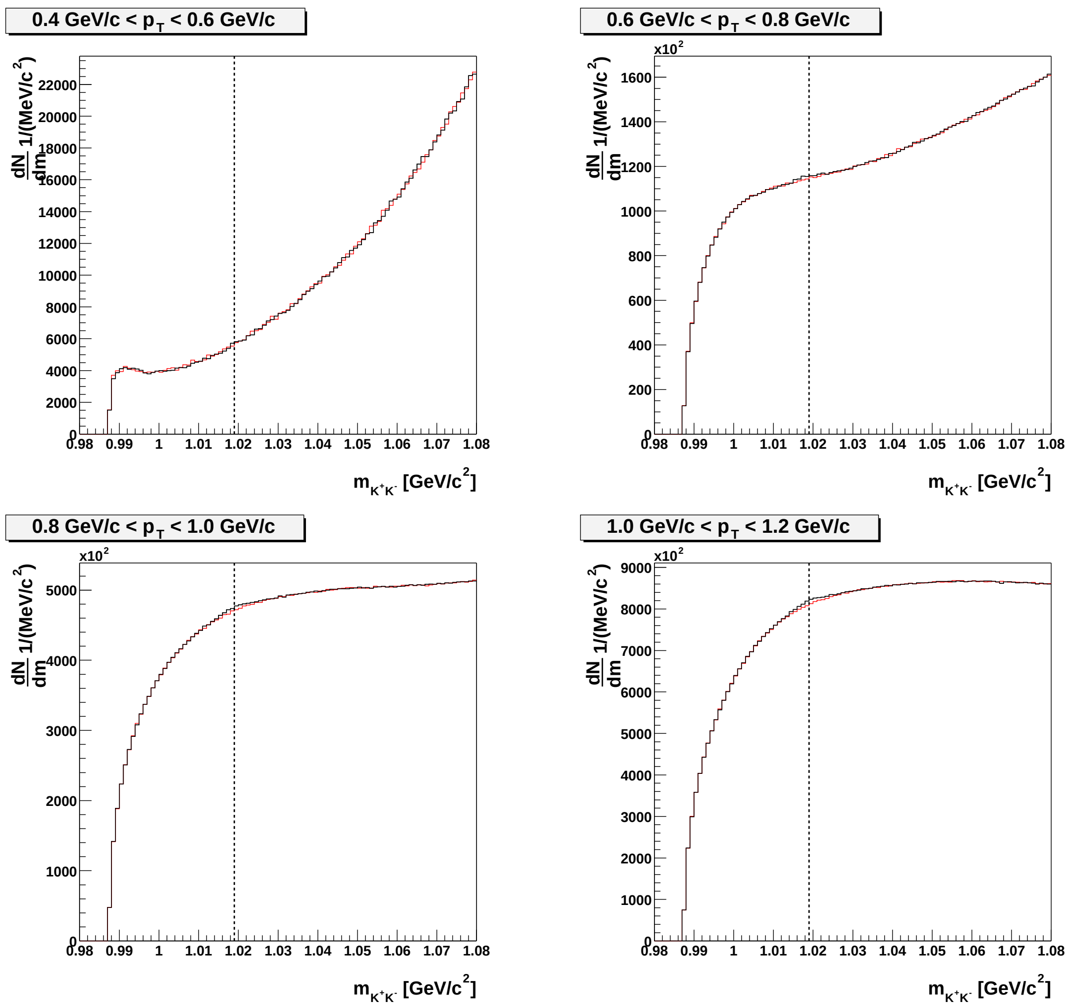

Figure 5.18: K^+K^- invariant mass distributions for the event sample II and for four p_T bins in the range $[0.4; 1.2] GeV/c$. The like-sign distributions are also shown.

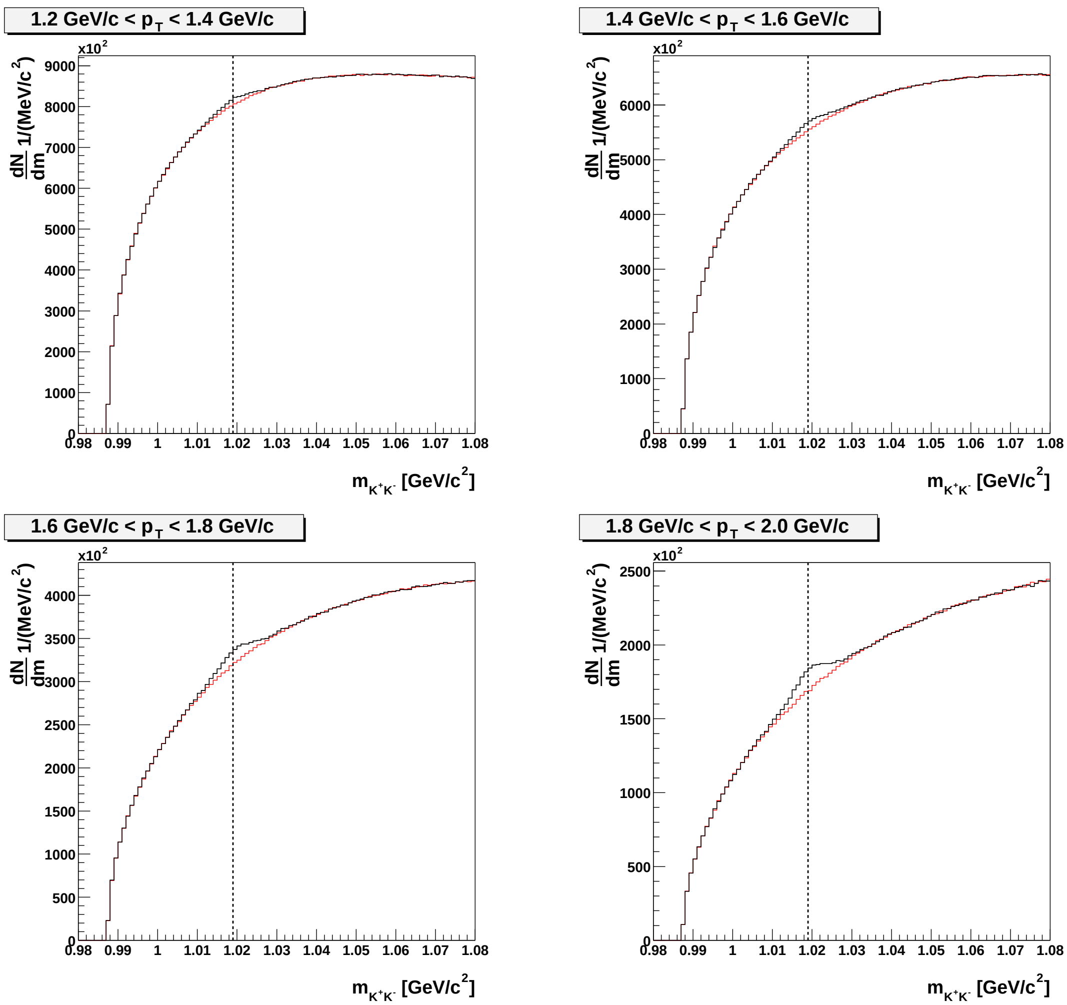

Figure 5.19: Same as fig. 5.18, for four p_T bins in the range $[1.2; 2.0]\, GeV/c$.

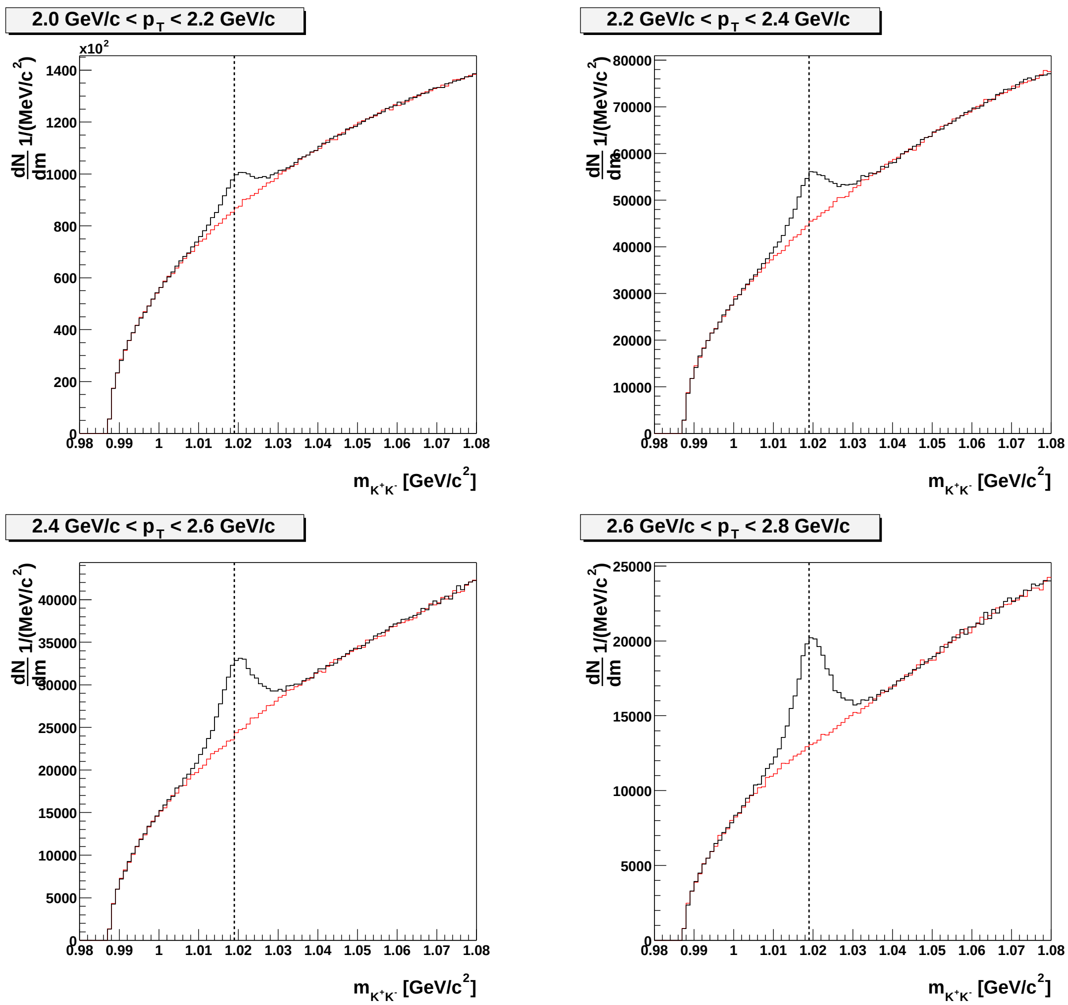

Figure 5.20: Same as fig. 5.18, for four p_T bins in the range $[2.0;2.8]\,GeV/c$.

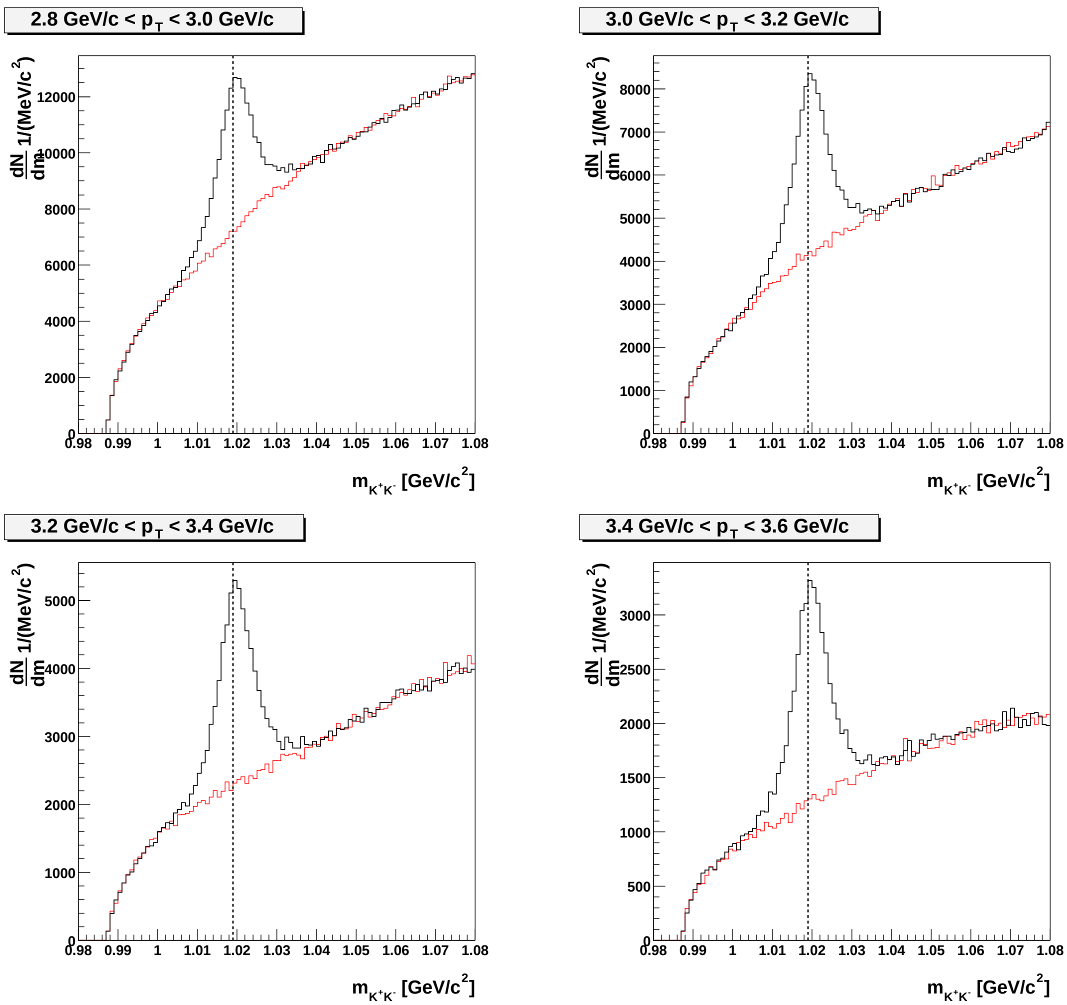

Figure 5.21: Same as fig. 5.18, for four p_T bins in the range $[2.8;3.6]\,GeV/c$.

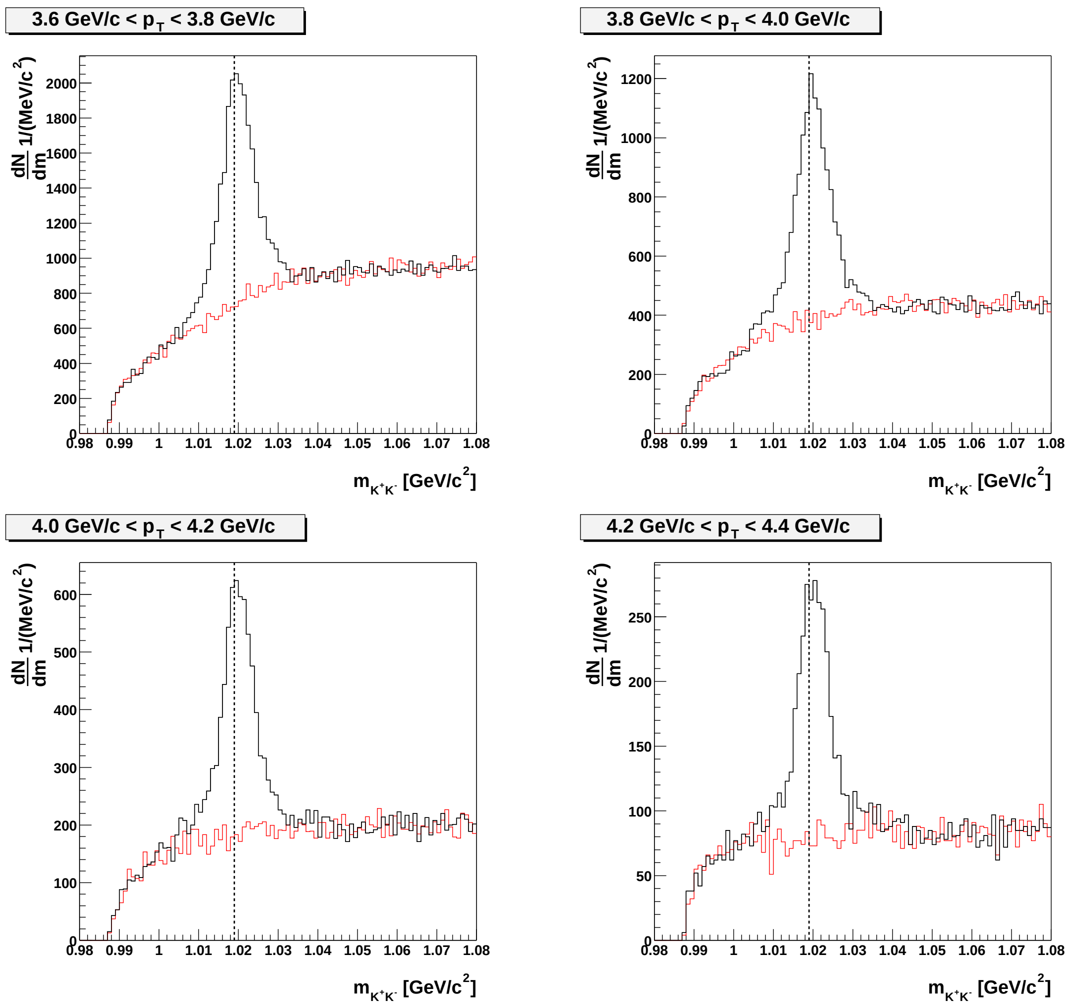

Figure 5.22: Same as fig. 5.18, for four p_T bins in the range $[3.6; 4.4]\, GeV/c$.

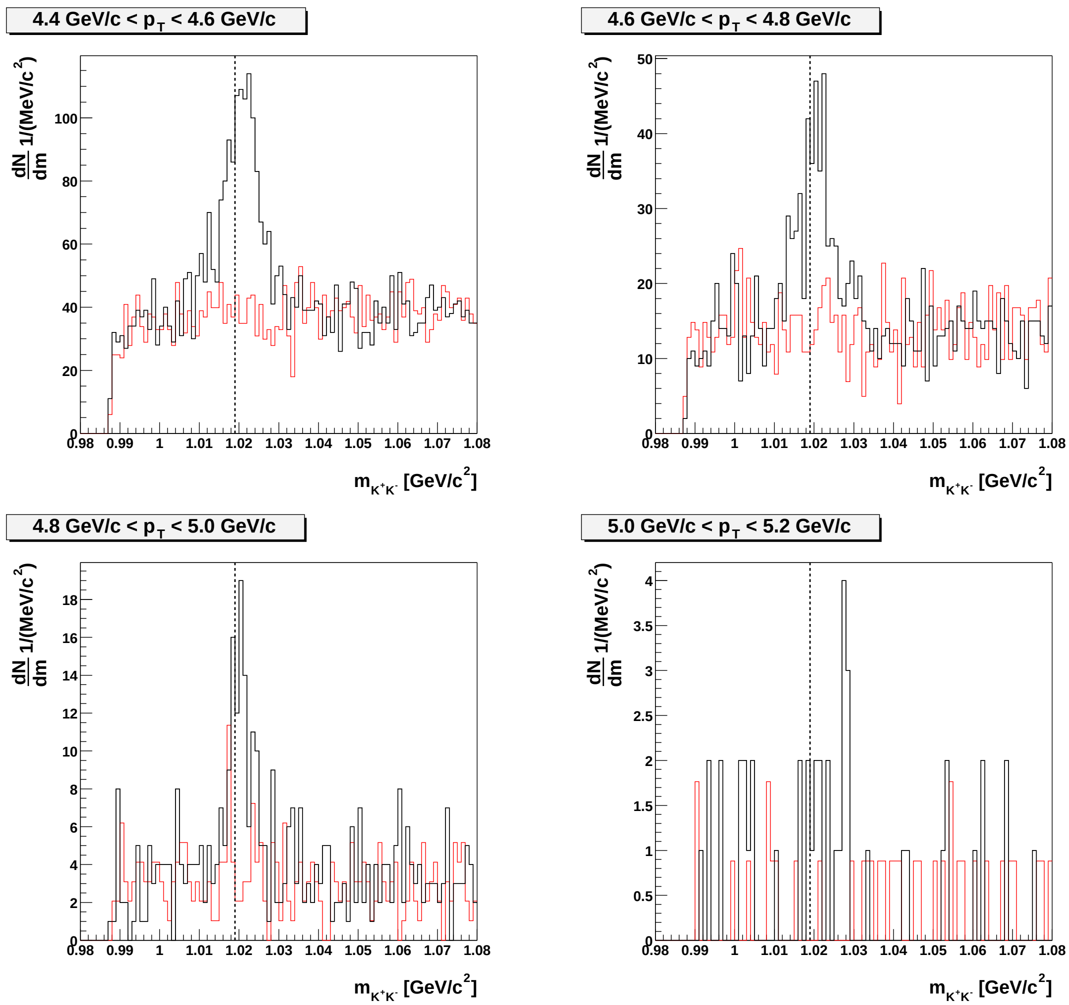

Figure 5.23: Same as fig. 5.18, for four p_T bins in the range $[4.4; 5.2]\,GeV/c$.

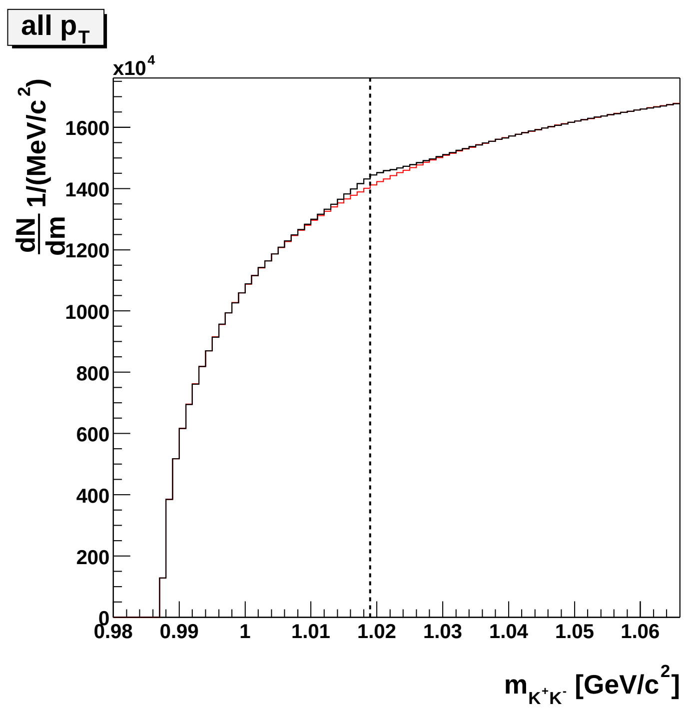

Figure 5.24: K^+K^- invariant mass distribution for the event sample III. The like-sign distribution is also shown.

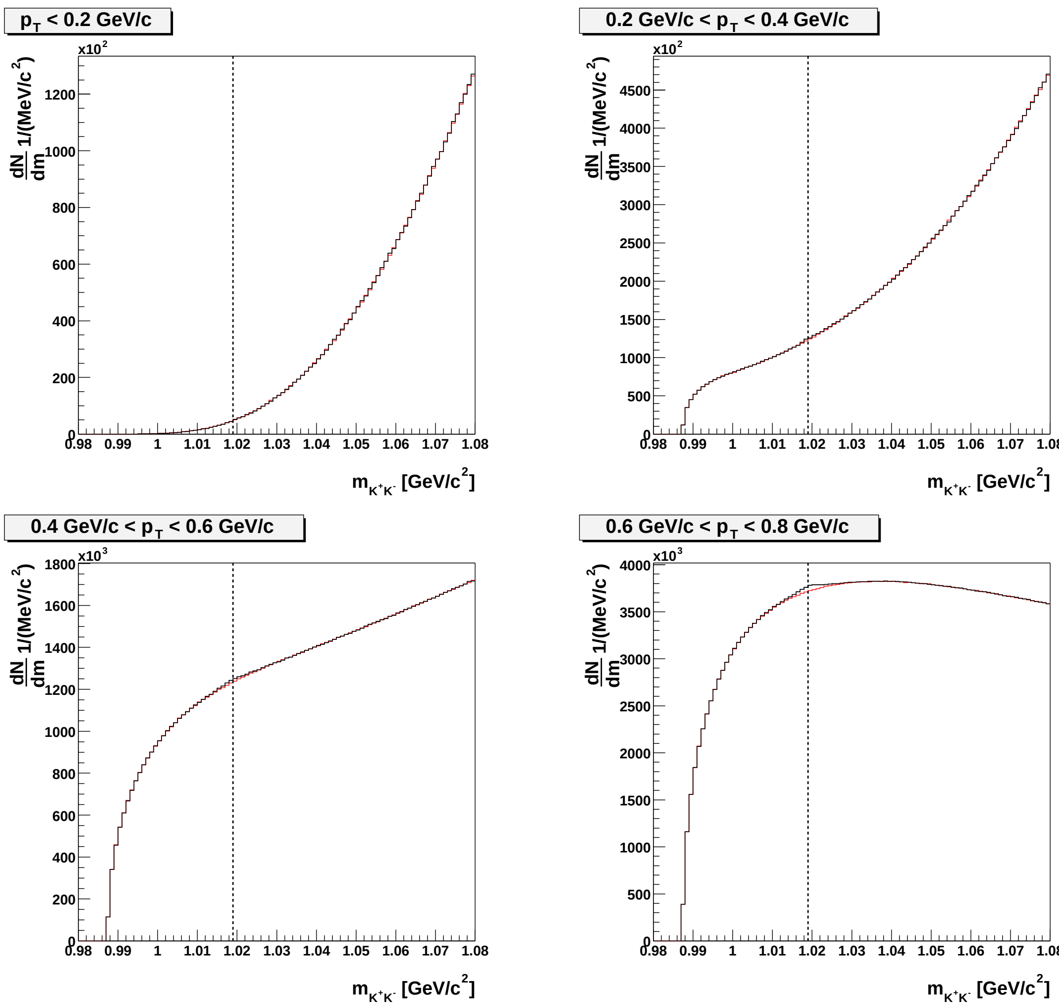

Figure 5.25: K^+K^- invariant mass distributions for the event sample III and for four p_T bins in the range $[0.;0.8] GeV/c$. The like-sign distributions are also shown.

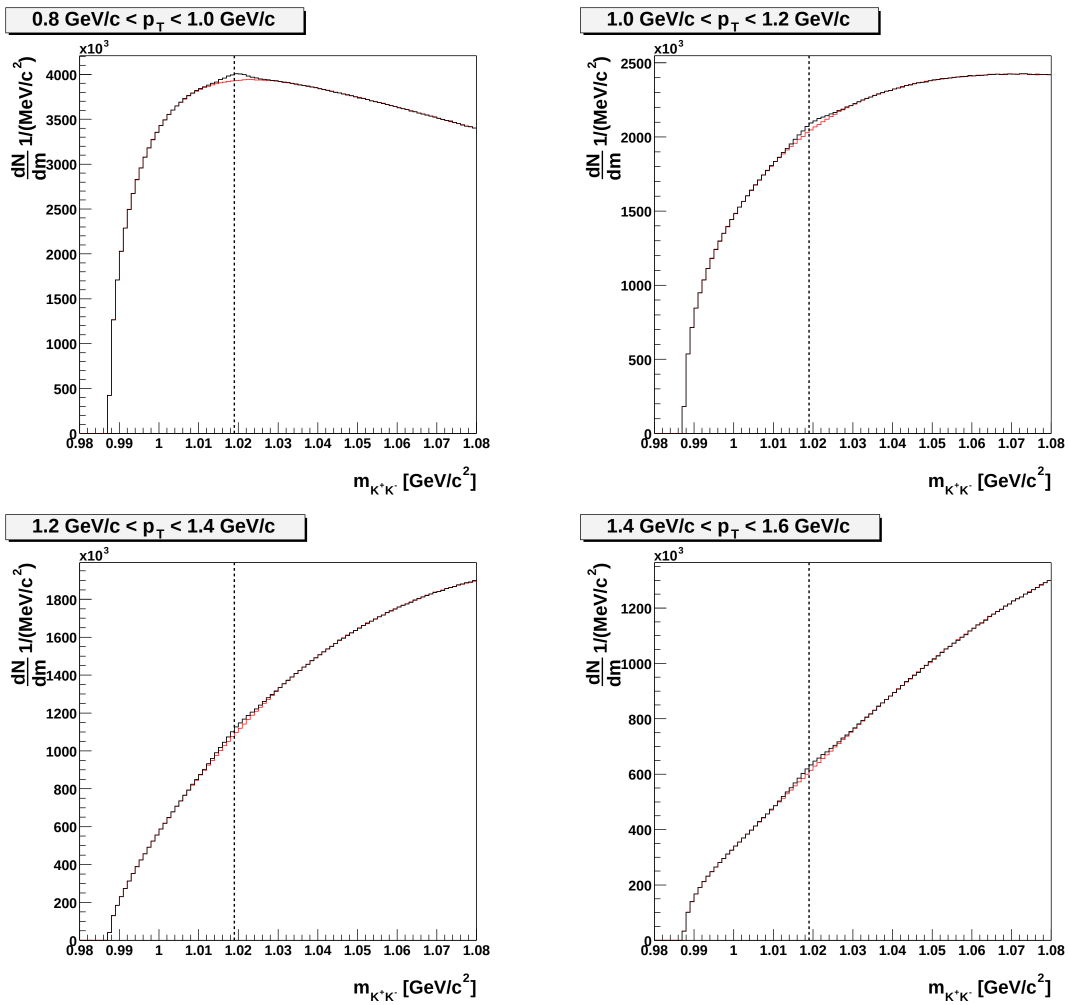

Figure 5.26: Same as fig. 5.25, for four p_T bins in the range $[0.8;1.6]\,GeV/c$.

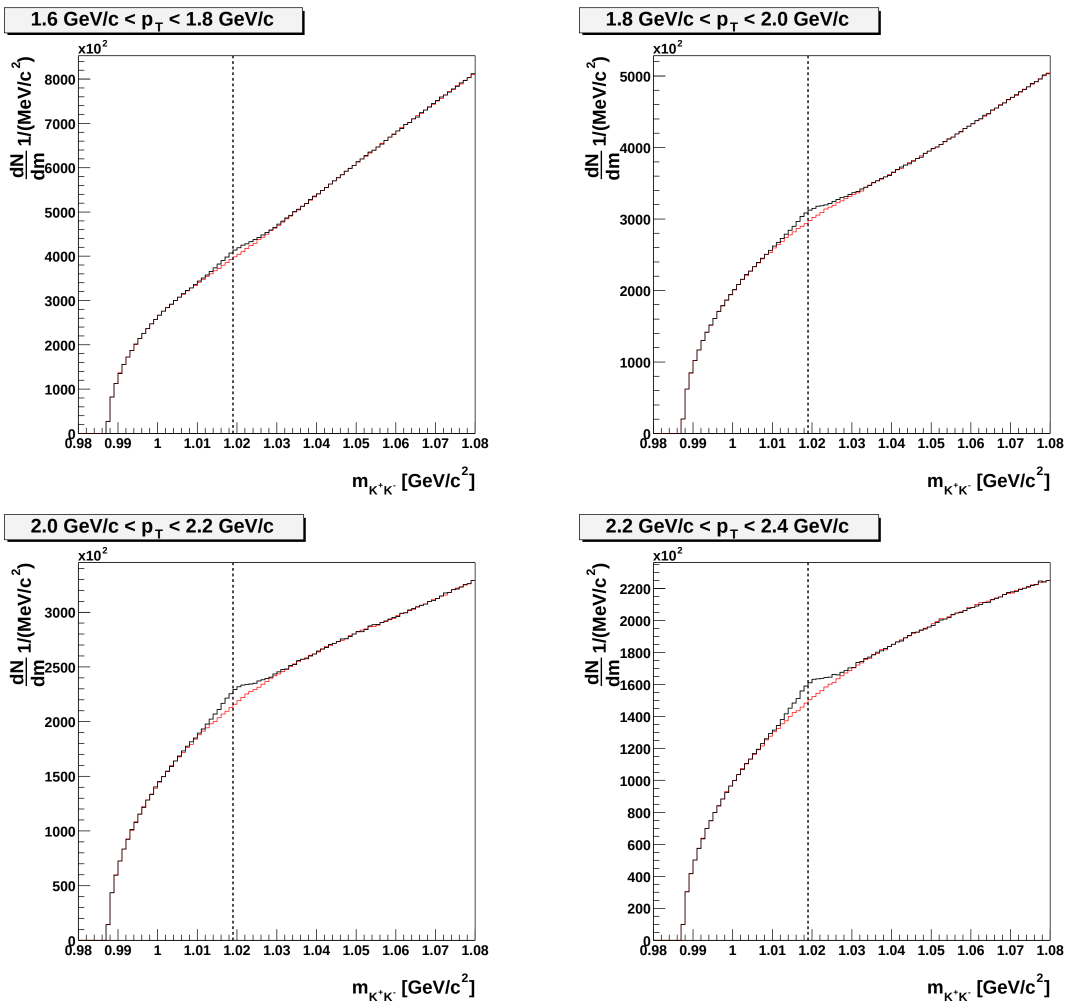

Figure 5.27: Same as fig. 5.25, for four p_T bins in the range $[1.6; 2.4]\, GeV/c$.

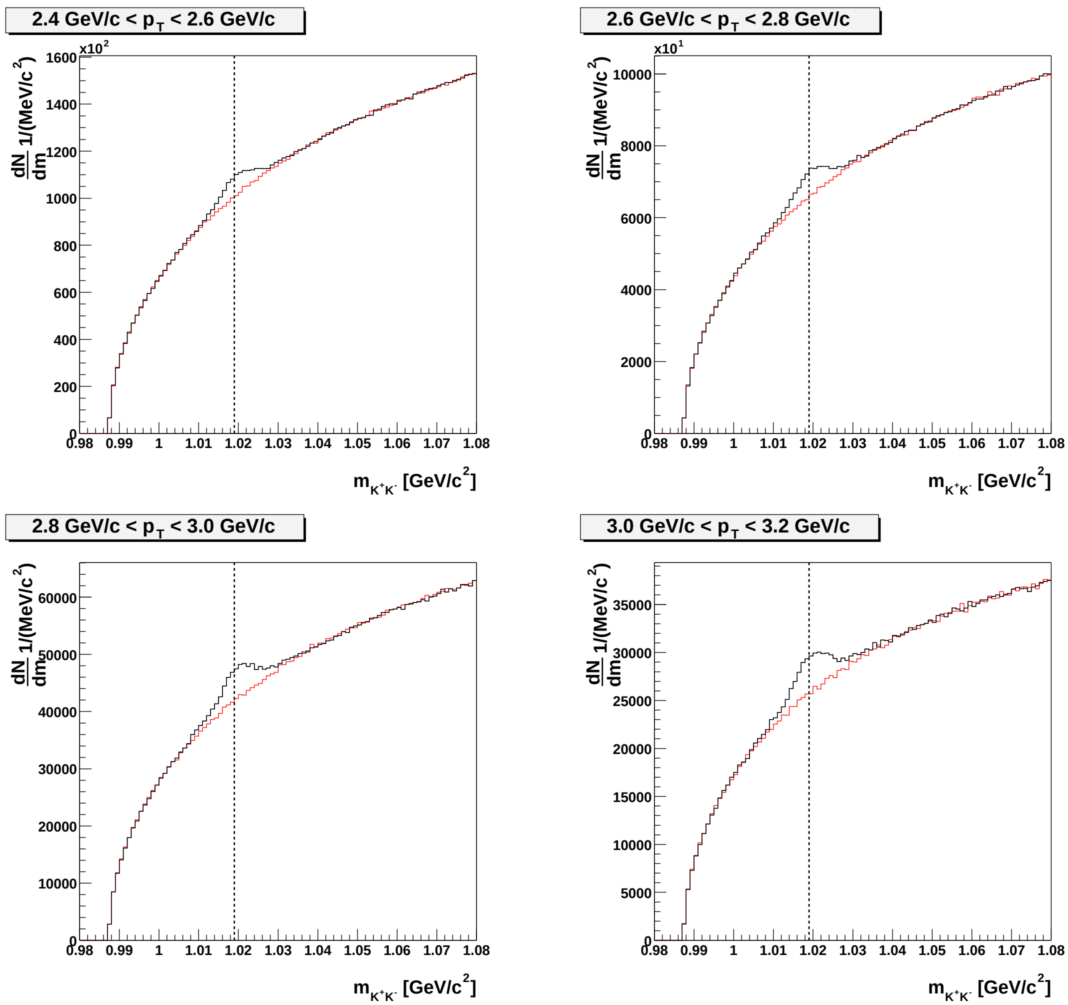

Figure 5.28: Same as fig. 5.25, for four p_T bins in the range $[2.4;3.2]\,GeV/c$.

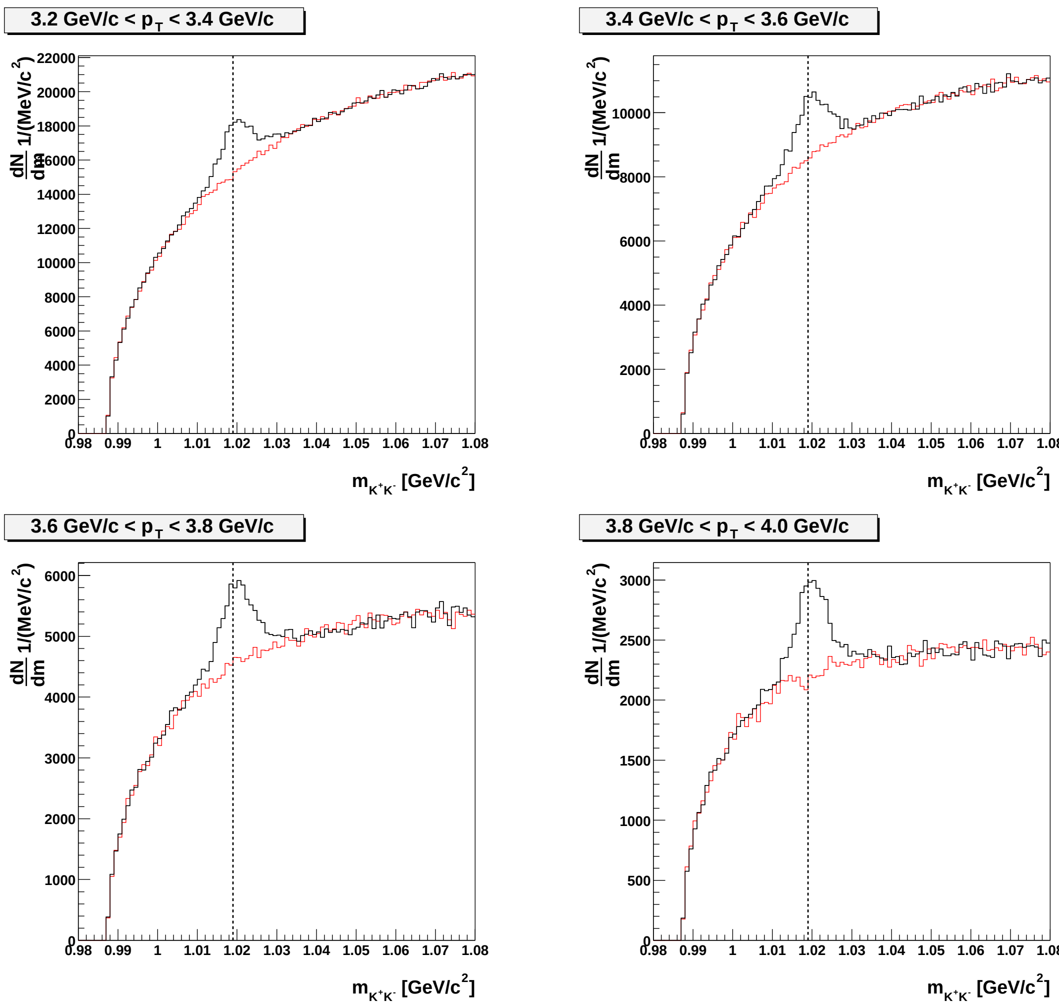

Figure 5.29: Same as fig. 5.25, for four p_T bins in the range $[3.2;4.0]\,GeV/c$.

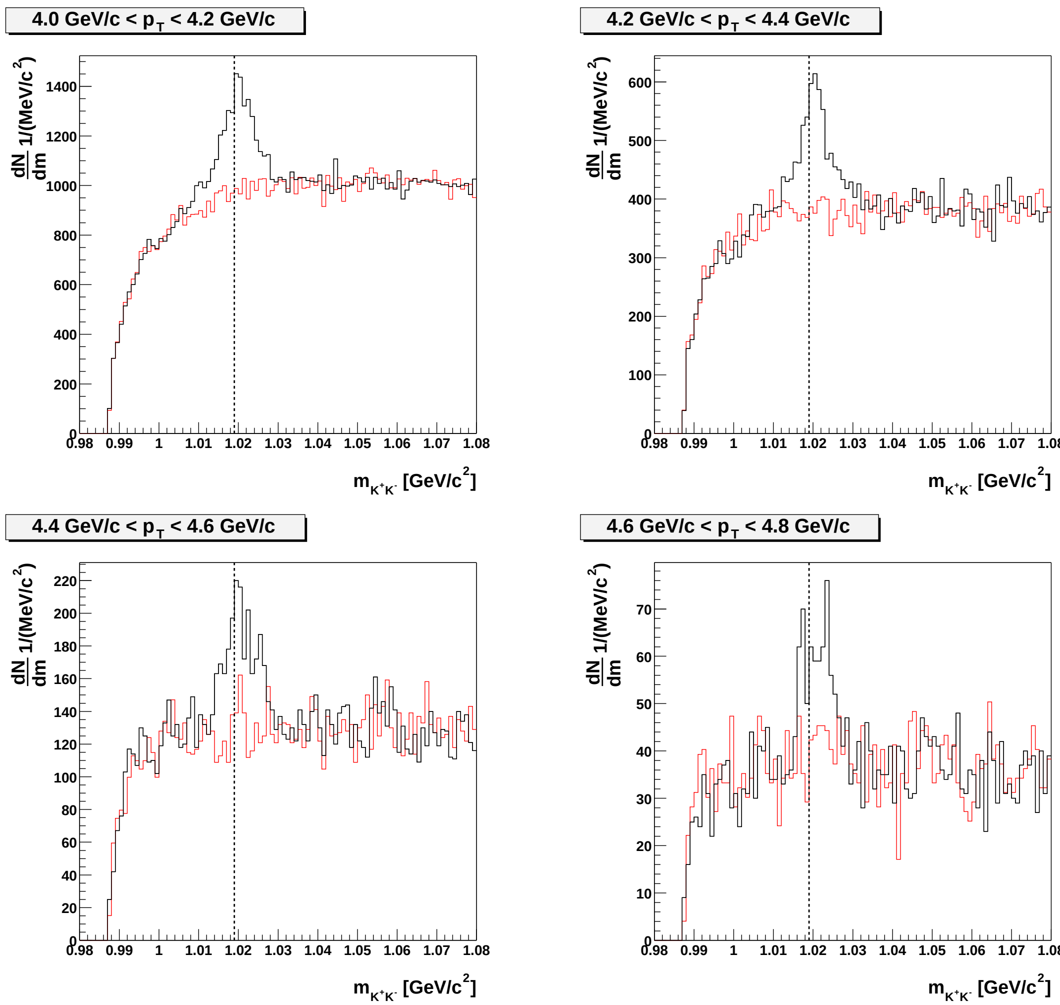

Figure 5.30: Same as fig. 5.25, for four p_T bins in the range $[4.0;4.8]\,GeV/c$.

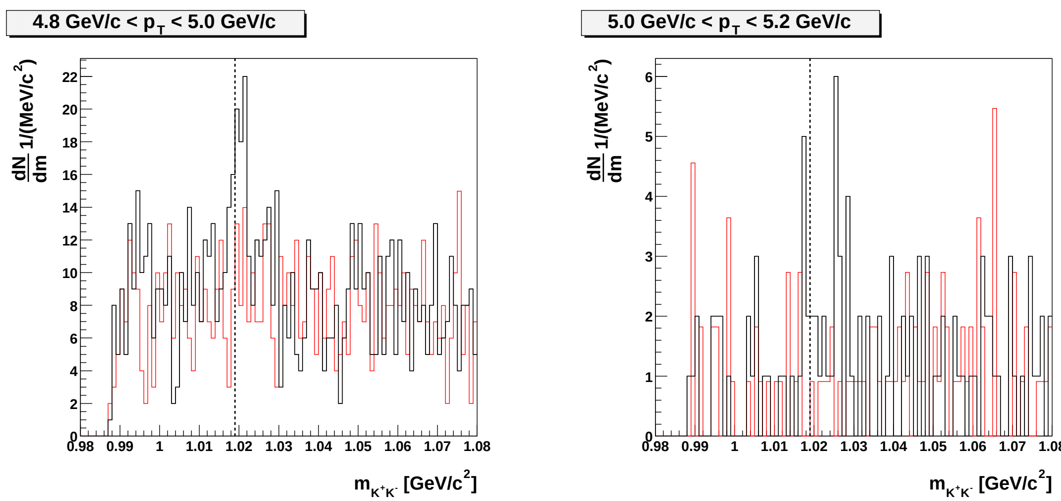

Figure 5.31: Same as fig. 5.25, for two p_T bins in the range $[4.8; 5.2]\,GeV/c$.

5.2.1 ϕ Signal Extraction

The ϕ spectrum was obtained by subtracting the like-sign distribution ($K^+K^+ + K^-K^-$) from the unlike-sign distribution (K^+K^-). Figures 5.32, 5.34 and 5.37 show the background-subtracted invariant mass distributions, respectively for the event samples I, II and III. The background-subtracted invariant mass distributions in different p_T bins are shown in figs. 5.33 (sample I), 5.35-5.36 (sample II) and 5.38-5.39 (sample III).

It is clear that the error bars drawn in the background-subtracted mass plots correspond to increased statistical fluctuations (by a $\sqrt{2}$ factor, approximately) with respect to those appearing in the original unlike-sign and like-sign mass histograms shown so far. For what concerns further alternatives in the K^+K^- background estimate, one possibility would be to perform a polynomial fit [78] to the like-sign distribution in each p_T bin and for each event sample. On the other hand, a more accurate K^+K^- background estimate could also be obtained by using an event-mixing technique [80].

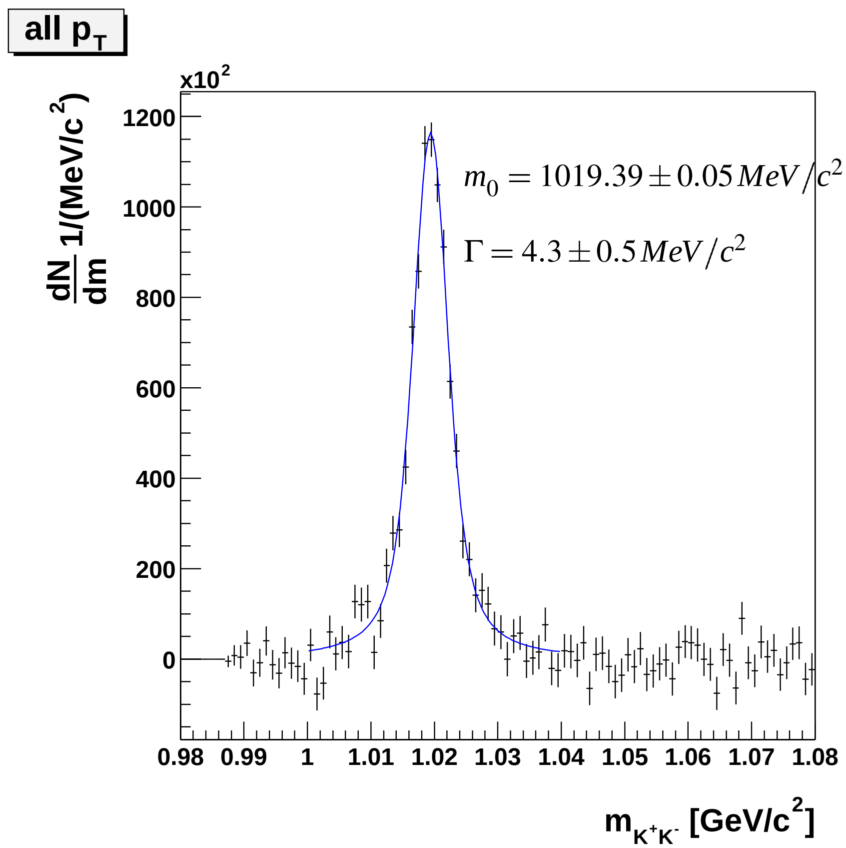

Figure 5.32: Background-subtracted K^+K^- invariant mass distribution for the event sample I. The solid line shows the fit result obtained with function 5.1.

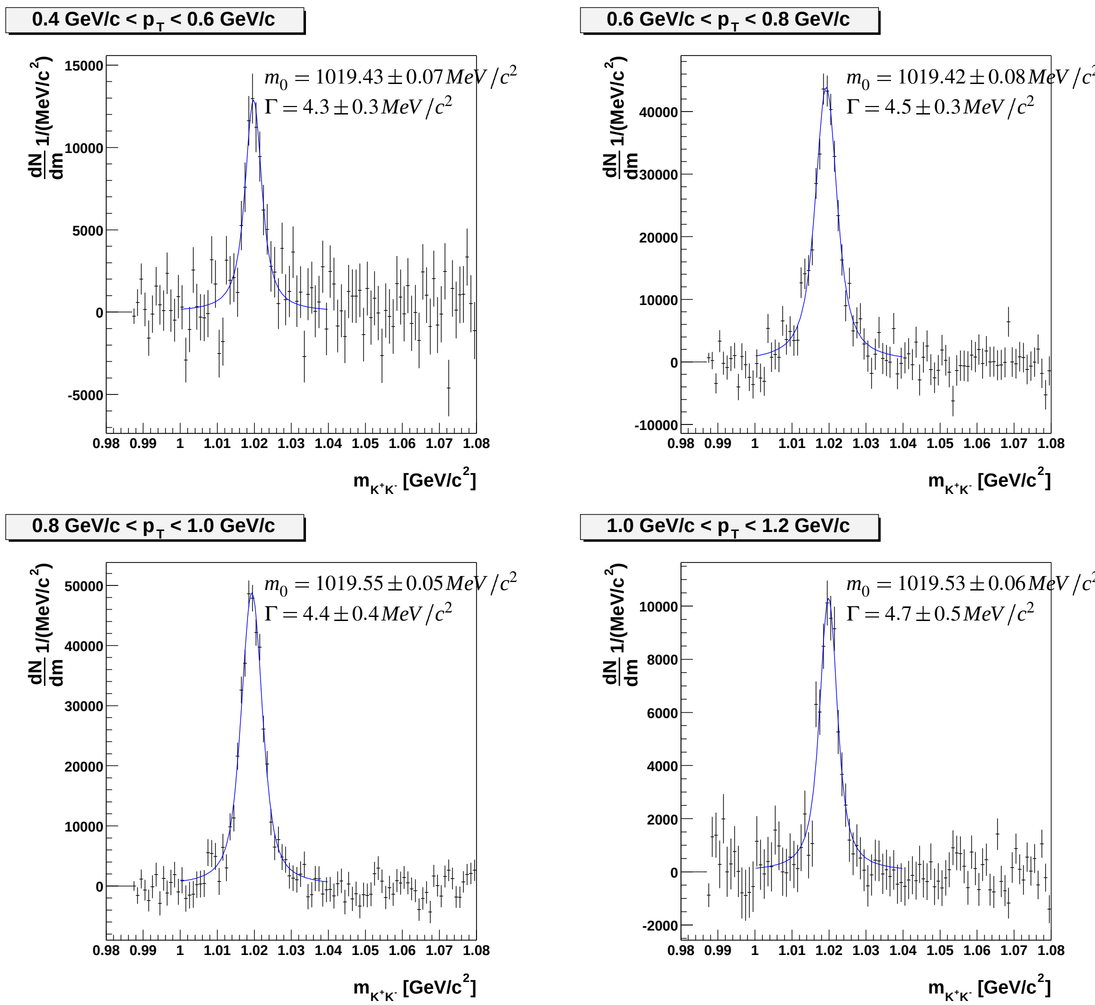

Figure 5.33: Background-subtracted K^+K^- invariant mass distributions for the event sample I and for four p_T bins in the range $[0.4;1.2]\,GeV/c$. The solid lines show the fit results obtained with function 5.1.

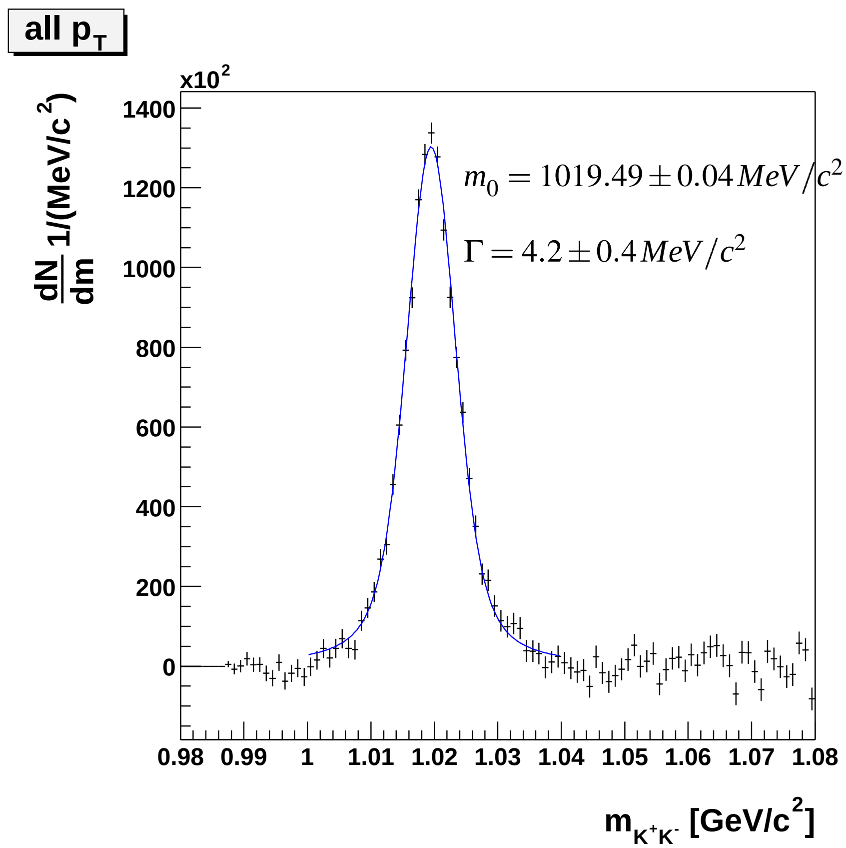

Figure 5.34: Background-subtracted K^+K^- invariant mass distribution for the event sample II. The solid line shows the fit result obtained with function 5.1.

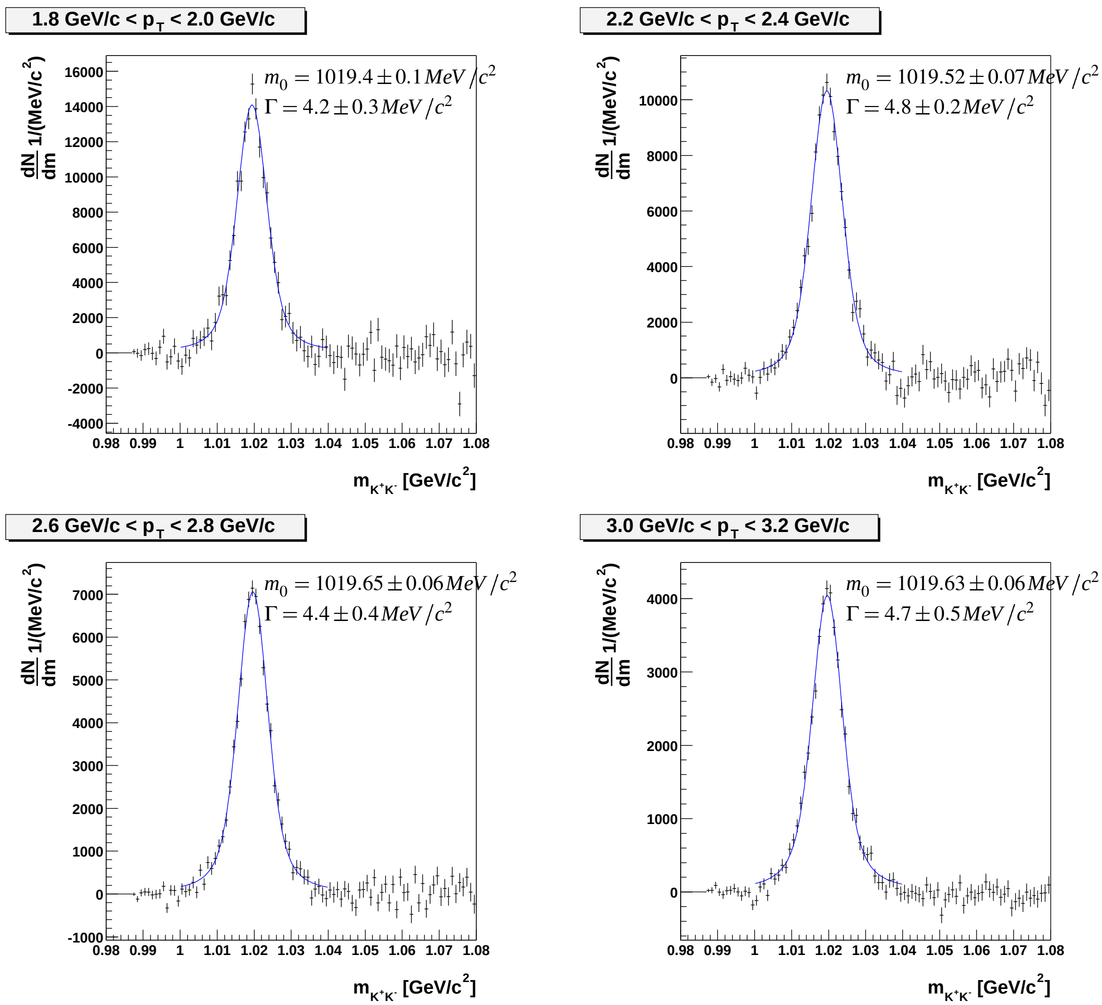

Figure 5.35: Background-subtracted K^+K^- invariant mass distributions for the event sample II and for four p_T bins as indicated in the plots. The solid lines show the fit results with function 5.1.

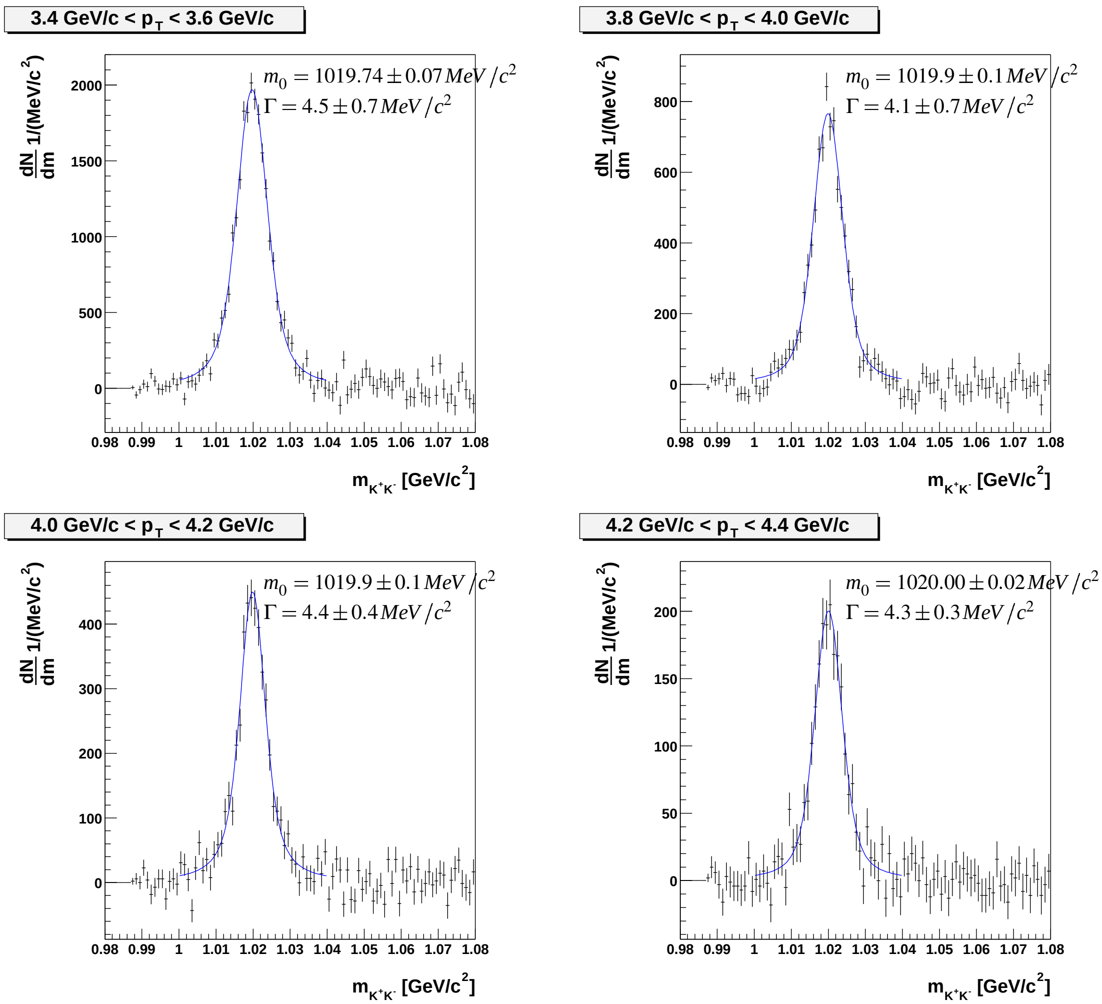

Figure 5.36: Same as fig. 5.35, for four p_T bins as indicated in the plots.

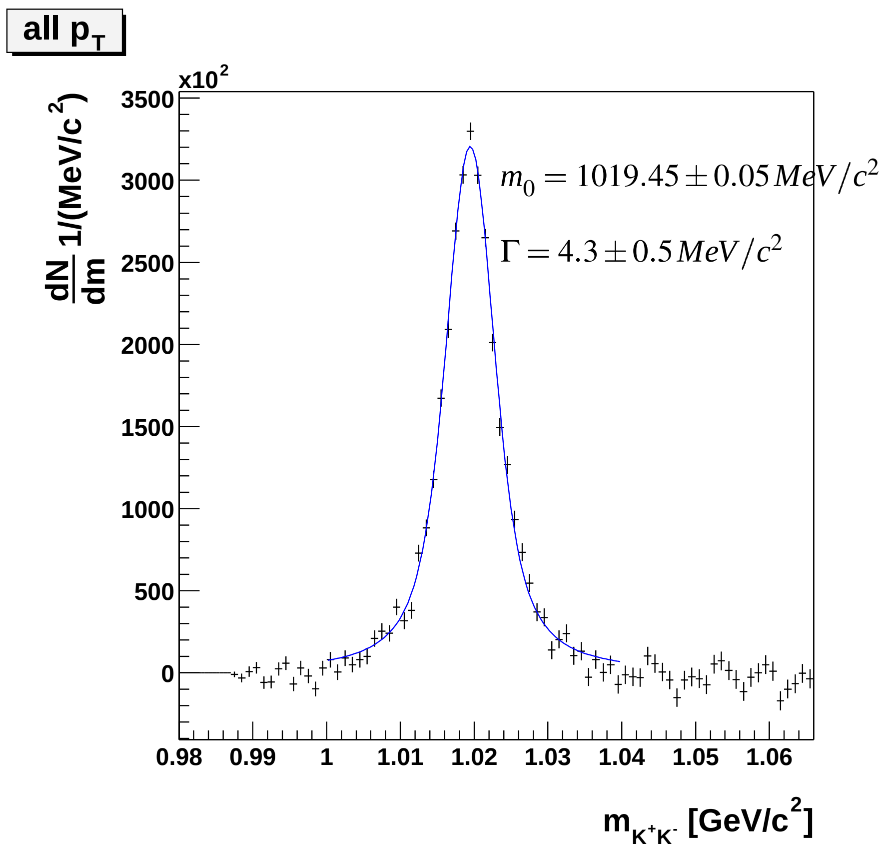

Figure 5.37: Background-subtracted K^+K^- invariant mass distribution for the event sample III. The solid line shows the fit results obtained with function 5.1.

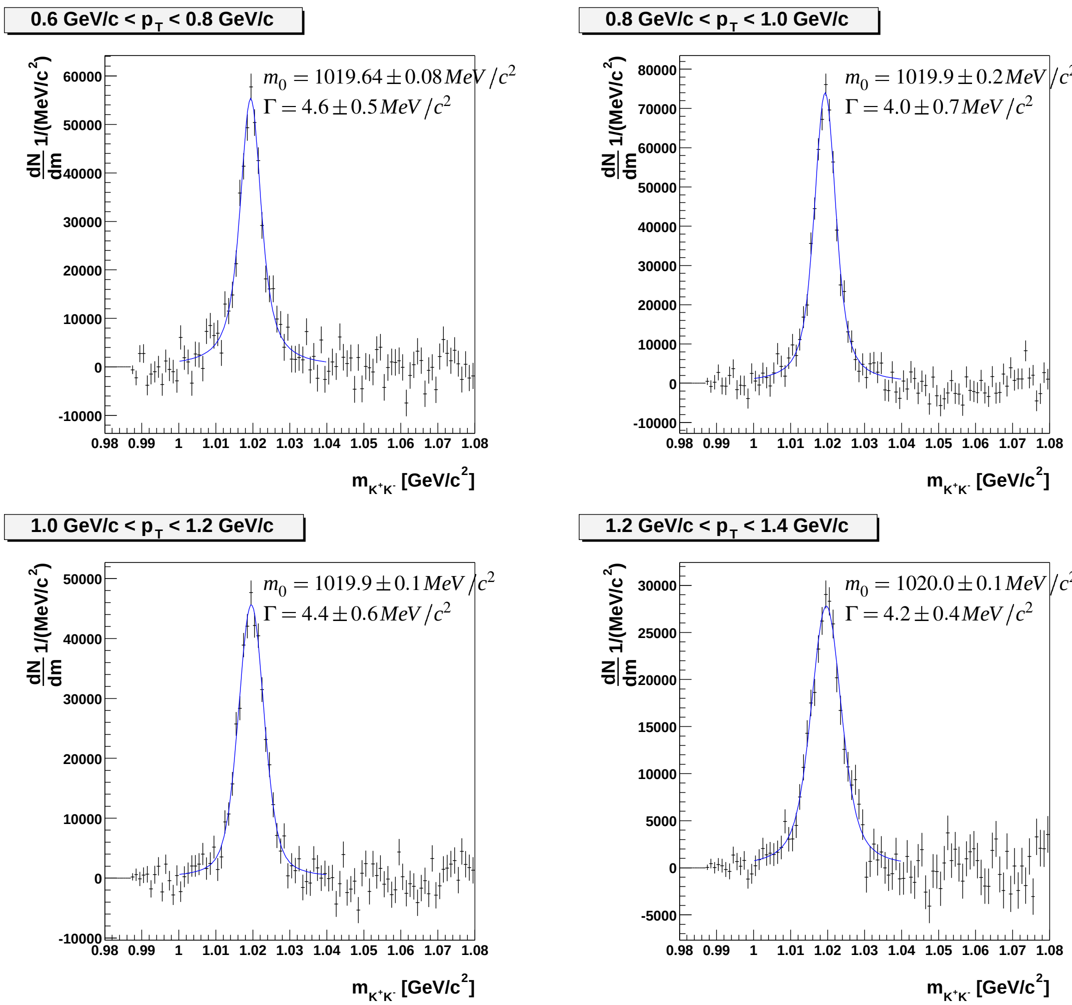

Figure 5.38: Background-subtracted K^+K^- invariant mass distribution for the event sample III and for four p_T bins in the range $[0.6; 1.4]\,GeV/c$. The solid lines show the fit results obtained with function 5.1.

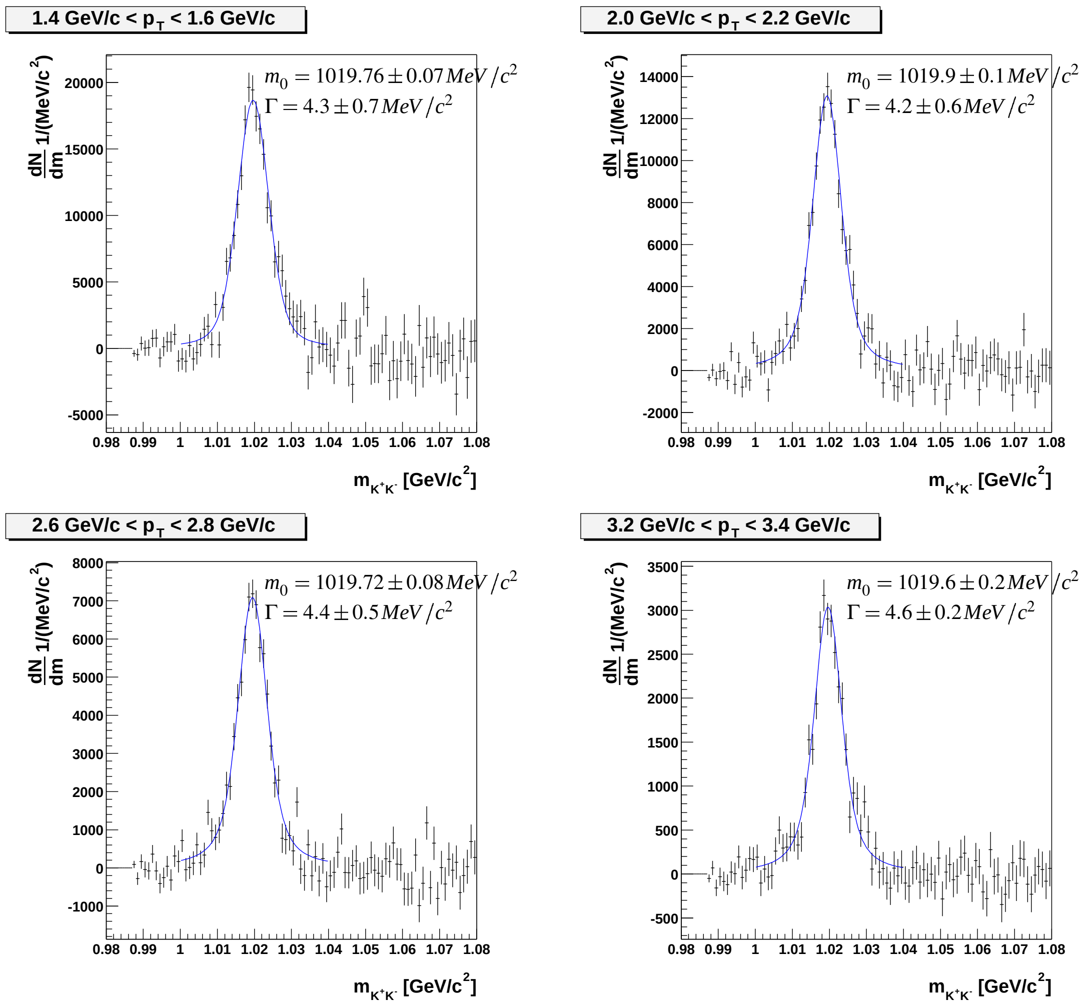

Figure 5.39: Same as fig. 5.38, for four p_T bins as indicated in plots.

5.2.2 Determination of the ϕ resonance parameters

Each of the background-subtracted invariant mass distribution fit was been performed using a Breit-Wigner function convoluted with a Gaussian function (to take into account the ALICE detector experimental mass resolution), plus a constant term (to take into account the residual background) [50, 45, 46, 47], according to the following expression:

$$\mathscr{A} \int_{M_1}^{M_2} \frac{1}{2\pi} \frac{\Gamma}{(m'-m_0)^2 + \frac{\Gamma^2}{4}} \quad \frac{1}{\sqrt{2\pi}\sigma} exp^{-\frac{(m-m')^2}{2\sigma^2}} dm' \quad + \quad \mathscr{B} \tag{5.1}$$

where: $M_1 = 1.00\,GeV/c^2$, $M_2 = 1.04\,GeV/c^2$, Γ and m_0 are the FWHM and the mean value of the Breit-Wigner resonance, σ is the standard deviation of the Gaussian distribution, $\mathscr{A}$ is the signal area, and $\mathscr{B}$ is the residual background level. Then, there are five free parameters. The curves shown in figs. 5.32-5.39 are the fit results. The ALICE detector experimental mass resolution values are consistent with those obtained by fitting the distributions of the difference between the ϕ reconstructed mass[6] and the nominal ϕ mass[7] to Gaussian functions [78, 79]: the σ values obtained range from $2.2\,MeV/c^2$ to $3.2\,MeV/c^2$ in the interval of ϕ transverse momentum considered in this study, i.e. $p_T < 5.0\,GeV/c^2$. The m_0 and Γ parameter values, as reported in the figs. 5.32-5.39, are consistent with the mass and natural width of the ϕ meson resonance (see §5.1 [8]), as reported in figs. 5.32-5.39.

Table 5.1 gives the significance values obtained in different p_T bins for the event samples I, II and III (figs. 5.15-5.16, figs. 5.18-5.23 and figs. 5.25-5.31), together with the overall significance in each of the three samples (figs. 5.14, 5.17 and 5.24). The significance $\mathscr{S}$ is defined as:

$$\mathscr{S} = \frac{S}{\sqrt{S+B}} \,,$$

where B is the background and S the signal estimated from the $K^{\pm}K^{\pm}$ (like-sign) and the K^+K^- (unlike-sign) invariant mass distributions. The signal S is obviously obtained by subtracting the like-sign distribution from the unlike-sign distribution. Signal and background pairs are counted in the mass window $|m_{K^+K^-} - m_0| < \Gamma/2$. Figure 5.40 shows the significance as a function of the K^+K^--pair transverse momentum p_T for all the event samples, I, II and III.

[6] Once the smearing procedure according to the momentum and angular resolutions has been applied to the K^+K^- decay pair.

[7] As given in the PDB [8].

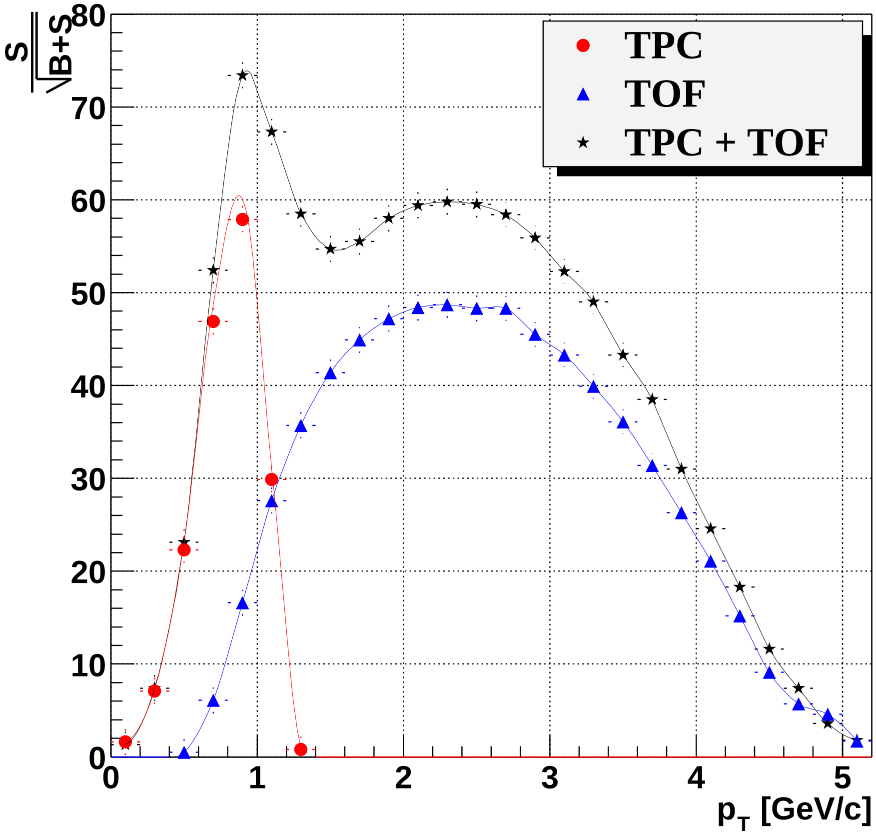

Figure 5.40: ϕ significance as a function of the transverse momentum of the K^+K^- decay pair for the event samples I, II and III. The solid lines are to guide the eye.

Table 5.1: Significance for the observation of a $\phi \to K^+K^-$ in the range $|m_{K^+K^-} - m_0| < \frac{\Gamma}{2}$ (see text), as a function of p_T in the event sample I, II and III. The overall significance values are reported in the first row of the table.

p_T range $[GeV/c]$	$\frac{S_I}{\sqrt{B_I+S_I}}$	$\frac{S_{II}}{\sqrt{B_{II}+S_{II}}}$	$\frac{S_{III}}{\sqrt{B_{III}+S_{III}}}$
all	84.3 ± 1.4	135.5 ± 1.4	174.2 ± 1.4
0.0 - 0.2	1.7 ± 1.4		1.3 ± 1.4
0.2 - 0.4	7.3 ± 1.4		7.4 ± 1.4
0.4 - 0.6	23.1 ± 1.4	0.5 ± 1.4	23.1 ± 1.4
0.6 - 0.8	48.7 ± 1.4	6.1 ± 1.4	52.4 ± 1.4
0.8 - 1.0	60.1 ± 1.4	16.6 ± 1.4	73.4 ± 1.4
1.0 - 1.2	31.0 ± 1.4	27.6 ± 1.4	67.3 ± 1.4
1.2 - 1.4	0.9 ± 1.4	35.7 ± 1.4	58.5 ± 1.4
1.4 - 1.6		41.4 ± 1.4	54.7 ± 1.4
1.6 - 1.8		44.9 ± 1.4	55.5 ± 1.4
1.8 - 2.0		47.2 ± 1.4	58.0 ± 1.4
2.0 - 2.2		48.4 ± 1.4	59.4 ± 1.4
2.2 - 2.4		48.7 ± 1.4	59.8 ± 1.4
2.4 - 2.6		48.3 ± 1.4	59.5 ± 1.4
2.6 - 2.8		48.3 ± 1.3	58.4 ± 1.3
2.8 - 3.0		45.5 ± 1.3	55.9 ± 1.3
3.0 - 3.2		43.3 ± 1.3	52.3 ± 1.3
3.2 - 3.4		39.9 ± 1.3	49.0 ± 1.3
3.4 - 3.6		36.1 ± 1.3	43.3 ± 1.3
3.6 - 3.8		31.4 ± 1.3	38.5 ± 1.2
3.8 - 4.0		26.3 ± 1.2	31.0 ± 1.2
4.0 - 4.2		21.1 ± 1.2	24.6 ± 1.2
4.2 - 4.4		15.2 ± 1.2	18.3 ± 1.2
4.4 - 4.6		9.1 ± 1.2	11.6 ± 1.1
4.6 - 4.8		5.7 ± 1.1	7.4 ± 1.1
4.8 - 5.0		4.6 ± 1.0	3.6 ± 1.0
5.0 - 5.2		1.7 ± 1.0	1.8 ± 0.8

5.3 Discussion

By comparing the results obtained when analysing the event samples I, II and III, i.e. using, respectively, only the ALICE-TPC, only the ALICE-TOF and both the ALICE-TPC and ALICE-TOF as particle identification detectors, one can conclude that the Time-Of-Flight detector increases by a factor of three the p_T range for ϕ identification: for p_T values greater than $1.5\,GeV/c$, the ϕ mesons are mostly identified by the TOF (see table 5.1 and fig. 5.40).

The increase of the acceptance in the ϕ transverse momentum, which reflects in an extended range for the m_T measurement, will also allow for a more precise determination of the ϕ inverse slope parameter (T_ϕ). This can be derived from the invariant transverse mass distribution which is expected to be:

$$\frac{1}{2\pi m_T}\frac{d^2N}{dm_T dy} \propto exp\left[-\frac{m_T - m_\phi}{T_\phi}\right].$$

Moreover, when comparing the overall significances of samples I and III, it clearly appears that the ϕ detection power is largely enhanced, namely more than doubled, when the TOF is added to the TPC to perform *kaon* identification.

The $\phi \to K^+K^-$ simulation presented herein is indeed a significant example of what the detection potential of the ALICE experiment will be thanks to the TOF.

Conclusion

A detailed Monte Carlo simulation study has been performed concerning the observation of the $\phi \rightarrow K^+K^-$ resonance in $Pb-Pb$ final states at LHC with the ALICE detector. The key role of the ALICE TOF detector in terms of the ϕ-meson signal $significance$ and of the ϕ-meson p_T and m_T ranges of observation has been cleary demonstrated.

Bibliography

[1] Deep Inalastic Scattering - DIS 2001, Proceedings of the 9th International Workshop, Bologna, Italy 27 Apr - 1 May 2001.

[2] E. Kolb, M. S. Turner, The Early Universe, Addison-Wesley, Redwood City, 1990.

[3] J. C. Collins and M. J. Perry, Superdense Matter: Neutrons and Asymptotically Free Quarks?, *Phys. Rev. Lett.* 34 (1975) 1353.

[4] J. Schukraft, Heavy Ion at the LHC: Physics Perspectives and Experimental Program, Invited talks given at the Quark Matter 2001 Conference, Stony Brook, USA, Januany 2001.

[5] B. Alessandro *et al*, ALICE Physics Theoretical Overview, ALICE Internal Note *ALICE-INT-2002-025*.

[6] F. Karsch *et al.*, *Phys. Lett.* B478 (2000) 447.

[7] T. Matsui and H. Satz, J/Ψ Suppression by Quark-Gluon Plasma Formation, *Phys. Lett.* B178 (1986) 416.

[8] K. Hagiwara *et al.* (Particle Data Group), Particle Physics Booklet, *Phys. Rev.* D 66, 010001 (2002) and 2003 partial update for edition 2004 (URL: http://pdg.lbl.gov/).

[9] J. Rafelski, Formation and Observables of the Quark - Gluon Plasma, *Phys. Rep.* 88 (1982) 331;

B. Müller and J. Rafelski, Strangeness Production in the Quark-Gluon Plasma, *Phys. Rev. Lett.* 48 (1982) 1066, and *Erratum Phys. Rev. Lett.* 56 (1986) 2234.

[10] J. Rafelski, Strangeness Production in the Quark Gluon Plasma, *Nucl. Phys.* A418 (1984) 215c.

[11] P. Kock, B. Müller and J. Rafelski, Strangeness in Relativistic Heavy Ion Collisions, *Phys. Rep.* 142 (1986) 167.

[12] S. Okubo, ϕ Meson and Unitary Symmetry Model, *Phys. Rev. Lett.* 5 (1963) 165;

G. Zweig, K. Okada, O. Shito, An SU(3) Model for Strong Interaction Symmetry and ITS Breaking. 2, CERN-TH-412, NP-14146 (74pp), Feb 1964;

J. Iizuka, Systematics and Phenomenology of Boson Mass Levels. 3, *Prog. Theor. Phys.* 35 (1966) 1061.

[13] A. Shor, ϕ Meson Production as a Probe of the Quark-Gluon Plasma, *Phys. Rev. Lett.* 54 (1985) 1122;

M. Berenguer, H. Sorge and W. Greiner, ϕ Meson Production in Ultra-Relativistic Heavy Ion Collisions, *Phys. Lett.* B332 (1994) 15.

[14] A. J. Baltz and C. Dover, Quark Model of ϕ Coalescence Kaons in Heavy Ion Reactions, *Phys. Rev.* C53 (1996) 362.

[15] V. Koch, Aspects of Chiral Symmetry *Int. J. Mod. Phys.* E6 (1997) 203;

F. Karsch, The Phase Transition to the Quark Gluon Plasma: Recent Results from Lattice Calculations, *Nucl. Phys.* A590 (1995) 367c.

[16] D. Lissauer, E. V. Shuryak, K Meson Modification in Hot Hadronic Matter may be Detected via ϕ Meson Decays, *Phys. Lett.* B253 (1991) 15.

[17] ALICE-TOF group (Bologna-CERN-Salerno-ITEP), Study of QGP signatures on $\phi \to K^+K^-$ signal in ALICE $Pb-Pb$ events, *in preparation*.

[18] NA45/CERES Coll., *Nucl. Phys.* A553 (1993) 857c.

[19] NA38 Coll., *Phys. Lett.* B220 (1989) 471.

[20] NA10 Coll., *Nucl. Inst. Methods* A223 (1984) 26.

[21] NA50 Coll., *Phys. Lett.* B410 (1997) 327.

[22] NA60 Coll., *Proposal*, CERN/SPSC2000-010, SPS/P316, March 2000.

[23] NA38/NA50 Coll., Enhancement of Intermediate Mass Dimuons in Nucleus Nucleus Collisions at the CERN SPS,*Nucl. Phys.* A698 (2002) 539;

NA38/NA50 Coll., Dimuon Enhancement in Nucleus Nucleus Ultrarelativistic Interactions, *Nucl. Phys.* A661 (1999) 538.

[24] WA85 Coll., *Proposal* CERN/SPSC84-76, SPS/P206 (1984), and CERN/SPSC87-18, SPS/P206 Add. I (1987).

[25] WA94 Coll., *Proposal*, CERN/SPSLC/91-5 P257 (1991).

[26] WA97 Coll., *Nucl. Phys.* A590 (1995) 139c;

NA57 Coll., *J. Phys. G* 25 (1999) 473.

[27] WA97 Coll., Strangeness Enhancement at Mid-rapidity in *Pb Pb* Collisions at $158 - A - Gev/c$, *Phys. Lett.* B449 (1999) 401.

[28] NA49 Coll., The NA49 Large Acceptance Hadron Detector, *Nucl. Instrum. Meth.* A430 (1999) 210.

[29] NA49 Coll., *Phys.Rev.* C66 (2002) 054902;

NA49 Coll., *Phys.Rev.Lett.*86 (2001) 1965;

[30] E802 Coll., *Phys. Rev.* C 57 (1998) R466;

E866 Coll., *Nucl. Phys.* A610 (1996) 139c .

[31] E802/E866 Coll., Simultaneous Multiplicity and Forward Energy Characterization of Particle Spectra in $Au+Au$ Collisions at $11.6 AGeV/c$, *Phys. Rev.* C59 (1999) 2173.

[32] PHENIX Coll., Results on Identified Charged Hadrons from the PHENIX Experiment at RHIC, *Nucl. Phys.* A721 (2003) 273c;

PHENIX Coll., Identified Charged Particle Spectra and Yields in $Au+Au$ Collisions at $\sqrt{s_{NN}} = 200\,GeV$, *nucl-ex/0307022*, 28 Jun 2003.

[33] http://www.brahms.bnl.gov;

BRAHMS Coll., *Nucl. Phys.* A566 (1994) 299c.

[34] http://www.phenix.bnl.gov;

PHENIX Coll., *Nucl. Phys.* A638 (1998) 565c.

[35] http://www.phobos.bnl.gov;

PHOBOS Coll., *Acta Physica Polonica* B27 (1996) 3103.

[36] http://www.star.bnl.gov/

STAR Coll., *Nucl. Phys.* A566 (1994) 277c.

[37] http://www.phy.duke.edu/SQM2003.

[38] PHENIX Coll., *arXiv:nucl-ex/0210021*, 22 Oct 2002;

STAR Coll., *arXiv:nucl-ex/0206006*, 25 Jan 2003;

PHENIX Coll., *arXiv:nucl-ex/0306021*, 5 Jul 2003;

STAR Coll., *arXiv:nucl-ex/0306024*, 18 Aug 2003.

[39] NA49 Coll., Production of ϕ mesons in $p+p$, $p+Pb$ and central $Pb-Pb$ collisions at $E_{beam} = 158\,AGeV$, *Phys. Lett.* B491 (2000) 59;

NA49 Coll., ϕ production in $158\,GeV/u$ $Pb+Pb$ collisions, *J. Phys. G* 23 (1997) 1837.

[40] NA50 Coll., The production of ϕ, ω and ρ mesons in $p-$, $d-$, $S-$ and $Pb-$induced reactions at the CERN SPS, *J. Phys. G* 30 (2004) S277;

NA50 Coll., ϕ and $\rho+\omega$ vestor-mesons produced in lead-induced collisions, *J. Phys. G* 28 (2002) 1809.

[41] E917 Coll., A Single Arm Spectromrter Detector System for High-Energy Heavy Ion Experiments, *Nucl. Instrum. Meth.* A290 (1999) 41.

[42] E917 Coll., Production of ϕ mesons in $Au-Au$ collisions at the AGS, *Nucl. Instrum. Meth.* A661 (1999) 506.

[43] Sven Soff, D. Zschiesche, M. Bleicher, C. Hartnack, M. Belkacem, L. Bravina, E. Zabrodin, S. A. Bass, H. Stöcker, W. Greiner, Enhanced of Strange Particle Yields - Signal of a Phase of Massless Particles?, *nucl-th/0010103*, 31 Oct 2000.

[44] S. C. Jonhson, B. V. Jacak, A. Dress, Rescattering of vector meson daughters in high energy heavy ion collisions, *Eur. Phys. J.* C18 (2001) 645.

[45] STAR Coll., Midrapidity *phi* production in $Au + Au$ collisions at $\sqrt{s_{NN}} = 130\,GeV$, *Phys. Rev.* C65 (2002) 041901(R).

[46] Jingguo Ma for the STAR Collaboration, Mid-rapidity ϕ meson production at $\sqrt{s_{NN}} = 200\,GeV$ $Au - Au$ and $p - p$ collisions from STAR, Proc. 19th Winteer Workshop on Nuclear Dynamics (2003), Breckenridge, Colorado, USA, February 8-15 2003; *nucl-ex/0306013*, 10 June 2003.

[47] Jingguo Ma (STAR Collaboration), *private comunication*, "Below are our latest numbers for $200\,GeV$ $AuAu$ collisions:
$0 - \ 5\%$ $\quad 363\,(8)$
$0 - 10\%$ $\quad 357\,(14)$
$10 - 30\%$ $\quad 353\,(8)$
$30 - 50\%$ $\quad 383\,(10)$
$50 - 80\%$ $\quad 344\,(9)$
The systematic errors on the T is 10% for all the centrality bins. It's hard to say whether these numbers are different from the $130\,GeV$ data [46]. They are consistent with each other within error bars", 30 October 2003.

[48] PHENIX Coll., ϕ meson production in $Au - Au$ collisions at $\sqrt{s_{NN}} = 200\,GeV$, *nucl-ex/02090028*, 28 Sep 2002;

ϕ meson production in $Au - Au$ collisions at $\sqrt{s_{NN}} = 200\,GeV$, *J.Phys.G* 30 (2004) S571-S576.

[49] A. Mischke for the NA49 Coll., Strangeness Production in Heavy Ion Collisions at SPS Energies, *hep-ex/0311010*, 5 Nov 2003.

[50] E802 Coll., Production of ϕ Mesons in Central $^{28}Si + {}^{196}Au$ Collisions at $14.6\,A\,GeV/c$, *Phys. Rev. Lett.* 76 (1996) 2021;

E917 Coll., Production of ϕ Mesons in $Au + Au$ Collisions at $11.7\,A\,GeV/c$, *nucl-ex/0304017*, 23 Apr 2003.

[51] ALICE Coll., Technical Proposal for A Large Ion Collider Experiment at the LHC, CERN/LHCC/95-71, LHCC/P3, 15 December 1995.

[52] ALICE Coll., Technical Design Reports of the ITS, CERN/LHCC 99-12, ALICE TDR 4, 18 June 1999.

[53] ALICE Coll., Technical Design Reports of the TPC, CERN/LHCC 2000-001, ALICE TDR 7, 7 January 2000;

ALICE Coll., Addendum to ALICE TDR 7, CERN/LHCC 2002-016, 24 April 2002.

[54] ALICE Coll., Technical Design Reports of the TRD, CERN/LHCC 2001-021, ALICE TDR 9, 3 October 2001.

[55] ALICE Coll., Technical Design Reports of the TOF CERN/LHCC 2000-12, ALICE TDR 8, 16 February 2000.

[56] ALICE Coll., Answers to the Questions of the LHCC Referees, CERN/ALICE, 5 May 2000.

[57] ALICE Coll., Addendum to ALICE TDR 8, CERN/LHCC 2002-016, 24 April 2002.

[58] ALICE TOF Group (Bologna-CERN-ITEP-Salerno), Algorithms and Methods for Particle Identification with the ALICE TOF Detector at Very High Particle Multiplicity, Submitted to *Eur. Phys. J.* 04 August 2003,
Published online: 13 October 2003,
ISSN: 1434-6044 (Paper) 1434-6052 (Online),
DOI: 10.1140/epjcd/s2003-01-0013-5.

[59] R. Santonico, R. Cardarelli, Development of Resistive Plate Counters, *Nucl. Instrum. Meth.* A377 (1981) 187;

R. Cardarelli, R. Santonico, Progress in Resistive Plate Chambers, *Nucl. Instrum. Meth.* A263 (1988) 200.

[60] I. Crotty, E. Cerron Zeballos, J. Lamas Valverde, D. Hatzifotiadou, M.C.S. Williams and A. Zichichi, The Wide Gap Resistive Plate Chamber, *Nucl. Instrum. Meth.* A360 (1995) 512;

E. Cerron Zeballos, I. Crotty, D. Hatzifotiadou, J. Lamas Valverde, S. Neupane, V. Peskov, S. Singh, M.C.S. Williams and A. Zichichi, A comparison of the Wide Gap and Narrow Gap Resistive Plate Chamber, *Nucl. Instrum. Meth.* A373 (1996) 35.

[61] E. Cerron Zeballos, I. Crotty, D. Hatzifotiadou, J. Lamas Valverde, M.C.S. Williams and A. Zichichi, The Multigap Resistive Plate Chamber, SLAC-PUB-7175B, Mar 1996

[62] E. Cerron Zeballos, I. Crotty, D. Hatzifotiadou, J. Lamas Valverde, R.J. Veenhof, M.C.S. Williams and A. Zichichi, Avalanche Fluctuations Within the Multigap Resistive Plate Chamber, *Nucl. Instrum. Meth.* A381 (1996) 569.

[63] E. Cerron Zeballos, I. Crotty, D. Hatzifotiadou, J. Lamas Valverde, M.C.S. Williams and A. Zichichi, Streamer Free Operation of a 2 mm Gap Resistive Plate Chamber with C_2F_5H, CERN/LAA-MC 97-06;

E. Cerron Zeballos, D. Hatzifotiadou,D.W. Kim, S.C. Lee, J. Lamas Valverde, E. Platner, J. Roberts, M.C.S. Williams and A. Zichichi, Effect of adding SF_6 to the gas mixture in a MultiGap Resistive Plate Chamber, *Nucl. Instrum. Meth.* A419 (1998) 475.

[64] Degree Thesis in Physics, A. De Caro, Alcuni Studi di R&D nell'Ambito del Progetto ELN, (in italian) tutors:L. Cifarelli and L. Maritato, Università degli Studi di Salerno, 2 December 1999.

[65] A. Akindinov *et al.*, A Study of the Multigap RPC at the Gamma Irradiation Facility at CERN, *Nucl. Inst. Meth.* A490 (2002) 58.

[66] http://aliweb.cern.ch/offline

[67] http://root.cern.ch

[68] http://wwwasdoc.web.cern.ch/wwwasdoc/geant_html3/geantall.html

[69] F. Antinori, ALICE Internal Note, *ALICE-INT-1993-09*.

[70] X.N. Wang and M. Gyulassy, *Phys. Rev.* D44 (1991) 3501;

X.N. Wang and M. Gyulassy, *Phys. Rev.* D45 (1992) 844;

X.N. Wang and M. Gyulassy, *Comp. Phys. Commun.* 83 (1994) 307.

[71] T. Jöstrand, *Com. Phys. Commun.* 39 (1986) 347.

[72] T. Alexopoulos *et al.*, *Phys. Rev. Lett.* 64 (1990) 991.

[73] M. Bourquin and J.M. Gaillard, *Nucl. Phys.* B114 (1976) 334.

[74] B. Batyunya, Yu. Belikov, K. Safarik, ALICE Internal Note, *ALICE-INT-1997-24*.

[75] F. Pierella, Study of the ALICE TOF detector performances and charm detection in Pb-Pb interactions at LHC, PhD thesis, Bologna 2003.

[76] http://sroesler.home.cern.ch/sroesler/dpmjet3.html;

A. Capella, U. Sukhatme, C-I Tan and J. Tran Thanh Van, *Phys. Rept.* 236 (1994) 225;

R. Engel, J. Ranft and S. Roesler, *Phys. Rev.* D55 (1997) 6957;

S. Roesler, R. Engel and J. Ranft, *Phys. Rev.* D57 (1998) 2889;

A. Ferrari, P.R. Sala, J. Ranft and S. Roesler, *Z. Phys.* C70 (1996) 413;

A. Ferrari, P.R. Sala, J. Ranft and S. Roesler, *Z. Phys.* C71 (1996) 75;

R. Engel, *Z. Phys.* C66 (1995) 203;

R. Engel, J. Ranft and S. Roesler, *Phys. Rev.* D52 (1995) 1459;

R. Engel and J. Ranft, *Phys. Rev.* D54 (1996) 4244;

R. Engel, M. A. Braun, C. Pajares and J. Ranft, *Z. Phys.* C74 (1997) 687;

J. Ranft, A. Capella and J. Tran Thanh Van, *Phys. Lett.* B320 (1994) 346;

H.J. Möhring and J. Ranft, *Z. Phys.* C52 (1991) 643.

[77] CDF Coll., Transverse Momentum Distributions Of Charged Particles Produced In $\bar{p}p$ Interactions At $\sqrt{s} = 630\,GeV$ and $1800\,GeV$, *Phys. Rev. Lett.* 61 (1988) 1819.

[78] B. Batyunya, G. Paić, N. Slavin, Simulation of K^+K^- pair production and detection in ALICE experiment, ALICE Internal Note, *ALICE-INT-1997-26*.

[79] B. Batyunya, A. De Caro, G. Paić, A. Pesci, S. Zaporozhets, Simulation of $\phi \rightarrow K^+K^-$ detection in ALICE experiment, ALICE Internal Note, *ALICE-INT-2003-067*.

[80] G.I. Kopylov, *Phys. Lett.* B50 (1974) 472;

D. Drijard, H.G. Fischer and T. Nakada, *Nucl. Instr. Meth.* A225 (1984) 367;

D. L'Hote, *Nucl. Inst. Meth.* A337 (1994) 544.